



# Quantifying the Impact of Inhomogeneity, Transport and Recombination in Emerging Thin-Film Solar Cells

Pascal Kaienburg

Energie & Umwelt / Energy & Environment

Band / Volume 481

ISBN 978-3-95806-440-9





Forschungszentrum Jülich GmbH  
Institut für Energie- und Klimaforschung  
IEK-5 Photovoltaik

# **Quantifying the Impact of Inhomogeneity, Transport and Recombination in Emerging Thin-Film Solar Cells**

Pascal Kaienburg

Schriften des Forschungszentrums Jülich  
Reihe Energie & Umwelt / Energy & Environment

Band / Volume 481

---

ISSN 1866-1793

ISBN 978-3-95806-440-9

Bibliografische Information der Deutschen Nationalbibliothek.  
Die Deutsche Nationalbibliothek verzeichnet diese Publikation in der  
Deutschen Nationalbibliografie; detaillierte Bibliografische Daten  
sind im Internet über <http://dnb.d-nb.de> abrufbar.

Herausgeber und Vertrieb: Forschungszentrum Jülich GmbH  
Zentralbibliothek, Verlag  
52425 Jülich  
Tel.: +49 2461 61-5368  
Fax: +49 2461 61-6103  
[zb-publikation@fz-juelich.de](mailto:zb-publikation@fz-juelich.de)  
[www.fz-juelich.de/zb](http://www.fz-juelich.de/zb)

Umschlaggestaltung: Grafische Medien, Forschungszentrum Jülich GmbH

Druck: Grafische Medien, Forschungszentrum Jülich GmbH

Copyright: Forschungszentrum Jülich 2019

Schriften des Forschungszentrums Jülich  
Reihe Energie & Umwelt / Energy & Environment, Band / Volume 481

D 464 (Diss. Duisburg, Univ., 2019)

ISSN 1866-1793  
978-3-95806-440-9

Vollständig frei verfügbar über das Publikationsportal des Forschungszentrums Jülich (JuSER)  
unter [www.fz-juelich.de/zb/openaccess](http://www.fz-juelich.de/zb/openaccess).



This is an Open Access publication distributed under the terms of the [Creative Commons Attribution License 4.0](https://creativecommons.org/licenses/by/4.0/), which permits unrestricted use, distribution, and reproduction in any medium, provided the original work is properly cited.

“Instead, at each level of complexity entirely new properties appear, and the understanding of the new behaviors requires research which I think is as fundamental in its nature as any other.”  
-P.W. Anderson in 'More is different', Science (1972)

“Ch-ch-ch-changes! Turn and face the strange!”  
-David Bowie

The cover art is based on two Scanning Electron Microscope images of an attempt to fabricate a compact film of  $\text{Bi}_2\text{S}_3$ . The typical size of one 'flower' is  $1\ \mu\text{m}$ . The processing closely followed that of  $\text{Sb}_2\text{S}_3$  films. The point cloud dividing the image was produced from solar cell performance simulations and shows the typical sigmoidal shape with low and high saturation regimes.

While the results of the simulations and the solar cells fabricated from  $\text{Sb}_2\text{S}_3$  are published in international peer-reviewed journals and presented extensively in this thesis, the  $\text{Bi}_2\text{S}_3$  'flowers' are not part of this thesis' scientific content as the structures are not feasible for solar cell applications. These - in many senses unsuccessful - experiments nevertheless yielded the most visually appealing results of my work. The cover art can be regarded as a tribute to those episodes of my doctoral research that did not produce valuable data and thus to a rarely reported side of scientific work.



# Contents

<b>Abstract</b>	<b>1</b>
<b>Zusammenfassung</b>	<b>3</b>
<b>1. Introduction</b>	<b>5</b>
<b>2. Background</b>	<b>11</b>
2.1. Key Characteristics of Solar Cells . . . . .	11
2.2. Emerging Solar Cell Absorbers . . . . .	13
2.2.1. Requirements for Bulk Absorbers . . . . .	13
2.2.2. Limits and Progress . . . . .	15
2.2.3. The Case of $\text{Sb}_2\text{S}_3$ . . . . .	19
2.3. Thin-Film Solar Cells . . . . .	20
2.3.1. Working Principle of $p$ - $i$ - $n$ Solar Cells . . . . .	22
2.3.2. Design Concept of Thin-Film Solar Cells . . . . .	27
2.3.3. Inhomogeneity in Thin-Film Solar Cells . . . . .	31
2.3.4. Fill Factor and Charge Collection . . . . .	33
2.4. Focus Technologies . . . . .	39
2.4.1. Organic Solar Cells . . . . .	40
2.4.2. $\text{Sb}_2\text{S}_3$ Solar Cells . . . . .	45
<b>3. Methods</b>	<b>49</b>
3.1. Drift-diffusion Simulations . . . . .	49
3.1.1. Mathematical Problem Description . . . . .	50
3.1.2. Generation and Recombination Models . . . . .	53
3.1.3. Physical Remarks . . . . .	55
3.2. Fabrication . . . . .	57
3.2.1. Solar Cell Stack . . . . .	57
3.2.2. $\text{Sb}_2\text{S}_3$ Layers . . . . .	58
3.2.3. Solar Cells . . . . .	60
3.2.4. Processing Conditions and Equipment . . . . .	62

Contents

3.3. Characterization . . . . .	64
3.3.1. Material and Layer Characterization . . . . .	64
3.3.2. Solar Cell Characterization . . . . .	70
<b>4. Pinholes and Non-linear Shunts in Thin-Film Solar Cells</b>	<b>75</b>
4.1. Qualitative Phenomenon . . . . .	76
4.2. Methodology . . . . .	79
4.3. Prediction of Pinhole Impact . . . . .	82
4.4. Comparison of Devices with and without Absorber . . . . .	87
4.5. Discussion . . . . .	89
4.6. Chapter conclusion . . . . .	91
<b>5. Charge Collection in Thin-Film Solar Cells</b>	<b>93</b>
5.1. Fill Factor and Electronic Quality . . . . .	94
5.1.1. Method . . . . .	96
5.1.2. Analytical Estimates . . . . .	99
5.1.3. Optimized <i>FF</i> Model . . . . .	101
5.1.4. Electronic Quality Factor and Model Precision . . . . .	105
5.1.5. Contacts . . . . .	107
5.1.6. Space-charge Region . . . . .	111
5.1.7. Transfer to Inorganic Absorbers . . . . .	116
5.2. Figures of Merit for the Efficiency . . . . .	119
5.2.1. Method . . . . .	121
5.2.2. The $(\alpha\mu\tau)$ -Product . . . . .	121
5.3. Application to Organic Solar Cells . . . . .	126
5.3.1. History of OSC Development . . . . .	126
5.3.2. NFAs with Tunable Absorption Bands . . . . .	130
5.3.3. Enhanced Absorption in OSCs . . . . .	136
5.3.4. Relation between FOMs . . . . .	139
5.4. Chapter Conclusion . . . . .	140
<b>6. Sb<sub>2</sub>S<sub>3</sub> Solar Cells</b>	<b>143</b>
6.1. Layer and Device Optimization . . . . .	144
6.1.1. Annealing Procedure . . . . .	144

6.1.2. Stoichiometry and Energy Levels . . . . .	150
6.1.3. Sb <sub>2</sub> S <sub>3</sub> /HTM Heterojunction . . . . .	154
6.1.4. Optimized Devices . . . . .	155
6.1.5. Summary and Literature Comparison . . . . .	159
6.2. Limiting Factors . . . . .	160
6.2.1. Performance Evaluation . . . . .	160
6.2.2. Impact of Pinholes . . . . .	162
6.2.3. Open-Circuit Voltage Losses . . . . .	164
6.2.4. Defect Density of States . . . . .	166
6.2.5. Charge Carrier Collection . . . . .	170
6.3. Chapter Summary and outlook . . . . .	174
<b>7. Conclusion and Outlook</b>	<b>179</b>
<b>Bibliography</b>	<b>182</b>
<b>A. Evaluation of Absorber Materials</b>	<b>220</b>
A.1. Determine the Band Gap Energy . . . . .	220
A.2. Calculate the Shockley-Queisser Limit . . . . .	221
A.3. Calculate (Non-)Radiative Voltage Losses . . . . .	222
A.4. Calculate the Scharber Efficiency . . . . .	223
A.5. Relations between Photocurrent and Open-Circuit Voltage Loss . . . . .	226
A.6. Organic Solar Cell Development Captured by Two FOMs . . . . .	228
<b>B. Literature Data</b>	<b>229</b>
<b>C. Charge Collection</b>	<b>233</b>
<b>D. Sb<sub>2</sub>S<sub>3</sub></b>	<b>241</b>
<b>E. Recipes</b>	<b>247</b>
<b>F. Glossary</b>	<b>250</b>
<b>Acknowledgements</b>	<b>255</b>
<b>List of Journal Publications</b>	<b>258</b>



# Abstract

Thin-film solar cells represent the most relevant technological extension of the photovoltaic energy conversion landscape, which is currently dominated by silicon technology. However, the very concept of thin-film solar cells brings inherent challenges. Firstly, the deposition of thin-film solar cells with large aspect ratio introduces inevitable lateral inhomogeneity in the structure. Secondly, absorber films deposited from the gas or liquid phase are of inferior electronic quality compared to monocrystalline silicon technology, meaning that charge carrier recombination is enhanced and charge transport is slowed down. This thesis provides methodologies to identify and assess critical parameters for the two major challenges of inhomogeneous absorber layers and absorber layers with low electronic quality. The presented concepts introduce metrics that allow quantitatively evaluating and comparing different materials or systems with respect to the given phenomena. Thus, these concepts will contribute to the continuous and structured technological progress of thin-film solar cells.

Specifically, a methodology is presented to assess any detrimental impact of inhomogeneity in the absorber film in the form of pinholes with regard to the solar cell performance. Different experimentally tested contact configurations turn out to behave qualitatively similar but show major quantitative differences. With regard to the electronic quality, a thorough analysis of the influencing factors on the fill factor is conducted and a material-based electronic quality factor is defined herein. The electronic quality factor functions as a figure of merit for the fill factor that reflects the interplay of charge carrier transport and charge carrier recombination. By providing a method to assess the electronic quality factor of thin-film absorbers through basic characterization methods, the study offers a widely applicable tool to evaluate different materials or technologies in terms of charge carrier collection. This approach is especially valuable for tracking the progress of organic solar cells,

## *Abstract*

where charge carrier collection is often deficient and a large range of different material blends are explored. By incorporating experimental data into simulation-based models, both of the discussed studies on inhomogeneity and electronic quality thus contribute to tackling critical technological challenges for thin-film solar cells.

On the experimental side, I fabricated and characterized layers and solar cells based on antimony sulfide ( $\text{Sb}_2\text{S}_3$ ), whose band gap is almost optimal for a potential application in a tandem solar cell with silicon. In this thesis, single-junction solar cells are produced in a planar device architecture via solution-based spin-coating, which achieve an efficiency approaching 5% for optimized processing conditions. Extensive optoelectronic material and solar cell characterization, as well as the application of the before-mentioned conceptual work to the specific case of  $\text{Sb}_2\text{S}_3$ , yield an unprecedented comprehensive analysis of the loss mechanisms in  $\text{Sb}_2\text{S}_3$  solar cells. The findings reported in this thesis are likely to apply to other literature reports on  $\text{Sb}_2\text{S}_3$  solar cells, meaning that this thesis provides a solid base for the advancement of the technology based on the critical parameters and suitable characterization methods identified herein.

# Zusammenfassung

Dünnschichtsolarzellen sind die relevanteste Ergänzung zu bestehenden Photovoltaiktechnologien, die derzeit durch herkömmliche Siliziumtechnologie dominiert werden. Jedoch birgt das Konzept von Dünnschichtsolarzellen inhärente Herausforderungen. Zum einen führt die Abscheidung von dünnen Schichten über große Flächen, also eine große 'aspect ratio', unvermeidlich zu einer lateral inhomogenen Struktur. Zum anderen weisen die aus der Gas- oder Flüssigphase abgeschiedenen Absorberschichten eine im Vergleich zur monokristallinen Siliziumtechnologie niedrigere elektronische Güte auf, die sich in erhöhter Ladungsträgerrekombination und verlangsamttem Ladungsträgertransport niederschlägt. In dieser Dissertation werden kritische Parameter identifiziert und Methoden entwickelt, mithilfe derer die elektronische Güte und der Einfluss von Inhomogenität des Absorbers auf die Solarzellenleistung evaluiert werden können. Die vorgestellten Konzepte beinhalten Metriken, die es ermöglichen, verschiedene Materialien oder Systeme im Hinblick auf die jeweiligen Phänomene quantitativ zu bewerten und zu vergleichen. Auf diesem Weg trägt diese Arbeit zum kontinuierlichen und strukturierten technologischen Fortschritt von Dünnschichtsolarzellen bei.

Im Einzelnen wird eine Methodik entwickelt, um die nachteiligen Auswirkungen von lateral inhomogenen Absorberschichten auf die Solarzelleneffizienz zu prognostizieren. Verschiedene experimentell untersuchte Kontaktkonfigurationen verhalten sich qualitativ ähnlich, zeigen jedoch große quantitative Unterschiede. In Bezug auf die elektronische Güte wird in dieser Arbeit eine umfassende Analyse des Füllfaktors durchgeführt und ein materialbasierter elektronischer Qualitätsfaktor definiert, der das Zusammenspiel von Ladungsträgertransport und Ladungsträgerrekombination widerspiegelt. Da diese Maßzahl mithilfe vergleichsweise einfachen und weit verbreiteten Charakterisierungsmethoden ermittelt werden kann, stellt der elektronische Qualitätsfaktor ein vielseitig einsetzbares Instrument zur Evaluati-

## Zusammenfassung

on von Dünnschichtabsorbern hinsichtlich der Ladungsträgersammlung dar. Dieser Ansatz ist besonders für organische Solarzellen wertvoll, welche zum einen in den meisten Fällen unter ineffizienter Ladungsträgersammlung leiden und zum anderen auf eine große Vielfalt an organischen Absorbermaterialien zurückgreifen können. Durch die komparative Evaluation verschiedener Materialien kann der Fortschritt innerhalb der Technologie aufgeschlüsselt und verfolgt werden. Somit ziehen beide Studien zur Inhomogenität und elektronischen Güte experimentelle Daten heran, um mittels simulationsgestützter Modelle technologische Herausforderungen von Dünnschicht solarzellen zu meistern.

Von experimenteller Seite wurden im Rahmen diese Arbeit Schichten und Solarzellen auf Basis von Antimonsulfid ( $\text{Sb}_2\text{S}_3$ ), dessen Bandlücke nahezu optimal für eine Anwendung in siliziumbasierten Tandemsolarzellen ist, hergestellt und charakterisiert. Diese Arbeit beschäftigt sich mit 'single-junction'  $\text{Sb}_2\text{S}_3$  Solarzellen in einer planaren Schichtarchitektur und hergestellt mittels nasschemischer Rotationsbeschichtung, für die unter optimierten Prozessbedingungen ein Wirkungsgrad von etwa 5% erreicht wird. Umfangreiche optoelektronische Material- und Solarzellencharakterisierung, sowie die Anwendung der konzeptionellen Evaluationsmethoden auf den spezifischen Fall von  $\text{Sb}_2\text{S}_3$ , münden in einer umfassenden Verlustanalyse von  $\text{Sb}_2\text{S}_3$  Solarzellen. Die Ergebnisse sind mit hoher Wahrscheinlichkeit auf andere Literaturberichte über  $\text{Sb}_2\text{S}_3$  Solarzellen übertragbar. Indem kritische Parameter, sowie geeignete Charakterisierungsmethoden identifiziert wurden, stellt diese Arbeit eine solide Grundlage für die technologische Weiterentwicklung von  $\text{Sb}_2\text{S}_3$  basierten Dünnschicht solarzellen dar.

# 1. Introduction

The photovoltaic (PV) market has been subject to continuous growth as indicated by global annual production and cumulative installed capacity [1]. The large market volume, a widespread consensus among scientists and policy makers on the necessity of renewable energies [2], as well as the diversification of photovoltaic applications [3–6] has driven increased interest into alternatives to conventional crystalline silicon (c-Si) technology, which is referred to as the first generation of solar cells [7]. The most explored pathway are thin-film solar cells which, instead of modifying a silicon wafer, rely on the subsequent layer deposition of different materials from the gas or liquid phase. The established thin-film solar cell technologies based on  $\text{Cu}(\text{In,Ga})\text{Se}_2$  (CIGS) and CdTe absorbers had a market share of around 5% in 2017 [1] and while the modules do not reach the efficiency of c-Si, they offer lower production costs [1]. This concept of low-cost second generation solar cells [7] is characteristic for thin-film PV technology, which at the same time prompts the quest of closing the efficiency gap to c-Si while maintaining low costs. With this aim, many emerging thin-film technologies based on different absorber materials other than the established CdTe and CIGS are investigated. The most successful examples in terms of solar cell efficiency are lead-based perovskites and polymer-based organic solar cells, which have exceeded an efficiency of 23% [8] and 14% [9], respectively. For comparison, established technologies have reached efficiencies above 26% for c-Si [10] and 22% for CIGS [11] and CdTe [11]. Despite these promising achievements of perovskites and organics, a successful introduction to the PV mass market remains to be demonstrated and obstacles towards technological maturity, which include long-term performance stability [12, 13] and up-scaled fabrication [14, 15], have to be overcome. Additionally, the toxicity of lead-containing perovskites is considered problematic [16, 17] and organic solar cells are still aiming for efficiencies well above 15% [18]. Consequently, many groups explore the potential of alternative absorber

## 1. Introduction

materials based on different material classes such as oxides, sulfides, iodides and lead-free perovskites [16, 17, 19–23]. In the context of emerging solar cell absorbers, special attention should be directed towards high-band gap absorbers. While band gaps between 1.1 eV and 1.4 eV are optimal for solar cells based on a single absorber layer [24], tandem solar cells apply one high gap and one low gap absorber material and thereby absorb a broader range of the solar spectrum. Therefore tandem solar cells may exceed the efficiency limit of single absorber cells [7, 25]. If c-Si is used as a low band gap absorber, a large band gap absorber with  $E_g=1.73$  eV would be optimal [26]. Perovskites are considered a promising option [27] but - apart from the challenges mentioned above - have a non-ideal band gap of  $E_g=1.55$  eV for the best performing devices. In conclusion, there are currently no well-performing, stable and non-toxic high band gap solar cell absorbers.

The efficiency that is actually attained by a certain technology depends on many material and device properties apart from the band gap, which merely sets an upper limit for the efficiency. Therefore it is necessary to study the specifics of each absorber technology. On top of any specific challenge, there are issues general to all thin-film technologies, which can thus be regarded as intrinsic characteristics of the thin-film approach. Two common challenges are lateral inhomogeneity and a low electronic quality of the absorber. Inhomogeneity can be attributed to the large aspect ratio of thin-film solar cells [28], which is on the order of  $10^6$ : in industrial module fabrication, the layers are deposited across  $m^2$ -sized areas but have a thickness that ranges from only 10 nm to several  $\mu m$ . Whereas minimizing the undesired variations across a layer is a matter of optimized processing conditions, another (complementary) approach is to mitigate the negative impact of fluctuating physical properties on the device performance. In this context, contact layers with suitable properties may partially compensate detrimental effects of an inhomogeneous absorber layer [28–30] by smoothing out fluctuating  $J$ - $V$  characteristics of different absorber domains. The layer sequence and the material choice for each layer offer ways to tailor the properties of the layers adjacent to the absorber and to improve the cell's robustness against inhomogeneity in the absorber. Regarding the absorber material itself, the thin film deposited from the gas or liquid phase is either amorphous or polycrystalline and generally has a lower electronic quality than monocrystalline silicon, meaning that charge carriers move more slowly and

recombine faster. Therefore, the bulk of the absorber is more likely to limit the solar cell performance than in the case of c-Si where the electronic quality of the bulk absorber is high enough so that the interfaces to the adjacent layers become limiting [31,32]. The electronic quality of the absorber acts in two ways on the solar cell performance. First, the recombination rate determines the photovoltage a solar cell can deliver - referring to a steady-state situation where no current is flowing in or out of the device. Second, at the operating point of a solar cell, where photogenerated charges need to be extracted efficiently from the device, charge carrier transport competes with charge carrier recombination. This means that in absorber materials with low electronic quality, charges are more likely to recombine before they have moved to the contacts, which results in a reduced power output.

Within the context of a specific absorber technology or a given contact configuration, stringent performance optimization supported by detailed study of specific material and device properties are the key to technological progress. Microscopic models of the involved physical phenomena as well as - often approximate - analytical treatments of the impact on device performance supply the qualitative understanding of the specific issues. In today's situation, where a large range of absorber materials and diverse contact configurations are being explored, there is an additional need for comparative methods with which the diverse approaches can be evaluated across different materials and technologies. Such a comparative evaluation method must be widely applicable and based on experimental input that is easy to obtain. It should furthermore yield quantitative data that can be related to the device performance. In the simplest case this would be a single number, referred to as a figure of merit (FOM). Finally, it must be based on a sound physical model that accounts for the complexity of the real-world situation which most likely eradicates the option of a simplified analytical treatment and might require the support by numerical simulations instead. Apart from enabling a comparison across different technologies, such evaluation methods allow to monitor the progress of a specific technology with respect to a certain criterion.

This thesis contributes conceptually to the prevalent challenges of inhomogeneity and low electronic quality in emerging thin-film solar cells by developing comparative methods for contact and absorber materials. The contacts are evalu-

## 1. Introduction

ated in terms of robustness against pinholes in the absorber layer and the absorber is evaluated in terms of charge carrier collection and fill factor. Thereby, two design criteria for thin-film solar cells are deduced and expressed in quantitative terms. Furthermore, this thesis advances the state of technology for the high band gap absorber antimony sulfide ( $\text{Sb}_2\text{S}_3$ ) and an efficiency of 5% is achieved with spin-coated  $\text{Sb}_2\text{S}_3$  solar cells in a planar configuration. Finally, insight into performance limitations is provided, along with routes for progress with a focus on the study of inhomogeneity, recombination, charge collection and the associated electronic quality of  $\text{Sb}_2\text{S}_3$ . The experimental case study of  $\text{Sb}_2\text{S}_3$  thus reflects and makes use of the conceptual work in this thesis.

Chapter 2 presents the background information that is necessary to follow this thesis. First, important requirements of a solar cell absorber are discussed and different emerging and established technologies are compared in terms of performance, whereby major challenges are identified. Next, the working principle of thin-film solar cells is depicted, which leads to a discussion of charge transport mechanisms and the associated photocurrent, charge carrier collection efficiency and fill factor. Then, the defining technological and physical characteristics of thin-film solar cells are compiled and the inherent challenge of inhomogeneity in large-area thin-film devices is introduced. Finally, the two most important material systems for this work - organic polymer:small molecule blends and  $\text{Sb}_2\text{S}_3$  - are presented in more detail.

Chapter 3 presents the experimental and computational methods applied in this thesis. On the simulation side, one-dimensional drift-diffusion modeling of solar cells receives special attention, since the method forms the basis for the studies of charge collection, fill factor and electronic quality in this work. The experimental methods comprise the cell fabrication with a focus on the  $\text{Sb}_2\text{S}_3$  absorber layer, as well as an overview of the applied characterization methods.

Chapter 4 presents the methodology and results for the evaluation of contact layer combinations with respect to the performance decrease caused by pinholes in the absorber layer. The characteristic of the current across the interface at a pinhole is recorded experimentally, which then allows to predict the impact on the performance of an ideal solar cell by a simple equivalent circuit model. Different contact layer combinations, that are typically used in today's solution-processed

solar cells – such as perovskites and  $\text{Sb}_2\text{S}_3$  – show substantial difference in the robustness against pinholes.

Chapter 5 presents the methodology and results for the evaluation of absorber materials with respect to their electronic quality which largely governs the attainable fill factor of the solar cell. The study is a detailed investigation of charge carrier collection in thin-film solar cells that goes beyond existing analytical approximations and instead applies drift-diffusion simulations to account for the complexity of the investigated systems. The focus lies on the case of an homogeneous electric field across the entire absorber but several deviations from the standard case are considered. By varying the simulation input over a large parameter space, a comprehensive model is obtained that yields a good correlation between a herein defined collection coefficient and the fill factor. While the study is of theoretical nature it is clearly aimed at experimental applications. Only using basic solar cell characterization of experimentally fabricated solar cells, the model allows to extract the material-specific electronic quality factor, which is also defined within the model. This figure of merit (FOM) for the fill factor allows to evaluate and compare different materials and track the progress of a certain material. Organic solar cells (OSCs) serve as a prime example for the model, because OSCs represent an entire class of materials with generally similar functionality but quantitatively varying transport and recombination properties. Only by taking the electronic quality factor as a second FOM in addition to the energy level matching in the device, the continuous historical progress of OSC efficiency can be rationalized. Furthermore the acquired insights are transferred to the question whether congruent or complementary absorption bands of donor and acceptor materials in organic solar cells are favorable. Finally, the absorption coefficient is included into the analysis as a third crucial material parameter in addition to mobility and lifetime and it is demonstrated how the interplay of these parameters governs the solar cell efficiency.

Chapter 6 presents the results of optimizing  $\text{Sb}_2\text{S}_3$  solar cells together with the technology's prospects and challenges. Among other emerging technologies – especially when only considering high band gap absorbers suitable as a tandem partner for c-Si –  $\text{Sb}_2\text{S}_3$  has reached promising efficiencies [20]. This work applies a planar layer configuration where the  $\text{Sb}_2\text{S}_3$  is deposited via spin-coating. Two

## *1. Introduction*

different processing routes reported in literature [33,34] are optimized, which results in an efficiency of 5.0% which is among the highest of solution-processed, planar  $\text{Sb}_2\text{S}_3$  solar cells. Since the device physics of  $\text{Sb}_2\text{S}_3$  solar cells is largely unknown, the focus shifts to identifying the technology's limiting factors. The study is centered around the eminent issues of losses in open-circuit voltage and fill factor and provides a coherent picture of the challenges that need to be tackled in the future.

## 2. Background

This chapter introduces the definitions, terminology and established concepts that this thesis builds on. To some extent the current state of relevant technology and literature is reviewed. Chapter 2.1 introduces the key parameters that quantify solar cell performance. Chapter 2.2 discusses the requirements for emerging solar cell technologies and evaluates the progress of different established and emerging technologies by comparing the reported record performances to their theoretical limit. Chapter 2.3 discusses the working principle of thin-film solar cells with a focus on *p-i-n* structures as well as charge transport mechanisms and the resulting charge carrier collection efficiency. Characteristic technological and physical design principles of thin-film solar cells are introduced and the inherent challenge of inhomogeneity in large-area thin-film devices is highlighted. Finally, chapter 2.4 reviews the technological progress and (relevant) device physics of the two absorber technologies that are central to this thesis - namely organic and  $\text{Sb}_2\text{S}_3$  solar cells.

### 2.1. Key Characteristics of Solar Cells

The main purpose of a solar cell is to convert radiative power of the sunlight (or any other light source) into electric power. The corresponding key parameter is the power conversion efficiency (PCE,  $\eta$ ) which is defined as the ratio between incident radiative power  $P_{\text{sun}}$  and electric power  $P_{\text{el}}$  at the optimum working point (maximum power point, *MPP*) of the solar cell where power conversion is maximized

$$\eta = \frac{P_{\text{el,MPP}}}{P_{\text{sun}}}. \quad (2.1)$$

## 2. Background

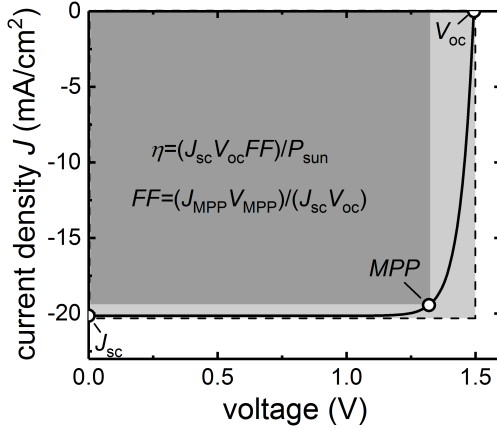


**Figure 2.1.:** Illuminated  $J - V$  characteristic defining a solar cell’s key characteristics. The area ratio of the rectangles yields the  $FF$ .

The efficiency is typically evaluated at a defined incident power of  $P_{\text{sun}} = 1000 \text{ Wm}^{-2}$  given by the standard global AM1.5g spectrum. Note that  $P_{\text{sun}}$  refers to a power per unit area and that this notion of ‘power’ as an area-normalized quantity is used in the following. At the  $MPP$ , the electric output power  $P_{\text{el}} = -J \times V$  given by the current density  $J$  and voltage  $V$ , is typically expressed in terms of the solar cell key parameters short-circuit current-density  $J_{\text{sc}}$ , open-circuit voltage  $V_{\text{oc}}$  and fill factor  $FF$ , which are illustrated in fig. 2.1. In this visual interpretation, the  $FF$  quantifies the degree in which one rectangle, spanned from the  $MPP$  to the current-density and voltage axis, “fills” another rectangle spanned by  $J_{\text{sc}}$  and  $V_{\text{oc}}$  which rationalizes the denomination “fill factor”. In a more physical interpretation the  $FF$  reflects the voltage dependence of the current. It is defined as

$$FF = \frac{J_{\text{MPP}} V_{\text{MPP}}}{J_{\text{sc}} V_{\text{oc}}}, \quad (2.2)$$

which yields the typical expression for the efficiency of a solar cell

$$\eta = \frac{J_{\text{sc}} V_{\text{oc}} FF}{P_{\text{sun}}}. \quad (2.3)$$

## 2.2. Emerging Solar Cell Absorbers

Emerging thin-film solar cell technologies are the main research field of this thesis. A solar cell technology is typically centered around the absorber material or a class of absorber materials. Section 2.2.1 therefore elaborates on the requirements for high-efficiency solar-to-electric power conversion with a focus on the absorber material and its bulk properties. Section 2.2.2 then compares several established and emerging solar cell technologies in terms of the Shockley-Queisser theory as an efficiency limit for solar cells based on a single absorber layer. Along with the overview on relevant photovoltaic properties and progress of different technologies, this chapter points out where certain aspects are discussed in more detail and which role they play in this thesis.

### 2.2.1. Requirements for Bulk Absorbers

A well-performing solar cell must fulfill several requirements concerning the absorber material, interfaces and device architecture. The following aspects mostly concern properties of the absorber material and can be considered as a prerequisite for successful solar cell operation.<sup>1</sup>

1. Suitable band gap

For a single absorber layer and quite general assumptions, Shockley and Queisser calculated an upper limit for solar cell performance that only depends on the band gap of the semiconducting absorber material [24]. The highest efficiencies above  $\eta = 32\%$  can be attained for band gaps between 1.1 eV and 1.4 eV. Section 2.2.2 recaps the achievements of several established and emerging PV absorber technologies in the context of the Shockley-Queisser limit. Tandem solar cells comprise two absorber layers that typically differ in band gap to cover larger parts of the solar spectrum. Consequently the optimum band gaps for the two absorbers differs from that of a single absorber solar cell as will be discussed briefly.

2. High absorptance

---

<sup>1</sup>The listed criteria reflect certain aspects of discussions in standard textbooks [35, 36] as well as refs. [37, 38].

## 2. Background

Photons with an energy higher than the band gap generate free electron-hole pairs in the absorber layer that can contribute to the photocurrent of the solar cell. A considerable photocurrent, which at  $V = 0$  is called  $J_{sc}$ , is mandatory for a decently performing solar cell and requires the absorption of as many incoming photons as possible. Section 2.2.2 touches upon the ways to ensure a high absorptance, which is the corresponding physical quantity defined as the ratio of absorbed to incident photons. In the case of excitonic systems such as organic solar cells, an absorbed photon creates an exciton that needs to be separated in order to create free charge carriers, adding one more criterion to the list of requirements for such solar cells. For many emerging solar cell absorbers a high absorptance and photocurrent (at short-circuit) is not the most critical issue as shown in section 2.2.2.

### 3. Low non-radiative recombination

Free charge carriers may recombine – implying a loss of energy – via several pathways. Radiative recombination cannot be avoided since it is thermodynamically coupled to absorption as stated by the principle of detailed balance [39] and Kirchhoff's law [40]. Any other recombination mechanism such as Shockley-Read-Hall [41, 42], non-radiative direct and surface recombination needs to be suppressed as much as possible in order to minimize losses in the number of free charge carriers. The study of the defect physics, recombination rates and recombination mechanisms with the goal of understanding and reducing losses in the open-circuit voltage is a broad field [38] and a major challenge for most solar cell technologies as will be shown in section 2.2.2. Important factors for non-radiative recombination are the (number) density and energetic position of electronic defects, the electron-phonon coupling and the phonon energies [43–46]. In this thesis the topic of recombination at open-circuit will be touched only sporadically in chapter 6. However, recombination also sets the available time for charge carriers to be extracted from the solar cell when it is not at open circuit. Thus, recombination directly affects the collection of charge carriers – a topic that is central to this thesis.

### 4. Efficient charge carrier collection

In order to contribute to the photocurrent, the photogenerated free charge car-

riers need to be extracted from the solar cell which is also referred to as collection at the contacts. During charge carrier extraction, charge transport to the contacts competes with the recombination of charge carriers. This competition is reflected by drift and diffusive transport models and the underlying product of the material properties charge carrier mobility and lifetime as explained in section 2.3.4. In diffusion-dominated systems, inefficient charge carrier collection mostly affects the short-circuit current, whereas in drift-dominated systems, charge carrier collection strongly depends on voltage, making the fill factor the most critical parameter. The latter case is found in many thin-film solar cells and is investigated in detail in chapter 5.

The discussed optoelectronic material properties of the absorber can be understood as a first order approach for high solar cell performance and thus a starting point to evaluate emerging solar cell absorbers. For an actual solar cell the processing conditions and tuning of material and film parameters such as crystal size are indisputably important. Unsuitable contact layers may reduce device performance as well and critical aspects are e.g. extraction barriers or low built-in fields resulting from unfeasible energy alignment of the bulk absorber with the adjacent layers as will be discussed in section 2.3.1. Nevertheless, the properties of the applied absorber material governs the upper limit of solar cell performance, sets the boundary conditions for the design of the remaining layers and the overall stack architecture and typically constitutes a major limitation during the initial stages of technological development. For more mature and successful technologies the interfaces and contacts gain importance and ultimately become limiting as in the case of crystalline silicon technology [31, 32].

### 2.2.2. Limits and Progress

The Shockley-Queisser (SQ) limit for a single absorber [24] is based on the following assumptions

- the absorptance is a step-function meaning all incident photons with energy  $E_\gamma > E_g$  are absorbed
- every absorbed photon creates one free electron-hole pair that instantly ther-

## 2. Background

malizes to the (sharply defined) band edge

- all recombination pathways are suppressed except the radiative one, implying a diode ideality factor of 1. The emissivity is given by the absorbance as required by detailed balance [39].
- the solar cell is at the same temperature as its surroundings
- the cell is illuminated by the sun. Here, the standard AM1.5g spectrum is assumed.

In this ideal case a solar cell is fully parameterized by the band gap  $E_g$  of the absorber. Analytic expressions for the full  $J - V$  characteristic together with the  $J_{sc}$ , the saturation current density  $J_0$ ,  $V_{oc}$ ,  $FF$  and  $\eta$  can be derived as elaborated in appendix A.2. The lines in fig. 2.2 indicate the SQ limit whereas the data points represent experimentally achieved record results for established [10, 11, 47–49] and emerging [8, 19, 21, 22, 50–56] solar cell technologies. The latter class also comprises organic polymer:small-molecule blends [9, 57–59] and inorganic  $Sb_2S_3$  [20, 60], which are displayed separately due to their central role in this thesis. Since the absorption edge of any real solar cell is to some extent broadened and not an ideal step function as assumed by SQ, a proper definition of  $E_g$  for the experimental data is required in order to locate them in the SQ plot. For this purpose  $E_g$  is defined via the inflection point [61] of the external quantum efficiency ( $EQE$ ) which was shown to allow the comparison across different PV technologies in terms of the SQ limit. See appendix A.1 for details. While the depicted absorber materials cover a wide range of band gaps (criterion 1 in section 2.2.1), there is no established high band gap absorber technology with  $E_g \approx 1.75\text{eV}$  that reaches high efficiencies comparable to the best performing technologies with band gaps in the optimum SQ range.

In order to compare the performance of various absorber technologies with different band gaps, the same data as in fig. 2.2 is displayed in fig. 2.3(a). Here, the losses relative to the SQ limit – deconvoluted into  $J_{sc}$  and  $FF \times V_{oc}$  product – are shown, as was done in ref. [63] with a reduced dataset. The indicated iso-efficiency lines relative to  $\eta_{SQ}$  allow to evaluate the progress of a certain absorber technology with regard to the theoretical SQ limit with more mature technologies located in the top right corner. Additionally, major challenges in terms of the solar cell’s key parameters can be identified. Most data points are located above the

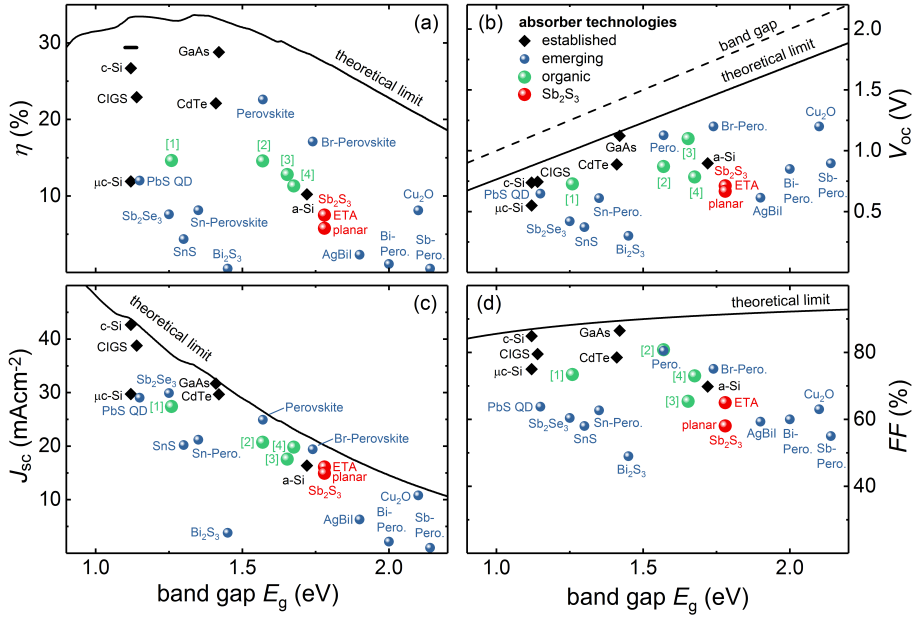


**Figure 2.2.:** Performance limit of a single junction solar cell in terms of (a) power conversion efficiency  $\eta$ , (b) open-circuit voltage  $V_{oc}$ , (c) short-circuit current density  $J_{sc}$  and (d) fill factor  $FF$  with the band gap as the only free parameter according to Shockley-Queisser (SQ) theory [24]. Data points represent today’s best-performing devices from various established [10, 11, 47–49] and emerging [8, 19, 21, 22, 50–56] absorber technologies (see appendix B for values). Two different device architectures are displayed for  $\text{Sb}_2\text{S}_3$ —namely the extremely thin absorber [20] (ETA) and the planar configuration [60]. The four organic polymer:small-molecule blends marked [1] PTB7-Th:COi8DFIC:PCBM [9], [2] PBDB-TF:IT-4F [57], [3] PBDB-TDZ:ITIC [58] and [4] PffBT4T:PCBM [59] reflect the versatility of organic solar cells. The  $E_g$  is determined from the long-wavelength inflection point of the  $EQE$  spectrum. The dash in (a) marks the limit of c-Si when Auger recombination and other effects are considered [62].

## 2. Background

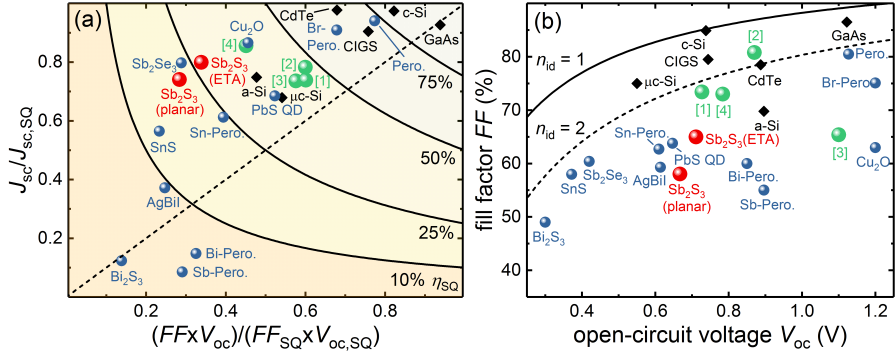


**Figure 2.3.:** (a) Solar cell performance relative to the SQ limit following Polman et al. [63]. Solid iso-efficiency lines relative to the SQ limit help to assert the overall progress of a technology. Most technologies are located above the dashed diagonal, indicating that  $J_{sc}$  losses, that can be partially overcome by optical light management, are less critical than  $FF \times V_{oc}$  losses, indicating the crucial importance of the material’s electronic quality. (b)  $FF$  losses when the  $V_{oc}$  dependence of the  $FF$  limit is accounted for as opposed to fig. 2.2(d). The lines result from Green’s analytical approximation [64]. The data points and legend in (a) and (b) are identical to fig. 2.2.

dashed diagonal of equal loss in  $J_{sc}$  and  $FF \times V_{oc}$  and almost none are located below the diagonal in the plot. Consequently, for the depicted technologies the  $J_{sc}$  and therefore the absorptance (criterion 2 in section 2.2.1) is generally less critical than the electronic quality (recombination and collection, criteria 3 and 4 in section 2.2.1). If all photogenerated charge carriers are collected at the contacts, the  $J_{sc}$  is given by the absorptance in the active layer which is characterized by the product of absorption coefficient and active layer thickness  $\alpha \times d$  [37]. A simple way to increase the  $J_{sc}$  is therefore the use of thicker absorber layers which might however conflict with reduced carrier collection. The  $J_{sc}$  can then still be improved via efficient light management [65–69] which comprises improved incoupling of light and decreased parasitic absorption, as well as light scattering – or more general – light trapping. The latter concept enhances the effective optical path length through the absorber layer – which is especially important for photons with energy close to the band gap where  $\alpha$  is low. Altogether, for most absorber materials,  $J_{sc}$  is less critical than  $FF \times V_{oc}$  and can be further enhanced by light management in the device, which is less dependent on the absorber material itself. The electronic quality encoded in

$FF \times V_{oc}$  (assuming no deteriorating impact of inhomogeneity and a feasible layer stack) is clearly the major challenge for the established and emerging technologies displayed in fig. 2.3(a).

Figure 2.3(b) further deconvolutes the critical parameters by comparing the  $FF$  to the theoretical maximum  $FF$  [64] which is a function of the  $V_{oc}$  and the ideality factor  $n_{id}$  as will be elaborated in section 2.3.4. Typically  $n_{id}$  has values between 1 and 2 and is determined by the mechanism that dominates recombination. Many emerging technologies do not achieve  $FF$ s well above 60% and losses in  $FF$  are clearly visible, even if the  $V_{oc}$  value is accounted for and the worst case (in terms of  $FF$  limit) of  $n_{id} = 2$  is assumed. Consequently charge carrier collection is an important issue that can either be attributed to a low electronic quality of the absorber or a flawed layer and device structure as will be discussed at various points of this thesis.

### 2.2.3. The Case of $Sb_2S_3$

The emerging solar cell absorber antimony sulfide ( $Sb_2S_3$ ) constitutes the major focus of experimental work in this thesis. The highest reported efficiency of 7.5% [20] meets that of other little investigated materials included in fig. 2.2, such as the best lead-free perovskites [52],  $Cu_2O$  [19] and  $Sb_2Se_3$  [23, 50] and outperforms bismuth-halides [21, 70],  $SnS$  [22] and  $Bi_2S_3$  [51, 71, 72]. However, it lacks behind more thoroughly studied material systems such as lead-based perovskites [8], organic solar cells [9, 57] or  $PbS$  [53]. As a little-investigated, but already well-performing high gap solar cell absorber,  $Sb_2S_3$  is predestined – once technological maturity is reached – to be applied in tandem solar cells with crystalline silicon.

Single junction solar cells, discussed in the previous section, are the simplest and most prominent application of photovoltaic absorber materials. Another common application are tandem solar cells, which may overcome the SQ limit for single junctions by reducing the two major loss mechanisms of thermalization and below band gap transmission. A tandem solar cell consists of two stacked single junctions, with a low band gap ( $E_{g,1}$ ) absorber as the bottom cell and a second, high band gap ( $E_{g,2}$ ) absorber as the top cell. Considering assumptions similar to the SQ limit,

## 2. Background

a tandem solar cell is fully parameterized by the band gaps of the two absorbers. The resulting maximum efficiencies are shown in fig. 2.4 for  $E_{g,1} = 1.12\text{eV}$  of c-Si, which is today's most established absorber technology and the natural choice for a bottom cell.<sup>2</sup> Note the sharp drop in tandem efficiency for a shift away from the optimum top cell band gap. Currently, perovskites receive the most attention as tandem partner for c-Si [27], despite their toxic lead content, due to their experimentally demonstrated high performance as single junction up to 23% [8] and two-terminal tandem solar cell [73] up to 25% [74]. However, the band gap of the best-performing perovskite cell is at  $\sim 1.55\text{eV}$ , where the efficiency limit in a tandem application is reduced to  $\sim 30\%$ . The best reported c-Si/perovskite tandem cells apply a perovskite with  $E_g \approx 1.6\text{eV}$  [73,74]. Higher band gaps are achieved by tuning the perovskite composition<sup>3</sup>, but the films become less stable and phase segregation as well as  $V_{oc}$ -saturation becomes a major issue at  $E_g \gtrsim 1.7\text{eV}$  [12, 75–77]. The maximum performance, toxicity and stability concerns for perovskite tandem cells motivates the study of less-explored high band gap absorbers for tandem application with c-Si.

The reported band gap of  $\text{Sb}_2\text{S}_3$  lies between 1.7-1.8 eV [79,80] - depending on the analysis method as discussed in appendix A.1. The data obtained in this thesis yields  $E_g = 1.78\text{eV}$ , which makes  $\text{Sb}_2\text{S}_3$  a perfectly suited candidate for the top cell in a tandem solar cell with c-Si. With reference to fig. 2.2,  $\text{Sb}_2\text{S}_3$  is also the most promising high band gap absorber, due to its superior performance in comparison to other little-investigated materials. However, there is a need for further technological progress, that is achieved best by studying, understanding and improving  $\text{Sb}_2\text{S}_3$  single junctions.

## 2.3. Thin-Film Solar Cells

This chapter introduces some of the key physical concepts relevant for the remainder of this thesis. Section 2.3.1 introduces an exemplary layer stack for thin-film

---

<sup>2</sup>The band gap of the best performing CIGS absorbers is close to that of c-Si.

<sup>3</sup>The band gap is reduced by replacing some of the iodide anions of the standard methylammonium-leadiodide (MAPI,  $\text{MAPbI}_3$ ) perovskite with bromide. Exchanging the MA cation also leads to smaller variations of the band gap.

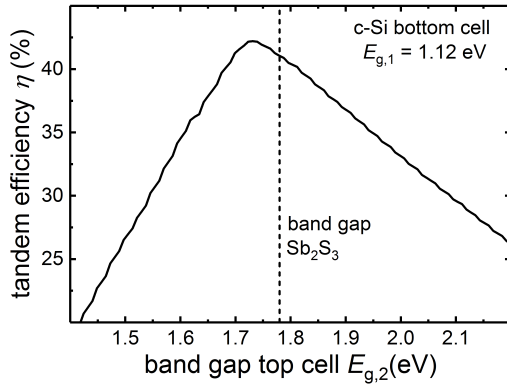


**Figure 2.4.:** Efficiency limit for tandem solar cells based on a SQ-like approach similar to ref. [78] with step function absorptance for top and bottom cell, as well as recycling of photons emitted from the top cell in the bottom cell. The band gap of the bottom cell is fixed at  $E_{g,1} = 1.12$  eV to represent c-Si, whereas the top cell band gap  $E_{g,2}$  is varied. The narrow range of suitable band gaps  $E_{g,2}$  for a c-Si tandem partner is matched by  $\text{Sb}_2\text{S}_3$  with  $E_{g,2} = 1.78$  eV.

solar cells along with each layer's basic functionality. The explanations focus on the band diagram and the consequences for the dominating charge transport mechanism whereby the working principle of *p-i-n*-like thin-film solar cells is demonstrated. Section 2.3.2 then depicts the defining elements of thin-film solar cells from a technological and a device physics point of view, where the latter one focuses on the electric field distribution in the active layer and the associated transport mechanisms. By comparing the essential features of thin-film solar cells to wafer-based crystalline silicon (c-Si) solar cells, a classification of solar cell technologies is obtained. On the technological side, the deposition of thin films across large areas implies an inevitable inhomogeneity in the deposited films, which is discussed in section 2.3.3 and motivates my work presented in chapter 4 on the impact of pinholes in the absorber layer on solar cell performance. Regarding the device physics of thin-film solar cells, the mechanism of charge transport and the resulting efficiency of charge carrier collection is of major importance as expressed by the classification in section 2.3.2. Section 2.3.4 presents existing models for the  $FF$ , photocurrent and charge carrier collection efficiency and thereby sets the framework for the simulation-based results

## 2. Background

on the determining factors of the  $FF$  in thin-film solar cells presented in chapter 5. The focus of this chapter on charge carrier transport results from its implications for the design and architecture of thin-film solar cells. Charge carrier recombination, although crucial for the open-circuit voltage, is discussed mostly as a competing mechanism to charge transport to the contacts, which is fundamental to the fill factor study in chapter 5. However, chapter 3.1 will briefly cover different recombination models and chapter 3.3 discusses voltage losses in the context of experimental electroluminescence measurements.

### 2.3.1. Working Principle of $p-i-n$ Solar Cells

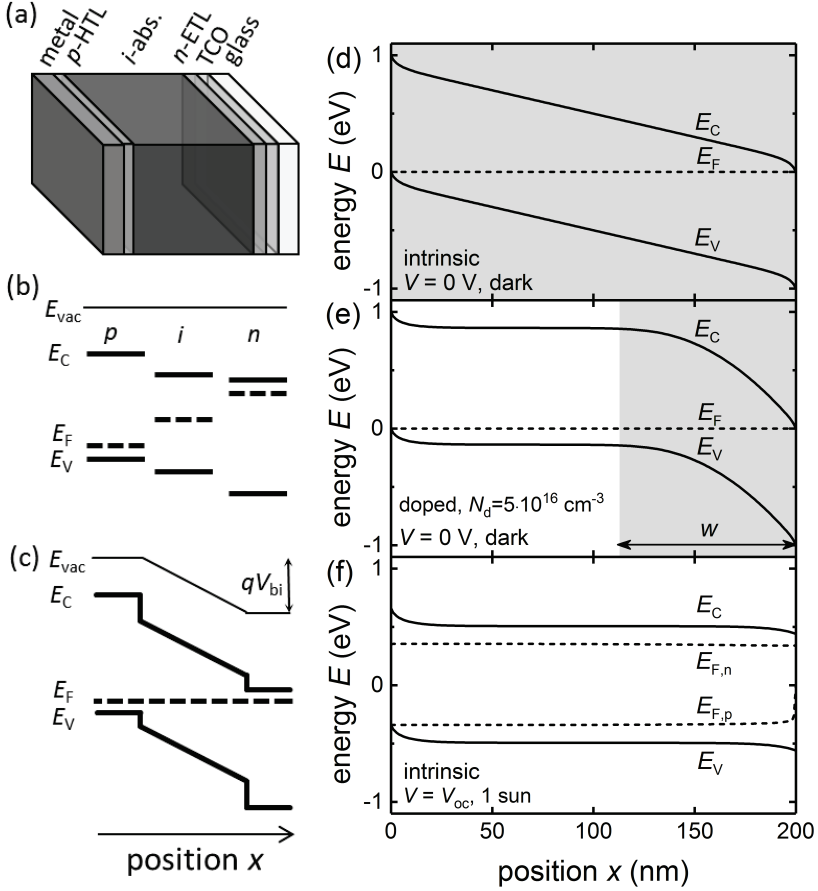
Thin-film silicon solar cells are an early example for a solar cell technology based on a  $p-i-n$  structure [81] and many of the developed models, simulation tools and experimental techniques were later transferred to other  $p-i-n$ -like solar cells. The idea is to induce a constant electric field across the entire absorber layer so that charge transport is driven by an electric field which is advantageous whenever charge carrier diffusion lengths are smaller than the anticipated device thickness [82] as will be explained in more detail in section 2.3.2.

Figure 2.5(a) shows a simple layer stack of a typical thin-film solar cell<sup>4</sup> that consists of a glass substrate and a  $p-i-n$ -like structure sandwiched between a transparent conductive oxide (TCO) front contact and a metal back contact. For reasons explained below, the  $n$ -layer is also referred to as electron transport layer (ETL) and the  $p$ -layer as hole transport layer (HTL). The  $i$ -layer forms the absorber layer, also referred to as active layer.

One important function of the  $p$ - and  $n$ -layer is to create an electric field in the absorber, the so-called built-in field, which results from the equilibration of Fermi levels as illustrated in fig. 2.5(b) and (c). In the isolated state drawn in fig. 2.5(b), the Fermi levels  $E_F$  of the three materials differ: the materials that later form the  $p$ - and  $n$ -layers are doped  $p$ - and  $n$ -type, respectively, and the material that forms the  $i$ -layer is intrinsic, meaning undoped with equal equilibrium electron and hole concentration. When brought into contact, the equilibrium charge carrier concen-

---

<sup>4</sup>The schematic actually shows an  $n-i-p$  solar cell since the light entering through the glass, first passes the  $n$ -layer.



**Figure 2.5.:** (a) Typical layer stack of a  $p$ - $i$ - $n$ -like thin film solar cell. (b) and (c) Schematically drawn energy diagram of the semiconducting layers with conduction and valence band energy ( $E_c$  and  $E_v$ ), Fermi level  $E_f$  and vacuum energy  $E_{vac}$  in (b) the separated state and (c) in contact where the equilibration of the Fermi levels produce the built-in voltage  $V_{bi}$ . (d)-(f) Simulated band diagrams of the active layer in (d,e) equilibrium for a (d) undoped and (e) doped  $i$ -absorber material. The grey areas indicate the space charge region with width  $w$  according to eq. 2.6. (f) Quasi-equilibrium band diagram at open-circuit with flat quasi-Fermi levels for electron  $E_{F,n}$  and holes  $E_{F,p}$ . In contrast to (d,e) a Schottky barrier of  $\varphi_f = 0.1\text{eV}$  is present at the front, causing the offset between  $E_{F,n}$  and  $E_c$ . A high minority carrier surface recombination rate  $S_{f,min} = 10^7\text{cm/s}$  causes an up-bending of the  $E_{F,p}$  at the front contact, while  $S_{b,min} = 1\text{cm/s}$  leads to a flat  $E_{F,n}$  at the back.

## 2. Background

trations – especially in the  $i$ -layer – are altered<sup>5</sup> so that the Fermi level aligns across the whole device (which is by definition required for thermodynamic equilibrium) as shown in fig. 2.5(c). As a consequence, the desired built-in electric field forms in the  $i$ -layer, as indicated in fig. 2.5(c), which is characterized by the built-in voltage  $V_{\text{bi}}$ . In general, the electric field in each point of the device is given by the gradient of the conduction and valence band energies,  $E_c$  and  $E_v$  respectively, or by the gradient of the vacuum energy  $E_{\text{vac}}$

$$F = \frac{1}{q} \frac{\partial E_{\text{vac}}}{\partial x} \quad (2.4)$$

also drawn in fig. 2.5(b) and (c). Here,  $q$  is the elementary charge. The latter definition is more precise since it excludes energetic offsets between two materials at a heterojunction.

Note that in the depicted example the  $p$ - and  $n$ -layer are indeed  $p$ - and  $n$ -doped, respectively. Nevertheless, there are other mechanisms than doping that can influence the Fermi level position in the layers which is in the end defined by the solution of the Poisson equation. Especially when undoped materials are used as  $p$ - or  $n$ -layer, the adjacent layers – such as a metal or a TCO – or a dipole layer at an interface might determine the Fermi level in the  $p$ - and  $n$ -layer. In this generalized sense, the terms  $p$ - or  $n$ -layer have to be understood in the context of a full device as layers where electrons or holes, respectively, are the majority carriers rather than strictly referring to the doping level of a material.

In the schematics in fig. 2.5(b) the conduction bands of the  $n$ - and  $i$ -material as well as the valence band of the  $p$ - and  $i$ -material are not perfectly aligned. These offsets translate to the respective heterojunctions in the full device in fig. 2.5(c) and should not become too large since they reduce the voltage across the  $i$ -layer which can eventually limit the open-circuit voltage and impair charge-carrier collection. On the other hand, a large band offset between the valence band of  $n$ - and  $i$ -layer as well as the conduction band of the  $p$ - and  $i$ -layer as indicated in fig. 2.5(b) and (c) is beneficial because it prevents the minority carriers from traveling to the “wrong” contact, which effectively reduces surface recombination. With regard to minority

---

<sup>5</sup>The charge carrier concentrations depend exponentially on the energetic difference between the Fermi level and the respective band as will be stated mathematically in chapter 3.1.

carriers the  $p$ - and  $n$ -layers thus function as blocking layers, while they act as charge transport layers for majority carriers (therefore the denomination as ETL and HTL). Note that the notion of a minority and a majority carrier species in the active layer is only valid close to the contacts since one carrier type is the minority at one contact and the majority at the other contact while the carrier concentration in the middle of the device is equal for both carrier types.<sup>6</sup>

Figures 2.5(d)-(f) show simulated band diagrams of the active layer without the charge transport layers and the vacuum energy level. The schematic in fig. 2.5(c) and the calculated band diagram in fig 2.5(d) show similar situations that depict a truly intrinsic  $i$ -layer where there are no (net) active dopants and the Fermi level is exactly in the middle of the band gap of the isolated material. The induced electric field  $F$  is then constant across the entire active layer with thickness  $d$  and is given by

$$F = \frac{1}{q} \frac{\partial E_{\text{vac}}}{\partial x} = \frac{V_{\text{bi}} - V}{d}, \quad (2.5)$$

with the built-in voltage  $V_{\text{bi}}$ , also indicated in fig. 2.5(c), and the applied voltage  $V$ . In the presence of active dopants, the electric field redistributes and a space-charge region (SCR) is formed whose width is estimated by the Mott-Schottky analysis [83]

$$w = \sqrt{\frac{2\epsilon_0\epsilon_r(V_{\text{bi}} - V)}{qN_A}}, \quad (2.6)$$

where  $\epsilon_0$  is the vacuum permittivity,  $\epsilon_r$  the (material-specific) relative permittivity,  $q$  the elementary charge and  $N_A$  the density of – in this case acceptor – dopants. The gray areas in fig. 2.5(d) and (e) indicate the SCR of the respective device. For sufficiently low doping levels of the  $i$ -layer, the SCR extends over the entire active layer ( $w = d$ ), as e.g. in the case of an intrinsic absorber simulated in fig. 2.5(d), and the active layer is referred to as fully depleted. For high enough doping levels the space-charge region becomes smaller than the active layer, as is the case in fig. 2.5(e), which increases the electric field strength in the SCR compared to eq. 2.5, while it leaves a certain region – referred to as neutral zone – field-free, where the bands are

---

<sup>6</sup>This situation is fundamentally different to wafer-based silicon technology where a minority carrier species is defined for the largest part of the absorber.

## 2. Background

flat. Note that by applying eq. 2.6, a space-charge region wider than the absorber may result ( $w > d$ ) which is however not physically meaningful (the device is already fully depleted at  $w = d$ ) and must be regarded as an hypothetical width of the space charge region. Apart from intentionally introducing dopants, doping can result from intrinsic defects in a semiconductor material or through its interaction with the atmosphere, e.g. during processing, as was shown for example for organic solar cells [84].

So far, the band diagram in equilibrium was considered. Figure 2.5(f) shows the band diagram of an intrinsic absorber under illumination at open-circuit. The photogeneration of electron-hole pairs leads to the splitting of the Fermi level into quasi-Fermi levels for electron  $E_{F,n}$  and holes  $E_{F,p}$ . A voltage applied in forward direction counteracts the built-in voltage according to eq. 2.5 which leads to a redistribution of charge carriers and thus a flattening of the bands. At  $V_{oc}$ , no net current flows into or out of the solar cell, implying flat quasi-Fermi levels. At the *MPP*, the voltage is typically closer to  $V_{oc}$  than to short-circuit ( $V = 0V$ ), resulting in flattened bands and reduced electric field compared to short-circuit. Nevertheless, a gradient in the quasi-Fermi levels is present due to the current flow out of the device.

As a last aspect to the working principle of *p-i-n*-like and thin-film solar cells in general, I will elaborate on the consequences of the band diagram for charge transport. The presence or absence of an electric field at a certain point in the device determines the transport mechanism of photogenerated charges at that point. An electric field exerts a force on a free charge carrier that causes a directed motion along the electric field, which is referred to as drift. In addition, a charge carrier moves around randomly, implying that the motion is not directed and not initiated by a force. Nevertheless, in the presence of a gradient in charge carrier concentration the random movement leads to an effective displacement of the statistical ensemble of charge carriers, which is referred to as diffusion. At short-circuit, diffusive movement (or transport) of photogenerated charge carriers dominates in the neutral zone with vanishing electric field, while drift transport dominates in the SCR in the presence of an electrical field. In a competing process to transport, the photogenerated charge carriers recombine after a certain time  $\tau$ . Consequently, charge carriers travel a

certain (average) distance before they recombine – the drift length  $L_{\text{dr}}$  or diffusion length  $L_{\text{diff}}$  given by

$$L_{\text{dr}} = \mu\tau F \text{ and} \quad (2.7a)$$

$$L_{\text{diff}} = \sqrt{D\tau} = \sqrt{\frac{k_{\text{b}}T}{q}}\mu\tau, \quad (2.7b)$$

with the mobility  $\mu$ , lifetime  $\tau$ , electric field  $F$ , diffusion constant  $D$ , Boltzmann constant  $k_{\text{b}}$  and temperature  $T$ . These transport lengths, or similar quantities, are central for the efficiency of charge carrier collection at the contacts and thereby impact the optimum design of solar cells from a device physics point of view, as will be discussed at different points in the following sections.

### 2.3.2. Design Concept of Thin-Film Solar Cells

Thin-film photovoltaics can be understood as an alternative fabrication and design concept that contrasts wafer-based solar cells such as crystalline silicon. During the typical fabrication of the latter one, wafers are converted into functional solar cells by local treatments that modify material properties, such as the interdiffusion of dopants. Only few process steps such as the metallization and anti-reflection coating are not based on a modification of the wafer. Thin-film solar cell fabrication on the other hand is based on subsequently depositing several layers to build a full solar cell. The approach can be described as strictly additive in contrast to transformative as in the case of wafer-based technologies. Thin-film solar cells typically comprise multiple functional layers that fulfill different tasks, resulting in a more complex layer stack. For example, a glass superstrate provides mechanical stability, a structured front contact provides light trapping and the contact and charge transport layers generate the built-in electrical field. For wafer-based cells all these functionalities are covered by the (modified) wafer itself [85]. Additional common features of thin-film PV technologies include the polycrystalline or amorphous nature of the absorber layer in contrast to the case of mono- or multi-crystalline silicon wafer technology. Enabled by the additive approach, the materials used in the remaining functional layers

## 2. Background

differ from the absorber material for many thin-film solar cells (apart from most thin-film silicon devices). This results in non-epitaxial growth and the formation of heterojunctions in contrast to the homojunctions formed during the transformation of a wafer.

The major motivation for thin-film solar cells is a cost reduction compared to standard silicon technology which directly sets the challenge to obtain a high efficiency at low production and system costs. A potential cost advantage stems from the reduced use of material and deposition via gas-phase-based vacuum or wet-chemical solution processes that require lower process temperatures compared to crystal growth processes needed for wafers. Additional advantages include a reduced energy payback time due to low process temperatures and the possibility to use flexible and light-weight substrates which opens up new applications and potentially lowers systems costs [86]. Wafer-based solar cells measure a couple of inches and are assembled into a solar module by soldering the bus bars of different cells in series. In the case of thin-film technology the various layers are deposited across large areas of several square meters. After deposition, a layer is typically patterned into multiple stripes via mechanical or laser scribing before the next layer is deposited – leading to serially interconnected cell stripes in the final module. As opposed to assemblage in the case of c-Si modules, thin-film module fabrication is monolithic. Here, the alternating sequence of deposition and patterning might be advantageous for solution processes, since gas-phase processing requires a vacuum break between deposition and laser scribing.

All of the emerging solar cell absorbers introduced in chapter 2.2 are thin-film technologies. In addition, there are industrially established thin-film technologies such as CIGS, CdTe and thin-film silicon that together have a market share of around 5% [1]. In an interesting technological development, the fabrication of silicon heterojunction (SHJ) solar cells as a wafer-based technology integrates and adapts the additive approach of thin-film fabrication.

Apart from technological aspects, the classification into thin-film and wafer PV can be understood from a device physics point of view that focuses on how photogenerated charge carriers are transported to the extracting contacts [37, 82], which is crucial for the collection efficiency of charge carriers. The prevailing mechanism

**Table 2.1.:** Distinct features of wafer-based crystalline silicon (c-Si) and thin-film solar cells. Details and precise values depend on the technology and might be subject to technological advance.

	(c-Si) wafer	thin-film
layer growth	crystal growth epitactic	gas- or liquid phase non-epitactic
process temperature	high, $> 1000$ °C	low, $\sim 100$ °C
crystallinity	mono or multi	poly or amorphous
absorber thickness	$> 100$ $\mu\text{m}$	$\sim 1$ $\mu\text{m}$ other layers $\sim 10$ nm
cell size (diameter)	$\sim$ inches	$\sim$ m
cell fabrication	(mostly) transformative	additive
module fabrication	assemblage	monolithic
mechanical stability	wafer	glass, plastic
number of layers	$\approx 4$	$\approx 8$
functionality	incorp. in wafer	distrib. to var. layers
junction types	homo	mostly hetero
electronic quality	high	lower
$w/d$	$\ll 1$	$\lesssim 1$
main transport mech.	diffusion	drift, in cases partially diffusive
band gap	indirect	direct

## 2. Background

of charge transport is determined by the distribution of the electric field within the active layer. As mentioned in section 2.3.1, in the presence of an electric field – meaning in the space-charge region (SCR) – carrier transport is drift-dominated, while in the absence of an electric field – meaning in the neutral zone – carriers move via diffusion. The characteristic ratio  $w/d$  [82] between SCR width  $w$  and absorber layer thickness  $d$  reflects the size of the SCR and the neutral zone and thereby which charge transport mechanism prevails for the largest (average) distance traveled by the charge carriers on their path to the contacts. Note that for any well-working solar cell a built-in electric field is required or at least advantageous [38, 83, 87]. Charge carriers (or more precisely for the case of  $w/d \ll 1$ : at least one charge carrier species) thus always cross a region with electric field where transport is drift-dominated. However in the case of  $w/d \ll 1$ , charge carriers move via diffusion for the largest part of their way to the contacts. For the purpose of classifying different solar cell technologies according to their  $w/d$  ratio [82], a device in equilibrium is considered so that  $V = 0$  V in eq. 2.6. Wafer-based silicon solar cells represent an extreme case where  $w \ll d$  so that the largest part of the device is field-free and transport is mostly diffusive. In the other extreme case of a fully depleted device  $w = d$  and charge transport is governed by drift. Thin-film solar cells comprise devices where  $w \leq d$  meaning that  $w$  and  $d$  are roughly on the same order of magnitude [82].<sup>7</sup>

The choice of absorber thickness  $d$  is mainly a result of the tradeoff between high absorptance – preferring a thick absorber – and efficient charge carrier collection at short-circuit and the *MPP* – preferring a short distance from the position of free carrier generation to the extracting contact. The absorption length  $L_\alpha = \alpha^{-1}$ , where  $\alpha$  is the absorption coefficient, can provide an estimate for an absorber thickness that enables high absorptance in a simple Lambert-Beer picture. However, this estimate bears imprecision since  $L_\alpha$  is wavelength dependent and increases with increasing wavelength. In any case,  $L_\alpha$  should be evaluated at long wavelengths close to the absorption edge. At the same time, the absorber layer must not be thicker than the drift or diffusion length ( $d \lesssim L_{\text{dr}}, L_{\text{diff}}$ ) to enable efficient charge carrier collection.

---

<sup>7</sup>The classifications according to technological aspects and device physics coincide for most absorber technologies except for dye-sensitized solar cells (DSSCs). From the technological point of view, DSSCs belong to thin-films but regarding the electrical field distribution  $w \ll d$  for DSSCs [82] (like for c-Si wafers).

The polycrystalline or amorphous nature of thin-film solar cells comes along with shorter drift and diffusion lengths compared to c-Si wafers. Apart from saving material and processing time this is the main reason for the low thickness of thin-film technology. A thin device directly sets the demand for a strongly absorbing material to achieve  $L_\alpha \lesssim d$ . Semiconductors with an indirect band gap  $E_{g,\text{indir}}$  are thus mostly unsuitable for thin-film solar cells, because of the slow rise of the absorption coefficient with energy. A direct band gap  $E_{g,\text{dir}}$  (or quasi-direct one where  $E_{g,\text{dir}} \approx E_{g,\text{indir}}$  [88]) is favorable, which amorphous and molecular semiconductors always fulfill but often face bigger issues with charge carrier collection. Typical absorber thicknesses for thin-film solar cells are between a few hundreds of nm (organics, a-Si, perovskites, CdTe) and few  $\mu\text{m}$  ( $\mu\text{c-Si}$ , CIGS) and more or less provide full absorptance. In summary, the absorber layer thickness  $d$  is a critical parameter for solar cell performance and needs to fulfill  $L_\alpha \lesssim d \lesssim L_{\text{dr}}, L_{\text{diff}}$  where the latter comparison depends on the dominant transport mechanism.

The characteristic technological and functional differences between wafer-based silicon solar cells and thin-film technologies are again summarized in table 2.1.<sup>8</sup>

### 2.3.3. Inhomogeneity in Thin-Film Solar Cells

The defining elements of thin-film solar cell technology given in the preceding section 2.3.2 include a large aspect ratio of  $\sim 10^6$  between the layer thickness and one of the the lateral layer dimensions for the case of industrial module production.<sup>9</sup> It has been argued that lateral inhomogeneity regarding structural and functional properties is unavoidable in such structures and should therefore be regarded as intrinsic to thin-film solar cell technology [28], which seems to hold true in practical cases. In an early stage of technology, which is characterized by small-scale fabrication in research laboratories, new polycrystalline absorber materials tend to suffer from inhomogeneous films and especially pinholes in the absorber layer [89]. Examples include emerging absorber technologies introduced in section 2.2.2 such as  $\text{Sb}_2\text{S}_3$  [90, 91],  $\text{SnS}$  [92] and lead-free perovskites [16, 93]. In the case of better

<sup>8</sup>The listed criteria are mostly based on refs. [82, 85].

<sup>9</sup>Given a film thickness between 10 nm (in case of interlayers) and up to 100-1000 nm (in case for the absorber layer) and a module size on the order of  $\text{m}^2$ . For  $\text{cm}^2$ -sized cells on the lab scale it is still  $\sim 10^4$

## 2. Background

investigated lead-based perovskites, the complex mechanisms of film formation from solution [94, 95] can be controlled in certain optimized spin-coating processes which yield compact, homogeneous and pinhole-free perovskite layers [96–100]. However, up-scaled industrial fabrication requires deposition methods other than spin coating [101] and faces more processing constraints such as high yields, high throughput and low solvent toxicity [102, 103]. As of today, pinholes in the absorber layer remain a challenge in up-scaled perovskite fabrication [14, 102] as well as in the already established thin-film photovoltaic technologies CdTe [104–106], Cu(In,Ga)Se<sub>2</sub> (CIGS) [107, 108] and thin-film silicon [107–109]. In a simplified picture, different (lateral) domains of a solar cell – represented by diodes with different characteristics – are connected in parallel, meaning that domains with inferior photovoltaic properties may dominate the behaviour of the complete device. Inhomogeneity must thus be regarded as being potentially critical to the performance of thin-film solar cells.<sup>10</sup>

Regarding the consequences of pinholes in the absorber layer, the choice of contact layers plays a critical role since at a pinhole, the electron transport layer (ETL) and hole transport layer (HTL) come in direct physical and electrical contact. A pinhole thus represents a parasitic current path - parallel to the regular absorber domains - which is commonly denoted as shunt. For the case of CIGS solar cells it has been shown that incorporation of an layer of undoped zinc oxide (*i*-ZnO) as part of the front contact reduces the detrimental impact on solar cell performance caused by inhomogeneity across the absorber film [29] – including the worst case of a pinhole. The *i*-ZnO is unfavorable when considered only in a one dimensional band diagram, but its benefit can be understood in terms of two-dimensional variations of the electronic properties across the absorber film [29]. As demonstrated by a detailed experimental study [111], the impact of shunts from pinholes in the CIGS absorber is further reduced reliably by an additional layer of CdS deposited in a chemical bath that ensures a more closed coating than the sputtered *i*-ZnO. The example of CIGS shows that careful engineering of the contact layers also with respect to inhomogeneity or shunts is mandatory to achieve a high solar cell performance.

For the case of perovskite, Sb<sub>2</sub>S<sub>3</sub> and other solution-processed thin film solar

---

<sup>10</sup>Parts of this section (2.3.3) reflect or are identical to my contributions to the first-author publication “How Contact Layers Control Shunting Losses from Pinholes in Thin-Film Solar Cells”. Reprinted in part with permission from ref. [110]. © 2018 American Chemical Society.

cell technologies, a large variety of electron and hole contact layer combinations is applied which represents a powerful degree of freedom in the stack design. Certain interlayers were also reported to increase the robustness of perovskite solar cells towards shunts [112,113]. This observation is understandable since the current voltage characteristic of the ETL/HTL contact at a pinhole determines whether or not the resulting shunt is detrimental for the solar cell [112, 114]. Consequently, different ETL/HTL combinations are expected to cause different shunt characteristics. However, although a detrimental impact of pinholes is widely recognized and postulated [115–118], the electronic nature of pinholes is not well understood and models that describe the impact of pinholes on the solar cell performance are missing. Additionally, neither a systematic evaluation of contact layers with respect to their robustness against shunting from pinholes, nor a suitable method to do so has been reported so far.

### 2.3.4. Fill Factor and Charge Collection

Apart from the technological particularities of thin-film solar cells leading to the implications discussed in section 2.3.3, section 2.3.2 introduced a classification of solar cells according to the ratio  $w/d$  between absorber thickness and width of the space-charge region, that focuses on the device physics. The associated distribution of the electric field across the absorber layer largely affects the mechanism of charge transport, which ultimately determines the efficiency of charge carrier collection at the contacts and the fill factor  $FF$  of a solar cell as will be discussed in the following.

An idealized solar cell, that follows Shockley's diode equation and includes the (at this point empirical) diode ideality factor  $n_{id}$  and the saturation current density  $J_0$ , is described via

$$J = -J_{sc} + J_0 \left( \exp\left(\frac{qV}{n_{id}k_bT}\right) - 1 \right), \quad (2.8)$$

which corresponds to the simple equivalent circuit in fig. 2.6 without the dashed circuit elements that indicate parasitic resistances.

By installing this analytical relation between  $J$  and  $V$ , the solar cell's  $MPP$  - and thereby the  $FF$  - is found from maximizing the electrical output power

## 2. Background

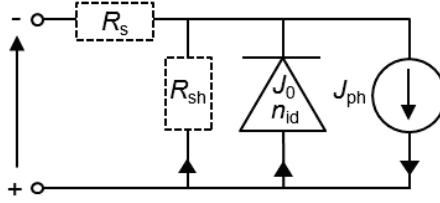


**Figure 2.6.:** Simple equivalent circuit of a solar cell consisting of a Shockley diode and photocurrent source. More realistic parasitic resistances (dashed elements) that might be voltage-dependent. The arrows indicate the direction of the current.

$P_{el} = -J(V) \cdot V$ . The absolute maximum  $V_{MPP}$  obtained from solving

$$\frac{dP_{el}}{dV} = \frac{d}{dV}(-J(V) \cdot V) \stackrel{!}{=} 0 \quad (2.9)$$

directly yields  $J_{MPP}$  via eq. 2.8 and the  $FF$  via eq. 2.2. Equation 2.9 cannot be solved analytically. However, several analytical approximations [64, 119–121] of the numerical solution were suggested with a prominent one [64] being

$$FF = \frac{v_{oc} - \ln(v_{oc} + 0.72)}{v_{oc} + 1}, v_{oc} = \frac{qV_{oc}}{n_{id}k_bT} \quad (2.10)$$

where  $v_{oc}$  is the open-circuit voltage normalized to the ideality factor. The analytic approximation was shown to be accurate for solar cells with appreciable  $V_{oc}$  [119, 120]. More specifically a very good agreement is observed for values of  $v_{oc} > 5$  [120] which corresponds to  $V_{oc} = 130\text{mV}$  for  $n_{id} = 1$  or  $V_{oc} = 260\text{mV}$  for  $n_{id} = 2$  and the value at  $v_{oc} = 10$  is accurate to the fourth significant digit [119]. Equation 2.10 and the corresponding graphs in fig. 2.3 express that the theoretical limit of the fill factor depends on the attained  $V_{oc}$  of the solar cell.

A more realistic solar cell model includes an ohmic series resistance  $R_s$  indicated as a dashed circuit element in fig. 2.6 which can e.g. originate from the resistance of contact layers such as the metal grid in the case of c-Si solar cells or the TCO in the case of thin-film solar cells. The series resistance introduces a characteristic slope at  $V_{oc}$  and leads to a decrease in  $FF$ , which can be approximated analytically [64, 119]. Similarly, an ohmic parallel (or shunt) resistor  $R_{sh}$  introduces a characteristic slope at  $J_{sc}$  and its impact on the  $FF$  can be approximated ana-

lytically. However, an ohmic shunt resistor cannot grasp, for example, the effect of pinholes in the absorber which presents a significant source for shunts in thin-film solar cells as will be discussed in chapter 4.

So far, a low open-circuit voltage, an ideality factor larger than one and ohmic series and parallel resistance have been identified to decrease the fill factor, which can be expressed via analytical approximations. In general the discussed parameters may depend on voltage. Even more important for many thin-film solar cells, the superposition principle  $J = -J_{sc} + J_{\text{dark}}$  was assumed to be valid so far. In other words the photocurrent ( $J_{\text{ph}}$ ) was assumed to be independent of voltage and thus equal to the short-circuit current for all voltages  $J_{\text{ph}}(V) = J_{sc}$ . This assumption does not hold true for many thin-film solar cells [122]. Since the  $FF$  reflects the voltage-dependency of the total solar cell current, a voltage-dependent photocurrent will affect the  $FF$ . In the following, this voltage dependency is discussed together with the closely related concept of charge carrier collection efficiency.

Crandall derived an analytical approximation for the photocurrent of fully depleted  $p$ - $i$ - $n$ -like solar cells where transport is drift-dominated [123]. The expression is deduced from the continuity equations and assumes a constant electric field across the absorber as well as negligible diffusive transport of charge carriers. Recombination follows Shockley-Read-Hall statistics which implies that surface recombination is neglected and the collection of charge carriers is given by the properties of the bulk absorber. Crandall's work refers to amorphous silicon as the archetype of  $p$ - $i$ - $n$  solar cells but was later successfully applied to other material systems such as organic solar cells [124]. Under the discussed assumptions the photocurrent is approximated by

$$J_{\text{ph}}(V) = q\bar{G}(L_{\text{dr,n}} + L_{\text{dr,p}}) \left( 1 - \exp\left(-\frac{d}{L_{\text{dr,n}} + L_{\text{dr,p}}}\right) \right), \quad (2.11)$$

$$L_{\text{dr,n/p}} = \mu_{\text{n/p}} \tau_{\text{n/p}} \frac{V_{\text{bi}} - V}{d},$$

where  $q$  is the elementary charge,  $\bar{G}$  is the spatially averaged generation rate and  $d$  is the thickness of the active layer and  $L_{\text{dr,n}}$  and  $L_{\text{dr,p}}$  are the characteristic

## 2. Background

drift lengths of electron and holes, respectively. The voltage dependence of the photocurrent is contained in the dependence of the drift lengths on the electric field in the absorber  $F = (V_{\text{bi}} - V)/d$  where  $V_{\text{bi}}$  is the built-in voltage across the active layer and  $V$  is the applied voltage. A crucial factor for the drift length and therefore the photocurrent is the material-specific mobility-lifetime ( $\mu\tau$ )-product which can vary over several orders of magnitude. Note that the calculation of the  $FF$  from analytical solutions of the photocurrent still requires solving eq. 2.9 by numerical means.

Next, the relationship between photocurrent and collection efficiency is established. Generally, the photocurrent of a solar cell can be expressed via the external quantum efficiency ( $EQE$ )

$$J_{\text{ph}}(V) = q \int_0^{\infty} EQE(\lambda, V) \phi_{\text{AM1.5}} d\lambda \quad (2.12)$$

where  $\phi_{\text{AM1.5}}$  is the solar spectrum and  $\lambda$  is the wavelength of the incident light. Equation 2.12 merely assumes a linear dependence of the photocurrent on light intensity. The  $EQE$  can be further divided into an optical and an electrical term

$$EQE(\lambda, V) = \int_0^d g(\lambda, x) f_c(x, V) dx \quad (2.13)$$

where  $g(\lambda, x)$  is the generation rate of free charge carriers as a result of absorption and  $f_c(x, V)$  is the collection efficiency that expresses the probability with which a generated electron-hole pair is extracted at the contacts and contributes to the photocurrent. So far it is assumed that  $g(\lambda, x)$  is independent of voltage - meaning that light absorption is independent of voltage. In the case of organic solar cells (OSCs) this assumption also implies that exciton dissociation is independent of voltage which certainly holds true for most high-performing OSCs where all geminate recombination is negligible [125–128].

To reconcile eq. 2.11 with eq. 2.12 the spatially averaged collection efficiency

$$\bar{f}_c(V) = \frac{1}{d} \int_0^d f_c(x, V) dx = \frac{J_{\text{ph}}(V)}{q\bar{G}d} \quad (2.14)$$

is defined in two ways. The notion of an average collection efficiency in eq. 2.14

provides a qualitative understanding of the collection process. However in terms of  $EQE$  and  $J_{\text{ph}}$  calculation, the averaging is only reasonable if either charge generation  $g(\lambda, x)$  or charge collection efficiency  $f_c(x, V)$  are independent of position because otherwise the convolution of both quantities and their dependence on position will affect the  $EQE$  in eq. 2.13. For the discussed case of drift-dominated transport the definitions are consistent if the drift collection efficiency is spatially constant  $f_{c,\text{dr}}(x) = \text{const.}$  which was shown for representative numerical studies in the case of OSCs [124]. The remaining integrals over  $g(\lambda, x)$  then result in the spectrally and spatially averaged generation rate  $\bar{G}$  and the average collection efficiency is given by

$$\bar{f}_{c,\text{dr}}(V) = \frac{(L_{\text{dr},\text{n}} + L_{\text{dr},\text{p}})}{d} \left( 1 - \exp\left(-\frac{d}{L_{\text{dr},\text{n}} + L_{\text{dr},\text{p}}}\right) \right). \quad (2.15)$$

In the other extreme case of negligible electric fields, transport is governed solely by diffusion. The diffusion collection efficiency  $f_{c,\text{diff}}(x)$  may then vary with position and is given by the spatial variation of excess charge carrier density  $\Delta n$  as stated by the Donolato theorem [129]  $f_{c,\text{diff}}(x) = \Delta n(x) / \Delta n(0)$ . For a device with defined minority carrier species and negligible surface recombination, resulting e.g. from a  $p$ - $n$  junction with large base, the analytical solution gives

$$f_{c,\text{diff}}(x) = \exp\left(-\frac{x}{L_{\text{diff}}}\right), \quad L_{\text{diff}} = \sqrt{D\tau} = \sqrt{\frac{k_{\text{b}}T}{q}} \mu \tau \quad (2.16)$$

with the diffusion constant  $D$ , mobility  $\mu$  and lifetime  $\tau$  of the minority carrier species that define the corresponding diffusion length  $L_{\text{diff}}$ . From the first expression in eq. 2.16 the average collection efficiency can be calculated

$$\bar{f}_{c,\text{diff}} = \frac{L_{\text{diff}}}{d} \left( 1 - \exp\left(-\frac{d}{L_{\text{diff}}}\right) \right), \quad (2.17)$$

which is equal to the last expression in eq. 2.16 under the assumption of a spatially constant generation rate. Note that only the properties of the carrier species that makes up the minority carriers is relevant for this case. In the drift case the sum of both carrier types and thereby the longer drift length is relevant since no minority or majority carrier species exists over the entire region of the active layer and charge transport is ambipolar. There are more notable differences between the drift- and

## 2. Background

diffusion- dominated case even if eq. 2.15 and eq. 2.17 have the same form. There is no voltage dependence in the diffusive case which implies that the  $FF$  is not affected even if the collection efficiency is generally low - implying a low  $J_{sc}$ . For both drift and diffusive transport the  $(\mu\tau)$ -product sets the characteristic length scale but for drift it goes in linear and for diffusion it goes in with the square root.

From an experimental point of view, the voltage dependence of the photocurrent and the spectral dependence of the  $EQE$  [130] can be used to obtain information on the charge transport mechanism in the tested solar cell [131]. Purely diffusive transport does not result in a voltage dependency of the  $J_{ph}$  and  $EQE$  as opposed to the case of drift transport as is evident from eq. 2.15 and eq. 2.17. Furthermore, the spectral information obtained from  $EQE$  encodes spatial information through  $g(\lambda, x)$ , stemming from the wavelength-dependence of the absorption coefficient: in general, high energetic blue photons are absorbed within the first few nanometers of the absorber while low energy red photons are absorbed weakly by the material and thus lead to a more homogeneous generation profile. Note that the spatial variation of the generation profile becomes more complex in the presence of interference effects from untextured thin-films [124]. For known  $g(\lambda, x)$ , obtained e.g. from optical simulations, the position dependence of the charge carrier collection efficiency  $f_c$  can be extracted from the  $EQE$ . For diffusive transport and incomplete collection,  $f_c$  heavily depends on the distance of the generated minority carrier to the extracting contact and is thus position-dependent. For drift-transport  $f_c(x)$  is difficult to compute analytically since recombination rates are not constant across the absorber, but must be symmetric around the center of the absorber (for same values of electron and hole mobility and lifetime) due to the homogeneous electric field and symmetric bands. Furthermore, numerical simulations allow to compute the collection efficiency as has been done in ref. [124] resulting in a mostly position independent  $f_c(x) = const.$

Real thin-film solar cells might not be governed purely by diffusive or drift transport. In a partially depleted device, the neutral region is almost field-free while the electric field is enhanced in the space-charge region. The size of the regions will change with applied voltage [84]. Even in fully depleted devices, at voltages close to  $V_{oc}$  the bands become flat, the electric field is low and diffusion might become

relevant. Finally, for sufficiently long drift or diffusion lengths of the bulk absorber, recombination at the surface or interface will contribute to recombination. The problem can again be solved analytically in the case of diffusive transport in a  $p$ - $n$  junction by replacing the bulk diffusion length with an effective diffusion length that includes recombination processes at one surface. For drift transport the problem is more complicated [132]. Many of the discussed scenarios are hard to describe analytically and one-dimensional drift-diffusion simulations can give more insight.

The different models for the fill factor can be organized as follows: When the superposition principle is valid, a simple 0D model illustrated by an equivalent circuit can successfully describe the  $FF$ 's behaviour. For a voltage-dependent photocurrent 1D models that are based on drift-diffusion equations need to be applied. As described in section 2.3.3, 2D models are needed to describe the influence of lateral inhomogeneity on the  $FF$  (although an effective parametrization might be possible). This thesis studies effects of 1D-transport and 2D-inhomogeneity on the fill factor.

## 2.4. Focus Technologies

This chapter introduces the two solar cell technologies that are most central to this thesis. Organic polymer:small molecule blends form an entire class of materials that is in the focus of simulation-based studies on the competition between charge transport and recombination in chapter 5. Section 2.4.1 presents the particularities of organic solar cells and recapitulates the progress in efficiency enabled by the large variety of available material combinations. I focus on an existing figure of merit (FOM) for the solar cell performance to interpret these achievements and point out literature reports that the FOM cannot capture, which leads up to my contribution in chapter 5. The fabrication and characterization of the emerging absorber material antimony sulfide ( $\text{Sb}_2\text{S}_3$ ) in chapter 6 draws the main experimental efforts of this thesis. Section 2.4.1 reviews the state of reported research on  $\text{Sb}_2\text{S}_3$  based solar cells, which covers different device architectures and deposition methods, certain material properties, as well as technological progress and major challenges.

## 2. Background

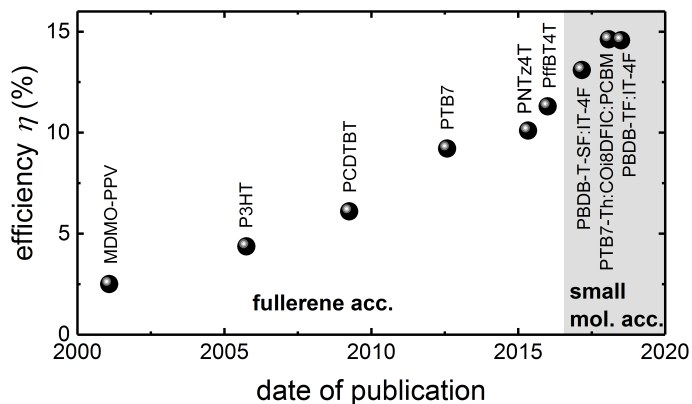


**Figure 2.7.:** Historical progress in efficiency of the best-performing polymer-based organic solar cells [9, 57, 59, 133–138]. Until roughly 2016 the indicated polymers were blended with PCBM. Since then other small molecule acceptors delivered the highest efficiencies.

### 2.4.1. Organic Solar Cells

Organic solar cells have experienced a continuous increase in efficiency as depicted in fig. 2.7 and the versatility in the design of organic materials<sup>11</sup> makes organic photovoltaics an interesting, interdisciplinary and broad field of research. Organic solar cells comprise semiconducting polymers and small molecules which both have a low dielectric constant of  $\epsilon_r \sim 3.5$  so that excitons form upon photon absorption, as indicated in fig. 2.8(a), which subsequently need to be split into free charge carriers. This is achieved by a so-called bulk heterojunction (BHJ), illustrated in fig. 2.8(b), which combines two (or more [139]) suitable organic materials into a blend with nanometer-sized domains. In a BHJ, the photogenerated exciton may diffuse to the heterointerface as shown in in fig. 2.8(a), where it is split into a free electron-hole pair, driven by an increase in free energy. During the separation process the charge carriers pass through a bound state at the interface that is referred to as charge transfer state (CT state) before they reach the unbound charge separated state (CS state). The electron transfers to the (electron) acceptor material, typically a small molecule indicated by the darker shade in fig. 2.8, and the hole transfers to the

<sup>11</sup>See appendix F for the full names of organic materials.

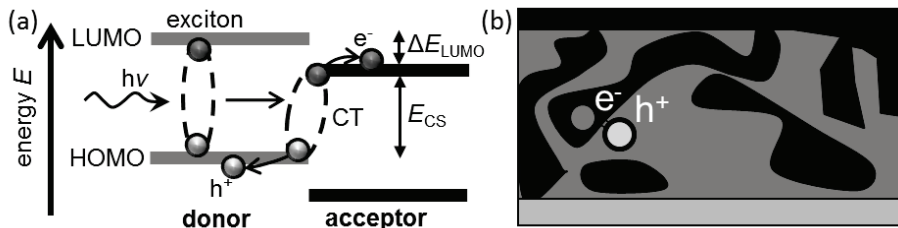


**Figure 2.8.:** Simplified energy scheme (a) and morphology (b) of an organic BHJ. The heterointerface of the material blend allows the splitting of the photogenerated exciton into free charge carriers which are then transported to the respective extracting contacts.

donor material, typically a polymer and indicated by the lighter shade in fig. 2.8. Roughly speaking, the acceptor material transports free electrons and the donor materials transports free holes to the respective extracting contact, although the actual mechanisms of charge transport are complex and related to the morphology and phase mixture of the material blend [140–144]. The lowest unoccupied molecular orbital (LUMO) of the acceptor thus takes the role of the conduction band and the highest occupied molecular orbital (HOMO) of the donor takes the role of the valence band when comparing an organic BHJ to an inorganic semiconductor. The resulting effective band gap for free charges is given by the energy difference  $E_{CS}$  between acceptor LUMO and donor HOMO.

The impressive efficiency increase evident from fig. 2.7 was driven by the development, synthesis and design of new organic semiconductor materials. Until roughly 2016 the most efficient blends contained the UV-absorbing fullerene derivative PCBM as electron acceptor. In fig. 2.7, the first depicted polymers MDMO:PPV and P3HT have an unfavorably large band gap  $E_g \gtrsim 2\text{eV}$  far away from the Shockley-Queisser optimum which implies an inefficient use of the solar spectrum and a low attainable short-circuit current  $J_{sc}$ . Additionally, a large HOMO energy of the polymer relative to the PCBM acceptor leads to a large LUMO offset  $\Delta E_{LUMO}$  and a small effective 'diagonal' band gap  $E_{CS}$  of the separated charge carriers and therefore a large loss in open-circuit voltage  $\Delta V = 1/qE_g - V_{oc}$ .<sup>12</sup> The subsequent improvements in efficiency - achieved by reducing the polymer's band gap and lowering its

<sup>12</sup>Although this voltage loss definition is common for OSCs, the theoretical SQ  $V_{oc}$  limit is actually below  $E_g$  as shown in fig. 2.2. Also see appendix A.4.

## 2. Background

HOMO - is captured by the so-called Scharber plot [145].<sup>13</sup> Assuming PCBM as acceptor material and a fixed  $EQE$  and  $FF$ , organic solar cell efficiencies  $\eta_{\text{Sch}}$  were predicted by Scharber et al. from the polymer band gap and HOMO position. The voltage loss was assumed to be given by the resulting LUMO offset  $\Delta E_{\text{LUMO}}$  and an additional empirically obtained loss of 0.3 V, which was later attributed to non-radiative losses via the CT state [146, 147]. Since the predicted Scharber efficiency  $\eta_{\text{Sch}}$  evaluates the energy alignment of the BHJ, I also refer to  $\eta_{\text{Sch}}$  as energy level matching. Figure 2.9 shows a generalized version of the Scharber plot which takes the open-circuit voltage loss  $\Delta V$  as an independent variable instead of deducing  $\Delta V$  from the polymer-PCBM energy alignment. Thereby acceptor materials other than PCBM can be included in the analysis. Appendix A.4 describes the calculations in detail and comments on the applied method to determine the band gap energy from experimental data.

A breakthrough in OSC efficiency was the discovery of efficient blends that apply small molecules other than PCBM. This discovery introduced another degree of freedom in organic solar cell material development beyond the path of optimizing the polymer's energy levels as indicated by Scharber. Such blends based on so-called non-fullerene acceptors (NFAs) enabled the further increase in efficiency up to almost 15% [9] as shown in fig. 2.7. Blends based on NFAs could further reduce voltage losses, mainly by shifting the CT state energy closer to the absorption offset of the blend. Most experimental reports entered in the Scharber plot in fig. 2.9(a) have a slightly higher band gap than the calculated optimum, which indicates that there is room for improvement in the design of OSC materials with regard to the band gap. This is supported by the fact that the record OSC [9] has a low band gap close to 1.2 V, with similar band gaps for efficient solar cells reported recently [148, 149]. Altogether, the data in fig. 2.9(a) tends towards the optimum region predicted by the Scharber analysis. The Scharber efficiency  $\eta_{\text{Sch}}$  is thus a valuable figure of merit for the design of organic solar cell materials, which is further supported by the correlation shown in fig. 2.9(b) between Scharber efficiency  $\eta_{\text{Sch}}$  and actual efficiency  $\eta$  of selected noticeable experimental reports. However, there are several material

---

<sup>13</sup>The following considerations partially reflect my contributions to the second-author publication "Figures of Merit Guiding Research on Organic Solar Cells". Reprinted in part with permission from ref. [110]. © 2018 American Chemical Society

blends, including the two best performing OSCs as-of-today, that achieve a similar efficiency but differ significantly in Scharber efficiency as marked by the circles in fig. 2.9(b). This discrepancy suggests that the Scharber analysis neglects at least one other important performance aspect of OSC materials. The  $FF$ s of the experimental data points in fig. 2.9(c) all lie between 60% and  $\sim 75\%$  but certain polymer:PCBM based blends reach this  $FF$  at a much higher optimum thickness. One of them is PffBT4T [59] which reaches a high efficiency at comparably low energy level matching as can be seen from fig. 2.9(c), which hints towards a difference in charge carrier collection efficiency between blends with high and low optimum thickness.

Part of the protocol for optimizing a given material blend is to find the optimum thickness  $d$  of the active layer. Most of the record OSCs, including all NFA-based systems, reach optimum performance at  $\sim 100$  nm and few perform best above 200 nm as can be seen in fig. 2.9(c). The discrete nature of this distribution can be rationalized by optical interference in the flat layer stack that evokes maxima in the maximum attainable  $J_{sc,max}$ -thickness relation shown in fig. 2.9(d). The curve is based on optical transfer matrix method simulations of the generation rate in the active layer of a typical OSC layer stack, which translates to the  $J_{sc}$  in the case of ideal carrier collection. The reason for a low optimum thickness is that the  $FF$  sharply drops with increasing thickness for many OSCs [154–157], meaning that charges are not collected efficiently for a large active layer thickness. Here, another important feature of OSC comes into play: compared to inorganic materials, organic materials generally have a lower mobility. Figure. 2.9(c) shows drift-diffusion simulations of the fill factor's thickness dependence for typical OSC parameters. The mobility  $\mu$  is varied between the curves which causes large differences in  $FF$  when comparing points with identical thickness and an overall qualitatively different thickness dependence. Note that not all light is absorbed at an active layer thickness of  $d = 100$  nm. By setting the  $EQE$  and  $FF$  to constant values, the Scharber analysis neglects differences in charge carrier collection and optimum thickness between different material blends. However, certain blends that include the well-studied benchmark polymer P3HT [134] and the best performing PCBM-based blends with  $\eta \approx 10\%$  [59, 137], have an optimum active layer thickness above 200 nm. This sets the motivation for studying collection issues and the determining factors for the  $FF$  of organic solar cells as a low-mobility system in chapter 5. In particular, mate-

## 2. Background

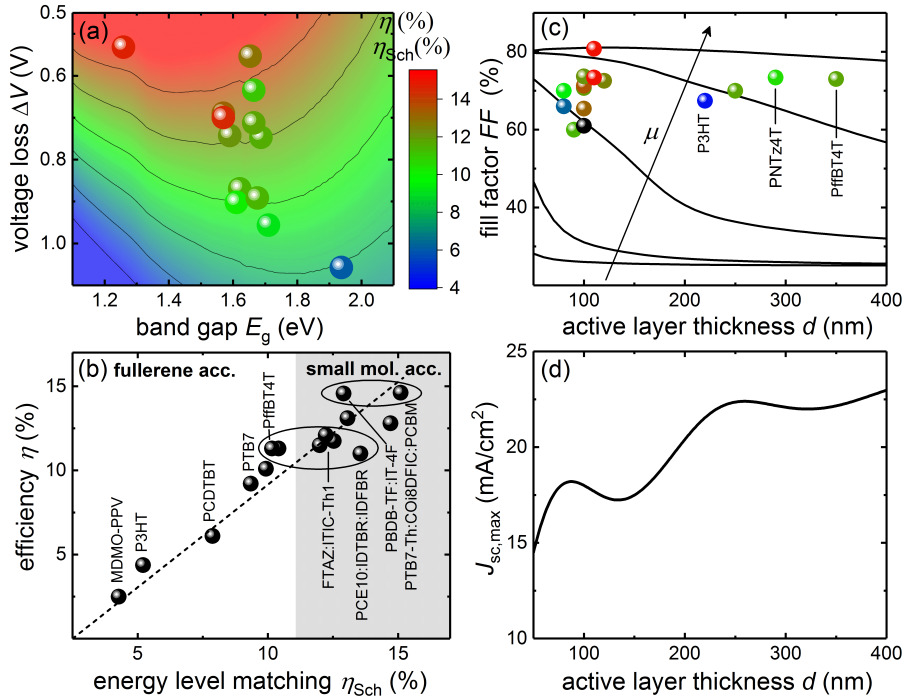


**Figure 2.9.:** Key aspects of organic solar cell material development. Data points are extracted from selected noticeable literature reports [58, 139, 150–153], in addition to all points shown in fig. 2.7 (see appendix B for values). (a) The colormap shows the Scherbar efficiency  $\eta_{Sch}$  based on  $EQE = 0.8$  and  $FF = 70\%$  that reflects the energy level matching of the BHJ, while the data points show the experimentally obtained efficiency. Overall, the two quantities show a good correlation in (b) but some material blends with almost equal efficiency, marked by the circles, show a significant spread in  $\eta_{Sch}$ . The dashed line is drawn as a guide to the eye. (c) The degree in which the simulated  $FF$  drops with thickness depends heavily in the mobility  $\mu$ . While the experimental data points have similar  $FF$ s, they differ in the optimum layer thickness hinting towards different material properties regarding charge carrier collection. The gap in optimum efficiency around  $d = 150$  nm stems from interference in the flat layer stack that causes minima in the attainable short-circuit current shown in (d).

rial parameters shall be identified that set the solar cell's potential of reaching a large  $FF$  at high optimum thicknesses required for full absorptance. The analysis, together with Scharber's considerations, enables a comprehensive interpretation of OSC evolution up to the present day. The study of charge collection furthermore serves as guide for future development of OSCs beyond the reduction of voltage losses as discussed by Scharber.

### 2.4.2. $Sb_2S_3$ Solar Cells

Antimony sulfide is a high band gap absorber, that is suitable for tandem solar cells and that has demonstrated comparably high efficiencies as discussed in chapter 2.2. In this thesis, I work with spin-coated  $Sb_2S_3$  solar cells in a planar configuration, which I will rationalize in the following.

$Sb_2S_3$  has first reached considerable attention as a photovoltaic absorber in Extremely Thin Absorber (ETA) solar cells for which  $Sb_2S_3$  holds the efficiency record of 7.5% [20]. The device architecture and working principle of ETA devices is similar to that of dye-sensitized and quantum-dot sensitized solar cells [158]. A thin  $Sb_2S_3$  layer of around 10 nm [159] is deposited on a mesoporous  $TiO_2$  scaffold and the pores are subsequently filled with a solid-state hole transport material (HTM) - typically a polymer or small molecule. The first  $Sb_2S_3$ -based ETA solar cell was reported in 2009 [80] with a power conversion efficiency of  $\eta = 3.4\%$ . The choice of HTM has been one driving factor in the improvement of  $Sb_2S_3$ -ETA solar cells. While the small molecules CuSCN [80] and spiro-OMeTAD [160] reached efficiencies below 4%, conjugated polymers yielded higher efficiencies of  $\eta > 5\%$  for P3HT [161] and  $\eta > 6\%$  for PCPDTBT [20, 162].

In general, planar geometries reduce the interface area of the  $Sb_2S_3$  and should better prevent direct contact between the electron and hole transport layers compared to the ETA configuration. Both aspects should reduce recombination [163]. Indeed, despite lower efficiencies, planar geometries have reached slightly higher  $V_{oc}$ s [164, 165] than the best performing ETA cells [20, 162] - especially when devices are compared that apply the same  $Sb_2S_3$  deposition method [161, 164] or the same HTM [34, 60, 90, 160, 161] or both [20, 33, 91, 163, 164, 166]. Having a less

## 2. Background

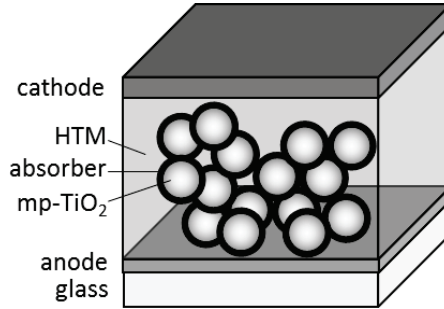


**Figure 2.10.:** Device architecture of an extremely thin absorber (ETA) solar cell – similar to that of DSSCs.

complex morphology than ETA devices which require the proper infiltration of the mesoporous  $\text{TiO}_2$  scaffold [159], planar architectures can be fabricated via various deposition methods. *p-i-n* structures were realized via evaporation [167] ( $\eta = 1.7\%$ ), CBD [164] ( $\eta = 4.1\%$ ) and ALD [60] ( $\eta = 5.8\%$ ). Early reports from the 90s apply a TCO/ $\text{Sb}_2\text{S}_3$ /Au stack [168,169] and reach  $\eta = 5.8\%$  under non-standard AM1 illumination [165] and in analogy to the CdTe technology, TCO/CdS/ $\text{Sb}_2\text{S}_3$ /Au cells were fabricated via rapid thermal evaporation [170] ( $\eta = 3.5\%$ ). Apart from a broader choice of processing routes, planar architectures can generally rely on detailed device models that allow a better applicability of characterization methods and their proper interpretation in comparison to ETA architectures.

Most reports on ETA architectures employ Chemical Bath Deposition (CBD) to coat the mp- $\text{TiO}_2$  covered substrates with  $\text{Sb}_2\text{S}_3$ . During CBD the substrates are submerged in an aqueous solution of suitable precursors, typically  $\text{SbCl}_3$  and  $\text{Na}_2\text{S}_2\text{O}_3$  [80, 168, 171, 172]. The resulting  $\text{Sb}_2\text{S}_3$  film is, like for most fabrication routes, amorphous and needs to be crystallized at temperatures above  $250^\circ\text{C}$  [173]. While CBD only requires a simple setup, the precise control of processing conditions is challenging which – in combination with heterogeneous nucleation and a complex, exponential growth mechanism - impedes the process' reproducibility [33, 60]. During chemical reactions in the water bath, various antimony oxides, hydroxides and sulfates form [20, 174–176]. Deep Level Transient Spectroscopy measurements showed a reduced density of deep traps after post-treating the CBD-deposited  $\text{Sb}_2\text{S}_3$  with sulfur from a liquid source [20]. Surface-sensitive XPS measurement revealed a

simultaneous decrease in oxide phases such as  $\text{Sb}_2\text{O}_3$ . The resulting increase in  $V_{\text{oc}}$  and  $J_{\text{sc}}$  mark today's record efficiency of  $\eta = 7.5\%$  indicating that an oxide-free synthesis route would be beneficial.<sup>14</sup> As a faster and simpler deposition method that additionally excludes oxygen, several spin-coating routes have been reported more recently [33,34,90,91,178]. As a common feature, an antimony- and sulfur-containing complex is formed in a precursor solution. After spin-coating, the precursor is thermally decomposed at intermediate temperatures around  $200^\circ\text{C}$ . Just as with CBD, the resulting film is amorphous and needs to be crystallized at higher temperatures. While an ETA cell prepared via spin-coating reached an efficiency of  $\eta = 5.3\%$  (and  $\eta = 6.4\%$  by mixing PCBM in the hole transporting polymer) [33], most reports apply a planar *p-i-n* geometry [34, 90, 91, 178] and have reached efficiencies up to  $\eta = 4.3\%$  [34] as of early 2018.

Given that the community working on  $\text{Sb}_2\text{S}_3$  photovoltaics is comparably small, it is likely that many of the discussed deposition routes and device architectures are far from their full potential. It is therefore advisable to consider certain material properties relevant to PV performance, which supplies an understanding of the device functionality, identifies possible challenges and limitations to device performance and can further elude on the feasibility of device structures. High activation energies of dark conductivity at room temperature [179–182], Hall measurements [168] and UPS studies [60, 183] point towards the intrinsic nature of antimony sulfide. Taken into account that Mott-Schottky analysis of capacitance-voltage data might only give an upper limit for the doping concentration for lowly doped films [83], several reports support this finding [169, 170]. One study even showed that excess antimony or sulfur concentrations lead to similarly high activation energies of conductivity between  $0.5\text{eV}$  and  $0.6\text{ eV}$  [179]. However, one report claims activation energies below  $0.2\text{ eV}$  [184]. There are no reports that prove successful intentional doping of  $\text{Sb}_2\text{S}_3$  by incorporating other atomic species which would allow the tailoring of the electric field distribution in the  $\text{Sb}_2\text{S}_3$  absorber. The most-likely intrinsic nature of  $\text{Sb}_2\text{S}_3$  implies that planar junctions are fully depleted, meaning that a homogeneous electrical field is present in the absorber. This also holds true

---

<sup>14</sup>One study [177] on ETA  $\text{Sb}_2\text{S}_3$  solar cells showed a short air exposure to be beneficial – which was attributed to reduced interface recombination – while longer exposure times deteriorate the solar cell.

## 2. Background

for the mentioned structures that include one or two metal contacts instead of a  $p$ -type or  $n$ -type semiconductor. For a depleted  $\text{Sb}_2\text{S}_3$  absorber, charge transport is drift-governed which is favorable over diffusion for low  $(\mu\tau)$ -products [37, 82] as described in section 2.3.4 and underlines the feasibility of a planar  $p$ - $i$ - $n$  geometry.

Altogether, even though  $\text{Sb}_2\text{S}_3$  planar devices have not yet reached the efficiency of ETA devices, reported efficiencies above 4-5% [34, 60, 164] for different deposition methods - including spin-coating - demonstrate the general feasibility of planar structures. These literature results, together with the expected benefit of an oxide-free process route, rationalizes the approach of spin-coated, planar  $\text{Sb}_2\text{S}_3$  solar cells taken in this thesis. Nevertheless, fig. 2.3(b) shows that the  $FF$  of planar devices lags behind that of ETA devices and achieves only mediocre values compared to other technologies. The Shockley-Queisser and Polman plots in fig. 2.2 and fig. 2.3(a), respectively, show that the  $J_{sc}$  of  $\text{Sb}_2\text{S}_3$  is less critical, but apart from the  $FF$ , the  $V_{oc}$  is strongly reduced compared to its theoretical potential. There is little and not fully conclusive experimental research [20, 185] on the defect physics of  $\text{Sb}_2\text{S}_3$  that might explain the voltage loss. In summary,  $\text{Sb}_2\text{S}_3$  has been proven a promising high band gap solar cell absorber that requires further progress in technology and especially understanding of the device physics by studying charge collection and recombination to explain the losses in  $FF$  and  $V_{oc}$ . An enhanced understanding eventually allows to identify challenges, limitations and routes for progressing  $\text{Sb}_2\text{S}_3$  technology.

## 3. Methods

This chapter presents the simulation and experimental methods applied in this thesis. Chapter 3.1 covers the equations, assumptions and limitations of the drift-diffusion model which can be regarded as the standard model for the physics of solar cells and reflects some of the aspects discussed in previous chapters. Chapter 3.2 depicts the fabrication of  $\text{Sb}_2\text{S}_3$  layers and solar cells. Chapter 3.3 introduces the applied characterization methods. Data analysis and theoretical calculations involved Matlab for the most part, which I will not describe here.

### 3.1. Drift-diffusion Simulations

Numerical drift-diffusion simulations enable the computation of current-voltage curves and associated quantities from a set of parameters that describe the involved materials, layers and contacts, with modest computational effort.<sup>1</sup> Drift-diffusion simulations were successfully applied to many different thin-film solar cell technologies, including disordered systems such as amorphous silicon [186] and organic solar cells [187]. Chapter 5 of this thesis is largely based on drift-diffusion simulations in order to study the relation between transport, recombination and the fill factor in low-mobility solar cells. I furthermore make use of drift-diffusion simulations to support and offer interpretations for the experimental results on  $\text{Sb}_2\text{S}_3$  in chapter 6, with the construction of the device's band diagram being a simple example. In section 3.1.1, I present the drift-diffusion model in mostly mathematical terms.<sup>2</sup> In section 3.1.2 I briefly discuss models for the generation and recombination of free charge carriers. The generation rate serves as input for the actual drift-diffusion

---

<sup>1</sup>The computation of one  $J-V$  characteristic in the context of chapter 5 takes less than 30 s on a standard office PC.

<sup>2</sup>The equations follow refs. [186, 187].

### 3. Methods

simulation and is computed from optical models, that are typically part of drift-diffusion simulation software. Finally in section 3.1.3 I comment on some of the assumptions and limitations of drift-diffusion simulations. At the same, the equations presented in this chapter represent the mathematical formulation of concepts, such as recombination, mentioned at different parts of this thesis. Drift-diffusion simulations were performed with Advanced Semiconductor Analysis (ASA).

#### 3.1.1. Mathematical Problem Description

The so-called “drift-diffusion” model is a semi-classical description of a semiconductor device with the density of free charge carriers in the bands and the electric potential as central quantities. The model is expressed by three coupled partial differential equations, namely the Poisson equation and a continuity equation for each of the two types of charge carriers. The model is usually considered in one dimension with  $x$  as the position along the cell stack. In the following, a homogeneous material is considered meaning that the material parameters mobility  $\mu_{n,p}$  and thus the diffusion constant  $D_{n,p}$ , relative permittivity  $\epsilon_r$ , band gap  $E_g$ , electron affinity  $\chi$  and effective density of states in the bands  $N_{c,v}$  are assumed to be independent of position so that they can be moved before the spatial derivatives. The Poisson equation governs the electrostatic potential  $\varphi$  in the device

$$\frac{\partial^2 \varphi}{\partial x^2} = -\frac{\varrho}{\epsilon_0 \epsilon_r} \quad (3.1a)$$

with the net charge density  $\varrho$  and the vacuum permittivity  $\epsilon_0$ . The net charge density is given by the sum of the carrier densities of free electrons  $n$  in the conduction band, free holes  $p$  in the valence band, localized charges  $p_{\text{loc}}$  and  $n_{\text{loc}}$  trapped in defects and band tails, and ionized (active) donors  $N_d$  and acceptors  $N_a$ .

$$\varrho = q(p - n + p_{\text{loc}} - n_{\text{loc}} + N_d - N_a).$$

The continuity equations for free charge carrier density of electrons  $n$  and holes  $p$  directly follow from the law of charge conservation and are given by

$$\frac{\partial n}{\partial t} = G - R + \frac{1}{q} \frac{\partial J_n}{\partial x} \quad (3.1b)$$

$$\frac{\partial p}{\partial t} = G - R - \frac{1}{q} \frac{\partial J_p}{\partial x}. \quad (3.1c)$$

Equations 3.2 connect generation rate  $G$  and recombination rate  $R$  of free charge pairs with charge transport expressed by the respective charge currents  $J_n$  and  $J_p$ . By applying semi-classical transport models such as the Boltzmann transport equation, the current in the volume of the solar cell can be expressed via a drift and a diffusive term as

$$J_n = qD_n \frac{\partial n}{\partial x} + qF\mu_n n \quad (3.2a)$$

$$J_p = -qD_p \frac{\partial p}{\partial x} + qF\mu_p p \quad (3.2b)$$

where  $D_n$  and  $D_p$  are the diffusion constants of the respective charge carriers,  $\mu_n$  and  $\mu_p$  are the charge carrier mobilities and  $F = \partial\varphi/\partial x$  is the electric field (for a spatially uniform material and in the absence of heterojunctions as will be discussed below). These relations leave the electrostatic potential and the free charge carrier densities of electrons and holes as the only three independent variables in the drift-diffusion model. To simplify eqs. 3.1 steady-state situations are considered where  $\partial n/\partial t = 0$  which converts the set of partial differential equations into ordinary ones with  $x$  as the only variable. The set of drift-diffusion equations is then given by

$$\frac{d^2\varphi}{dx^2} = -\frac{\rho}{\epsilon_0\epsilon_r} \quad (3.3a)$$

$$G - R = -D_n \frac{d^2 n}{dx^2} - \mu_n \frac{d}{dx} \left( \frac{d\varphi}{dx} n \right) \quad (3.3b)$$

$$G - R = -D_p \frac{d^2 p}{dx^2} + \mu_p \frac{d}{dx} \left( \frac{d\varphi}{dx} p \right) \quad (3.3c)$$

### 3. Methods

Suitable boundary conditions complete eqs. 3.3 so that a well-posed problem is obtained. Since there are three second-order differential equations, six boundary conditions are required. The boundaries are represented by the metallic contacts referred to as anode and cathode. One common option are Schottky contacts where band offsets and surface recombination at both contacts define the boundary conditions. For the Poisson equation Dirichlet boundary conditions are applied by defining the electrostatic potential at the anode (assumed at  $x = 0$ ) and cathode (assumed at  $x = d$ )

$$\varphi(x = 0) = \varphi_a \tag{3.4a}$$

$$\varphi(x = d) = \varphi_c. \tag{3.4b}$$

As boundary conditions for the continuity equations the currents at both contacts are specified via surface recombination velocities of both majority  $S_{\text{maj}}$  and minority carriers  $S_{\text{min}}$ . In a bipolar device, electrons are the majority carriers at the anode and holes are the majority carriers at the cathode. With this nomenclature the four remaining boundary conditions are given by

$$J_n(x = 0) = qS_{n,\text{maj}}(n(0) - n_0(0)) \tag{3.5a}$$

$$J_p(x = 0) = qS_{p,\text{min}}(p(0) - p_0(0)) \tag{3.5b}$$

$$J_p(x = d) = qS_{p,\text{maj}}(p(d) - p_0(d)) \tag{3.5c}$$

$$J_n(x = d) = qS_{n,\text{min}}(n(d) - n_0(d)). \tag{3.5d}$$

Here  $n_0$  and  $p_0$  refer to the equilibrium charge carrier concentrations so that the difference in eqs. 3.5 refers to the excess charge carrier density of free carriers  $\Delta n = n - n_0$ . Equating the current at the boundary and the current in the volume by taking e.g. eq. 3.5a and eq. 3.2a shows that these boundary conditions for the charge carriers are Robin-like.

### Relation to Band Diagram

While eqs. 3.3 with the boundary conditions in eqs. 3.4 and eqs. 3.5 represent a full description of the mathematical problem it is helpful in terms of understanding and fixing boundary conditions to relate the carrier densities to the device's band diagram that was discussed in section 2.3.1. The occupation probability of the fermionic (free) electron and hole quasi-particles can be approximated with Maxwell-Boltzmann statistics so that the carrier density is given by

$$n = N_c \exp\left(\frac{E_{F,n} - E_c}{k_b T}\right) \quad (3.6a)$$

$$p = N_v \exp\left(\frac{E_v - E_{F,p}}{k_b T}\right) \quad (3.6b)$$

where  $E_c$  represents the conduction band,  $E_v$  the valence band,  $N_{c,v}$  the effective density of states of the respective band and  $E_{F,n}$  and  $E_{F,p}$  the quasi-Fermi levels for the respective charge carrier type that takes the role of the particle's chemical potential. In equilibrium where  $E_{F,n} = E_{F,p} = E_f$  the equilibrium charge carrier densities  $n_0$  and  $p_0$  follow the law of charge neutrality

$$n_i^2 = n_0 p_0 = N_c N_v \exp\left(-\frac{E_g}{k_b T}\right) \quad (3.7)$$

where  $n_i$  is the intrinsic carrier concentration and  $E_g$  is the band gap. In terms of the band diagram the electrostatic potential  $\varphi_a$  at the anode in eq. 3.4 describes the offset (or Schottky barrier) between the semiconductor conduction band and the metal work function  $E_f$  so that the electron (majority) charge carrier density in equilibrium is given by eq. 3.6 with  $E_F - E_c = \varphi_a$  and the hole (minority) carrier density is defined by eq. 3.7. The situation at the cathode is analogous.

### 3.1.2. Generation and Recombination Models

In the following the terms in eqs. 3.3 describing generation  $G$  and recombination  $R$  are discussed briefly. When only the total amount of generated charges is relevant the generation rate can be set constant across the absorber. If a target short-circuit

### 3. Methods

current  $J_{sc}$  is known, e.g. from the experimental model system, the generation rate can be estimated via  $G = J_{sc}/(qd)$ . Lambert-Beer's law offers a simple physical picture of absorption and results in a generation rate  $G = \phi/hc\lambda(1 - \exp(-\alpha z))$  with the photon flux  $\phi$ , Planck constant  $h$ , speed of light  $c$ , photon wavelength  $\lambda$ , absorption coefficient  $\alpha$  and position in the absorber  $z$ . In thin-film solar cells with flat interfaces, reflection at e.g. a metallic back contact leads to interference which alters the generation profile. The transfer matrix method [187, 188] accounts for interference and calculates for normal incidence and each wavelength the electric field traveling in both directions along the layer stack from which the net electric field and thus the absorption and generation at any point in the solar cell can be calculated. In the TMM layers are specified via their complex refractive index and thickness and the reflection and reflection at an interface is given by the Fresnel coefficients. Note that the electronic processes described by the drift-diffusion equations do not influence the generation rate as long as e.g. photon recycling is not considered. Because of this missing feedback mechanism, it is relatively easy to decouple optical from electronic effects in experimental data with the help of simulations - provided that a sufficiently accurate optical model of the considered device exists.

For many thin-film solar cells, recombination via deep traps is the dominating recombination mechanism. For organic solar cells also direct non-radiative band-to-band recombination is relevant due to the large phonon energies [45, 46] found in soft matter. Direct recombination is given by

$$R_{\text{dir}} = k \times np, \quad (3.8)$$

where  $k$  is the coefficient of direct recombination and  $n$  and  $p$  the free charge carriers in the bands. Note that inevitable radiative band-to-band recombination takes the same form but the factor is different and directly related to the absorption coefficient. Shockley-Read-Hall recombination of a single defect in steady-state is given by

$$R_{\text{srh}} = N_t \beta_n \beta_p \frac{np - n_i^2}{n\beta_n + p\beta_p + e_n + e_p} \quad (3.9)$$

where  $N_t$  is the trap density,  $\beta_{n,p}$  are the capture coefficients of a trap and  $e_{n,p}$  are the emission coefficients. Equation 3.9 becomes largest when no re-emission of

captured charge carrier happens so when  $e_n + e_p$  is minimized which is the case for a trap in the middle of the band gap (assuming  $\beta_n N_c = \beta_p N_v$ ). For a deep trap where emission from the defect is negligible, eq. 3.9 simplifies to

$$R_{\text{srh}} = \frac{np}{n\tau_p + p\tau_n} \quad (3.10)$$

where the lifetimes are defined as  $\tau_{n,p} = 1/(N_t \beta_{n,p})$ . Sometimes the capture coefficients  $\beta_{n,p} = v_{\text{th}} \sigma_{n,p}$  are expressed in terms of thermal velocity  $v_{\text{th}}$  and capture coefficients  $\sigma_{n,p}$ . For equal electron and hole lifetimes  $\tau_p = \tau_n = \tau$ , eq. 3.10 has a maximum at  $n = p$ . At this position of equal carrier concentration in the device the recombination rate simplifies to

$$R_{\text{srh}} = \frac{n}{\tau}. \quad (3.11)$$

Note that in both discussed bulk recombination processes an electron and hole are annihilated simultaneously while for surface recombination in eq. 3.5 only one carrier type recombines with the other carrier coming from the metal.

### 3.1.3. Physical Remarks

The focus of the first paragraph was to present a mathematically consistent formulation of the problem rather than discussing the physical meaning of the assumptions which will be done in the following. The one-dimensional approach neglects lateral inhomogeneity which could result e.g. from a thickness variation of the layers with the extreme case of holes in a layer as discussed in section 2.3.3 and chapter 4. Another manifestation of inhomogeneity is presence of domains with varying physical material properties that could be related e.g. to different crystal size or orientation. However, if certain regions dominate the device behavior or if the variations can be averaged to obtain effective parameters, the 1D approach is still valuable. For anisotropic materials where a physical quantity is expressed as a matrix instead of a scalar, the 1D approach requires to enter the matrix element in the direction of charge transport into the drift-diffusion simulations. Organic bulk-heterojunction solar cells where a blend of two materials that is highly heterogeneous on the nm-

### 3. Methods

scale, can be successfully described as a single effective medium [187] and assigning an effective “material” parametrization to the blend. In general the drift-diffusion model allows to take an effective parametrization without precise knowledge of the microscopic material or interface properties that are governed by quantum mechanics. The idea of an effective parametrization also applies to including the dominating elements of a physical system instead of capturing the entire system. One example is to include the defect that dominates SRH recombination instead of including all existing defect states. Many advanced characterization methods exist that help to determine the input parameters of the simulations [187]. However, it can be difficult to directly extract the material properties from experimental measurements as the interpretation of a probed (macroscopic or averaged) quantity and its relation to a (microscopic) parameter used in drift-diffusion simulations is sometimes not straightforward [83, 189, 190].

Aside from the parametrization more assumptions go into eqs. 3.1. Any magnetic or thermoelectric effects are neglected. For modeling the current-voltage characteristics as done in this thesis, the steady-state drift-diffusion equations 3.3 together with the boundary conditions in eqs. 3.4 and eqs. 3.5 are sufficient. The time dependent formulation in eqs. 3.1 is relevant for example when transient measurements are simulated [191]. As mentioned above, the presented drift-diffusion equations apply to a homogeneous material with boundary conditions. When not a single layer shall be simulated but a full device stack consisting of different materials, the material properties are set for each layer and abruptly change at the resulting heterojunctions. Because of energetic offsets at the heterojunction and a possible change of effective DOS the electric field in eq. 3.2a is not simply given by the gradient of the electrostatic potential  $\varphi$  but includes several “loss” terms. The electric field is then given by  $qF = -q d\varphi/dx - d\chi/dx - kT/N_c dN_c/dx$  for electrons and  $qF = -q d\varphi/dx - d\chi/dx - dE_g/dx - kT/N_v dN_v/dx$ . The gradients in electron affinity  $\chi$  and band gap  $E_g$  represent the energetic offsets evident from the band diagram shown in section 2.3.1. The presented drift-diffusion model can be extended to amorphous systems that include localized charges in the band tails via multiple trapping models. Quantum-mechanical features of a physical system such as tunnel contacts cannot be directly included into drift-diffusion simulations.

In summary, drift-diffusion simulations are a powerful tool to qualitatively understand observed phenomena in thin-film solar cells and to quantitatively analyze experimental data, given that the assumptions for the modeled system hold true and that the limitations of drift-diffusion modeling are taken into account.

## 3.2. Fabrication

The experimental part of this thesis deals with the emerging solar cell absorber antimony sulfide  $\text{Sb}_2\text{S}_3$  and focuses on the optimization of the  $\text{Sb}_2\text{S}_3$  itself and the polymeric hole transport layer (HTL). Section 3.2.1 describes and motivates the applied layer stack, section 3.2.2 introduces the two major  $\text{Sb}_2\text{S}_3$  processing routes of this thesis and section 3.2.3 describes the processing of the remaining layers that make up the solar cell. Finally, section 3.2.4 comments on the utilized equipment and general processing conditions. Detailed recipes can be found in appendix E.

### 3.2.1. Solar Cell Stack

The general cell stack that I used in this thesis is shown in fig. 3.1(a). As for many wet-chemically processed solar cells, glass is used as the bottom-most layer that provides the mechanical stability of the stack. All other layers are subsequently deposited on top of the glass. Although this stack is actually a superstrate configuration, the glass - sometimes together with the TCO - is referred to as substrate in the following. FTO which functions as front contact,  $n$ -type  $\text{TiO}_2$  as electron transport layer (ETL),  $\text{Sb}_2\text{S}_3$  as absorber, a semiconducting polymer as hole transport layer (HTL) and  $\text{MoO}_x/\text{Ag}$  as metallic back contact follow on top of the glass. The choice of materials and the  $n$ - $i$ - $p$  configuration are motivated by the following: As mentioned in section 2.4.2 there are no reports on controlled doping of  $\text{Sb}_2\text{S}_3$  which could allow to fabricate  $p$ - and  $n$ -type  $\text{Sb}_2\text{S}_3$  and thereby a device based on homo-junctions of the same material - an approach that a-Si solar cells followed. Instead the charge transport layers need to be constructed from different materials with energy levels that are suitable with respect to  $\text{Sb}_2\text{S}_3$  in order to avoid large energetic offsets at the heterojunctions as discussed in section 2.3.1. For the HTL the large

### 3. Methods

variety of semiconducting polymers known from organic solar cells offer a range of materials with different HOMO levels whereby the likelihood of finding a suitable one is increased. Since most  $\pi$ -conjugated polymers cannot withstand a temperature of 250 °C that is at least needed for the crystallization of  $\text{Sb}_2\text{S}_3$  the HTL has to be processed on top of the  $\text{Sb}_2\text{S}_3$ . This processing constraint together with the superstrate arrangement demands the *n-i-p* configuration. The different polymeric HTLs investigated in this thesis are always contacted with  $\text{MoO}_x/\text{Ag}$ , which has been successfully applied in many 'inverted' organic solar cells [139, 192–194] where the same (or similar) polymers are used.  $\text{MoO}_x$  is a *n*-type semiconductor whose large work function lies even below most polymer's HOMO so that a tunnel junction to the polymeric HTL is formed [195] that allows efficient charge extraction. The additional Ag layer offers good reflectivity and lateral conductivity. On the other side of the solar cell stack, a compact layer of anatase  $\text{TiO}_2(\text{c-TiO}_2)$  serves as *n*-type ETL below the planar  $\text{Sb}_2\text{S}_3$ . While *c-TiO*<sub>2</sub> is the most common choice [60, 80, 91, 164], in general other ETLs [196] – e.g. made from metal oxides with similar energy levels such as ZnO and  $\text{SnO}_2$ – could be applied as well as long as they can withstand the crystallization temperature of  $\text{Sb}_2\text{S}_3$ . A variation of the ETL material is however beyond the scope of this thesis, although different processing routes for *c-TiO*<sub>2</sub> were explored. Given that anatase  $\text{TiO}_2$  only forms above 450 °C, the underlying TCO needs to withstand this temperature. This request is fulfilled by fluorine-doped tin oxide ( $\text{SnO}_2:\text{F}$ , FTO) in contrast to ITO - another commonly applied TCO - whose sheet resistance drastically increases at such elevated temperatures [197].

#### 3.2.2. $\text{Sb}_2\text{S}_3$ Layers

As mentioned in the introduction the absorber layer is at the heart of the solar cell. In this thesis two different wet-chemical process routes [33, 34] were explored to obtain a compact layer of  $\text{Sb}_2\text{S}_3$ . Both routes are based on a metal-organic precursor that contains antimony and sulfur and that is dissolved in a polar solvent. The precursor solution is spin-coated onto a substrate which is then transferred to a hot plate where the precursor is thermally decomposed at a temperature of 180° C or 200 °C leaving an amorphous  $\text{Sb}_2\text{S}_3$  film. Subsequently the sample is transferred to a second hot plate where the film is crystallized at a temperature

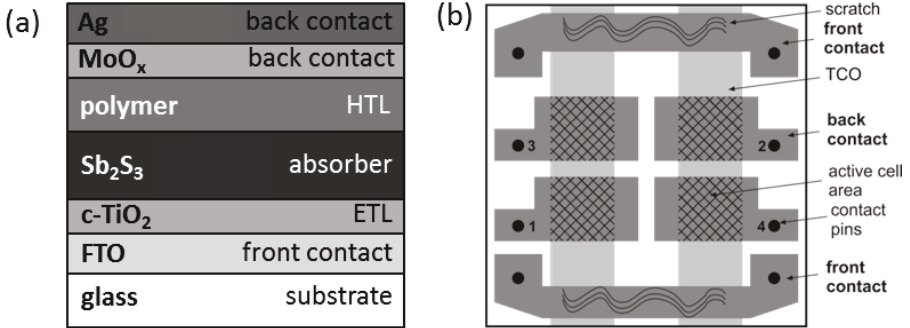


**Figure 3.1.:** (a) Applied layer stack (cross-section) with the material written on the left and the layer's functionality on the right. Different semiconducting polymers were applied. (b) Substrate and cell configuration viewed from the back. The substrate size is  $2\text{ cm} \times 2\text{ cm}$  and the overlap of front and back contact defines four  $4\text{ mm} \times 4\text{ mm}$ -sized solar cells.

above  $250\text{ }^\circ\text{C}$  [79, 173, 198]. In the following the two optimized process routes are described while the optimization process itself is depicted in chapter 6 along with the corresponding material, layer and solar cell characterization. Detailed recipes can be found in the appendix E. With reference to the Sb-S complex that is formed, one process route is referred to as Sb-TU and the other one as Sb-BDC.

In the Sb-TU process [33] an antimony-thiourea  $[\text{Sb}(\text{TU})_2]\text{Cl}_3$  precursor complex is formed in the high boiling point solvent *N,N*-dimethylformamide DMF by antimony chloride  $\text{SbCl}_3$  and thiourea  $\text{SC}(\text{NH}_2)_2$  (short: TU). The solution concentration of  $\text{SbCl}_3$  in DMF is  $1\text{ mmol/ml}$  and the molar  $\text{SbCl}_3$ :TU ratio is 1:1.8. The sulfur excess in the precursor above the stoichiometric ratio of 1:1.5 was shown to give the best performance for ETA solar cells and to yield stoichiometric  $\text{Sb}_2\text{S}_3$  in the final thin film [33] – indicating that sulfur is lost at some point in the process. After spin-coating the precursor solution at 70 rps for 40 s the sample is slowly annealed for 60 min at  $100\text{ }^\circ\text{C}$ . The hot plate is then heated to  $180\text{ }^\circ\text{C}$  where the sample remains for another 10 min to decompose the precursor after which the amorphous  $\text{Sb}_2\text{S}_3$  layer is crystallized on a different hot plate for 30 min at  $265\text{ }^\circ\text{C}$ . The annealing procedures are presented in more detail in chapter 6.1 as part of the layer and solar cell optimization.

In the Sb-BDC process [34] an antimony-butyldithiocarbamate  $\text{Sb}(\text{S}_2\text{CNHC}_4\text{H}_9)_3$

### 3. Methods

precursor complex is formed in ethanol. For this, 0.5 mmol of  $\text{Sb}_2\text{O}_3$  is mixed with 1 ml of ethanol and 0.75 ml of  $\text{CS}_2$  before 1 ml of *n*-butylamine was added slowly and dropwise to reduce heating effects that are caused by the exothermal reaction. After spin-coating the precursor solution at 133 rps for 30 s the sample is annealed for 1 min at 200 °C to decompose the precursor after which the amorphous  $\text{Sb}_2\text{S}_3$  layer is crystallized on a different hot plate for 2 min at 265 °C. Note that no slow-annealing step is applied and that the annealing times are significantly shorter than for the Sb-TU process as will be further elaborated in chapter 6.1. For both processes, the optimized crystallization temperature differs from the original reports [33, 34]. Apart from this, the Sb-BDC process closely follows the original report, while the Sb-TU required further adjustments due to the transfer from a mesoporous  $\text{TiO}_2$  scaffold to a compact  $\text{TiO}_2$  layer as substrate.

#### 3.2.3. Solar Cells

In the following, the processing sequence starting from the substrate till the metal evaporation are presented. The cell geometry displayed in fig. 3.1 results from the custom-ordered FTO patterning and the metal evaporation mask. The overlap of the FTO stripes and the metal pads defines four pixels, each of which is a complete solar cell with an active area of  $4i_j \frac{1}{2}\text{mm} \times 4i_j \frac{1}{2}\text{mm} = 0.16\text{cm}^2$ . The electrical contact points, where electrical contact to the solar cells is made during sample characterization, are indicated by filled circles in fig. 3.1(b). To ensure a good electrical contact between a samples holder's contact pins and the TCO front contact, the metal is also evaporated directly onto the TCO. For this, the spin-coated layers were removed in the corresponding region by scratching before metal evaporation and a mask covering the edges of the substrates is used during spray-coating since the hard  $\text{TiO}_2$  cannot be scratched off.

Ready-made  $2i_l \frac{1}{2}\text{cm} \times 2i_l \frac{1}{2}\text{cm}$  glass substrates with patterned FTO were purchased from Kintec (Hong Kong). The TEC7 with a specified sheet resistance of  $7\Omega/\square$  from the community's standard manufacturer TEC Glass<sup>TM</sup> from Pilkington<sup>TM</sup> served as FTO, whose mean square roughness was measured to be 28.5 nm. The substrates were cleaned in several iterations of soap, acetone and isopropanol baths, some of which were done in an ultrasonic bath, and then stored in

isopropanol. When taken out of the storage in a laminar flow box the substrates were dry-blown with nitrogen to avoid any residues on the substrate. After additional drying on a hot plate at 100 °C for 5 min, the samples were placed in an ELG100S ozone chamber by Dienies technologies for at least 30 min. A compact layer of TiO<sub>2</sub> was obtained by spray-coating a 0.2 M solution of titanium diisopropoxide bis(acetylacetonate) 75 wt% in ethanol on a hot plate at roughly 470 °C. To create the spray nebula from a glass nozzle an Aldrich chromatography sprayer was used. Spray-coating provides a conformal coating of the substrate as can be seen from fig. 3.2 and the thickness can be adjusted by the number of spray cycles. After cooling down to about 200 °C, samples were transferred to a glovebox where they were further processed on the next day. The substrates were blown with a nitrogen gun before each spin-coating step. The Sb<sub>2</sub>S<sub>3</sub> precursor solution was typically prepared a day before use and then filtered with a 0.5 µm PTFE filter on the day of use. Sb<sub>2</sub>S<sub>3</sub> layers were fabricated as described in section 3.2.2. Different polymers were used as HTM<sup>3</sup>, so that the exact processing condition for each polymer are given in appendix E or at the corresponding position in the main text. Generally, polymers require a non-polar solvent such as chlorobenzene (CB) or 1,2-dichlorobenzene (DCB). All polymers in this work were stirred at temperatures between 60 °C and 110 °C and the stirring time varied from several hours to overnight. Aiming for layer thicknesses between 30 nm and 50 nm, the typical solution concentration of P3HT was 15 mg/ml and the coating was done at 6000 rpm while other polymers were typically prepared at a lower concentration of 10 mg/ml or lower and spun at slower speeds around 1500 rpm. Depending on the polymer, the solution was casted in a hot or cooled-off state. Spin times were typically about 2 min. Also the drying procedure varied for the different HTMs and some polymers were dried on a hot plate between 80 °C and 130 °C for several minutes while other polymers were dried in a petri dish for several hours. Finally 30 nm of MoO<sub>x</sub> was thermally evaporated at a rate of 0.2 Å/s and 200 nm of Ag was thermally evaporated at a rate of 2 Å/s.

---

<sup>3</sup>See appendix F for the full names of organic materials.

### 3. Methods

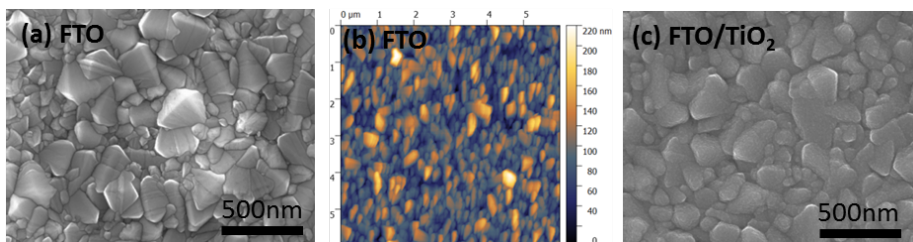


**Figure 3.2.:** (a) SEM and (b) AFM image of a FTO TEC7 substrate as-delivered. The mean square roughness is 28.5 nm. (c) SEM image after spray-coating of a conformal TiO<sub>2</sub> layer, onto which Sb<sub>2</sub>S<sub>3</sub> is spin-coated in the next step.

#### 3.2.4. Processing Conditions and Equipment

Since many of the used chemicals and materials might or are known to be reactive to oxygen or moisture, most of the processing was done in an MBRAUN glovebox under N<sub>2</sub>-atmosphere with low O<sub>2</sub> and H<sub>2</sub>O content with a base level of  $\leq 0.1$  ppm. More precisely, the TiO<sub>2</sub> was spray-coated in a fumehood under ambient conditions after which the samples were transferred into a glovebox. All consecutive steps, including Sb<sub>2</sub>S<sub>3</sub> deposition, HTL deposition and metal evaporation were performed inside gloveboxes. Especially the annealing of Sb<sub>2</sub>S<sub>3</sub> is sensitive to air [177]. Whenever it was required, samples and vials were transferred between the gloveboxes in sealed plastic bags and as quickly as possible. For the purpose of characterization samples were mounted into inert-atmosphere providing sample holders inside the glovebox whenever possible. When setups did not allow for such a sample holder, samples were transferred and mounted as quickly as possible. To keep the water content in the solutions to a minimum the vials that were used to weigh chemicals and prepare solutions were heated in an oven and transferred to the glovebox in a hot state to remove the atomically-thin layer of H<sub>2</sub>O that is present on surfaces exposed to ambient atmosphere. Dried solvents with analytical (p.a.) quality were used and chemicals were generally obtained in a high quality and mostly from Sigma-Aldrich with information for the specific case given in the appendix. Chemicals were opened and stored inside a glovebox.

Solid chemicals were measured with a ACJ 120-4M scale by Kern with a specified accuracy of 0.1 mg. The substances were handled with one-way plastic spatula

or metal spatula that were exclusively used for the same material and cleaned before and after each use. Micropipettes were generally used to measure liquids such as solvents and solutions. Teflon stirring bars were re-used but only for the same type of solution and after thorough cleaning with the appropriate solvents and storage in an isopropanol/potassium hydroxide (KOH) bath. Substrates were handled with plastic tweezers or with metal tweezers when hot plates at high temperatures were involved. The samples were stored in a glass petri dish between processing steps and the final cells were stored in plastic containers inside a glovebox and protected from light until all characterization was done.

Weighing, solution preparation and filtering was done in the glovebox where the scale was located. The vials were then transferred to another glovebox where the  $\text{Sb}_2\text{S}_3$  was deposited and annealed. The  $\text{Sb}_2\text{S}_3$  was spin-coated with a SCC-200 by KLM. A custom-made Teflon chuck that allows spin-coating of differently sized substrates. For spin-coating a substrate is placed onto a chuck with tweezers and kept in position during rotation by vacuum. Then the solution is dispensed with a pipette and the chuck accelerates until the desired rotation speed is reached which is kept for the desired time. In a simple picture the liquid spreads due to centrifugal forces and the final layer thickness results from an interplay between those forces and the concentration and viscosity of the solution. Simultaneously volatile solvents evaporate during rotation so that the mechanism of film formation is quite complex and the film quality might depend on the detailed parameters of spin-coating. The first annealing steps up to thermal decomposition of the precursor film are done on a RCT basic hot plate by IKA that can heat up to 300 °C and was tested to accurately meet the set temperature over almost the entire metallic hot plate surface. It was made sure that the samples were placed outside the very center of the hot plate which is slightly curved and could not properly ensure a direct and homogeneous contact over the whole sample area. A second PC420D hot plate by Corning that can provide temperatures up to 450 °C was used to crystallize the  $\text{Sb}_2\text{S}_3$ . The ceramic surface of the hot plate showed temperature variations of more than 10 °C even in the center area of the hot plate and objects that were placed on the hot plate introduced heat sinks so that an aluminum plate was placed on the hot plate which could provide a homogeneous temperature distribution and thereby ensure controlled annealing conditions. Additionally, the set temperature  $T_{\text{set}}$  of

### 3. Methods

this hot plate was found to deviate from the measured temperature  $T$  obtained with a probe thermometer so that in all experiments a calibrated temperature that followed the measured relation  $T_{\text{set}} = 1.11 \times T + 14^\circ\text{C}$  was used. In a next step the polymer was coated in yet another glovebox on a SPIN150i coater by SPS-Europe which provided a smoother rotational movement which yielded better results for the polymer coating but was uncritical for  $\text{Sb}_2\text{S}_3$  coating. The annealing, if applicable, was done on an IKA hot plate identical to the one described before. In a last processing step the samples were transferred to the glovebox where the metal back contact was thermally evaporated with a Mini SPECTROS by Lesker.

## 3.3. Characterization

The objectives of the experimental work on  $\text{Sb}_2\text{S}_3$  in this thesis were to improve the efficiency of planar, spin-coated solar cells and to study the device physics to identify limitations and prospects of  $\text{Sb}_2\text{S}_3$  technology. The first objective of solar cell optimization requires the identification and variation of critical process parameters and the corresponding monitoring of the progress in material and layer quality as well as solar cell efficiency. The second objective requires the quantitative determination of parameters that are critical for solar cell performance as described in chapter 2.2. For both objectives I made use of techniques to characterize the materials and layers, described in section 3.3.1, as well as techniques that work with the full solar cell, described in section 3.3.2.

### 3.3.1. Material and Layer Characterization

#### Morphology

Scanning electron microscopy (SEM) was regularly used to observe lateral inhomogeneity of the spin-coated  $\text{Sb}_2\text{S}_3$  films. Especially the Sb-TU process yields layers with holes where the coverage depends on the process parameters. SEM measurements also allow the determination of the (lateral) crystal size. In SEM measurements an electron beam is produced by an electron gun which emits electrons and accelerates them with an electric field that is characterized by the applied voltage

### 3.3. Characterization

which is on the order of many kVs. The electron beam is directed and focused with magnetic lenses at a specimen where it interacts in different ways with the probed material. This leads to the emission of electrons and photons from the material, with an energy that depends on the kind of interaction, that can then be observed with a suitable detector. My measurements were typically based on secondary electrons which are produced when an incoming electron knocks out an electron from an atom's core shell which is then able to leave the sample and be captured by a secondary electron detector. An image is created by scanning the electron beam across the sample. The penetration depth of the electron beam as well as the escape depth of the secondary electrons are small so that the measurement is surface sensitive and the emission strength strongly depends on the angle between surface and incident beam. Consequently, sharp features like edges cause strong signals. Compared to optical microscopy, SEM can achieve a better lateral resolution due to the short wavelength of the electrons and a larger focus depth due to the smaller aperture. SEM measurements are carried out in vacuum and require a conductive substrate which conducts the extra electrons induced by the electron beam to ground in order to prevent charging of the specimen which would cause a blurring of the image. SEM measurements were performed on a Zeiss (Leo) Gemini 1550 with Schottky field-emission cathode and an in-lens detector. The lateral resolution was approximately 1 nm at 20 kV and the measurement was performed under a vacuum base pressure of  $10^{-6}$  mbar.

Atomic Force Microscopy (AFM) provided additional information on the height profile of the deposited  $\text{Sb}_2\text{S}_3$  films, since SEM measurements are not truly height sensitive but rather reflect differences in height. AFM measurements were carried out in non-contact mode where the cantilever oscillates around a fixed distance from the specimen in the attractive regime of the tip-specimen interaction. More details can be found in ref. [199]. The measurements were carried out in air by Pascal Foucart on a NANOSTATION 300 AFM by Surface Imaging Systems (S. I. S.).

Profilometer measurements were used to determine the thickness of the  $\text{Sb}_2\text{S}_3$  and polymer layers. The layer thickness is a basic information that is needed to interpret other measurements and is for example used to extract an absorption coefficient from UV-Vis measurements. Because the layer thickness was regularly

### 3. Methods

determined, it also served as an indicator for the stability and reproducibility of a certain deposition process. The measurement is similar to an AFM measurement in contact mode but the tip has a comparably large radius of 12.5  $\mu\text{m}$  and only one linescan is performed. To obtain meaningful thickness data flat glass substrates were used. After deposition the layer was scratched and measured at different positions to obtain an averaged layer thickness. Since different substrates were used for cell fabrication the values of the measured thickness may differ from the actual value in the solar cell stack, but changes between different fabrication days or recipes are reflected well in the measurement. A Veeco Dektak 6M Profilometer was used.

### Chemical Composition and Energy Levels

X-ray photoelectron spectroscopy (XPS) and Raman spectroscopy were used to identify the deposited absorber as  $\text{Sb}_2\text{S}_3$  by comparing the peaks in the recorded spectra to literature data or standard spectra from databases. Raman peaks broaden with decreasing crystal size which makes Raman measurements a suitable method to differ between the amorphous and crystalline state of  $\text{Sb}_2\text{S}_3$ . The Raman setup consists of a cooled CCD-sensor, a grating monochromator and a 532 nm solid state laser (Coherent Sapphire), which is used for excitation. The spectral resolution is about  $1.1\text{ cm}^{-1}$  wavenumbers. A detailed description of Raman spectroscopy and the setup used, can be found in ref. [200]. XPS was additionally used to observe trends in stoichiometry for varying processing conditions and to detect impurity phases. The XPS setup also allowed UPS measurements, which were used to determine the valence band edge and Fermi level of  $\text{Sb}_2\text{S}_3$ .

XPS and UPS measurements were performed and mostly analyzed by Benjamin Klingebiel. The measurement system required the use of relatively thin glass/ITO substrates. The XPS/UPS system is a MULTIPROBE MXPS system from Scienta Omicron ( $3 \times 10^{-11}$  mbar base pressure) with an ARGUS hemispherical electron spectrometer. The XPS measurements apply an XM1000  $\text{AlK}_\alpha$  x-ray source at 300 W. All spectra are collected in constant Analyzer-Energy (CAE) mode with a path energy (PE) of 150 eV for the survey spectrum and 10 eV for the high-resolution spectra. The source analyzer angle is  $90^\circ$  and the takeoff angle of the electrons with respect to the surface normal is  $21^\circ$ . The energy resolution for XPS

measurements as estimated by the full-width at half-maximum (FWHM) of the Au 4f peak was approximately 0.6 eV. Intensities were determined by measuring the peak area, after subtracting a Shirley-type background and fitting the experimental curve to a combination of Lorentzian and Gaussian lines with a fixed proportion of 30:70. Fitting was done with the help of the XPST Plugin (M. Schmid, Philipps University Marburg) in Igor Pro (Wavemetrics). The light source for UPS measurement is a HIS13 HeI gas discharge VUV source from FOCUS GmbH (main line HeI $_{\alpha}$  21.22 eV). Spectra are collected with at a path energy of 2 eV, a digital resolution of 0.01 eV and a sample bias of 9 V at a takeoff angle of 0°. The binding energy scale is referenced to the Fermi edge of a freshly evaporated gold sample measured under identical conditions. Work functions and valence band positions were determined from the spectra by measuring the position of the cut-off at high (or low) binding energies using linear fits of the background and the steep edge.

### **Photothermal Deflection Spectroscopy (PDS) & UV-Vis Photospectrometry**

By combining PDS and UV-Vis measurements different regimes of the absorption coefficient were measured. While UV-Vis measurements provide reliable absolute values of the absorption coefficient in the regime of strong absorption, PDS measurements cover a large dynamic range [201, 202] towards the regime of weak absorption with the drawback of a larger uncertainty of the absolute value. The absolute value of the absorption coefficient above the band gap – a fundamental quantity for thin-film solar cells as described in section 2.3 – was determined via UV-Vis measurements. The value of the absorption coefficient and especially the value of the band gap were used to identify the deposited material as Sb<sub>2</sub>S<sub>3</sub> and to distinguish between its amorphous and crystalline state. The band edge itself is the overlapping regime of UV-Vis and PDS measurements and was investigated with both methods. From the slope of the optical band edge the Urbach energy  $E_u$  was calculated according to

$$E_u = \left( \frac{d \ln(\alpha)}{dE} \right)^{-1},$$

### 3. Methods

with the absorption coefficient  $\alpha$ , the layer thickness  $d$  and the energy  $E$ . Assuming that all energetic states that constitute the band tails are optically active and contribute equally to absorption, the Urbach energy is equal to the sum of the characteristic energies of the valence and conduction band tail, which characterize the exponentially decaying density of states of the corresponding bands, and is thus a measure for the energetic disorder of the material [202–205]. Finally, the weak sub-bandgap absorption measured via PDS allowed the study of detection of (optically active) defects in the band gap [202–205] which may act as recombination centers in a solar cell.

In UV-Vis measurements the transmittance  $T$  and reflectance  $R$  of a thin layer is measured with a photospectrometer over a large wavelength range from the UV over the visible towards the infrared range. The absorption coefficient is then calculated for a known layer thickness via

$$\alpha = 1/d \ln(T/(1-R)).$$

The resulting absorption coefficient is free of interference but is only reasonable when  $T \neq 0$ , meaning when the absorptance has not saturated. UV-Vis measurements were performed with a Lambda 950 photospectrometer from PerkinElmer equipped with an integrating sphere in a typical range from 300 nm to 1000 nm.

PDS measures the absorptance of a thin film which is deposited on a smooth substrate and placed in a cuvette. The cuvette is filled with the liquid CCl<sub>4</sub> or FC75 whose refractive index is highly temperature sensitive. A monochromatic beam of light is directed perpendicularly at the sample which absorbs the incoming photons - according to its absorption coefficient - which causes a heating of the sample. The change in refractive index of the liquid caused by the heat transfer from the sample is detected via the change in deflection of a laser beam that runs parallel to the sample surface. Eventually the measurement signal is proportional to the absorptance of the thin film. A more detailed explanation of the method can be found elsewhere [200, 202, 205]. Oliver Thimm performed the PDS measurements and basic data analysis. For the scaling of the absorptance, the transmission signal as well as two data points with equal reflectance but significantly different absorptance is required. If the reflection is not measured but only the transmission, the fact can

be used that the reflectance is equal at the inflection points of the transmittance signal. In order to finally obtain the absorption coefficient from the absorbance the thickness and refractive index is needed. Again, the analysis in terms of absorption coefficient is only sensible when  $T \neq 0$ . Regarding the setup, a Xenon lamp combined with a monochromator provide the monochromatic light. Because of the low signal intensity, lock-in technique is used to improve the signal-to-noise ratio. The phase of the lock-in signal reflects the time delay between excitation and detection signal and thus provides information on the depth where heat is generated in the film and thus where the light is absorbed. This is especially valuable to distinguish between absorption in the thin film and in the substrate. For energies well below the band gap, the substrate absorption becomes comparable to the absorption in the film. Corning glass was used as substrate for PDS measurements since the FTO used in the solar cells shows, like any other conductive substrate, free carrier absorption at low energies from conductive substrates dominates the subbandgap absorption of the material that shall be observed.

#### **Constant Photocurrent Measurement (CPM)**

CPM was used to determine the mobility-lifetime product of  $\text{Sb}_2\text{S}_3$  which governs the photocurrent as described in section 2.3.4 and is thus an essential material parameter for solar cell absorbers. Furthermore, the absorption coefficient and thereby the band tails were studied with CPM. CPM is based on the co-planar measurement of the wavelength-dependent photocurrent  $I_{\text{ph}}$  which is given by Ohm's law

$$I_{\text{ph}} = \sigma_{\text{ph}} \frac{V}{l} wd,$$

with the photoconductivity  $\sigma_{\text{ph}}$ , the length  $w$  of the metal contacts and the thickness  $d$  of the sample that give the cross-section of the semiconductor, and the applied voltage  $V$  and the distance  $l$  between the contacts. The photoconductivity is given by

$$\sigma_{\text{ph}} = q(\Delta n\mu_n + \Delta p\mu_p)$$

### 3. Methods

with the mobilities  $\mu_{n,p}$  and the equally large excess charge carrier densities  $\Delta n = \Delta p$  that result from the optical generation of electron-hole pairs. Since the photoconductivity is a differential quantity, lock-in detection is applied and the incident light is chopped - similar to EQE and PDS measurements. The excess charge carrier density is related to the generation rate  $G$  via

$$\Delta n = G\tau.$$

The minority carrier lifetime  $\tau$  may in general depend on the splitting of the Fermi levels and thus  $\Delta n$ . To ensure a constant excess charge carrier density the photocurrent is kept constant which in turn requires to adapt the incident monochromatic photon flux  $\phi(E)$  since the absorption coefficient depends on the wavelength - especially in the region of the band gap. The generation rate is given by

$$G = \frac{a(E)}{d}(1 - R)\phi,$$

where the spectrum of the absorptance  $a(E)$  is obtained from PDS measurements of the same sample and the scaling of the saturation regime is given by the reflection  $R$ . Putting all of the above equations together the mobility-lifetime product is obtained

$$(\mu_n + \mu_p)\tau = \frac{I_{ph}l}{qwV} \frac{1}{(1 - R)\phi(E)a(E)}. \quad (3.12)$$

CPM measurements require a non-conductive substrate such as glass. Here, I used the same substrates as for PDS to allow the measurement of the absorptance which is needed to obtain the mobility-lifetime product. The setup was operated by Oliver Thimm.

## 3.3.2. Solar Cell Characterization

### Current-voltage ( $J$ - $V$ )

Illuminated current-voltage measurements were used to determine the solar cell efficiency and the associated performance parameters  $J_{sc}$ ,  $V_{oc}$  and  $FF$ . Dark  $J$ - $V$  and illumination dependent measurements were used to study recombination. Two

### 3.3. Characterization

setups with different light source were used. A calibrated class AAA solar simulator that closely matches the AM1.5g spectrum was used to accurately measure devices. A second setup with white LEDs as light source is located in a glovebox next to the metal evaporator and was used to initially screen all fabricated solar cells. Thereby, samples could be selected for further characterization or accurate illuminated  $J$ - $V$  measurements at the solar simulator. The LED setup also allowed to compare samples within a series. Figure 3.3(a) shows the spectra of the LED, the solar simulator and the AM1.5g. The solar simulator matches the norm spectrum well while the LED setup shows large deviations, especially in the UV and IR region. By adjusting the LED current and thereby the light intensity, the  $J_{sc}$  measured at the LED setup is matched to the  $J_{sc}$  measured at the solar simulator. This calibration of the short-circuit current needs to be adjusted for different absorber materials or more generally for a varying absorptance. The LED setup's advantage of a variable light intensity allows the measurement of illumination-dependent  $J_{sc}$  and  $V_{oc}$  and is shown to be linear in fig. 3.3(b). The class AAA solar simulator is based on a WACOM-WXS-140S-Super-L2 system with a combined xenon/ halogen lamp and a Series 2420 SourceMeter by Keithley Instruments. The LED solar simulator is equipped with a white light LED (Cree XLamp CXA3050, 2700 K, 100 W) and a 2450 Keithley source measure unit.

#### **External Quantum Efficiency (EQE)**

External quantum efficiency ( $EQE$ ) measurements were used to accurately determine the  $J_{sc}$  of a solar cell according to eq. 2.12 in section 2.3.  $EQE$  was also used to gain position dependent information on the charge carrier collection efficiency following eq. 2.13 which expresses that the spectrally resolved measurement of the photocurrent depends on optical and electronic effects.  $EQE$  measurements were performed inside the sample holder described in chapter 3.2. The glass cover introduces an additional reflection that is corrected for via

$$EQE_{\text{corrected}} = (1 + R_{\text{glass}}) EQE_{\text{measured}}.$$

### 3. Methods

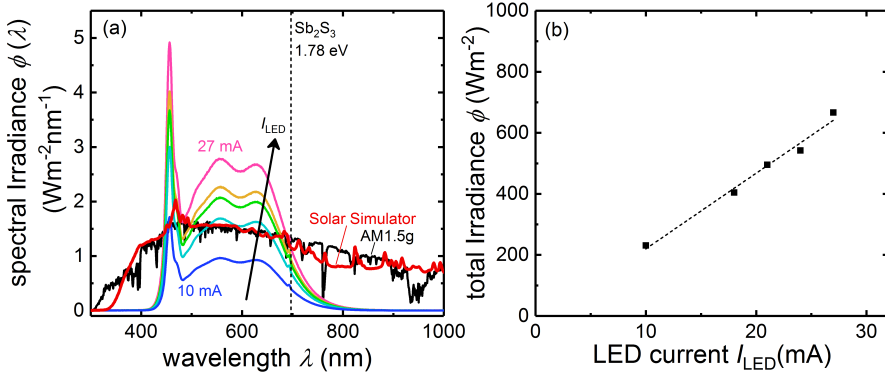


**Figure 3.3.:** (a) Spectra of the LED used for illuminated  $J$ - $V$  measurements show no spectral shift, but a general mismatch with the AM1.5g norm spectrum. The class AAA solar simulator matches the AM1.5g very well. (b) Illumination intensity is linear with the LED's operating current.

The reflection of the glass cover was measured with UV-VIS. Details of the working principle of EQE can be found [122, 206]. The used setup consists of a xenon light source (Osram XPO150W), a Bentham monochromator (TMC300) with a spectral range of 300-1100 nm and a HMS500 Lock in amplifier. The photocurrent was calibrated with a calibrated silicon photodiode (Gigahertz-Optik SSO-PD100-04) as a reference. The chopper frequency was set to 72 Hz and the wavelength step size to 10 nm.

#### Fourier Transform Photocurrent Spectroscopy (FTPS)

FTPS measurements were used to study the band edge and sub-bandgap states of the fabricated solar cells. In FTPS, the photocurrent is probed with a dynamic range that is significantly large than in the described EQE measurements. A detailed description of the method can be found in ref. [202]. FTPS measurements were carried out with a FTIR spectrometer (Bruker Vertex 80v), that is equipped with a halogen lamp. A low noise current amplifier (Femto DLPCA-200) amplified the photocurrent generated upon modulated illumination of the solar cell via the FTIR. The output voltage of the current amplifier was feedback to the external detector port of the FTIR and the FTIR's software collected the photocurrent spectrum.

A scan speed/ mirror speed of 2.5 kHz and a resolution of  $12 \text{ cm}^{-1}$  was used. To increase the dynamic range of the measurement, different edge filters were used to measure the FTPS spectrum at lower energies. By cutting off stronger signals at higher energies, the amplification can be increased and a better signal-to-noise ratio reached in the relevant regime. The different spectra are later stitched together.

### Electroluminescence (EL)

Electroluminescence was used to distinguish open-circuit voltage losses into radiative and non-radiative contributions [207]. In EL measurements the solar cell is operated as an LED, meaning that a current is driven into the solar cell and the light emission is measured. A detailed description of the method can be found in ref. [208]. The reciprocity theorem [207] connects the EL emission ( $\phi_{\text{EL}}$ ) to the quantum efficiency ( $Q_e$ ) of a solar cell via

$$\phi_{\text{EL}}(E) \propto Q_e(E) \phi_{\text{bb}}(E) \quad (3.13)$$

with the black body spectrum  $\phi_{\text{bb}}$ . Thereby, EL measurements allow to determine the quantum efficiency over a wide dynamic range. The proportionality factor is obtained by scaling the  $Q_e$  to the corresponding *EQE* measurement. The scaled  $Q_e$  may then serve to calculate the before mentioned voltage losses as depicted in appendix A.3 and carried out for  $\text{Sb}_2\text{S}_3$  solar cells in chapter 6.2.

The EL spectra were detected, as the Raman spectra, via a spectrometer (Andor Shamrock 303) with an Andor Si (deep depletion) CCD camera (iDus Series). For the electroluminescence measurements a constant current through the devices was applied being supplied by an external current/voltage source (Keithley SMU 2400). Photoluminescence measurements were performed on layers of  $\text{Sb}_2\text{S}_3$  to obtain information on electronic defects. The same setup as for Raman measurements is used and the measurement principle is similar to EL, but instead of applying a voltage to the solar cell, a 532 nm laser excites charge carriers in the film. Low temperature measurements were carried out in a Linkam cryostat. Raman and PL measurements in this thesis were performed by Markus Higlbeck.



## 4. Pinholes and Non-linear Shunts in Thin-Film Solar Cells

Pinholes in the absorber layer are a common form of inhomogeneity in thin-film solar cells. While keeping the undesired variations to a minimum is a matter of optimized processing conditions, another (complementary) approach is to mitigate the negative impact of fluctuating physical properties on the device performance. Throughout this chapter, the existence of pinholes in the absorber layer is regarded as a given feature of real-world thin-film solar cells. Furthermore, the physical nature of pinholes is acknowledged which give way to a direct physical and electrical contact between the semiconducting electron and hole transport layers (ETL and HTL, respectively). Experimentally obtained current-voltage characteristics of the semiconductor heterojunction at a pinhole show a diode-like and thus clearly non-linear characteristic. Chapter 4.1 illustrates how non-linear shunting affects the current-voltage characteristic of a solar cell and compares it to the qualitatively different behavior of a linear shunt. The experimental data is used to predict the impact of pinholes on solar cell performance with numerical simulations and simple equivalent circuits. Chapter 4.2 outlines the methodology that is then used in chapter 4.3 to investigate different ETL/HTL combinations that are commonly used as contact layer materials for emerging solar cell absorbers such as perovskites and  $\text{Sb}_2\text{S}_3$ . In this context, ETL/HTL combinations are identified that reduce the impact of shunting from pinholes. Furthermore, I discuss the critical parameters and scenarios for which pinholes have a severe impact on fill factor and open-circuit voltage. Chapter 4.4 compares the predicted impact of pinholes for different ETL/HTL combinations with experimental results on complete solar cells based on perovskite and  $\text{Sb}_2\text{S}_3$  absorbers that apply the same ETL/HTL combinations. This leads to the discussion in chapter 4.5 in how far the effect of pinholes can be distinguished

#### 4. Pinholes and Non-linear Shunts in Thin-Film Solar Cells

from other effects when only considering the solar cell  $J$ - $V$  characteristic. Here, further options to improve the contacts' tolerance against pinholes are mentioned and the transfer of the methodology to related problems is discussed. Altogether, this study highlights the importance of optimizing contact layers also with respect to real-world solar cells that contain pinholes instead of only considering the unharmed absorber domains.<sup>1</sup>

### 4.1. Qualitative Phenomenon

This section considers the physical and electrical situation at a pinhole and illustrates the consequence of such inhomogeneity in the absorber layer on the current density-voltage ( $J$ - $V$ ) characteristic of a solar cell. Figures 4.1(a) and (b) show scanning electron microscope (SEM) images of two absorber layers that were deposited via spin coating from solution and suffer from incomplete substrate coverage. Lead-based perovskites [12, 96, 209] in fig. 4.1(a) are prominent candidates for highly efficient thin film solar cells and  $\text{Sb}_2\text{S}_3$  [210] in fig. 4.1(b) serves as an example for a less-optimized absorber technology that is also investigated experimentally in this thesis. Both films contain pinholes with sizes in the range of 10-100 nm.

The layer sequence at a pinhole and at the regular domains with absorber is illustrated in fig. 4.1(c) for a typical solar cell. The regular cell stack consists of a hole transport layer (HTL), an absorber and an electron transport layer (ETL) that are sandwiched between a metal and a TCO electrode. Given that the material deposited on top of the absorber infiltrates the pinholes, these pinholes become domains where the ETL and HTL are in direct physical contact. The pinhole domains thus form parasitic current paths - indicated by the arrow in fig. 4.1(c). The schematic energy level diagram of the ETL/HTL interface in fig. 4.1(d) reveals the nature of this shunt: the two (doped or undoped) semiconductors that function as electron and hole transport material form a (type-II) heterojunction - meaning that

---

<sup>1</sup>Large parts of the text and figures in this chapter (4) closely follow or are identical to my contributions to the first-author publication "How Contact Layers Control Shunting Losses from Pinholes in Thin-Film Solar Cells". Reprinted in part with permission from ref. [110]. © 2018 American Chemical Society. Some of the ETL/HTL diodes as well as the perovskite containing samples were prepared and measured by others. The PVMOS calculations were performed by Paula Hartnagel and Bart E. Pieters.

both the conduction and valence band of the ETL are energetically below those of the HTL – which is expected to result in a diode-like, and thus clearly non-linear, current-voltage  $J$ - $V$  characteristic.

Regarding the influence on the solar cell  $J$ - $V$  characteristic, textbooks typically discuss shunts in terms of an Ohmic resistor [35, 36, 122, 211] which allows the development of simple models and approximations, concerning e.g. the fill factor [64, 119]. An Ohmic shunt is sometimes also used to describe pinholes in thin-film solar cells [212] with layer stacks similar to the one depicted in fig. 4.1(c) although the shunt characteristic should be clearly non-linear as discussed before. The non-linearity of shunts has been discussed in different contexts [213–219] but not with a focus on pinholes in the absorber and their impact on solar cell performance. In the following the qualitative difference between the influences of linear (Ohmic) versus non-linear (non-Ohmic, diode-like) shunts is illustrated. The top panels of fig. 4.1(e) depict the  $J$ - $V$  characteristics of an Ohmic and non-Ohmic shunt. To illustrate the shunts' impacts on an ideal solar cell as depicted in the bottom panels, the current of a simple equivalent circuit is calculated. The circuit is defined by the parallel connection of the shunt current  $J_{sh}$ , the current of an ideal diode  $J_{d,id}$  and a photocurrent  $J_{sc}$  resulting in

$$J(V) = -J_{sc} + J_{d,id} + J_{sh} = -J_{sc} + J_0 \left( \exp\left(\frac{qV}{n_{id}k_b T}\right) - 1 \right) + J_{sh}. \quad (4.1)$$

Here,  $q$  is the elementary charge,  $k_b$  is the Boltzmann constant,  $T$  is the temperature,  $n_{id}$  is the diode ideality factor,  $J_0$  is the saturation current density and  $V$  is the externally applied voltage. The parameter values for the ideal diode are given in the figure caption and all series resistances are neglected in this simple model. According to eq. 4.1, the shunt current from a pinhole can be interpreted as an additional recombination current, as is suggested by the arrow in fig. 4.1(d). The Ohmic shunt in fig. 4.1(e) introduces a characteristic slope at  $J_{sc}$  and reduces the fill factor  $FF$ . Only for very large shunts (small Ohmic shunt resistance) the  $V_{oc}$  is slightly affected but at the same time the  $FF$  has decreased more dramatically to almost 25%. Compared to the Ohmic case, the diode-like (exponential) shunt in fig. 4.1(e) has a substantially different impact on the ideal solar cell. The current at low voltages is

#### 4. Pinholes and Non-linear Shunts in Thin-Film Solar Cells

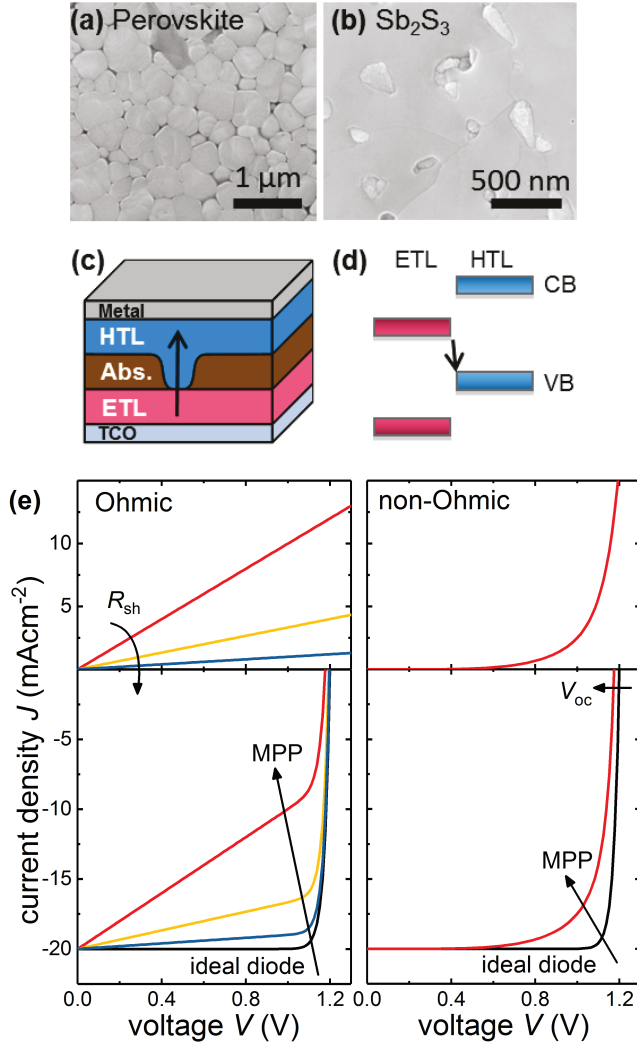


**Figure 4.1.:** SEM images of (a) perovskite and (b)  $\text{Sb}_2\text{S}_3$  absorber films with pinholes that expose the underlying substrate. (c) Typical layer stack with a pinhole in the absorber that results in a shunt current at the physical contact between ETL and HTL. (d) Schematic energy diagram at the ETL/HTL interface pinhole. The bars indicate the conduction (CB) and valence (VB) bands. The arrows in (c) and (d) indicate the diode-like recombination current. (e) Shunt characteristics (top panels) and impact on an ideal solar cell (bottom panels) with  $J_{sc} = 20 \text{ mAcm}^{-2}$ ,  $n_{id}=1$  and  $J_0$  chosen such that  $V_{oc}=1.2 \text{ V}$ . The non-Ohmic shunt has the form  $a(\exp(qV/(n_{id}k_bT)) - 1) + bV^c$  to model a non-linear but also not purely exponential shunt. The maximum power point (MPP) is affected in different ways for the two cases.

not affected at all and the decrease in fill factor differs qualitatively from the Ohmic case. Even more strikingly, there is a decrease in  $V_{oc}$  whereas the value of the  $FF$  is still decent. This behaviour can be rationalized from the exponential drop in resistance of a diode-like shunt.

In summary, Ohmic and non-Ohmic shunts might – in general - reduce the maximum power point to the same degree. However, while an Ohmic shunt reduces the total current at lower voltage; the non-Ohmic shunt becomes radically more harmful towards higher voltage. Consequently, the key to a qualitative understanding of the influence of pinholes on the  $J$ - $V$  characteristic of a solar cell is to consider the non-linear nature of the diode-like shunt source in some detail. Going one step further, a quantitative model is developed to analyze potential differences between ETL/HTL combinations.

## 4.2. Methodology

To evaluate differences in shunt behavior between various ETL/HTL combinations, the respective current-density-voltage ( $J$ - $V$ ) characteristic at the pinholes must be known. Therefore, devices from ETL/HTL combinations in a stack without absorber layer were produced as displayed in the inset of fig. 4.2(a). For the  $n$ - $i$ - $p$  case, the stack is thus TCO/ETL/HTL/metal. Such structures, which I refer to as ETL/HTL diodes, are thought to mimic the pinhole domains in a full solar cell. The devices turned out to be imperfect diodes that cannot be easily parameterized, so that the full  $J$ - $V$  characteristic of the ETL/HTL diode obtained from measurements was used for further processing. The dark  $J$ - $V$  characteristic of the ETL/HTL diode displayed by the black circles in fig 4.2(a) basically represents the shunt characteristics at a pinhole. However, for large voltages this experimental  $J$ - $V$  characteristic is dominated by the series resistance of the TCO ( $R_{ETL/HTL}$ ) stemming from the lateral charge transport across the TCO, so that the measured current of the ETL/HTL diode underestimates the current through a pinhole. Consequently,  $R_{ETL/HTL}$  has to be removed in order to obtain the  $J$ - $V$  characteristic of the pinholes themselves. By fitting the experimental data the pinhole's  $J$ - $V$  characteristic shown in red in fig 4.2(a) is obtained. The fitting is done with the open-source [220] numerical device

#### 4. Pinholes and Non-linear Shunts in Thin-Film Solar Cells

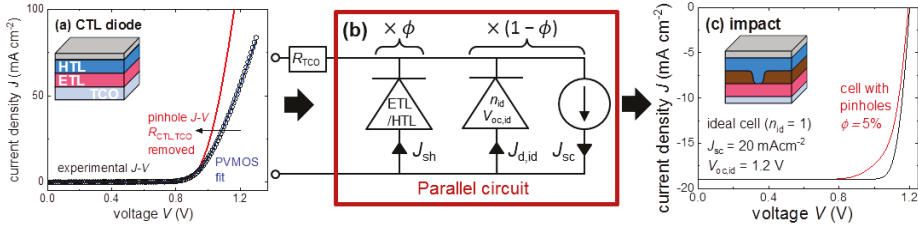


**Figure 4.2.:** Methodology to predict the impact of pinholes on device performance. (a) A device without absorber layer, termed ETL/HTL diode, is produced to mimic the situation at a pinhole. The measured  $J$ - $V$  characteristic is corrected for the TCO series resistance  $R_{ETL/HTL}$  and then serves as shunt characteristic for the simple parallel equivalent circuit in (b). The current of the shunt and the ideal solar cell are weighted by the cumulative pinhole area fraction  $\phi$  and in a last step the effective series resistance  $R_{TCO}$  of the TCO is added again. (c) Exemplary result of the equivalent circuit model.

simulator PVMOS [221], that applies the network simulation method for a network of resistances and diodes that are interconnected laterally via resistors.<sup>2</sup> The subsequent calculations build on the pinhole's  $J$ - $V$  characteristic simulated with PVMOS.

A simple parallel circuit model is proposed to predict the impact of the pinhole's experimentally obtained shunt characteristic on the performance of the solar cell. The validity of this quasi-zero-dimensional approximation is shown in the Supporting Information of ref. [222]. I call The percentage of uncovered area with respect to the total cell area the (cumulative) pinhole area (fraction)  $\phi$ . Thus, for  $\phi = 0\%$ , the absorber layer completely covers the substrate whereas  $\phi = 100\%$  means that there is no absorber at all. The study focuses on realistic cases of reasonably efficient solar cells with pinhole area fractions up to 10%. The parallel circuit indicated by the red frame in fig. 4.2(b) consists of a non-linear shunt  $J_{sh}$  – given by the pinhole's characteristic - and an ideal diode  $J_{id}$  with photocurrent source  $J_{sh}$  that represents the ideal pinhole-free parts of the solar cell. To obtain the current of the parallel circuit  $J_{par}$ , the current contributions from the ideal solar cell and the shunt are weighted according to the pinhole area fraction  $\phi$  via

$$J_{par} = \phi J_{sh} + (1 - \phi) (J_{d,id} - J_{sc}). \quad (4.2)$$

<sup>2</sup>The details of all simulations done with PVMOS can be found in the Supporting Information of ref. [222]. The discussion within this thesis is restricted to the relevant conclusions since the simulations were mainly carried out by Paula Hartnagel and Bart Pieters.

## 4.2. Methodology

As a standard parametrization of the ideal solar cell a photocurrent of  $J_{sh} = 20 \text{ mA cm}^{-2}$ , an ideal diode with ideality factor  $n_{id} = 1$  and a saturation current density  $J_0$  that yields an open-circuit voltage of  $V_{oc,id} = 1.2 \text{ V}$  are chosen.

To finally obtain the  $J$ - $V$  characteristic of a full solar cell, the series resistance of the TCO has to be added to the  $J$ - $V$  characteristic of the parallel circuit. This can be done via modeling the distributed series resistance of the TCO with PVMOS or by replacing it by an effective Ohmic series resistance  $R_{TCO}$  as indicated in the equivalent circuit in fig. 4.2(b). For the considered TCO sheet resistance and cell geometry displayed in fig. 3.1,  $R_{TCO} \approx 17 \Omega$  when ITO is used and  $R_{TCO} \approx 14 \Omega$  when FTO is used. This effective series resistance can be either estimated by a simple calculation or by fitting it to the results obtained from PVMOS as described in the Supporting Information of ref. [222]. The resulting  $J$ - $V$  characteristic of the equivalent circuit is displayed in fig. 4.2(c) for a pinhole area fraction of 5% and an ETL/HTL diode based on PEDOT/PCBM. The deviations from the ideal solar cell characteristic indicate the detrimental impact of the shunt from pinholes on the device performance. The impact on  $FF$  and  $V_{oc}$  is similar to the illustration in fig. 4.1(e).

Although an inhomogeneous device can always be described by a single effective  $J$ - $V$  characteristic, a validation is needed that the simple zero-dimensional equivalent circuit proposed in fig. 4.2(b) approximates this effective  $J$ - $V$  characteristic well. More complex simulations of a pinhole-containing solar cell were performed with PVMOS. Thereby the actual lateral inhomogeneity of the solar cell consisting of randomly distributed nanoscopic pinholes within domains of an ideal absorber were modeled. Details of the model employed in PVMOS, the results and the comparison to the parallel circuit model can be found in the Supporting Information of ref. [222]. Deviations between the parallel circuit model and the full solar cell amount to less than 2% for all investigated ETL/HTL combinations and pinhole areas. Consequently this study continues with the simple parallel circuit model which also facilitates the qualitative understanding of the pinhole's impact.

### 4.3. Prediction of Pinhole Impact

In the following, different contact layer combinations are compared, that are typically used in today's solution-processed thin-film solar cells. The experimental dark  $J$ - $V$  data of the corresponding ETL/HTL diodes is shown in fig. 4.3(a) after the TCO's series resistance has been removed. All  $J$ - $V$  characteristics are indeed non-linear and resemble a diode rather than an Ohmic resistor. Despite the qualitative similarity, different ETL/HTL combinations differ substantially in quantitative terms. Common layer stacks used with perovskites in an  $n$ - $i$ - $p$  configuration are mesoporous titanium dioxide with Spiro-OMeTAD (mp-TiO<sub>2</sub>/spiro) and compact TiO<sub>2</sub> with Spiro-OMeTAD (c-TiO<sub>2</sub>/spiro), whereas the  $p$ - $i$ - $n$  configuration is typically based on a combination of Poly(3,4-ethylenedioxythiophene)-poly(styrenesulfonate) (PEDOT:PSS, short: PEDOT) with phenyl-C<sub>60</sub>-butyric acid methyl ester (PEDOT/PCBM). Other new absorber materials like Sb<sub>2</sub>S<sub>3</sub> that are embedded in an  $n$ - $i$ - $p$  stack make use of the versatility of conjugated polymers to choose an appropriate hole transport material. Here compact TiO<sub>2</sub> with Poly(3-hexylthiophene) (c-TiO<sub>2</sub>/P3HT) and compact TiO<sub>2</sub> with KP115 (c-TiO<sub>2</sub>/KP115) is investigated. Figure 4.3(a) shows that certain interlayer combinations like TiO<sub>2</sub>/P3HT reach high current densities at much lower voltages than other combinations such as mp-TiO<sub>2</sub>/spiro.

The difference in shunt characteristic directly translates into solar cell performance as shown by the calculated illuminated  $J$ - $V$  curves at a pinhole area fraction of  $\phi = 5\%$  in fig. 4.3(b). While the  $J$ - $V$  characteristic of the mp-TiO<sub>2</sub>/spiro configuration is almost identical to that of the ideal solar cell, all other ETL/HTL combinations show a reduced fill factor  $FF$ . In the extreme case of c-TiO<sub>2</sub>/P3HT not only the  $FF$  decreases but also the open-circuit voltage  $V_{oc}$  drops by several hundreds of meV. I qualitatively refer to the degree to which an ETL/HTL combination prevents a pinhole-induced decline in performance as its ability to block shunts. In this sense mp-TiO<sub>2</sub>/spiro would be a good shunt blocker and c-TiO<sub>2</sub>/P3HT would be a bad one.

The shunt impact on  $FF$ ,  $V_{oc}$ , and efficiency  $\eta$  is further analyzed for varying pinhole area fractions in fig. 4.3(c). As expected, the performance drops with increasing pinhole area fraction. Solar cells based on ETL/HTL combinations with

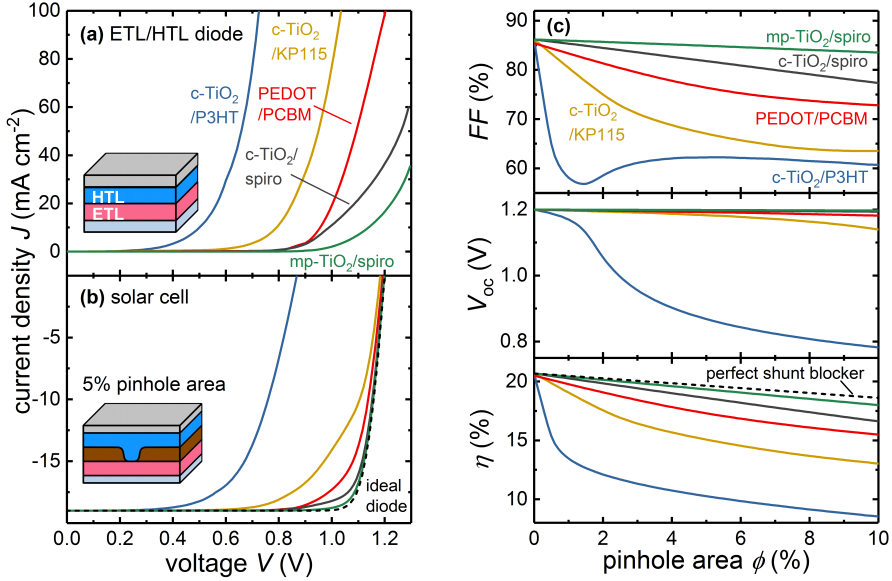


**Figure 4.3.:** Results for five commonly used contact layer combinations: (a) Experimental  $J$ - $V$  characteristics of ETL/HTL combinations without absorber after correcting for the TCO's series resistance. (b) Resulting simulated light  $J$ - $V$  curves of a full solar cell with a pinhole area fraction of  $\phi = 5\%$ . The dashed line represents an ideal solar cell that covers 95% of the cell area and, just like the other curves, takes  $R_{\text{TCO}}$  into account. (c) Fill factor  $FF$ , open-circuit voltage  $V_{oc}$ , and efficiency  $\eta$  for different cumulative pinhole area fractions. The perfect shunt blocker indicated in the bottom panel describes an ideal ETL/HTL combination where the solar cell only suffers from the decrease in active cell area and additional shunt losses are avoided.

#### 4. Pinholes and Non-linear Shunts in Thin-Film Solar Cells

good shunt blocking properties are affected less than those that conduct high shunt currents at the pinholes. With the exception of c-TiO<sub>2</sub>/P3HT all ETL/HTL combinations mostly suffer from a decline in  $FF$  rather than  $V_{oc}$ . A slight impact on  $V_{oc}$  can be identified for c-TiO<sub>2</sub>/KP115 and PEDOT/PCBM at pinhole area fractions >5%. For the case of the bad shunt blocker c-TiO<sub>2</sub>/P3HT the  $FF$  drops sharply at very small pinhole area fractions whereas the  $V_{oc}$  is barely affected. However, for pinhole area fractions larger than 1% the  $FF$  almost saturates around 60% whereas the  $V_{oc}$  declines heavily. The strong impact of pinholes on the  $V_{oc}$  also explains the qualitatively different behaviour of the  $FF$  for c-TiO<sub>2</sub>/P3HT. For pinhole area fractions below 1% the shunt current is not large enough to decrease the  $V_{oc}$  and only affects the maximum power point ( $MPP$ ) and thus the  $FF$ . Towards larger pinhole area fractions the  $V_{oc}$  is affected in addition to the  $MPP$ . The  $FF$  is composed by the ratio of the voltage at  $MPP$  and the  $V_{oc}$  via  $FF = (J_{MPP}V_{MPP}) / (J_{sc}V_{oc})$ , which yields the irregular shape of the  $FF$  in the transition regime from a decrease only in  $V_{MPP}$  to a regime with decrease also in  $V_{oc}$ . The  $MPP$  itself behaves more regular as can be seen from the monotonous decrease in efficiency that is proportional to the power at the  $MPP$ . Between the different ETL/HTL combinations, the resulting efficiency varies over several (absolute) per cent for a given pinhole area fraction. With increasing pinhole area fraction there is always a decrease in efficiency mediated by the short-circuit current and caused by the decreased active cell area. The dashed line in fig. 4.3(c) represents this obvious loss, which can also be regarded as the upper limit of a perfectly shunt-blocking ETL/HTL combination. The mp-TiO<sub>2</sub>/spiro stack comes very close to this ideal case even for large pinhole area fractions. It can be concluded that with increasing pinhole area fraction or decreasing shunt blocking capability, the  $FF$  is affected first but eventually the  $V_{oc}$  becomes limiting to device performance.

It is important to note that this behaviour directly results from the specific  $J$ - $V$  characteristic of the pinhole, which is not linear, but not a single exponential either. If the pinhole was an ideal diode described by an exponential function, the current of the parallel circuit would be given by the sum of two exponentials according to eq. 4.2. If the exponential pinhole current was then dominant, it would determine the total current according to its ideal diode properties, formally taking the role of the recombination current. This means it would decrease the  $V_{oc}$  but yield the  $FF$

### 4.3. Prediction of Pinhole Impact

of an ideal diode. However, the data of the ETL/HTL diodes show that the pinhole characteristic is not a simple exponential and the impact on the  $FF$  is stronger than on the  $V_{oc}$  which can be rationalized by the fact that the current density through the pinholes is much higher than the current density through the absorber domains. This is illustrated by considering the situation where the current through the pinholes fully compensates the current through the absorber domains. According to eq. 4.2 this requires the shunt current to be a factor of  $(1-\phi)/\phi$  larger than the current through the absorber domains which is a factor of 19 for  $\phi = 5\%$ . At such high currents, non-exponential terms seem to dominate the pinhole  $J-V$  characteristic with one possible cause being the series resistance of the ETL and HTL.

As stated above, the impact of a shunt is determined by the ratio between the current through the pinhole and the current through the absorber layer of the solar cell. Therefore not only the shunt characteristic and the pinhole area fraction affects the shunt impact but also the electrical properties of the absorber domains – in this case the parametrization of the ideal diode. As a consequence of their non-linear shunt characteristic, pinholes have a stronger influence at higher voltages. In fig. 4.3(a) the  $V_{oc,id}$  of the ideal diode was varied while the pinhole area fraction was fixed at 5%. With increasing  $V_{oc,id}$  of the ideal diode the  $V_{oc}$  of the device with pinholes increases almost proportionally for four of the five tested ETL/HTL combinations. Only *c*-TiO<sub>2</sub>/P3HT deviates and even saturates at a certain voltage that depends on the pinhole area fraction which then leads to a saturated efficiency as well. The initial increase of the  $FF$  for the discussed ETL/HTL combinations with increasing  $V_{oc,id}$  can be simply attributed to the larger  $V_{oc}$  [64,119]. At a certain  $V_{oc,id}$  the detrimental impact of the shunt becomes large enough to affect the  $FF$  which then reaches a maximum and decreases for higher  $V_{oc,id}$  which in some cases also leads to a saturation of the efficiency. This means that by limiting the  $V_{oc}$  as for *c*-TiO<sub>2</sub>/P3HT or the  $FF$  as for *c*-TiO<sub>2</sub>/KP115 and PEDOT/PCBM, the presence of pinholes can – depending on the ETL/HTL's shunt blocking quality and the pinhole area fraction – set a firm upper limit for the solar cell efficiency even if the intact absorber domains are further improved. Moreover, the issue of pinholes becomes more critical for solar cells that reach high open-circuit voltages in the absence of pinholes. Exactly these materials are of special interest for photovoltaic research and industrial application which underlines the practical relevance of pinholes and the

#### 4. Pinholes and Non-linear Shunts in Thin-Film Solar Cells

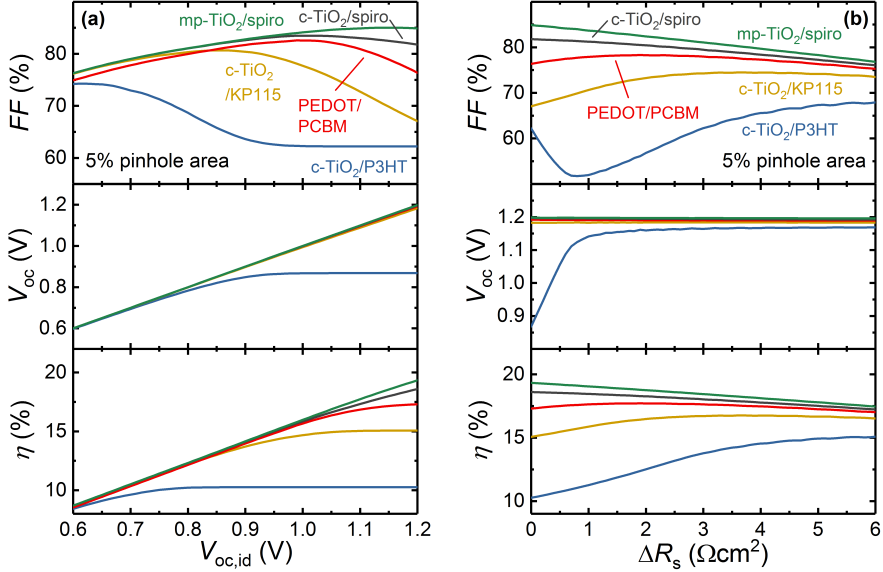


**Figure 4.4.:** (a) For higher  $V_{oc,id}$  of the absorber domains, pinholes become more critical to device performance due to significantly higher shunt currents at higher voltages. (b) An additional series resistance  $\Delta R_s$  of the ETL/HTL combination suppresses the shunt current through the pinhole and can be beneficial for the device performance. The trade-off with the increased overall series resistance leads to an optimum performance at finite  $\Delta R_s$  in some cases.

need for charge transport layer combinations that effectively suppress the resulting shunts.

There are few parameters to tune and improve the shunt blocking properties for a given ETL/HTL material combination because the ETL/HTL interface largely determines the shunt characteristic. One available option is to increase the series resistance of the ETL/HTL stack, for example by simply increasing the layer thickness or introducing an additional resistive layer as in the case of CIGS solar cells [29, 111]. An increased series resistance restricts the exponential shunt current at high voltages. However the same series resistance will act on the intact absorber domains. The described effect is illustrated by adding an Ohmic series resistance  $\Delta R_s$  to the pinhole's  $J$ - $V$  characteristic as well as to the ideal diode that represents the absorber domains of the solar cell. The trade-off between better shunt blocking

#### 4.4. Comparison of Devices with and without Absorber

and increased overall series resistance can be clearly seen in  $FF$  and efficiency for  $c\text{-TiO}_2/\text{KP115}$  and  $\text{PEDOT}/\text{PCBM}$  in fig. 4.3(b) where a maximum in efficiency is reached for a finite additional series resistance. For  $c\text{-TiO}_2/\text{P3HT}$  a higher series resistance also improves the  $V_{oc}$ . Altogether, more resistive electron and hole transport layers can improve the efficiency of certain ETL/HTL combinations but the optimized efficiency still stays behind that of  $mp\text{-TiO}_2/\text{spiro}$  or  $c\text{-TiO}_2/\text{spiro}$ . Here, no benefit of an additional series resistance is observed because these ETL/HTL combinations are already good shunt blockers. A similar effect of beneficial finite series resistance was pointed out by Rau et al. [30] for inhomogeneous diode properties where an optimum series resistance was found that – depending on the degree of fluctuations – balances the benefits of smoothing electronic fluctuations and the decrease in  $FF$  caused by the additional series resistance.

## 4.4. Comparison of Devices with and without Absorber

Experimental  $J$ - $V$  characteristics of full solar cells based on the pinhole-bearing spin-coated absorber layers  $\text{Sb}_2\text{S}_3$  shown in fig. 4.5(b) and perovskite shown in fig. 4.5(d) support the proposed impact of non linear shunts. Both cases apply an  $n$ - $i$ - $p$  layer stack where the hole transport layer HTL is varied which changes the shunt characteristic at the pinholes. The underlying ETL is not varied so that differences in the film formation of the absorber can be dismissed. Figure 4.5(a) and (c) show the experimental  $J$ - $V$ -curves of the stacks without absorber and fig. 4.5(b) and (d) show the illuminated  $J$ - $V$  characteristic of the full cell.

Antimony sulfide  $\text{Sb}_2\text{S}_3$  is employed in fig. 4.5(b) according to the Sb-TU process described in chapter 3.2 as an example of a relatively unexplored absorber material, which is discussed more extensively in chapter 6. It can be seen from fig. 4.5(a) that the interlayer combination  $c\text{-TiO}_2/\text{P3HT}$  causes worse shunts than  $c\text{-TiO}_2/\text{KP115}$ . The  $V_{oc}$  of the corresponding  $c\text{-TiO}_2/\text{Sb}_2\text{S}_3/\text{P3HT}$  solar cell is significantly lower compared to  $c\text{-TiO}_2/\text{Sb}_2\text{S}_3/\text{KP115}$ . This behaviour is expected from the model developed in this chapter and can be attributed to the higher shunt currents of  $c\text{-TiO}_2/\text{P3HT}$  at open circuit. The pinholes thus represent a significant

#### 4. Pinholes and Non-linear Shunts in Thin-Film Solar Cells

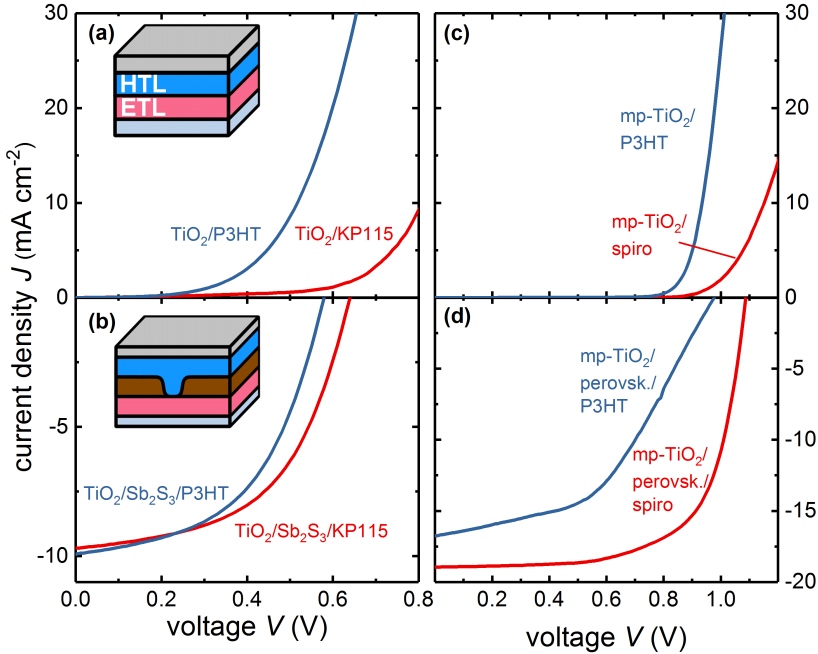


**Figure 4.5.:** Experimental current density vs. voltage ( $J$ - $V$ ) characteristics of (a),(c) different ETL/HTL diodes in the dark and (b),(d) full solar cells under illumination based on (a),(b)  $\text{Sb}_2\text{S}_3$  and (c),(d) perovskite absorbers. In both cases the interlayer combination with higher shunt currents shows a decrease in  $V_{oc}$  and  $FF$ . For perovskite (d) other effects seem to be superimposed on the shunt deterioration. The solar cell parameters in (b) are  $J_{sc} = 9.9 \text{ mA cm}^{-2}$ ,  $FF = 51\%$ ,  $V_{oc} = 0.578 \text{ V}$  for  $\text{c-TiO}_2/\text{Sb}_2\text{S}_3/\text{P3HT}$  and  $J_{sc} = 9.7 \text{ mA cm}^{-2}$ ,  $FF = 53\%$ ,  $V_{oc} = 0.641 \text{ V}$  for  $\text{c-TiO}_2/\text{Sb}_2\text{S}_3/\text{KP115}$ . Data in (d) yields  $J_{sc} = 16.8 \text{ mA cm}^{-2}$ ,  $FF = 47\%$ ,  $V_{oc} = 0.977 \text{ V}$  for  $\text{mp-TiO}_2/\text{perovskite}/\text{P3HT}$  and  $J_{sc} = 19.0 \text{ mA cm}^{-2}$ ,  $FF = 67\%$ ,  $V_{oc} = 1.09 \text{ V}$  for  $\text{mp-TiO}_2/\text{perovskite}/\text{spiro}$ .

limitation of the  $V_{oc}$  and the solar cell performance in the case of the c-TiO<sub>2</sub>/P3HT contact layer combination. Again, the drop in  $V_{oc}$  in conjunction with a still appreciable  $FF$  cannot be explained by an Ohmic shunt but only by a non-linear one. A more quantitative estimation of the pinhole-related losses for Sb<sub>2</sub>S<sub>3</sub> solar cells is presented in fig. 6.8.

As a second example, lead-based perovskite is applied in a solar cell with the interlayer combinations mp-TiO<sub>2</sub>/spiro and mp-TiO<sub>2</sub>/P3HT in fig. 4.5(c) and (d). The mp-TiO<sub>2</sub>/P3HT diode in fig. 4.5(c) conducts much larger currents around the  $V_{oc}$  and  $MPP$  than the mp-TiO<sub>2</sub>/spiro. The strong suppression of shunts in the case of the mp-TiO<sub>2</sub>/perovskite/spiro allows a solar cell with decent performance while  $V_{oc}$  and  $FF$  are reduced in the case of mp-TiO<sub>2</sub>/perovskite/P3HT. However, the  $J_{sc}$  also decreases which cannot be explained within the framework described in this work. By applying P3HT instead of spiro-OMeTAD more properties of the solar cell seem to change than just the shunt currents at the pinholes.

## 4.5. Discussion

Generally, it is difficult to experimentally distinguish between shunting and other effects that are superimposed on the  $J$ - $V$  characteristic. As an obvious example, when one interlayer is exchanged by another not only the interface at the pinhole which dictates the shunt characteristic is altered, but also the band diagram of the pinhole free absorber domains. When the underlying interlayer is exchanged, the growth conditions and resulting properties of the absorber may change as well [223]. Neglecting this influence on absorber layer formation and taking a broader perspective, the capability of a certain charge transport layer combination to suppress shunt currents at a pinhole can be regarded as a contact property. Other contact properties include optical aspects such as parasitic absorption and light management [63, 68] as well as selectivity - comprising surface recombination of minority carriers and series resistance of majority carriers [224] - and built in electric field. While the optical contact properties mostly affect the cell's  $J_{sc}$ , selectivity and built-in field directly affect  $V_{oc}$  and  $FF$  [83, 224] (as will be discussed in chapter 5). These properties mainly depend on one of the contacts - namely its geometric dimensions, the choice

#### 4. Pinholes and Non-linear Shunts in Thin-Film Solar Cells

of material (including details of processing) and the interface it forms with the absorber layer which for example determines trap densities. In contrast, the non-linear shunting behavior results from the combination of both contacts and the interface they form. In the final illuminated  $J$ - $V$  characteristic, all of the mentioned contact characteristics are superimposed so that the impact of shunting cannot be clearly identified experimentally. Nevertheless, the shunt blocking properties are crucial for the quality of the contact with regard to solar cell performance in the presence of pinholes in the absorber layer.

Different concepts to circumvent pinholes or moderate their impact on device performance have been proposed or established. The resistive shunt mitigation discussed in fig. 4.4 appears as a general concept for optimizing the efficiency of real world thin-film solar cells [28, 30, 225]. In the case of CdTe, pinholes are avoided by simply depositing an absorber layer that is much thicker than is required for efficient photon absorption [104, 105] which could generally reduce charge carrier collection efficiency (see i.e. chapter 5) and increase fabrication time and costs. Given that the absorber film contains pinholes, these could be passivated via selectively depositing a highly resistive polymer as is done for CdTe [226, 227] – a route that has also been explored for perovskites [112]. However, such extra effort and tradeoff can be spared if a shunt-blocking ETL/HTL is used as shown in this work and has been argued recently for CdTe [106].

The presented methodology can be applied straightforward to other thin-film technologies like CdTe and CIGS that typically use different contact layer materials than the ones discussed here. Additionally, pinholes may not only appear in the absorber layer of a thin-film solar cell but also in any of the other layers including the directly adjacent ETL and HTL. Then, a more refined contact configuration consisting of a sequence of different layers, maybe deposited via different methods, might prevent a deterioration from pinholes as was shown in the systematic study [111] on CIGS solar cells mentioned in the introduction. Finally, the methodology and general findings should also be applicable to other (opto-) electronic devices with large aspect ratios such as photodetectors based on thin films [228–230].

## **4.6. Chapter conclusion**

Pinholes in the absorber layer are a common feature of real-world thin-film solar cells. The physical contact between electron and hole transport layer at the pinhole leads to non-linear shunting that can decrease the solar cell's fill factor and even drastically reduce its open-circuit voltage. This study provides an easy-to-apply parallel equivalent circuit model that predicts the impact of an experimentally obtainable shunt characteristic on the solar cell performance. Different charge transport layer combinations result in substantially different shunt currents which are reflected in the degree of performance deterioration – with certain advantageous combinations having a vanishing impact on the solar cell.

For today's novel thin-film solar cells that apply a large variety of contact layers, criteria to evaluate the quality of a contact are needed. This study demonstrates that the current characteristic at pinholes, which is determined by the contact layer configuration, may dictate the solar cell performance. This finding highlights the importance of not only optimizing the contacts with regard to the absorber layer, but to pay equal attention to the contacts' behaviour at pinholes. In other words, it may be that the optimum contact configuration of a pinhole-free thin-film solar cell differs from the optimum contact configuration of a real-world, imperfect thin-film solar cell that contains pinholes. Especially when aiming at up-scaled production of perovskite solar cells, a high tolerance of the contact layer combination against shunting from pinholes is likely to increase fabrication yields and reduce process requirements for the absorber film deposition which will eventually reduce production costs.



## 5. Charge Collection in Thin-Film Solar Cells

The fill factor  $FF$  is one of the three quantities that determine the solar cell efficiency. For many technologies it is far from its theoretical maximum as evident from fig. 2.2. Especially organic solar cells often apply thin absorber layers of about 100 nm as shown in fig. 2.9(c). At such low absorber thickness, absorption is incomplete (especially close to the band edge), but increasing the absorber thickness often causes inefficient charge carrier collection and a sharp drop in  $FF$  [154–156, 231]. Broadly speaking, the  $FF$  is determined by the competition of charge carrier extraction and recombination, but a detailed understanding the  $FF$  of thin-film solar cells remains challenging due its complex dependence on a multitude of parameters. By means of drift-diffusion simulations, I thoroughly analyze the  $FF$  of typical thin-film absorbers in chapter 5.1 with a focus on low-mobility systems such as organic solar cells and demonstrate its good correlation to a collection coefficient defined in this thesis. I systematically discuss the effect of different recombination mechanisms, space-charge regions and contact properties. Based on these findings the thickness dependence of the fill factor for different experimental studies from literature can be interpreted. The presented model provides a facile method to extract the absorber materials's electronic quality factor  $Q$  defined herein, which is of particular importance for the  $FF$ . Specifically,  $Q$  serves as a figure of merit for the  $FF$  and thus quantifies an absorber material's prospects in terms of charge carrier collection. Chapter 5.2 extends the  $FF$  analysis of the previous chapter and includes the absorption coefficient as a third material property, next to mobility and lifetime (or recombination coefficient), that, for a given band gap, determines the solar cell efficiency. Different regimes depending on the value of mobility and surface recombination velocity are found. Within a regime, a good correlation between the solar cell

## 5. Charge Collection in Thin-Film Solar Cells

efficiency and the specific figure of merit is found, making the proposed expressions the ultimate FOMs for the efficiency of *p-i-n*-like thin-film solar cells. Chapter 5.3.1 applies the developed models to organic solar cells, which constitute one of the most promising material classes for future thin-film solar cells. A meta-study of literature reports on noticeable and high-performing OSCs in terms of the electronic quality factor together with the Scharber efficiency offers a consistent interpretation of the development of high efficiency OSCs over the past 15 to 20 years. In a future perspective, OSCs based on non-fullerene acceptors (NFAs) that often show well-matched energy levels and high Scharber efficiency can overcome current efficiency limits if the electronic quality of the blends is improved. Next, the interplay between electronic quality and absorption of an organic material blend is studied in terms of the efficiency. For the promising class of NFA-based blends, either complementary or congruent absorption bands of the donor and acceptor molecules are advantageous, depending on the value of the electronic quality factor. Finally, the efficiency increase for enhanced absorption strength of organic absorbers is assessed as an alternative approach to overcome efficiency limits of today's organic solar cells.

### 5.1. Fill Factor and Electronic Quality

There is a general understanding of the influencing factors on the  $FF$ , such as mobility, lifetime, built-in voltage and active layer thickness. Basic models for the collection of charge carriers, such as Crandall's expression for the photocurrent presented in section 2.3.4 exist as well. However, there is a lack of analytical expressions that directly relate the  $FF$  to these quantities. Apart from the mathematical challenge of solving implicit equations of the optimization problem in eq. 2.9, the charge carrier dynamics in thin-film solar cells are complex and thus hard to grasp with simple analytical derivations. A slightly different approach is to demonstrate the correlation between the fill factor and quantities that I term collection coefficients, which contain the above mentioned material and device parameters. The goal is then to find an expression for the collection coefficient that correlates well with the fill factor, which provides a clear and quantitative understanding of the  $FF$ . At the same time, the boundaries of the model must be defined and further insight is gained

from the  $FF$  behavior in cases where the model's assumptions are violated. A comprehensive understanding of the  $FF$  and a precise model for the relation between the  $FF$  and a collection coefficient allows to deduce quantitative information from the  $FF$  about the collection coefficient and its constituting quantities that include the mobility  $\mu$  and lifetime  $\tau$ . This approach is highly practical and beneficial for experimentalists because the  $FF$  can be determined from relatively simple  $J$ - $V$  measurements under illumination, whereas measurements of  $\mu$  and  $\tau$  require far more sophisticated equipment and/or analysis [85]. As discussed on the basis of eq. 2.11 in section 2.3.4, the  $(\mu\tau)$ -product is of special importance for charge collection and is widely associated with the, mostly not properly defined, electronic quality of a semiconductor.

The model presented in this chapter follows this rationale and in section 5.1.3 provides, based on numerical drift-diffusion simulations, an optimized collection coefficient that closely correlates with the  $FF$ . The method is described in detail in section 5.1.1. Two limiting cases of non-radiative direct band-to-band and trap-assisted Shockley-Read-Hall (SRH) recombination are considered. Both mechanism have been observed previously in organic solar cells [232–234], while inorganic solar cells mostly suffer from SRH recombination. Surface recombination only becomes relevant for good bulk properties and acts on the  $FF$  mostly via the solar cell's  $V_{oc}$  which sets the maximum attainable fill factor [64]. An additional dependence of the fill factor on the surface recombination velocity is described in section 5.1.5. The parametrization of most simulations refers to organic solar cells, but section 5.1.7 shows that the results are very similar for inorganic materials that have higher dielectric constants and typically higher mobilities. The model mathematically defines an electronic quality factor  $Q$  in section 5.1.4, composed of mobility and lifetime or recombination coefficient, that can be extracted from illuminated  $J$ - $V$  curves for known thickness of the active layer. The  $Q$  extracted from the optimized model is significantly more precise than the analytical estimates based on previous literature reports [123, 124, 235] presented in section 5.1.2. The electronic quality factor is a valuable tool for the optimization of a technology that is experimentally accessible to a large community. The model is valid for fully depleted absorber layers and equal electron and hole mobilities so that transport is largely drift-dominated. A violation of the model's assumptions, namely the presence of a space charge region discussed

## 5. Charge Collection in Thin-Film Solar Cells

in section 5.1.6 or a  $FF$  limitation by the contacts discussed in section 5.1.5, shows characteristic signatures in the thickness dependence of the  $FF$ . The applicability of the model can thus be tested experimentally within the framework of the model itself, by preparing a series of devices with varying active layer thickness. At the same time the experimental observation of such signature provides a first indication for suboptimal device properties that can then be further investigated with more specific characterization methods.<sup>1</sup>

### 5.1.1. Method

In an approach similar to Bartesaghi et al. [235] this study is based on drift-diffusion simulations carried out over a wide range of parameter values. Huge datasets of  $10^4$  points are created and the behavior of the ensemble is analyzed. For each device simulation, the value of each parameter is chosen at random within its respective range specified in tab. 5.1, which in the first section reflects typical values of organic solar cells. In an effective-medium approach, spatially independent properties are assigned to the photoactive material blend which is thus described as a homogeneous medium. The energy difference between acceptor lowest unoccupied molecular orbital LUMO and donor highest occupied molecular orbital HOMO is taken as the effective band gap [125–127, 187, 237–239]. By condensing microstructural effects into device parameters – such as mobility  $\mu$  and direct recombination coefficient  $k$  – effective-medium simulations were successfully performed in many studies [125–128]. The free-charge-carrier generation rate  $G$  is assumed to be constant across the entire active layer. To prevent unrealistically high short-circuit currents for thick devices, the generation rate is adjusted for different active layer thicknesses and interference caused by flat interfaces is taken into account by simulations based on the transfer matrix method [188, 240] as shown in fig. 5.1(a). Regarding the application to organic solar cells, voltage-dependent geminate recombination (recombination of excitons) is negligible for many of today’s OSCs [135, 241–247] and is not considered here. Note that geminate recombination, which is independent of the applied electric field, merely reduces the generation rate of free carriers  $G$

---

<sup>1</sup>Large parts of the text and figures in this chapter (5.1) closely follow or are identical to my first-author publication “How to extract information on electronic quality of organic solar cell absorbers from fill factor and thickness” [236]. © 2016 American Physical Society

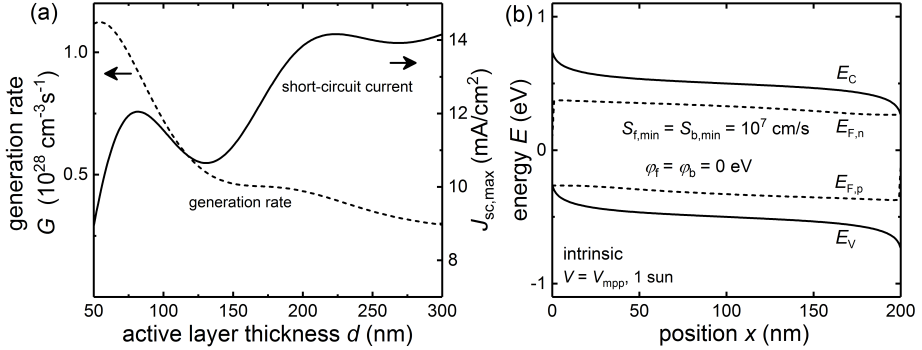


**Figure 5.1.:** (a) Thickness dependent generation as used throughout chapter 5.1 and resulting short-circuit current in the case of complete carrier collection (100% internal quantum efficiency). The calculation is done with the transfer matrix method [188, 240] for a representative cell stack of glass, 110 nm of ITO, 25 nm of PEDOT:PSS, varied thickness of P3HT:PC<sub>61</sub>BM blend, 7 nm of calcium and 200 nm of aluminum for normal incidence of AM1.5G illumination. Because interference is considered, maximums in the attainable short-circuit current appear slightly below 100 nm and slightly above 200 nm active layer thickness. (b) Band diagram at the *MPP* with indicated standard contact properties.

which does not affect the extraction and recombination dynamics of free carriers as long as charge-carrier concentrations are not changed drastically. The analysis is carried out for both direct (bimolecular, band-to-band or free-to-free) and trap-assisted (monomolecular, Shockley-Read-Hall, SRH) free-charge-carrier recombination models. The range of the direct recombination coefficient  $k$  or Shockley-Read-Hall lifetime  $\tau$  is taken from comprehensive studies of various polymer:fullerene blends [248–250]. Direct recombination in organic bulk-heterojunctions is often described to follow Langevin kinetics, where the mobility determines the recombination coefficient [235, 244]. For many polymer blends a mostly empirical and blend-specific Langevin-reduction factor is required to reproduce experimentally determined recombination coefficients [235, 244, 251] whereby the Langevin expression becomes merely an upper limit for direct recombination. For the presented model, the coefficient of direct recombination is randomly chosen from a wide parameter range which automatically covers the case of reduced Langevin recombination. The properties of interlayers and metallic contacts are implemented via energetic barriers at the contacts, surface recombination velocities and an external series resistance.

5. Charge Collection in Thin-Film Solar Cells

**Table 5.1.:** Parameter values and ranges used in the different simulations.

Parameter	figs. 5.2,5.3	fig. 5.4	fig. 5.5	fig. 5.6	fig. 5.7	unit
Thickness	$d$ 50 – 300	100	100	see fig.	50-300	nm
Effective band gap	$E_g$ 0.8 – 1.3	1	1, see fig.	1	0.8 – 1.3	eV
Mobility	$\mu_{e,h}$ $10^{-6} - 10^{-2}$	$10^{-6} - 10^{-2}$	$2 \times 10^{-3}$ , see fig.	see fig.	$10^{-6} - 10$	$\text{cm}^2(\text{Vs})^{-1}$
Direct rec. coeff.	$k$ $10^{-10} - 10^{-13}$	$5 \times 10^{-13}$	$5 \times 10^{-13}$	$10^{-12}$	–	$\text{cm}^3\text{s}^{-1}$
SRH lifetime	$\tau$ $10^{-6} - 10^{-4}$	–	–	–	$10^{-6} - 10^{-4}$	s
Illumination	$G$ $G(d)$	$G(d)$	$G(d)$	$G(d)$	$G(d)$	$\text{cm}^{-3}\text{s}^{-1}$
Doping	$N_d$ 0	0	0	see fig.	0	$\text{cm}^{-3}$
Ext. series res.	$R_s$ 0	0,3,5	0	0	0	$\Omega\text{cm}^2$
Schottky barriers	$\varphi$ 0	0	0	0	0	eV
Min. surf. rec. vel.	$S_{\text{min}}$ $10^7$	$10^7$	see fig.	$10^7$	$10^7$	$\text{cms}^{-1}$
Maj. surf. rec. vel.	$S_{\text{maj}}$ $10^9$	$10^9$	$10^9$	$10^9$	$10^9$	$\text{cms}^{-1}$
Dielectric constant	$\epsilon_r$ 3.5	3.5	3.5	3.5	3.5 – 100	–
Effective DOS	$N_{\text{cv}}$ $10^{19}$	$10^{19}$	$10^{19}$	$10^{19}$	$10^{19}$	$\text{cm}^{-3}$

The analysis starts by looking at undoped devices with balanced mobilities in sections 5.1.2 and 5.1.3 – implying the absence of space-charge regions so that the active layer is fully depleted. There is no external contribution to the series resistance from the metallic contacts.<sup>2</sup> Vanishing Schottky barriers  $\varphi$  to the contacts and high and equal minority surface recombination velocities of  $S = 10^7$  cm/s are assumed. Deviations from this standard case are denoted in the text. Note that in the whole discussion there is no preferential cell orientation related to the direction of light incidence on the device. Because of the spatially homogeneous generation rate, this also holds true in presence of a space-charge region at one of the contacts.

### 5.1.2. Analytical Estimates

Two analytical expressions for a collection coefficient have been derived in literature for the case of fully depleted absorber layers and different recombination mechanisms – namely trap-assisted Shockley-Read-Hall [123, 124] and direct band-to-band [235]. In the following, I will recap and relate the expressions for the simple case of equal electron and hole mobilities and, if applicable lifetimes, and evaluate their correlation to the fill factor based on drift-diffusion simulations following the method in section 5.1.1.

Crandall's model for the photocurrent [123] in systems dominated by Shockley-Read-Hall recombination, such as amorphous silicon, is given in eq. 2.11. The constant lifetime approximation is applied to achieve an analytical treatment, meaning that the recombination rate is characterized by a single lifetime  $\tau$  as in eq. 3.11 ( $R_{\text{srh}} = n/\tau$ ). The characteristic quantity of the associated charge carrier collection efficiency in drift-dominated systems in eq. 2.15 is the ratio of drift length  $L_{\text{dr}}$  over active layer thickness  $d$  [124]

$$\frac{L_{\text{dr}}}{d} = \mu\tau \frac{V_{\text{bi}} - V}{d^2}, \quad (5.1)$$

which naturally depends on the the electric field  $F = (V_{\text{bi}} - V)/d$  and thus on the applied voltage  $V$ . Equation 5.1 should be evaluated for the electric field present

---

<sup>2</sup>Note that in low-mobility systems such as organic solar cells the active layer contributes to the overall series resistance.

## 5. Charge Collection in Thin-Film Solar Cells

at the *MPP* ( $V = V_{\text{MPP}}$ ). However, to determine the  $V_{\text{MPP}}$  from material and device properties is actually a similar problem as determining the *FF*. This is the major drawback in the attempt to analytically derive a collection coefficient that correlates with the *FF*. Eventually, the most feasible option is to set  $V = 0$  in eq. 5.1, meaning that charge collection is evaluated at short-circuit, and hoping for a similar behavior at the *MPP*. However, the driving electric field is significantly weaker at the *MPP* (see fig. 5.1(b), the  $V_{\text{MPP}}$  is actually closer to  $V_{\text{oc}}$  than  $V = 0$ ) and the recombination profile differs from short-circuit. In order to obtain a model compatible with experimental work that can also be applied to reported data from literature, the built-in voltage in eq. 5.1 is replaced with the open-circuit voltage  $V_{\text{oc}}$  yielding an collection coefficient

$$\sqrt{\theta_{\text{SRH}}} = \mu\tau \frac{V_{\text{oc}}}{d^2}, \quad (5.2a)$$

where the squareroot is written simply for the sake of obtaining similar exponents as in the expression for direct recombination discussed in the following.

The same problem of properly parameterizing the system at the *MPP* is faced for the case of direct recombination ( $R_{\text{dir}} = k \times np$ , eq. 3.8), which is often assumed to be the dominant recombination mechanism in organic solar cells. Bartesaghi et al. [235] therefore also refer to a system at  $J_{\text{sc}}$ . The authors take a similar approach and calculate the ratio between the time that charge carriers are free before they recombine  $t_{\text{rec}}$  and the time that charge carriers need to be extracted  $t_{\text{ex}}$  which yields the collection coefficient<sup>3</sup>

$$\theta_{\text{dir}} = \frac{t_{\text{rec}}}{t_{\text{ex}}} = \frac{\mu^2}{k} \frac{V_{\text{oc}}^2}{d^3 J_{\text{sc}}}. \quad (5.2b)$$

Again, eq. 5.2b applies experimentally accessible quantities as opposed to the original expression in ref. [235] given in eq. C.1b in appendix C, which applies the homogeneous generation rate  $G$  and internal voltage  $V_{\text{int}}$ . See appendix C on the details of the substitutions, which are also used by Bartesaghi et al. in order to compare their experimental data to the simulation. Equation 5.2b can be deduced from eq. 5.2a by identifying  $\tau^{-1} = kp$  according to the corresponding recombination

<sup>3</sup>Bartesaghi et al. actually take the corresponding rates which are the inverse of the times considered here, resulting in the reciprocal expression to eq. 5.2b.

### 5.1. Fill Factor and Electronic Quality

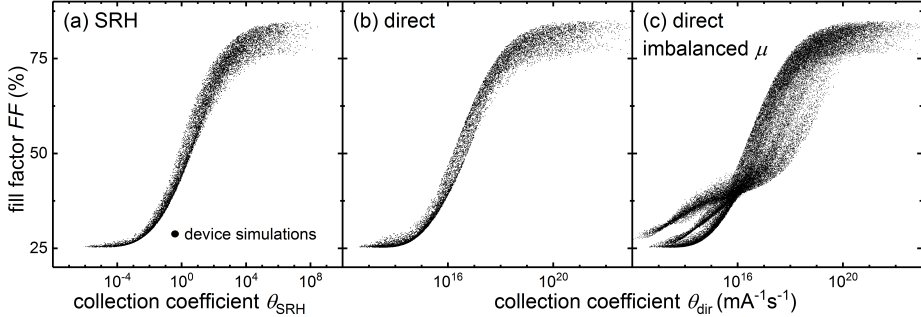
rates  $R_{\text{srh}} = \tau^{-1}n$  and  $R = k \times np$  and using the expression for the charge carrier density  $p$  in ref. [235]. For this, recombination is assumed strongest close to the contacts where the minority carrier density  $p$  is obtained from considering charge transport to the contact, actually neglecting recombination as mentioned also in ref. [235].

Figure 5.2 shows the correlation between the fill factor  $FF$  and the collection coefficients for SRH (fig. 5.2, eq. 5.2a) and direct (fig. 5.2(b), eq. 5.2b) recombination. The coordinates of each data point are obtained through extraction of  $FF$ ,  $V_{\text{oc}}$  and  $J_{\text{sc}}$  from the computed  $J$ - $V$  curves while mobility  $\mu$ , recombination coefficient  $k$ , lifetime  $\tau$  and thickness  $d$  are inputs to the simulations. Although the overall trend of large collection coefficients leading to large fill factors is evident for both cases, the data is considerably scattered in the linear and the saturation regime of the distribution. The scatter makes it difficult to quantitatively relate the measured  $FF$  with e.g. the mobility-lifetime product of the absorber material. In other terms, any value of such material properties extracted with the help of a model that produces significant scatter has a large error bar. As can be seen from fig. C.1 in appendix C, this scatter does not originate from the introduction of  $V_{\text{oc}}$  instead of built-in voltage  $V_{\text{bi}}$  or internal voltage  $V_{\text{int}}$  – and  $J_{\text{sc}}$  instead of generation rate  $G$  in the case of direct recombination – to the collection coefficients as defined from Crandall [123] and by Bartesaghi [235] and written in eq. C.1. For the case of imbalanced charge transport depicted in fig. 5.2(c) – also shown in the publication of Bartesaghi et al. and discussed later in section 5.1.6 – the scatter becomes much stronger.

#### 5.1.3. Optimized $FF$ Model

To obtain a collection coefficient with reduced scatter, a normalized fill factor  $FF_{\text{n}}$  is introduced and the exponents in eq. 5.2b are varied to find the relative weight of the constituting quantities and attain an optimized collection coefficient  $\gamma_{\text{dir}}$ . The normalization of the fill factor accounts for the dependence of the maximum fill factor  $FF_{\text{max}}$  on the open-circuit voltage  $V_{\text{oc}}$  as described in section 2.3.4. Several analytical functions which describe the solution of the problem exactly or approximately with varying accuracy were discussed by Green [119, 121]. Following Green's

## 5. Charge Collection in Thin-Film Solar Cells



**Figure 5.2.:** Correlation between the  $FF$  and analytically derived collection coefficients for (a) Shockley-Read-Hall (red) and (b) direct recombination (green) that reflect the competition between charge-carrier extraction and recombination in fully depleted thin-film solar cells. Each of the  $10^4$  data points in (a) and (b) corresponds to a device simulation for balanced mobilities  $\mu_e = \mu_h$  with input parameters chosen at random from the intervals given in tab. 5.1 that represent typical values for organic solar cells. (c) contains the data of (b) and two additional point clouds with imbalanced mobilities  $\mu_e = 10\mu_h$  and  $\mu_e = 100\mu_h$ . The mobility in eq. 5.2b splits into two terms  $\mu^2 \rightarrow \mu_e\mu_h$  as proposed by Bartesaghi et al. [235], which results in the enhanced scatter observed in that publication.

earlier work [119], we choose the simple relation

$$FF_{\max} = \frac{a \cdot V_{\text{oc}}}{V_{\text{oc}} + b} \quad (5.3)$$

and set the lower limit of possible fill factors to

$$FF_{\min} = 25\%, \quad (5.4)$$

corresponding to a non-rectifying device with linear  $J$ - $V$  curve. Subsequently, the fill factor is normalized via

$$FF_n = 2 \cdot \frac{FF - FF_{\min}}{FF_{\max} - FF_{\min}} - 1 \quad (5.5)$$

which maps the  $FF$  onto the range  $(-1, 1)$ . The constants  $a$  and  $b$  in eq. 5.3, along with the optimized exponents of the collection coefficient  $\gamma_{\text{dir}}$  are found by fitting the data pairs of normalized fill factor  $FF_n - \gamma_{\text{dir}}$  to the fit function

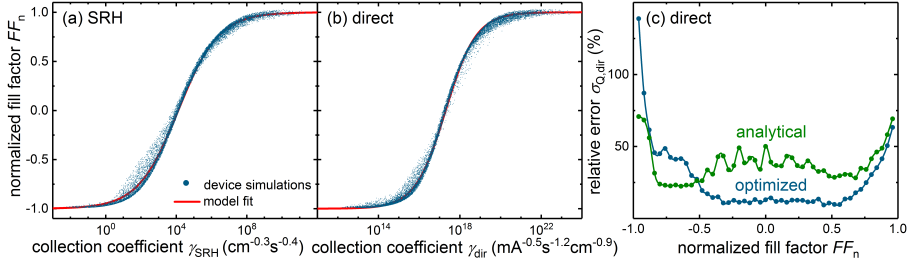


**Figure 5.3.:** Correlation between the  $FF$  and optimized collection coefficients for (a) Shockley-Read-Hall and (b) direct recombination. The improved models, based on a normalized fill factor  $FF_n$  (eq. 5.5) and optimized relative weights (eqs. 5.7) of the quantities that constitute the collection coefficients, show less scatter than the analytical counterparts in fig. 5.2. (c) The error (eq. 5.10) of extracting the here-defined electronic quality factor  $Q$  (eq. 5.8) via the proposed models for direct recombination through eq. 5.9, quantifies the enhanced precision of the optimized over the analytical model over several intervals of  $FF_n$ .

$$FF_{n,\text{fit}}(\gamma_{\text{dir}}) = \tanh(\alpha_{\text{dir}} \ln(\gamma_{\text{dir}}/\gamma_{0,\text{dir}})), \quad (5.6)$$

where  $\alpha_{\text{dir}}$  and  $\gamma_{0,\text{dir}}$  are fit parameters as well. The function fulfills the requirements of a monotonous and bounded function that produces the S-shapes discernible in fig. 5.2 and shares the range  $(-1, 1)$  of  $FF_n$ . The optimized collection coefficient is found to be

$$\gamma_{\text{dir}} = \frac{\mu^2}{k \cdot 0.8} \cdot \frac{V_{\text{oc}}^2}{d^{3.5} J_{\text{sc}}^{0.5}}. \quad (5.7a)$$

Comparing fig. 5.3(b) and 5.2(b) shows that the introduction of the normalized fill factor  $FF_n$  reduces the scatter at high  $FF$ s close to  $FF_{\text{max}}$  where the  $FF$  is restricted only by the fundamental dependence on  $V_{\text{oc}}$  in eq. (5.3). The optimized exponents of the collection coefficient  $\gamma_{\text{dir}}$  substantially narrow the linear part of the distribution. Note that the density of points that deviate the most from the fit function [red curve in fig. (5.3)(b)] is much lower than the point density along the curve. The improved precision of the optimized collection coefficient will be quantified in the next section.

For the case of trap-assisted Shockley-Read-Hall (SRH) recombination, where

## 5. Charge Collection in Thin-Film Solar Cells

the lifetime  $\tau$  replaces the direct recombination coefficient, the optimization procedure yields

$$\gamma_{\text{SRH}} = \mu^2 \tau^{1.6} \cdot \frac{V_{\text{oc}}^2}{d^{4.3}} \quad (5.7b)$$

and gives similarly good results displayed in fig. 5.3(a) as the collection coefficient for direct recombination. The fit parameters  $a$ ,  $b$ ,  $\gamma_0$  and  $\alpha$  are given in tab. (5.2) for both recombination models. Equations (5.7) use the units given in tab. (5.1), except for the device thickness  $d$  which needs to be entered in cm.  $V_{\text{oc}}$  is in V,  $J_{\text{sc}}$  in  $\text{mAcm}^{-2}$  and  $FF$  in %. Note that both collection coefficients are not dimensionless. Results differ for exceptionally strong or weak recombination shown in fig. C.2 in appendix C, which is however uncommon for organic solar cells. Although the models for direct and trap-assisted recombination represent limiting cases, they produce similar results. The obtained expressions for both recombination types show minor deviations from the theoretical models in eqs. (5.2a) and (5.2b). In particular, the exponents of the quantities that describe recombination are slightly lower than in the analytical expressions ( $\mu^2/k$  for direct recombination and  $(\mu\tau)^2$  for Shockley-Read-Hall recombination). The deviations can be understood from the differences between the approaches: while the analytical models describe the efficiency of charge carrier collection and are then merely plotted against the  $FF$ , the collection coefficients found herein are optimized to precisely predict the  $FF$ . Lower recombination improves charge collection at the maximum power point and at the same time increases  $V_{\text{oc}}$ . Thereby, the numerator and the denominator of the fill factor definition  $FF = (V_{\text{MPP}}J_{\text{MPP}})/(V_{\text{oc}}J_{\text{sc}})$  are increased, which leads to a decreased weight of the recombination parameter. For direct recombination, the thickness dependence is almost the same in eq. (5.7a) and eq. (5.2b). The splitting from  $J_{\text{sc}} \rightarrow J_{\text{sc}}^{0.5}d^{0.5}$  can be explained by an additional thickness dependence of  $J_{\text{sc}}$  due to incomplete collection at short-circuit. It also turned out that the weight distribution between  $J_{\text{sc}}$  and  $d$  is not very critical for the fitting and optimized result. Since SRH recombination is linear with excess charge-carrier concentration, it is (nearly) independent of the generation rate and thus the  $J_{\text{sc}}$ , which translates to the collection coefficient  $\gamma_{\text{SRH}}$  being independent of  $J_{\text{sc}}$ . The weights of the constituting quantities in eqs. (5.7) were optimized relative to the weight of the

**Table 5.2.:** Fit parameter values for direct and Shockley-Read Hall recombination (top) displayed in fig. 5.3 and for varying  $\epsilon_r$  (bottom) for the case of SRH recombination and an extended mobility range discussed in section 5.1.7 and displayed in fig. 5.7.

case	section	$a$	$b$	$\alpha$	$\gamma_0$	$[\gamma_0]$
<b>standard</b>	5.1.3-5.1.6					
Direct		0.92	0.09	0.29	$2 \times 10^{17}$	$\text{mA}^{-0.5} \text{s}^{-1.2} \text{cm}^{-0.9}$
SRH		0.92	0.09	0.19	$1.3 \times 10^4$	$\text{s}^{-0.4} \text{cm}^{-0.3}$
<b><math>\epsilon_r</math> varied, SRH</b>	5.1.7					
$\epsilon_r = 3.5$		0.94	0.095	0.18	$1.5 \times 10^4$	$\text{s}^{-0.4} \text{cm}^{-0.3}$
$\epsilon_r = 10$		0.93	0.090	0.18	$1.0 \times 10^4$	$\text{s}^{-0.4} \text{cm}^{-0.3}$
$\epsilon_r = 30$		0.91	0.085	0.19	$6.2 \times 10^3$	$\text{s}^{-0.4} \text{cm}^{-0.3}$
$\epsilon_r = 100$		0.89	0.079	0.19	$3.6 \times 10^3$	$\text{s}^{-0.4} \text{cm}^{-0.3}$

mobility whose exponent was fixed at two. The fitting procedure yielded stable results up to the given digit and was particularly sensitive to the weight of the recombination coefficient.

### 5.1.4. Electronic Quality Factor and Model Precision

A crucial factor in the collection coefficient in eq. (5.7a) is the ratio of mobility  $\mu$  and recombination coefficient  $k$  – both properties of the material blend composing the active layer – which defines an electronic quality factor

$$Q_{\text{dir}} = \frac{\mu^2}{k^{0.8}}. \quad (5.8a)$$

In the case of trap-assisted recombination the electronic quality factor is defined by

$$Q_{\text{SRH}} = \mu^2 \tau^{1.6}. \quad (5.8b)$$

Substituting the collection coefficient from eq. (5.8a) into the fit function  $FF_{\text{n,fit}}$  in eq. (5.6), setting  $FF_{\text{n,fit}} = FF_{\text{n}}$  and solving for  $Q_{\text{dir}}$ , allows to accurately estimate the electronic quality factor

$$Q_{\text{dir,fit}} = \gamma_{0,\text{dir}} \frac{d^{3.5} J_{\text{sc}}^{0.5}}{V_{\text{oc}}^2} \exp\left(\frac{\text{arctanh}(FF_{\text{n}})}{\alpha_{\text{dir}}}\right) \quad (5.9)$$

## 5. Charge Collection in Thin-Film Solar Cells

from basic device characterization by applying the presented fitted model. Only the measurement of the active layer thickness  $d$  and the current-voltage curve, which provides  $V_{oc}$ ,  $J_{sc}$  and  $FF$ , is required to obtain  $Q_{dir}$ . This is remarkable because mobility and recombination coefficient are difficult to obtain individually in experiments and values vary for different methods [252–254]. On top of this, there is a discussion on the correct interpretation of lifetimes and recombination coefficients obtained from transient measurements of the full device [189]. The probed quantities result from different processes in the solar cell and especially transport and recombination phenomena are superimposed in certain experiments [189, 190]. Altogether, the macroscopically probed quantities might not reflect the microscopic defined material properties that also form the basis of the drift-diffusion model and the corresponding simulations.

By comparing the actual value of  $Q_{dir}$  defined by eq. (5.8a) to the electronic quality factor  $Q_{dir,fit}$  predicted from the model, the model's uncertainty is evaluated via

$$\sigma_{Q,dir} = \frac{|Q_{dir} - Q_{dir,fit}|}{Q_{dir}}. \quad (5.10)$$

$Q_{dir}$  is recalled from the simulation input (parametrization) and  $Q_{dir,fit}$  is obtained from the simulation output ( $J$ - $V$  curve) via eq. (5.9). A different electronic quality factor  $Q_{\theta,dir} = \mu^2/k$  is defined by the collection coefficient of Bartesaghi et al. in eq. (5.2b). Following the previous procedure of introducing a normalized fill factor and fit function as displayed in fig. C.1(c), the model's estimated electronic quality factor  $Q_{\theta,dir,fit}$  and its error  $\sigma_{Q,\theta,dir}$  is evaluated and compared to the model developed in this thesis. The two regions with lowest and highest  $FF_n$  in fig. (5.2)(c) are difficult to interpret in terms of electronic quality as indicated by the large error of the estimated quality factor for both models. Even large changes in mobility and lifetime only lead to moderate changes in  $FF$  if the  $FF$  is nearly ideal or if it is already close to 25 % which results in the flat regions for the lowest and highest collection coefficients in fig. (5.2)(a). However, the exact value of  $Q$  for an absorber that reaches the highest  $FF_n$  for reasonably thick layers is of minor importance for photovoltaic performance, since charge collection is in any case highly efficient. At intermediate  $FF$ s the enhanced precision of the collection coefficient  $\gamma_{dir}$  is obvious.

In this linear regime, changes in mobility and recombination constant (or lifetime) directly translate into changes in  $FF_n$  which allows the precise extraction of the electronic quality factor  $Q_{\text{dir}}$ .

### 5.1.5. Contacts

Figure 5.4(a) compares the presented model with two literature reports based on PTPD3T:PC<sub>71</sub>BM [255] and DT-PDPP2T-TT:PC<sub>71</sub>BM [241] blends, which reached high  $FF$ s at thicknesses around the second absorption maximum. In both studies the thickness of the active layer was varied which enables the verification of the  $FF_n$ - $d$  relation proposed by the presented model. One data point is used to extract  $Q_{\text{dir}}$  which is then assumed to be constant for all thicknesses of the series. Both series agree well with the model except for the highest values of  $\gamma_{\text{dir}}$  which correspond to the devices with the lowest absorber thickness. This behavior is typical because at high  $FF$  and  $\gamma_{\text{dir}}$  the external series resistance becomes a limiting factor of the  $FF$  as discussed below. Additionally, shunts may affect the  $FF$  at low active layer thickness. Consequently, the  $FF$  stays short of its potential if purely judged by the efficiency of charge collection. Further experimental evidence for the validity of the proposed model is given by several thickness series reported in literature displayed in fig. C.6 in appendix C.

For efficient transport in the bulk active layer indicated by a high  $FF_n$  and large collection coefficient, imperfect contacts become limiting to the  $FF$ . More specifically, the highest obtainable fill factor decreases. In this context the term ‘contact’ does not exclusively refer to the metallic connection to the external circuit but also includes the interlayers. For example, in terms of device modeling, the high charge selectivity of a good electron-blocking HTL can be represented by a high surface recombination velocity for holes (majority carriers,  $S_{\text{maj}}$ ) and a low surface recombination velocity for electrons (minority carriers,  $S_{\text{min}}$ ) instead of including an additional layer in the simulated stack. Interlayers whose energy levels are well matched to the active layer translate to a low Schottky barrier  $\varphi$  used in simulations. A Schottky barrier between active layer and contacts reduces the built-in voltage which impedes the extraction of charge carriers and deteriorates the fill factor [256]. Finally, since interlayers are non-ideal conductors they will also contribute to the

## 5. Charge Collection in Thin-Film Solar Cells

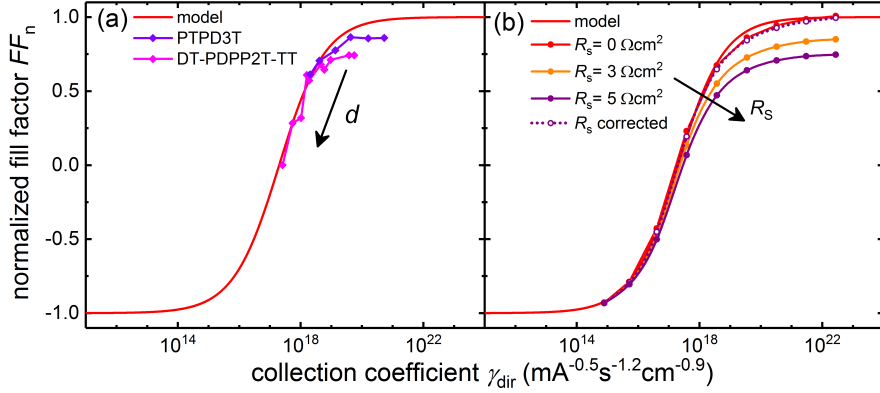


**Figure 5.4.:** (a) Literature data on solar cells with varying active layer thickness made from two high- $Q$  polymer blends [241,255] are in good agreement with the optimized model. Thin devices reach the highest  $FF$  values but stay below the model's prediction which can be explained by external series resistances that lower the maximum obtainable  $FF$  as shown in (b). The mobility is varied along one curve to cover a large range of collection coefficients. For a known external resistance the data can be corrected by eq. 5.11 to obtain the zero-resistance curve as shown for  $R_s = 5 \Omega\text{cm}^2$ .

external series resistance  $R_s$  in addition to the TCO at the front contact and thereby reduce the fill factor. Figure 5.4(b) shows the normalized fill factor  $FF_n$  for a set of curves with varying external series resistance.<sup>4</sup> While the linear regime is barely influenced, the curves saturate at lower levels for increasing series resistance. The discussed parameter series on the behavior of the  $FF$  discussed here and in the following, are exemplary for a large ensemble of devices and reflect the trends evident from the point clouds displayed in fig. C.3 in appendix C for the case of an external series resistance. It is noteworthy that the curve without any external resistance ( $R_s = 0 \Omega\text{cm}^2$ ) can be recovered for a known resistance by adapting the maximum fill factor definition from eq. 5.3 to [64]

$$FF_{\max, R_s} = FF_{\max} \left( 1 - \frac{R_s J_{sc}}{V_{oc}} \right). \quad (5.11)$$

as is done for the dashed line in fig. 5.4(b).

<sup>4</sup>Note that low-mobility organic material blends or generally intrinsic absorber layers contribute to the overall series resistance in addition to any external series resistance

### 5.1. Fill Factor and Electronic Quality

It is well known that higher values of the open-circuit voltage  $V_{oc}$  can be achieved in different types of solar cells by reducing the surface recombination velocity of minority charge carriers [257], which is the base of many improvements in c-Si technology [32]. Higher  $V_{oc}$ s then allow higher  $FF$ s as captured by eq. 5.3. In the following the impact of the surface recombination velocity of minority carriers  $S_{min} =: S$  is analyzed under the assumption that the majority carriers are injected and extracted fast enough [256]. Just as for the external series resistance, effects related to surface recombination become visible only if the bulk properties are good, referring to high values of the collection coefficient  $\gamma_{dir}$  and normalized fill factor  $FF_n$ .

Figure 5.5(a) shows no significant deviation from the  $FF_n$ - $\gamma_{dir}$  relation for a variation of  $S$  between  $10^5$  and  $10^{-1}$  cm/s in the low-mobility case (pink and blue diamonds), because poor bulk properties limit the  $FF$ . For a high mobility (green diamonds) and associated high  $Q_{dir}$ , low surface recombination values lead to an  $FF_n$  above the model's predictions, which are based on a high  $S$ , although the  $FF$  normalization already accounts for the  $V_{oc}$  dependence. The general validity of the  $FF$  normalization is confirmed by a variation of the band gap  $E_g$  (brown circles), which exclusively acts on the  $V_{oc}$  and nicely follows the predicted  $FF_n$ . Figure 5.5(b) shows the  $FF$ - $V_{oc}$  relation for the high mobility case and varying  $S$  or  $E_g$ . The  $V_{oc}$  changes with both varied parameters and the  $E_g$  range is actually chosen in such a way that the  $E_g$  and  $S$  variation cover a similar  $V_{oc}$  range. The difference in the  $FF$ - $V_{oc}$  relation indicates that the  $FF$  dependence on  $S$  goes beyond the expected indirect influence via the  $V_{oc}$ . While the low- $S$  device is almost at the theoretical  $FF$  limit in the Green [64] approximation, the  $FF$  deviates significantly from its maximum towards higher  $S$ .

Figure 5.5(c) depicts the simulated  $J$ - $V$  curves of two high- $\gamma_{dir}$  devices with different surface recombination velocities  $S$ . For the larger  $S$ , there is an expected reduction in  $V_{oc}$ . In addition, there is a clear voltage dependence of the current at low voltages which – to my knowledge – has not been covered in literature yet and can be assigned to the surface recombination current. For an illuminated device the total current is constituted by a generation current  $J^{gen}$ , a recombination current coming from the bulk  $J_{bulk}^{rec}$  and one coming from the surfaces  $J_{surf}^{rec}$ .

## 5. Charge Collection in Thin-Film Solar Cells

$$J = J^{\text{gen}} + J_{\text{bulk}}^{\text{rec}} + J_{\text{surf}}^{\text{rec}} \quad (5.12)$$

For the fully symmetric device with equal surface recombination velocities of electrons and holes at the respective contact  $S_n = S_p = S$ , both surfaces contribute in the same way so that the recombination current from the surfaces is given by

$$J_{\text{surf}}^{\text{rec}} = qS_n \cdot n(0) + qS_p \cdot p(d) = 2qS \cdot n(0) \quad (5.13)$$

where the minority charge-carrier densities at the corresponding contact are denoted by  $n(0)$  and  $p(d)$ . For the illuminated device in fig. 5.5(d), there is an almost flat regime of the surface current at low voltages and a steeper regime around  $V_{\text{oc}}$ . The latter one is responsible for the change in open-circuit voltage  $V_{\text{oc}}$  with  $S$ . The inverse slope of  $\log(J_{\text{surf}}^{\text{rec}})$  vs.  $V$  is proportional to the diode's ideality factor. Around  $V_{\text{oc}}$  the ideality factor of the surface current is 1 and therefore equal to the bulk ideality factor for the case of direct recombination so that bulk and surface current have the same voltage dependence. Consequently, a change in  $S$  does not immediately affect the  $FF$  via the high voltage regime. However,  $S$  contributes to the diode saturation current  $J_0 = J_0^{\text{bulk}} + J_0^{\text{surf}}$  and thereby affects  $V_{\text{oc}}$ . This mechanism of an indirect influence on the  $FF$  via  $V_{\text{oc}}$  is covered by the fill factor normalization in eq. 5.3 and cannot explain the deviation from the presented model observed in fig. 5.5(b). The additional dependence of the fill factor  $FF$  on the surface recombination velocity  $S$  originates from the low voltage regime where a slight voltage dependence is observed – which implies a large ideality factor – that is known to be detrimental for the  $FF$  [64]. However, this high-ideality contribution is only relevant for large  $S$  because only then the surface recombination current exceeds values of at least  $10^{-2} \text{ mAcm}^{-2}$  as can be seen from the logarithmic depiction of the surface recombination current in fig. 5.5(d). Only then the contribution of  $J_{\text{surf}}^{\text{rec}}$  to the total recombination current (fig. 5.5(c) shows  $J_{\text{bulk}}^{\text{rec}} \approx 12 \text{ mAcm}^{-2}$ ) is significant. The voltage dependence visible in the drift-diffusion simulations in fig. 5.5(d) stems, according to eq. 5.13, from the minority charge carrier density at the contact  $n(0)$  that is determined by the charge carrier dynamics which cannot be explained in simplified terms. The order of magnitude of  $J_{\text{surf}}^{\text{rec}}$  is strongly influenced by the value of  $S$ , evident from eq. 5.13 as well. For large  $S$ , the surface recombination

current reproduces the entire  $J$ - $V$  curve well as can be seen from the dashed line in fig. 5.5(c), while in the favorable case of low  $S$  no significant contribution from the surface recombination current can be observed. This leads to an enhancement of the  $FF$  from 81% for high surface recombination velocities to 85% for low surface recombination velocities which has not been recognized by Bartesaghi et al. who report no difference of the  $FF$  for infinite and low ( $S = 10^{-2} \text{ cm s}^{-1}$ ) surface recombination velocity. Differences in  $FF$  are partly discarded by the large scatter at high  $FF$ s in that study.

### 5.1.6. Space-charge Region

A fully depleted active layer with homogeneous electric field is advantageous for a wide range of electronic qualities or  $(\mu\tau)$ -products [82]. A space-charge region along with the corresponding neutral region depicted in the band diagram in fig. 2.5(e) form in the presence of intentional or unintentional doping or large concentrations of injected or photogenerated electrons and holes with asymmetric mobilities [84, 124, 258–263]. Transport of the minority carriers through the flat-band region degrades the solar cell performance when diffusion lengths are not sufficiently long, mainly because of a reduction in short-circuit current  $J_{sc}$  [84, 124, 259–261, 264]. For the case of organic bulk heterojunction solar cells, the electric field in is often assumed to be constant, which is reasonable apart from band bending at the contacts. Both unintentional doping and asymmetric mobilities have been reported for OSCs [84, 124, 258–263] with a detrimental impact on device performance since the low mobilities of the active layer blends lead to short diffusion length. Devices based on polymers with improved electronic properties recently achieved high fill factors even for thick active layers [137, 231, 241, 242, 255, 265–267]. This underlines the growing importance of space-charge effects because the width of the active layer and the space-charge region can be of the same order even for moderate doping levels or asymmetries in charge-carrier mobility.

Doping of a device (for OSCs typically unintentional  $p$ -type doping [84, 268–270]) leads to a space-charge region whose width decreases with increasing doping concentration. The impact on the fill factor can be seen from fig. 5.6 showing simulations of a typical OSC with a doping level of  $N_d = 5 \times 10^{16} \text{ cm}^{-3}$  for thicknesses

## 5. Charge Collection in Thin-Film Solar Cells

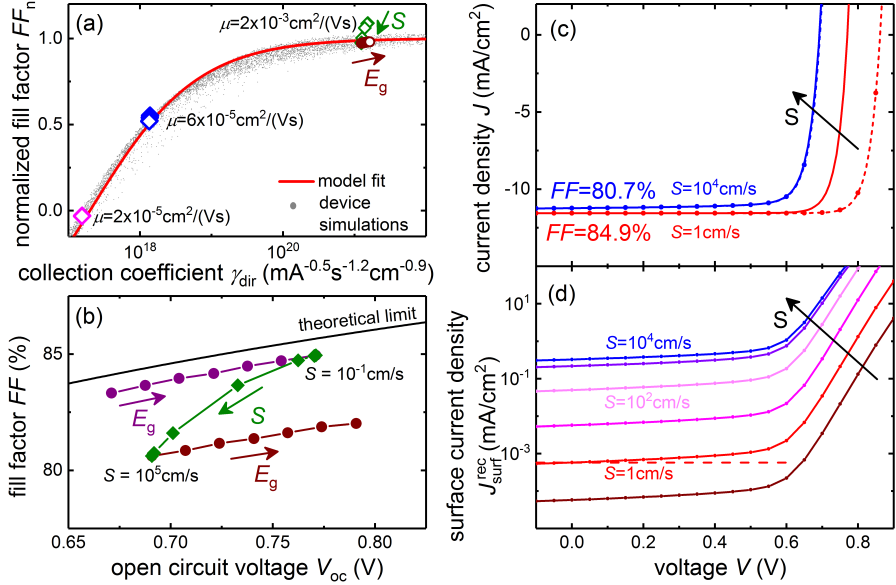


**Figure 5.5.:** Influence of surface recombination velocity  $S$  on the  $FF$ . (a) Variation of  $S$  between  $10^5$  and  $10^{-1} \text{ cm/s}$  for different mobilities. Data points with low  $S$  and high collection coefficient  $\gamma_{\text{dir}}$  exceed the  $FF_n$  predicted by the model that is based on a high  $S$ . For lower  $\gamma_{\text{dir}}$  no deviation from the model is observed since bulk recombination dominates over surface recombination. The  $E_g$  series agrees well with the model, which indicates the validity of the  $FF_n$  normalization. (b) The  $FF$ - $V_{\text{oc}}$  relation differs between simulation series where  $S$  or  $E_g$  is varied, indicating that  $S$  affects the  $FF$  beyond the indirect influence of  $S$  on  $V_{\text{oc}}$ . Towards high  $S$ , the deviation from the maximum  $FF$  [64] increases. (c) Solid lines show the simulated  $J$ - $V$  characteristic of a device with high  $\gamma_{\text{dir}}$  for a high (blue) and an intermediate (red)  $S$ . Apart from the expected drop in  $V_{\text{oc}}$ , a decrease in  $FF$  for the high- $S$  case stems from the slight voltage dependence of the current at low voltages that is attributed to surface recombination current density  $J_{\text{surf}}^{\text{rec}}$  depicted in (d). The voltage dependence of  $J_{\text{surf}}^{\text{rec}}$  (made better visible by the dashed line which marks  $J_{\text{surf}}^{\text{rec}}$  at  $V = 0 \text{ V}$ ) originates from the minority charge carrier density at the contact  $n(0)$  according to eq. 5.13. The equation also indicates that the value of  $J_{\text{surf}}^{\text{rec}}$  scales with  $S$ . Only for large enough  $S$ ,  $J_{\text{surf}}^{\text{rec}}$  contributes significantly ( $J_{\text{surf}}^{\text{rec}} \gtrsim 10^{-2} \text{ mAcm}^{-2}$ ) to the total current density  $J$  displayed in (c). Consequently,  $J_{\text{surf}}^{\text{rec}} - J_{\text{sc}}$  indicated by the dashed lines in (c) reproduces the entire  $J$ - $V$  curve for high  $S$ . For intermediate  $S$ , the  $J_{\text{surf}}^{\text{rec}}$  contribution to  $J$  is negligible and the  $J$ - $V$  curve is determined by the bulk recombination current, which explains the different voltage dependence and  $FF$ .

### 5.1. Fill Factor and Electronic Quality

between 50 nm (highest  $\gamma_{\text{dir}}$ ) and 750 nm (lowest  $\gamma_{\text{dir}}$ ). The main difference between the model curve describing undoped devices and the simulated thickness series of a doped device, is the saturation of the normalized fill factor  $FF_n$  above the model curve for thick, doped devices. In this regime, low mobilities and/or high recombination coefficients are predominant which implies short diffusion lengths and that only carriers from a narrow collection zone can diffuse to the space-charge region where they get separated. This process is independent of the applied voltage as soon as the space-charge region and the collection zone are smaller than the device thickness for all voltages. Thus, the presence of space-charge leads to an overall poor carrier collection for systems with short diffusion length, causing a low  $J_{\text{sc}}$  and decreased efficiency. However, the collection in the neutral zone does not depend on the applied voltage so that the  $FF$  decreases less for increasing thickness and decreasing collection coefficient  $\gamma_{\text{dir}}$ . The same behavior is observed for the point clouds in fig. C.4 and fig. C.5 in appendix C, which comprise simulations of different doping levels and asymmetry ratios of the mobilities, with the latter one being discussed below. The precise saturation level of the  $FF_n$  depends on the doping level or asymmetry ratio and can explain the elevated  $FF$  of the 1000 nm thick device based on the polymer blend PBnDT-FTAZ:PC<sub>61</sub>BM [242] in fig. 5.6(a).<sup>5</sup> Figure 5.6(b) shows that high doping concentrations  $N_d = 10^{17} \text{ cm}^{-3}$  change the slope of the  $FF_n$ - $\gamma$  relation. Here a wide  $\gamma$  range is covered by a varying the mobility between  $\mu = 10^{-6} \text{ cm}^2 (\text{Vs})^{-1}$  and  $10^{-2} \text{ cm}^2 (\text{Vs})^{-1}$  while the thickness is fixed at 200 nm. The observed  $FF_n$ - $\gamma$  relation is similar to experimental literature data of a PBnDT-HTAZ:PC<sub>61</sub>BM active layer blend with varying thickness [242].

A space-charge region causing a similar saturation of the  $FF$  at large thickness and low  $\gamma_{\text{dir}}$  also results from unbalanced mobilities [124, 258, 264] as displayed in fig. 5.6(a). Differences in the mobilities cause an accumulation of charge at the contact that extracts the slow carrier species. The resulting SCR acts in the same way on the device performance as discussed above. In organic bulk heterojunctions, electrons are transported to the contacts via the acceptor material and holes via the donor material. In addition, the blend morphology strongly affects the transport paths and amount of usable transport channels. Thus, differences in the mobilities

---

<sup>5</sup>The decrease in  $FF$  of the thinnest device with largest  $\gamma_{\text{dir}}$  is expected to be due to a reduced shunt resistance

## 5. Charge Collection in Thin-Film Solar Cells

between both phases of several orders of magnitude are quite common. Optimized fabrication steps such as annealing help to accomplish a material blend with more balanced mobilities [254, 262, 271]. Note that electron and hole mobilities also differ by 1-2 orders of magnitude for the inorganic semiconductor a-Si:H [272].

In the presence of asymmetric mobilities, the mobility in the different collection coefficients introduced in section 5.1.2 splits into two separate factors. The analytical treatment by Bartesaghi et al. [235] predicts equal weight of both charge carriers in the collection coefficient  $\mu^2 \rightarrow \mu_e \mu_h$ . An effective mobility as the geometric average with equal weight of both charge-carrier species has also been proposed elsewhere [271]. However, several studies suggest a dominant influence of the slower charge-carrier species for transport in organic solar cells [232, 258, 273, 274]. This poses the question of the exact weight distribution between the slow and fast charge carrier species in the collection coefficient  $\gamma_{\text{dir}}$ . The simulations shown in C.5 in appendix C demonstrate that putting a strong weight on the mobility of the slow carriers

$$\mu^2 \rightarrow \mu_{\text{slow}}^{1.6} \mu_{\text{fast}}^{0.4} \quad (5.14)$$

yields the best overlap between data clouds with different asymmetry ratios. The data suggests a dominant but not exclusive contribution of the slower charge-carrier species to charge transport. The dominant role of the slow carrier species for transport agrees with the before mentioned publications [232, 258, 273, 274] and explains the enhanced scatter for equal weight of both charge carrier mobilities as proposed by Bartesaghi et al. in fig. 5.2(c) and their publication.

As a final remark, by observing the discussed signatures, evidence for the presence of a space charge region can be obtained from the experimental fabrication of thickness series. Space-charge effects will first manifest themselves in a drop in  $J_{\text{sc}}$  with increasing thickness. By increasing the active layer thickness further beyond the optimum efficiency, a deviation from the predicted  $FF$  enables first deductions on the presence of space charge by easy means which can then be further characterized by the suns- $J_{\text{sc}}$  method or voltage-dependent capacitance measurements [84, 275, 276].

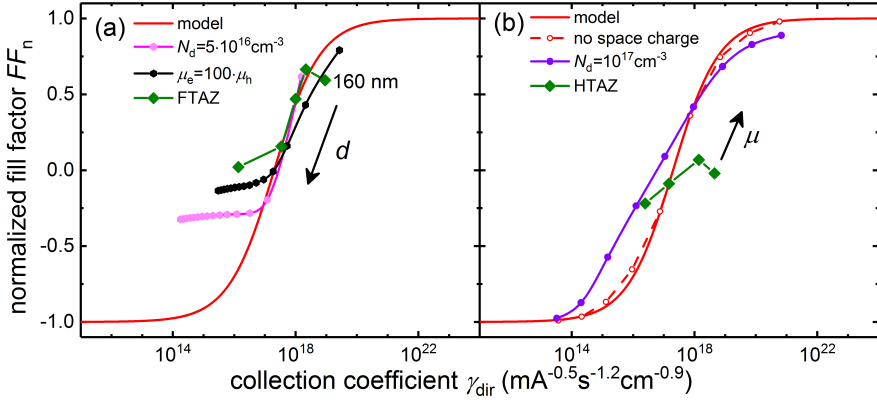


**Figure 5.6.:** The presence of a space-charge region caused by doping  $N_d$  or asymmetric charge-carrier mobilities  $\mu$  leads to inefficient carrier collection at  $J_{sc}$  and a drop in PCE. (a) The  $FF$  increases at low  $\gamma_{dir}$  because charge-carrier collection becomes independent of voltage. The reported [242]  $FF$  of the polymer FTAZ is similarly enhanced for the thickest device at 1000 nm. Along the simulated curves, the active layer thickness  $d$  is increased from 50 nm to 750 nm while  $\mu$  is kept constant at  $\mu = 10^{-4} \text{cm}^2(\text{Vs})^{-1}$  for the doped device and  $\mu_h = 10^{-5} \text{cm}^2(\text{Vs})^{-1}$  for the device with imbalanced mobility. (b) For very high doping levels the slope of  $FF_n$  vs.  $\gamma_{dir}$  changes, which can explain the reported [242]  $FF$  behavior of the polymer HTAZ with thickness up to 750 nm. The simulated device has a thickness of 250 nm while the mobility is varied between  $10^{-6}$  and  $10^{-2} \text{cm}^2(\text{Vs})^{-1}$  to cover a large  $\gamma_{dir}$  range.

### 5.1.7. Transfer to Inorganic Absorbers

The presented model is developed from a parameter space that is typical for organic solar cells. Taking a broader perspective, the study outlines a methodology based on drift-diffusion simulations which allows the definition of a charge carrier collection coefficient with a unique relation to the (normalized) fill factor of a thin-film solar cell. Applying this relation, the electronic quality factor can be extracted from experimental studies and basic solar cell characterization. The electronic quality factor serves as a FOM to evaluate the absorber material's PV potential in terms of charge carrier collection. It can also be used to comparatively evaluate different absorber technologies and to track and quantify the progress within a technology or a class of materials. Organic solar cells serve as a prime example to demonstrate the relevance of the model, because versatile organic donor:acceptor blends cover a range of transport and recombination properties. Consequently, the analysis was primarily conducted for this highly relevant case of polymer-based organic solar cells. However, the methodology can be transferred to other thin-film absorber materials that are embedded in a *p-i-n* like geometry where a mostly homogeneous electrical field prevails in the photoactive layer. This includes most of the emerging inorganic PV technologies in fig. 2.2, where collection issues are evident from non-ideal fill factor values. When transferring the methodology to other technologies, the higher dielectric constant of inorganic materials might yield quantitative differences in the resulting model parameters. Therefore, the standard case of an undoped active layer with balanced mobilities is simulated in fig. 5.7 for different dielectric constants ranging from  $\epsilon_r = 3.5$  representing organic blends up to  $\epsilon_r = 100$ . High mobilities up to  $1 \text{ cm}^2/(\text{Vs})$  are included in the simulations which are uncommon for organic blends but not so much for inorganic absorber materials. Shockley-Read-Hall recombination is assumed, which typically limits inorganic solar cell absorbers because of the lower phonon energies compared to OSCs, which makes direct band-to-band transitions unlikely [45, 46].

The data in the left column of fig. 5.7 shows the point clouds and the fit for the original parametrization of collection coefficient  $\gamma_{\text{dir}}$ , normalized fill factor  $FF_n$  and fit function resulting from the parametrization that reflects organic solar cells. The extended  $\mu$  range leads to slight deviations from the fit function for the largest

### 5.1. Fill Factor and Electronic Quality

$\gamma_{\text{SRH}}$  even for the same  $\epsilon_r = 3.5$  used before indicating that the parameter values of the  $FF_{\text{max}}$  in eq. 5.3 should be adjusted. More importantly, with increasing  $\epsilon_r$  in figs. 5.7(a,c,e,g), the upper saturation level of  $FF_n$  changes. At the same time the point cloud collectively shifts to lower  $\gamma_{\text{SRH}}$ . Consequently each simulated point cloud was fitted individually with the results plotted in fig. 5.7(b,d,f,h) and the parameters given in table 5.2. A monotonous trend in the parametrization of the  $FF_{\text{max}}$  and the inflection point  $\gamma_{0,\text{SRH}}$  of the fit function is observed. Only fitting the listed parameters turned out to produce the same fit quality as also fitting the exponents of the collection coefficient. The obtained fits in fig. 5.7(b,d,f,h) are of similar quality, but at higher  $\epsilon_r$  the scatter increases in both saturation regimes at high and low  $FF_n$ . Regarding the extraction of  $Q_{\text{SRH}}$  from  $J$ - $V$  measurements as described in section 5.1.4, the scatter in the saturation regimes is of little relevance because  $Q$ -extraction is anyways imprecise in those regimes as was shown in fig. 5.10. While the original fit deduced for  $\epsilon_r = 3.5$  reflects the point cloud well for  $\epsilon_r = 10$ , the adapted fit parameter values should be used to extract  $Q_{\text{SRH}}$  for higher values of  $\epsilon_r = 30$  and  $\epsilon_r = 100$ . If the original fit was used, the same  $FF_n$  would translate to higher  $\gamma_{\text{SRH}}$  and the extracted  $Q_{\text{SRH}}$  would overestimate the actual value. However, the value of the dielectric constant  $\epsilon_r$  does not qualitatively affect charge carrier collection. The major importance of a low value of  $\epsilon_r$  lies in the high exciton binding energy, which introduces the need of a BHJ to split up photogenerated excitons in the case of OSCs. In addition,  $\epsilon_r$  influences the electrostatics of the device as expressed by the Poisson equation in eq. 3.1a, which governs the band diagram of a device and thereby the mechanism of charge carrier collection.

In conclusion, higher  $\epsilon_r$  values typical for inorganic absorbers, require a slight adaptation of the fit function and the  $FF$  normalization, while the collection coefficient is independent of  $\epsilon_r$ . The signatures of doped active layers and an external series resistance should agree qualitatively with the analysis in section 5.1.5 and 5.1.6, although quantitative differences are expected, for example because the width of the space-charge region changes with  $\epsilon_r$ . Preparing thickness series then provides insight into whether the charge collection a device is limited by an unfavorable architecture rather than the absorber material itself. Simple  $J$ - $V$  measurements serve as an indicator for a potentially problematic aspect in the stack design, which can initiate a refined characterization of the contacts or a potential SCR. The presented

## 5. Charge Collection in Thin-Film Solar Cells

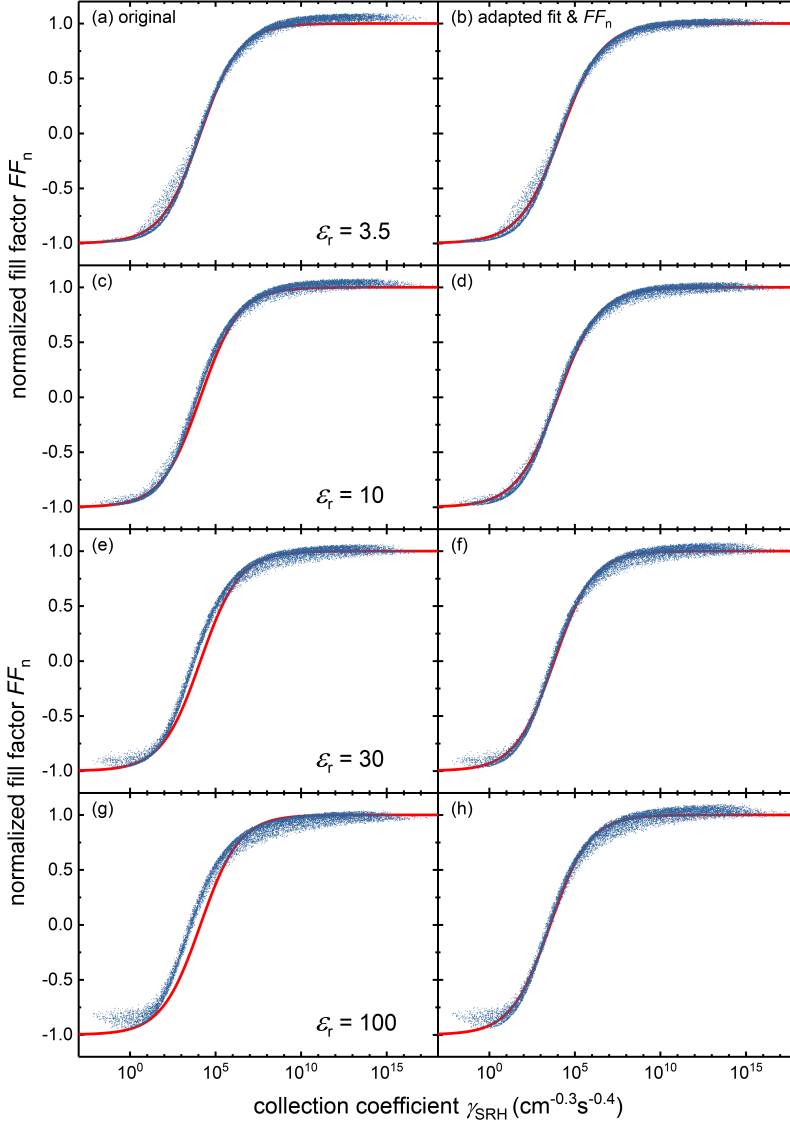


**Figure 5.7.:** Simulation results for SRH recombination with an extended mobility range up to and different dielectric constants  $\epsilon_r$ . The input parametrization better reflects inorganic absorbers than the previously applied ones that focused on organic materials. (a,c,e,g) use the coefficients from the fit in fig. 5.3(a) and show a slight mismatch between model and point cloud with increasing  $\epsilon_r$ . (b,d,f,h) By adapting the coefficients for the fill factor normalization and the fit function as listed in table 5.2, good fits are regained. No change in the expression for the collection coefficient is required.

model and proposed applications of thickness series and quantification of electronic quality help to improve and monitor the progress of emerging absorber technologies for thin-film solar cells. Especially materials and organic blends that are rather new to the field of photovoltaics and that have not been characterized in depth are of special interest. For these materials, the intriguing approach of concluding on microscopic material parameters ( $\mu\tau$ -product or  $\mu/k$ -coefficient) from simple  $J$ - $V$  measurements provides information that would otherwise require significantly more experimental efforts and circumvents the uncertainty in the interpretation of refined experiments [83, 189, 190] as well as relating the obtained values quantitatively to the microscopic material parameters or to the device performance.

## 5.2. Figures of Merit for the Efficiency

In addition to charge transport and recombination, charge generation and therefore photon absorption is crucial for solar cell performance. The three corresponding processes in the bulk absorber are characterized by the mobility  $\mu$ , lifetime  $\tau$  (or direct recombination coefficient  $k$ ) and absorption coefficient  $\alpha$ . While the interplay of the former two has been studied extensively in chapter 5.1 in the context of charge carrier collection, I proceed to include the absorption strength into a model for the efficiency of thin-film solar cells. The importance of  $\alpha_0$ ,  $\mu$  and  $\tau$  for the solar cell efficiency is undisputed and was already introduced at the beginning of this thesis in chapter 2.2. However, the relative importance of the three parameters for the device efficiency is not trivial and it is not self-evident whether a tenfold increase in the absorption strength is as beneficial for the solar cell performance as a tenfold increase in charge carrier lifetime. The following sections discuss the case of Shockley-Read-Hall recombination, characterized by the lifetime  $\tau$ . The case of direct band-to-band recombination is shown in appendix C and yields very similar results. Section 5.3.3 puts the calculations and results of this chapter in the context of organic solar cells and estimates the potential increase in efficiency that would result from an enhanced absorption strength of organic materials.

Figure 5.8(a) shows the absorption coefficient of various organic and inorganic semiconductors. The absorption coefficient can always be expressed as  $\alpha = \alpha_0 f(E)$ ,

## 5. Charge Collection in Thin-Film Solar Cells

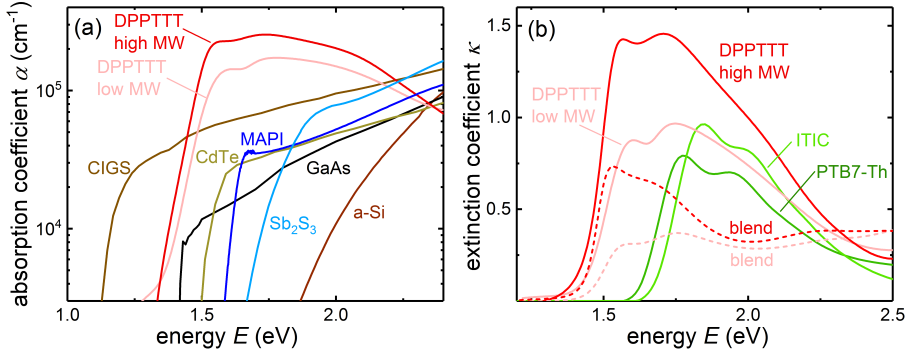


**Figure 5.8.:** (a) Absorption strength of several inorganic direct band gap semiconductors and the semiconducting polymer DPPTTT whose absorption strength can be tuned up to a factor of roughly 1.5 by changing the molecular weight (MW) [277]. The absorption spectra of organic materials are characterized by the maximum  $\alpha_0 \equiv \alpha_{\max}$ . (b) Extinction coefficient  $\kappa$  of several organic materials, which relates to the absorption coefficient via  $\alpha = 4\pi\kappa/\lambda$  and allows comparing absorption strengths of different materials independent of the band gap. The maximum extinction coefficient varies for different organic semiconductors but mostly does not exceed one [277], except for certain polymers and non-fullerene acceptors. The dashed lines show the extinction coefficient of the DPPTTT polymers blended with PCBM (color matches that of the pure materials), which decreases the maximum extinction but broadens the spectra due to absorption in the PCBM.

where a function  $f(E)$  defines the spectral shape and  $\alpha_0$  characterizes the absorption strength, which is characterized by the maximum value of the absorption coefficient  $\alpha_0 \equiv \alpha_{\max}$  for organic semiconductors. The values of  $\alpha$  in fig. 5.8(a) at energies slightly above the band edge cover more than an order of magnitude and reach the highest values for organic materials. It has been shown that the absorption strength value  $\alpha_0$  of the absorption coefficient of certain organic polymers can be tuned by changing the molecular weight [277] (MW), as is the case for DPPTTT displayed in fig. 5.8(a) resulting in an increase in  $\alpha_0$  by roughly 1.5. Figure 5.8(b) compares the absorption strengths of further organic absorber materials. Mixed donor-acceptor blends have a broader absorption spectrum but lower maximum absorption compared to the pure polymer data due to complementary PCBM absorption.

### 5.2.1. Method

In a similar approach to the  $FF$  study in section 5.1.1, a large ensemble of devices is generated via drift-diffusion simulations with an optical model that includes interference. Therefore, the three parameters of interest  $\alpha_0$ ,  $\mu$  and  $\tau$  (or  $k$ ) are varied over a wide range. For each parameter set, the efficiency at the optimum absorber thickness is evaluated. The optical simulations are based on the data of a DPPTTT:PCBM bulk heterojunction, that reflects typical organic absorber blends. Specifically, the absorption spectrum of the high MW blend, divided by a factor of 1.5, serves as default spectrum  $\alpha_{\text{dft}}$  as shown in fig. 5.9. The default spectrum is then scaled ( $\alpha = c_\alpha \alpha_{\text{dft}}$ ) by a factor  $c_\alpha \in [1, 1.5]$  in the simulations, which reflects the experimentally achieved [277] tuning of the DPPTTT:PCBM blend's absorption strength by a factor of 1.5. The optical simulations take interference into account and compute position- and wavelength-dependent generation profiles with the transfer matrix method [188] for a representative  $n-i-p$  OSC stack with flat interfaces consisting of glass/ ITO (150 nm)/ ZnO (40 nm)/ absorber blend/ MoO<sub>3</sub> (10 nm)/ Ag (100 nm). Electrical drift-diffusion simulations are done with Advanced Semiconductor Analysis [278] (ASA). Motivated by the relatively low  $V_{\text{oc}}$  of DPPTTT-based solar cells in ref. [277], the electrical band gap is fixed at  $E_g = 0.9\text{eV}$ , with Schottky barriers of 0.1 eV at each contact. Two different cases of vanishingly low ( $S = 10^{-3}\text{cm/s}$ ) and high ( $S = 10^7\text{cm/s}$ ) minority carrier surface recombination velocity are studied. For a given set of parameters, including a choice of  $\alpha_0$ ,  $\mu$  and  $\tau$  (or  $k$ ), the absorber thickness is varied between 50 and 500 nm and the optimum thickness and corresponding highest efficiency is extracted. All simulation parameters are listed in tab. 5.3. Just as for the simulations performed here, the optimized absorber thickness is easily obtained in experiments by simply preparing a series of solar cells with varying absorber thickness and selecting the thickness that performs best.

### 5.2.2. The $(\alpha\mu\tau)$ -Product

The simulation result for Shockley-Read-Hall recombination and low surface recombination velocities is shown in fig. 5.10, where – in analogy to chapter 5.1 each datapoint results from a simulation of different combinations of  $\alpha_0$ ,  $\mu$  and  $\tau$  at the

## 5. Charge Collection in Thin-Film Solar Cells

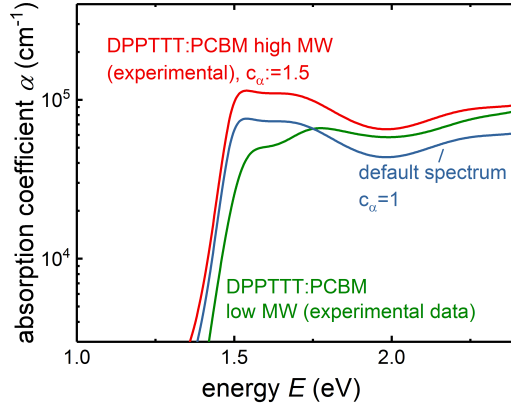


**Figure 5.9.:** Absorption spectra of DPPTTT:PCBM blends. The high MW blend spectrum, scaled by different factors, serves as input for the optical simulations. The default spectrum  $\alpha_{\text{dft}}$ , assigned with  $c_\alpha = 1$ , results from dividing the experimentally recorded high MW DPPTTT:PCBM spectrum by 1.5 and reflects the absorption strength of typical OSC blends. The original experimental data is recovered for  $c_\alpha = 1.5$ . By simply scaling a defined spectrum, any effects are avoided that may arise from different spectral shapes if e.g. the experimentally recorded high and low MW blends were used in the simulations.

**Table 5.3.:** Input parameters for the drift-diffusion simulations, where the optimum absorber thickness yielding the highest efficiency is chosen.

Parameter		value	unit
Thickness	$d$	50-500	nm
Mobility	$\mu_{e,h}$	$10^{-6} - 10^{-1}$	$\text{cm}^2 (\text{Vs})^{-1}$
Direct rec. coefficient	$k$	$10^{-10} - 10^{-14}$	$\text{cm}^3 \text{s}^{-1}$
SRH lifetime	$\tau$	$10^{-6} - 10^{-3}$	s
Scaling factor ( $\alpha = c_\alpha \alpha_{\text{dft}}$ )	$c_\alpha$	1 - 1.5	-
Effective band gap	$E_g$	0.9	eV
Schottky barriers	$\varphi$	0.1	eV
Min. surf. rec. vel.	$S_{\text{min}}$	$10^{-3}$ or $10^7$	$\text{cms}^{-1}$
Maj. surf. rec. vel.	$S_{\text{maj}}$	$10^9$	$\text{cms}^{-1}$
Dielectric constant	$\epsilon_r$	3.5	-
Effective DOS	$N_{c,v}$	$10^{19}$	$\text{cm}^{-3}$

## 5.2. Figures of Merit for the Efficiency

optimized thickness. The dataset is divided via the color into simulations based on low ( $\mu < 10^{-3} \text{ cm}^2/(Vs)$ , red) and high ( $\mu > 10^{-3} \text{ cm}^2/(Vs)$ , blue) mobilities. The efficiency of low-mobility devices in fig. 5.10 nicely correlates with the here-defined figure of merit  $FOM_{\text{SRH}}^{\text{low-}\mu} = \alpha_0 \mu \tau$ . In other words, the low degree of scatter of the red datapoints in panel (a) indicates, that the efficiency of thin-film solar cells with low mobilities depends on  $(\alpha_0 \mu \tau)$  and thus the conjunction of all three absorber material parameters. In contrast to this, the high-mobility devices in blue show considerable scatter, meaning that for high mobilities,  $FOM_{\text{SRH}}^{\text{low-}\mu}$  is not a good figure of merit. Figure 5.10(b) contains the same dataset as fig. 5.10(a), but the simulated efficiency is plotted against a different  $FOM_{\text{SRH}}^{\text{high-}\mu} = \alpha_0 \tau$ , that excludes the mobility. As expected, the red datapoints are largely scattered, because the mobility strongly affects the efficiency for low-mobility devices. However, the blue datapoints correlate well with  $FOM_{\text{SRH}}^{\text{high-}\mu}$ , making the  $(\alpha_0 \tau)$ -product a good FOM for high mobility devices. The remaining scatter of low-mobility devices with  $FOM_{\text{SRH}}^{\text{low-}\mu}$  in (a) and high-mobility devices with  $FOM_{\text{SRH}}^{\text{high-}\mu}$  in (b) largely originates from devices with mobilities around the threshold mobility of  $\mu_{\text{crit}} = 10^{-3} \text{ cm}^2/(Vs)$ . The degree of scatter in the FOMs varies with the choice of threshold mobility. Figure C.7 in appendix C additionally shows that the scatter increases if  $\alpha_0$  is omitted from the FOM expressions.

Next, the influence of surface recombination is examined in fig. 5.11, where surface recombination is non-negligible and eventually limits device performance for good bulk properties. The situation for the low mobilities is similar to the case of weak surface recombination and the efficiency depends on  $FOM_{\text{SRH}}^{\text{low-}\mu} = \alpha_0 \mu \tau$ . The major difference to the low-S case in fig. 5.10 is that the maximum efficiency is capped at a significantly lower value which goes along with a different behavior of devices with high mobility. For low bulk recombination, the  $V_{\text{oc}}$  and therefore the efficiency is limited by recombination at the surface. Above a certain  $\alpha_0 \mu \tau$  value, the surface recombination velocity thus determines the efficiency and higher values of  $\alpha_0 \mu \tau$  or  $\alpha_0 \tau$  are not beneficial. In fact, even a slight decrease in efficiency is observed for the highest  $\alpha_0 \mu \tau$  values in fig. 5.11(a), because the mobility couples to the  $V_{\text{oc}}$  in the high-S case: the time that charge carriers take to travel to the contacts influences the recombination rate at the surface. The impact of  $\mu$  on  $V_{\text{oc}}$  might also explain why the scatter reduces for low mobilities, when the weights of  $\alpha_0$ ,  $\mu$  and  $\tau$

## 5. Charge Collection in Thin-Film Solar Cells

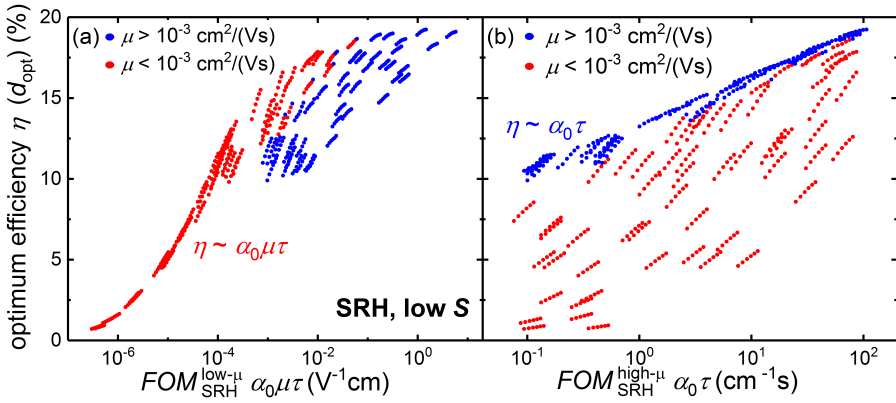


**Figure 5.10.:** Correlation between efficiency and different figures of merit (FOMs) based on  $\alpha_0$ ,  $\mu$  and  $\tau$  for weak ( $S = 10^{-3}$  cm/s) surface recombination and Shockley-Read-Hall bulk recombination. Each datapoint results from electrical drift-diffusion simulations and optical simulations that account for interference. For different simulations, the electrical band gap is fixed, the default absorption spectrum is scaled by a factor  $c_\alpha \epsilon [1, 1.5]$  and  $\mu$  and  $\tau$  are varied randomly over a wide range. For a given parameter set, the efficiency is evaluated at the optimum thickness. (a) and (b) contain the same dataset, which is separated into color-coded subsets of simulated devices with low (red) and high (blue) mobility values, because the mobility regime largely determines, which FOM is applicable. (a) The efficiency of low- $\mu$  dataset correlates well with  $(\alpha_0 \mu \tau)$ , whereas in (b), the efficiency of the high- $\mu$  dataset correlates well with  $(\alpha_0 \tau)$ , because the mobility becomes irrelevant once the collection is efficient.

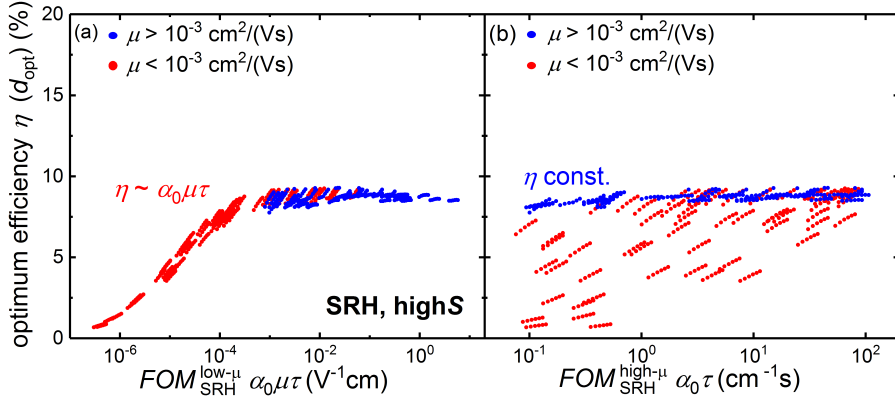


**Figure 5.11.:** Same type of plot as in fig. 5.10, but for a dataset based on strong ( $S = 10^7 \text{ cm/s}$ ) surface recombination. (a) As in fig. 5.10, the efficiency of the low- $\mu$  dataset correlates well with  $\alpha_0\mu\tau$ . (b) The efficiency of the high- $\mu$  dataset is independent of  $\alpha_0$ ,  $\mu$  and  $\tau$  because the efficiency is solely governed by the strong surface recombination for good bulk properties.

are slightly varied and the mobility is emphasized as shown in fig. C.8(b).

In summary, the thin-film solar cell efficiency correlates well to the  $(\alpha_0\mu\tau)$ -product as FOM in the low mobility regime. In this regime, where charge carrier collection – and thus bulk properties – govern the device performance, the statement holds true for low and high surface recombination velocities. In the high mobility regime, the efficiency correlates well with a different FOM – the  $(\alpha_0\tau)$ -product – in the case of low surface recombination velocity. In this case, the efficiency is thus determined by absorption and recombination processes and not by transport anymore, since charge carrier collection is saturated at the optimum value. The correlation between efficiency and the  $(\alpha_0\tau)$ -product has been previously demonstrated by an analytic model for the infinite-mobility case in the absence of surface recombination [37]. For high surface recombination velocity and high mobilities, the efficiency is governed by surface recombination and becomes almost independent of the bulk material parameters  $\alpha_0$ ,  $\mu$  and  $\tau$ .

## 5.3. Application to Organic Solar Cells

Organic solar cells are a promising candidate for future thin-film solar cells but often suffer from low mobilities. Inefficient charge carrier collection is thus a major obstacle towards higher efficiency, which remains compulsory for entering the photovoltaic market. In this context, the developed models provide invaluable insight into the development and present limitations of OSCs, as well as possible routes forward. This chapter also demonstrates the usefulness of figures of merit for organic solar cell research and compares the different concepts from a conceptual point of view at the end of the chapter.

### 5.3.1. History of OSC Development

Since  $FF$ ,  $V_{oc}$ ,  $J_{sc}$  and active layer thickness are almost always published along with the solar cell performance, the normalized fill factor and collection coefficient can be calculated from the presented model in retrospective, which provides a facile method to extract the electronic quality factor  $Q$  of the absorber material. This allows a comprehensive meta study of literature reports on organic solar cells and offers – in combination with the Scharber efficiency introduced in section 2.4.1 – a compact interpretation of the development of organic solar cell materials over the past 15 years.<sup>6</sup>

For the selected literature reports included in fig. 2.9, the  $FF_n$  is calculated and entered in fig. 5.12(a) along with the color-coded  $Q_{dir}$ . Regarding the model choice, direct, bimolecular recombination is assumed to dominate over SRH recombination (as is common for OSCs) and space-charge effect are assumed to be negligible for the depicted high efficiency solar cells. Although the selected data represent devices with exceptional performance that often constituted the record efficiency at the time of publication, none reach the highest possible  $FF_n$  of 1 and almost all reports stay below 0.75. The correlation between  $Q_{dir}$  and  $FF_n$  is naturally not perfect because  $\gamma_{dir} \propto d^{-3.5}$ , whereby the device thickness shifts data points along the

---

<sup>6</sup>Large parts of this chapter (5.3.1) closely follow or are identical to my contributions to the second-author publication “Figures of Merit Guiding Research on Organic Solar Cells”. The literature data has been complemented and updated with recent reports. Reprinted in part with permission from ref. [110]. © 2018 American Chemical Society

### 5.3. Application to Organic Solar Cells

curve. Especially devices with the highest  $Q_{\text{dir}}$  might have a slightly lower  $\gamma_{\text{dir}}$  and  $FF_{\text{n}}$  because they can be made much thicker than 100 nm, which is the optimum thickness for most active layer blends as shown in fig. 2.9(c). The slightly lower  $FF$  is compensated by a higher absorptance which is one route to overcome the issue of limited  $EQE$ , especially towards long wavelengths. The correlation between electronic quality and voltage loss is shown in fig. 5.12(b) for the same literature data. Most importantly, as of today there are no organic solar cell materials that simultaneously reach high electronic qualities above  $Q_{\text{dir}} = 10^3 \text{ cm}^{-1.6} \text{ V}^{-2} \text{ s}^{-1.2}$  and low voltage losses below 0.7 V. The apparent decline in  $Q_{\text{dir}}$  towards lower  $\Delta V$  might explain why the voltage loss for many of today's high-performing solar cells is larger than the 0.6 V that is predicted to be advantageous by the Scharber plot in fig. 2.9(a) which neglects collection problems. The color code in fig. 5.12(b) already shows that for the same  $\Delta V$ , a higher  $Q_{\text{dir}}$  (and for the same  $Q_{\text{dir}}$  a lower  $\Delta V$ ) yields higher efficiencies. Figure 5.12(b) further elaborates on this point and captures the development of organic solar cells in two relevant figures of merits (FOMs) denoted as electronic quality  $Q_{\text{dir}}$  and energy level matching  $\eta_{\text{Scharber}}$ . The former one is derived in this thesis and the latter one reflects the efficiency prediction by Scharber et al. as discussed in section 2.4.1 and appendix A.4.

In 2001 Shaheen et al. [133] reported the first organic solar cell with a notable efficiency of 2.5% based on MDMO-PPV although it scored low for both FOMs. The increase in record efficiency to almost 5% achieved by P3HT [134] can be mostly attributed to its high electronic quality. This high  $Q$  allowed for devices thicker than 200 nm [279] and results from the highly ordered film morphology of P3HT:PCBM which, for several years, remained exceptional for a high-performing solar cell. Then followed a phase during which the electronic quality was low but the energy level matching was improved drastically. Devices based on new polymers such as PCDTBT [135] and PTB7 [136] lead to efficiencies of 6% and 9%, respectively, by narrowing the band gap of the polymer and bringing its LUMO closer to the LUMO of PCBM that was the only well-performing acceptor material at that time. Only then – roughly a decade after the “high- $Q$ ” P3HT emerged – polymers such as PNTz4T [137] and PffBT4T [59] appeared that had a hundred times higher  $Q$  than the predecessor group while retaining a similarly good energy level matching. These polymers outperform P3HT in terms of  $Q$ , have an optimum thickness

## 5. Charge Collection in Thin-Film Solar Cells

around 300 nm and were able to reach 10% to 11% efficiency with PCBM as the acceptor material. A little later, reports that incorporated small molecules other than PCBM in the material blends caused a change in paradigm. High-performing non-fullerene acceptors (NFAs) show low voltage losses leading to even better energy level matching and efficiencies above 11% despite only moderate electronic qualities below  $Q_{\text{dir}} = 10^2 \text{ cm}^{1.6} \text{ V}^{-2} \text{ s}^{-1.2}$  [58, 138, 139, 153] for most NFAs. The data selection in fig. 5.12(c) highlights some promising approaches that produced highly efficient solar cells. The ternary blend PTB7-Th:IDTBR:IDFBR [139] of two NFAs with a polymer shows an extremely high energy level matching but very low electronic quality and an efficiency of 11%. In 2018, two remarkable publications reached an efficiency of 14.6% [9, 57] that was enabled by good energy level matching and an intermediate  $Q_{\text{dir}} > 10^2 \text{ cm}^{1.6} \text{ V}^{-2} \text{ s}^{-1.2}$  [57] or even high  $Q_{\text{dir}} > 10^3 \text{ cm}^{1.6} \text{ V}^{-2} \text{ s}^{-1.2}$  [9]. Again, the device with the better energy level matching [57] showed a lower electronic quality and vice versa. The report on PTB7-Th:COi8DFIC:PCBM [9] combines two interesting design features. First, the blend constitutes a low band gap absorber with  $E_g \approx 1.26 \text{ eV}$  which is untypical for organic solar cell materials as is evident from fig. 2.9(a). Second, it is a ternary blend that applies a polymer, an NFA and PCBM, which is likely to enable the intermediate  $Q_{\text{dir}} > 10^2 \text{ cm}^{1.6} \text{ V}^{-2} \text{ s}^{-1.2}$ . Previously, a blend of PTB7-Th:BTR:PCBM [152] reached a high  $Q_{\text{dir}} > 10^3 \text{ cm}^{1.6} \text{ V}^{-2} \text{ s}^{-1.2}$  in the range of well-performing pure FA blends but only reached a mediocre energy level matching leading to an efficiency of 11.3%. However, as demonstrated by different binary NFA blends, a PCBM component seems not to be obligatory for intermediate  $Q_{\text{dir}} \sim 10^3 \text{ cm}^{1.6} \text{ V}^{-2} \text{ s}^{-1.2}$  (FTAZ:ITIC [151]) or high  $Q_{\text{dir}} > 10^3 \text{ cm}^{1.6} \text{ V}^{-2} \text{ s}^{-1.2}$  (PBDB-TF:IT-4F [57]).

All NFAs mentioned above have an optimum thickness around 100 nm and as of today there have been hardly any reports of NFA-based blends reaching high fill factors also at thicknesses of about 300 nm with refs. [57, 280] being notable exceptions. Despite first promising results of NFA blends that combine good values for both FOMs, a material blend that combines the highest degree of energy level matching and electronic quality has yet to be shown.

### 5.3. Application to Organic Solar Cells

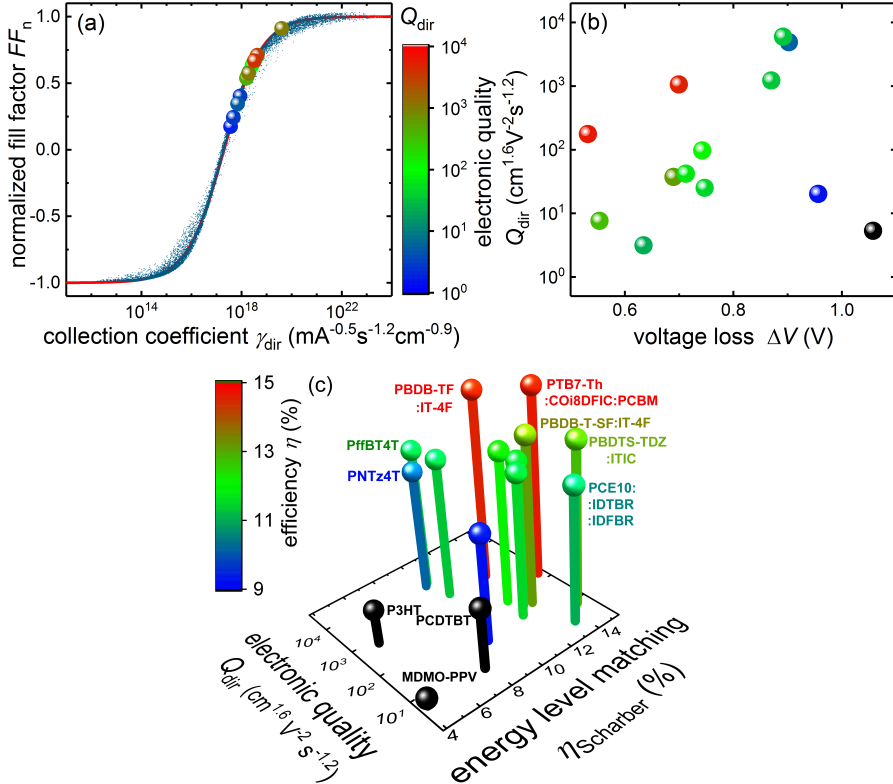


**Figure 5.12.:** Application of the  $FF$  model to organic solar cells based on the same data as fig. 2.9 (see appendix B for values). (a) A high  $FF_n$  is generally accompanied by a high  $Q$  (colorscale) but the saturation regime has not yet been reached by the best performing OSCs. (b) Correlation between electronic quality and voltage loss. Small-molecule NFA-based blends with low voltage loss have not reached high electronic qualities which explains the typical optimum thickness of about 100 nm of this recent class of organic solar cells. (c) Overview of the development of organic solar cells over the past 15 years expressed in terms of the two FOMs that are decisive for device performance. Panels (b) and (c) share the same colorbar encoding the reported efficiency, which is additionally represented by the height of the bars in (c). While considerable progress has been made for both FOMs, it remains an open challenge to create material blends that excel in both categories which would boost the power conversion efficiency of organic solar cells even further.

### 5.3.2. NFAs with Tunable Absorption Bands

Until non-fullerene acceptors (NFAs) emerged, PCBM was the only acceptor molecule that produced efficient OSC blends. Any acceptor contribution to the active layer blend's absorptance was thus constrained by the band gap of PCBM which corresponds to the UV. Due to the low photon flux in the UV region of the sunlight, PCBM contributes little to the photocurrent and almost all photogeneration originates in the polymer, which has a lower band gap. This is also one of the assumptions for Scharber's guidelines to optimize the polymer's energy levels in polymer:fullerene blends. Unlike inorganic semiconductor, whose absorption coefficient increases monotonously with energy, the organic materials applied in solar cells have relatively narrow absorption bands as can be seen from fig. 5.13(a). Consequently, the absorption coefficient of organic absorber blends often features shoulders and dips, exemplary shown in fig. 5.13(b), which translate to the absorptance and *EQE* spectra in the case of thin absorber layers. Polymer:fullerene blends cover the whole spectral range below the polymer's band gap since PCBM and most polymers have complementary absorption bands. NFAs introduce a new degree of freedom in the design of OSCs, which also extends to the tailoring of the absorption spectra since different NFAs have different band gaps, i.e. IDTBR and FBR displayed in fig. 5.13(a). Due to the relatively narrow absorption bands the question arises whether the NFA should absorb in the same (congruent) or in a different (complementary) spectral range as the polymer. For ideal charge carrier collection, the active layer can be made thick so that the absorptance is 1 in the spectral ranges where the organic blends absorb. Then, a higher  $J_{sc}$  and efficiency is achieved if a larger spectral range is covered – meaning that complementary absorption is favorable. However, experimentally optimized thicknesses yield  $d = 100\text{ nm}$  for most NFAs because of their relatively low electronic quality. For a thin device, it is not clear a priori whether to absorb most incoming photons of a narrow spectral range or only partially absorbing photons over a broad spectral range is advantageous. Making use of the insights from the previous analysis, this section considers the interplay between congruent or complementary absorption and charge carrier collection.<sup>7</sup>

---

<sup>7</sup>Large parts of this chapter (5.3.2) closely follow or are identical to my contributions to the second-author publication "Developing design criteria for organic solar cells using well-absorbing non-fullerene acceptors" [281]. © 2018 Krückemeier et al., used under CC BY 4.0

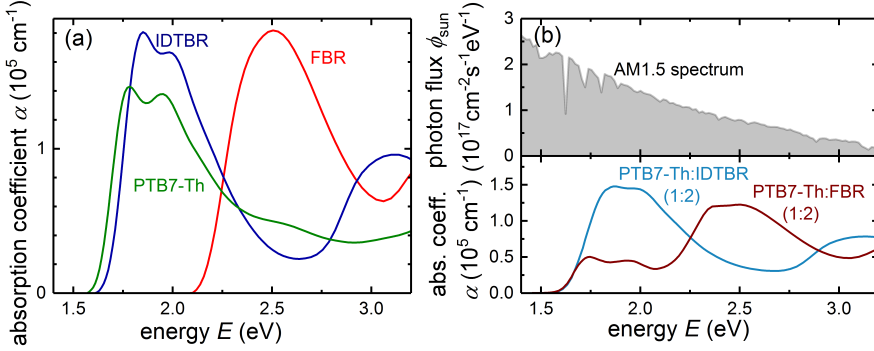


**Figure 5.13.:** (a) Absorption spectra of thin films of the donor polymer PTB7-Th and the two non-fullerene acceptors FBR and IDTBR. (b) Solar spectrum in terms of photon flux (top panel) as reference for the absorption spectra of the corresponding blends (bottom panel), which serve as example cases for congruent (PTB7-Th:IDTBR) and complementary (PTB7-Th:FBR) absorption bands. The sample preparation, measurements and analysis were done by Lisa Krückemeier.

**Table 5.4.:** Parameter values and ranges used in the simulations of NFA blends in figs. 5.14(a,b) and 5.15. Mobility values ( $\mu_e = \mu_h$ ) in  $\text{cm}^2 (\text{Vs})^{-1}$ :  $2 \times 10^{-4}$  (red),  $6 \times 10^{-4}$  (blue),  $2 \times 10^{-3}$  (yellow),  $6 \times 10^{-3}$  (green),  $2 \times 10^{-2}$  (dark blue),  $6 \times 10^{-2}$  (grey). For fig. 5.14(c-f) the values of mobility  $\mu$  and recombination coefficient  $k$  are given on the axes and the (optimized) thickness or efficiency are color-coded. All other parameters are the same as given in the table.

Parameter		value	unit
Thickness	$d$	50-500	nm
Effective band gap	$E_g$	1.5	eV
Direct rec. coefficient	$k$	$5 \times 10^{-10}$	$\text{cm}^3 \text{s}^{-1}$
Schottky barriers	$\varphi$	0.1	eV
Min. surf. rec. vel.	$S_{\text{min}}$	10	$\text{cm s}^{-1}$
Maj. surf. rec. vel.	$S_{\text{maj}}$	$10^9$	$\text{cm s}^{-1}$
Dielectric constant	$\epsilon_r$	3.5	—
Effective DOS	$N_{c,v}$	$10^{19}$	$\text{cm}^{-3}$

## 5. Charge Collection in Thin-Film Solar Cells

For the experimentally obtained optical data on the congruent absorbing PTB7-Th:IDTBR and complementary absorbing PTB7-Th:FBR blends, the generation profile of a generic n-i-p stack composed of glass/ ITO (150 nm)/ ZnO (40 nm)/ PTB7-Th:NFA (1:2) / MoO<sub>3</sub> (10 nm)/ Ag (100 nm) is computed with the Transfer Matrix method. The thickness  $d$  of the active layer is varied and the resulting generation profiles are used as input to numerical drift-diffusion simulations of the charge carrier dynamics with ASA. The electronic simulation parameters are listed in tab. 5.4. The absorption onset is given by the polymer for both blends, whereby the band gap in the electrical simulations can be set as a constant.<sup>8</sup> Again, direct recombination is assumed. Figure 5.14(a) and (b) shows the simulation results for complementary (PTB7-Th:FBR) and congruent (PTB7-Th:IDTBR) absorbing blends, respectively, for a varying active layer thickness and different values of the electronic quality factor  $Q_{\text{dir}}$  obtained from changing the mobility. Here, the interplay of absorptance – governing charge carrier generation and the  $J_{\text{sc}}$  – and charge carrier collection – governing the  $FF$  – is of interest. The ordinate thus displays the efficiency  $\eta$  instead of the  $FF$  that was investigated exclusively in the previous sections. As a result of optical interference in the flat layer stack, maxima appear in the thickness dependence of absorptance and  $J_{\text{sc}}$  evident from fig. 5.15 and similar to fig. 5.1(a). These maxima transfer to the  $\eta$ - $d$  relation for both cases in fig. 5.14(a) and (b). The corresponding  $J_{\text{sc}}$ ,  $FF$  and  $V_{\text{oc}}$  of the simulated solar cells are displayed in fig. 5.15. Apart from governing the  $FF$  as discussed extensively in the previous sections, the quantities that constitute  $Q_{\text{dir}}$  separately influence the device performance. The recombination coefficient  $k$  strongly influences  $V_{\text{oc}}$  while the mobility  $\mu$  mainly acts on the  $J_{\text{sc}}$ . In the simulations in fig. 5.14(a) and (b) and fig. 5.15,  $k_{\text{dir}}$  is kept constant and different  $Q_{\text{dir}}$  values are obtained by varying  $\mu$ . Therefore, the resulting efficiency curves mostly reflect the product of  $J_{\text{sc}}$  and  $FF$ , while the  $V_{\text{oc}}$  is almost constant over a wide range of thicknesses and electronic qualities shown in fig. 5.15(e) and (f). The  $J_{\text{sc}}$  in fig. 5.15(a) and (b) increases with increasing  $Q_{\text{dir}}$  due to the increase in mobility, since charge collection is inefficient even at short-circuit for low mobilities. Only for very high values of  $Q_{\text{dir}}$  the  $J_{\text{sc}}$  follows the absorptance up to high thicknesses. For decreasing  $Q_{\text{dir}}$  the thickness

---

<sup>8</sup>The implications of shifting the absorption onset energy is discussed in other sections of ref. [281], which are not based on my contribution and neglect collection issues.

### 5.3. Application to Organic Solar Cells

dependence of  $J_{sc}$  changes qualitatively and the higher maxima in  $J_{sc}$  decrease below the first absorption maximum. However, the thickness dependence of the  $FF$  in fig. 5.15(c) and (d) is significantly stronger and more critical for the efficiency.

At a given thickness, a higher  $Q_{dir}$  generally leads to a higher efficiency. For a sufficiently large  $Q_{dir}$ , the efficiency improves with increasing thickness and the optimum thickness  $d_{opt}$  shifts from the first to the second (or higher) maximum. Interference thus discretizes the optimum thickness, at which the highest efficiency is obtained for a fixed set of all other simulation parameters, at the first, second, or third absorption maximum. These jumps in optimum thickness show clearly in fig. 5.14(c) and (d) where the optimum thickness is plotted for a large range of mobilities and recombination coefficients. Higher mobilities and lower recombination coefficients – and thus larger  $Q_{dir}$  – also increase the efficiency at the optimum thickness as can be already seen from fig. 5.14(a) and (b) but more clearly from (e) and (f).

While complementary and congruent absorption behave qualitatively similar in many aspects, there are certain notable differences between the two cases. Most importantly, the increase in efficiency from the first to the second maximum – enabled by sufficiently large  $Q_{dir}$  – is less for the congruent case of IDTBR as can be seen by comparing fig. 5.14(a) and (b). The closer spacing of lines with equal efficiency in the case of complementary absorption in fig. 5.14(e) compared to congruent absorption in fig. 5.14(f) expresses the same effect. The thickness dependence of the efficiency is determined by the gain in absorptance and  $J_{sc}$  versus the loss in  $FF$  with increasing thickness. For congruent absorption a large part of the incident light in the covered spectral range is already absorbed in a thin active layer and the achievable gain in absorptance for a thicker layer is low compared to the case of complementary absorption. In the latter case, the absorptance is low over a larger spectral range for a thin device and by increasing the thickness, the absolute value of absorptance increases significantly. Since the drop in  $FF$  with thickness and electronic quality is the same for both systems, the attainable gain in absorptance decides whether a thicker layer is favorable in terms of device efficiency. For the same reasons not only the attainable gain in efficiency differs between a complementary and a congruent absorbing system but also the value of  $Q_{dir}$  that is necessary to reach an efficiency

## 5. Charge Collection in Thin-Film Solar Cells

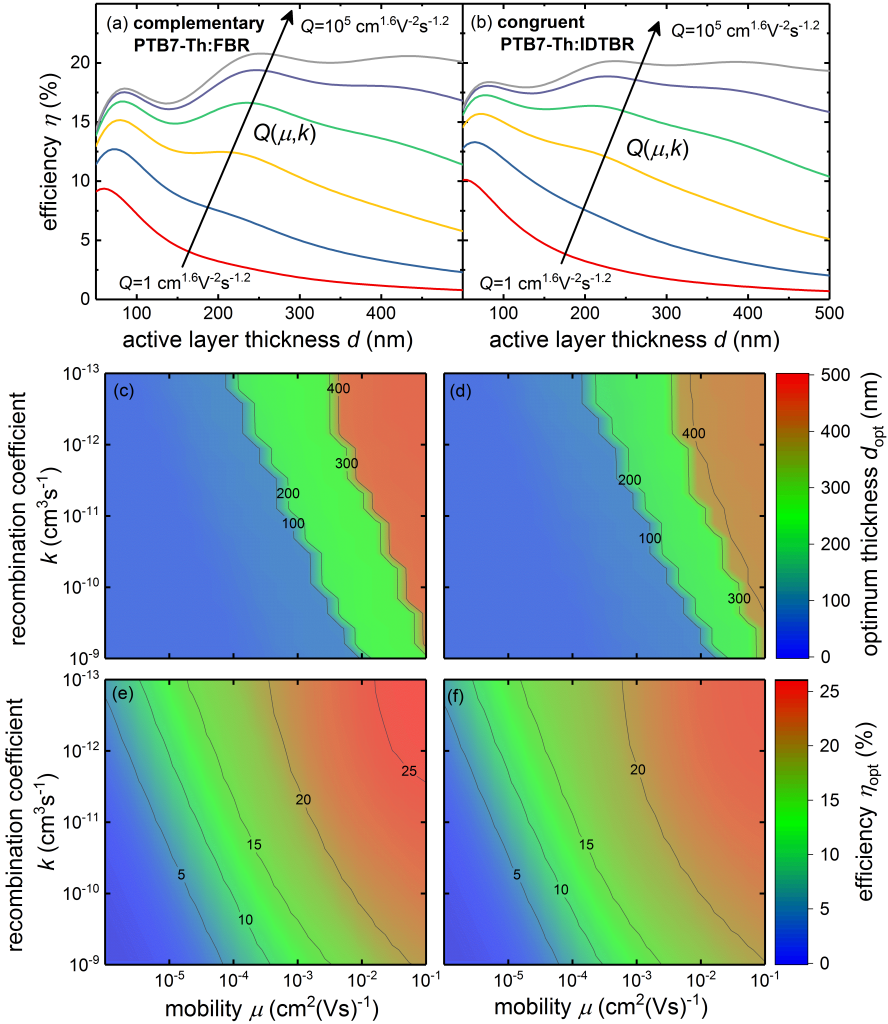


**Figure 5.14.:** Simulated solar cell performance of polymer:NFA blends with (a, c, e) complementary (PTB7-Th:FBR) and (b, d, f) congruent absorption (PTB7-Th:IDTBR). Optical simulations based on the blend data shown in fig. 5.13 account for interference which leads to efficiency maxima in (a) and (b). (a,b) The efficiency results from the interplay of charge carrier generation and collection, which changes qualitatively with varying electronic quality factor  $Q_{\text{dir}}$ . (c,d) The optimum active layer thickness takes discrete values, depending on the value of  $Q_{\text{dir}}$ , around the absorption maxima. (e,f) The solar cell efficiency at the optimum thickness generally increases with higher  $Q_{\text{dir}}$ . Comparing (a, c, e) with (b, d, f), a transition to a higher optimum thickness requires higher  $Q_{\text{dir}}$  values for congruent than complementary absorption. The increase in efficiency at a larger optimum thickness enabled by a higher  $Q_{\text{dir}}$  is stronger for complementary absorption.

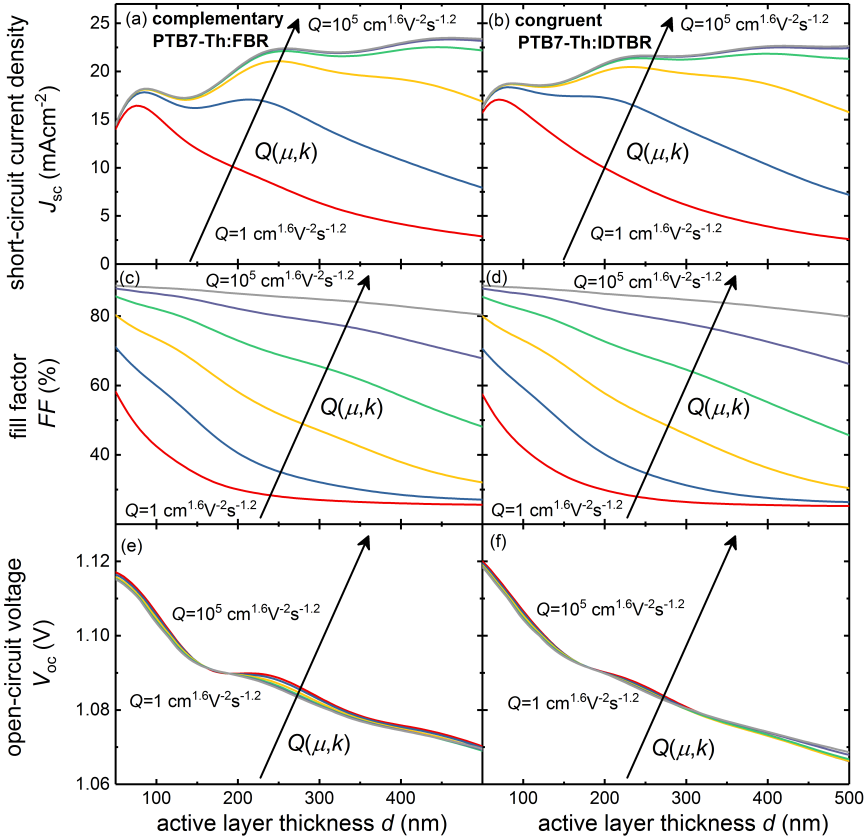


**Figure 5.15.:** Solar cell performance parameters (a, b)  $J_{sc}$ , (c, d)  $FF$  and (e, f)  $V_{oc}$  contribute equally to the device efficiency shown in fig. 5.14. The thickness dependence of the efficiency results from the product of  $J_{sc}$  and  $FF$  since the  $V_{oc}$  is almost constant for the simulated parameter space, where  $k$  is kept constant and  $\mu$  is varied to obtain a variation of  $Q_{dir}$ . The thickness dependence of the  $J_{sc}$  stems from the change in absorptance and to some degree – and especially for low  $Q_{dir}$  – from collection problems at short-circuit. However, the thickness dependence of the  $FF$  for the same  $Q_{dir}$  values is much stronger.

## 5. Charge Collection in Thin-Film Solar Cells

improvement. For the simulations in fig. 5.14(a) and (b), a jump to the second interference maximum requires  $Q_{\text{dir}} \gtrsim 10^3 \text{ cm}^{1.6} \text{ V}^{-2} \text{ s}^{-1.2}$  for complementary absorption, while congruent absorption requires  $Q_{\text{dir}} \gtrsim 10^4 \text{ cm}^{1.6} \text{ V}^{-2} \text{ s}^{-1.2}$ . Also, the transition to larger optimum thicknesses in fig. 5.14(c) and (d) is shifted to higher values of  $k$  and  $\mu$ , for the congruent compared to the complementary case. Thus, for a blend with complementary absorption the threshold for  $Q_{\text{dir}}$ , above which thicker active layers are more efficient, is generally lower.

In conclusion, covering a broad spectral range by combining two organic donor and acceptor materials that absorb complementarily is only more efficient if the absorptance of the absorber blend is sufficiently high. The required active layer thickness around the second (or higher) interference maximum is only feasible if charge-carrier collection at the maximum power point is efficient at the given thickness. Another option is to employ organic materials with higher absorption coefficients, which is subject of the next chapter.

### 5.3.3. Enhanced Absorption in OSCs

As demonstrated in the previous sections, most experimentally reported organic solar cells (OSCs), including almost all non-fullerene acceptor blends that represent today's most efficient OSCs, suffer from a low electronic quality that causes poor charge-carrier collection and an optimum thickness at the first absorption maximum around  $d \approx 100 \text{ nm}$ . Recently, an increased absorption strength has been demonstrated experimentally for certain polymers [277] and non-fullerene acceptors. In the following, I assess the increase in efficiency that can be achieved for molecular materials with enhanced absorption. Generally,  $\mu$  and  $\tau$  vary over several orders of magnitude between different materials (see previous chapters and refs. [252, 282]), whereas  $\alpha_0$  only varies over roughly one order of magnitude as presented in fig. 5.8. Nevertheless, for absorbers that reach intermediate efficiencies and an electronic quality (or  $\mu\tau$ -product) that does not enable very thick devices, an increase in  $\alpha_0$  may substantially increase the efficiency at the optimum thickness.

Figure C.9 in appendix C.8 shows the simulation results for the case of direct recombination, which typically dominates in organic solar cells and is characterized

### 5.3. Application to Organic Solar Cells

by the coefficient  $k$ . The data behaves very similar to the corresponding data obtained for Shockley-Read –Hall recombination in figs. 5.10 and 5.11. The expressions for the FOMs on the x-axis translate via  $\tau \leftrightarrow k^{-0.5}$  for the two recombination mechanisms. Note that the different units of  $\tau$  and  $k$  also translate to the expressions of the FOMs. From the data generated for fig. C.9, the gain in absorbance and efficiency for an increased absorption strength is calculated. Figure 5.16(a) displays the maximum attainable short-circuit current density ( $J_{sc,max}$ ), which is obtained for ideal charge carrier collection at  $V = 0V$ . Since the optical model takes interference effects into account, maxima appear in the absorbance-thickness relation that translate to the displayed  $J_{sc,max}$ . There is a notable difference in  $J_{sc,max}$  for different absorption strengths around the first absorption maximum. For thicker absorbers, this difference vanishes because  $J_{sc,max}$  saturates for all displayed absorption strengths. In quantitative terms, the attainable  $J_{sc,max}$  increases by around 15% at  $d = 100\text{nm}$  for an increase by factor 1.5 in  $\alpha_0$  as can be seen from fig. 5.16(b).

Figure 5.16(c) compares the resulting efficiencies for the case of a regular ( $c_\alpha = 1$  with  $\alpha = c_\alpha \alpha_{diff}$ ) and enhanced ( $c_\alpha = 1.5$ ) absorption strength in dependence of the  $\mu k^{-0.5}$ -product. As before, each device is evaluated at its individual optimum absorber thickness. The increase in efficiency with  $\mu k^{-0.5}$ , corresponding to the SRH ( $\mu\tau$ )-product, results from improved charge carrier collection. At any constant value of  $\mu k^{-0.5}$ , the efficiency of devices with enhanced absorption is clearly shifted upwards. Figure 5.16(d) further quantifies the gain in efficiency  $\eta(c_\alpha = 1.5)/\eta(c_\alpha = 1) - 1$  when moving from regular to strong absorption. This gain tends towards zero for the highest  $\mu k^{-0.5}$ -values, where charge carrier collection is perfectly efficient and the optimum thickness  $d_{opt}$  reaches several 100s of nm as shown in fig. C.10 in appendix C.8. For such thick layers, the absorbance saturates for both, regular and enhanced, absorption strengths and the gain in absorbance in fig. 6(b) vanishes, just as the gain in efficiency in fig. 5.16(d). For lower  $\mu k^{-0.5}$ -values, the gain in efficiency is generally higher. The specific  $\mu k^{-0.5}$  values at which the gain behavior changes, coincide with jumps to a higher absorption maximum as indicated by the gray areas in fig. 5.16(d) and shown in detail in fig. C.10 in appendix C.8. Generally, the optimum thickness of a regular absorbing blend jumps to the next higher absorption maximum at a lower  $\mu k^{-0.5}$  value compared to a strongly absorbing blend. For example, for  $\mu k^{-0.5}$  values in between the two gray

## 5. Charge Collection in Thin-Film Solar Cells

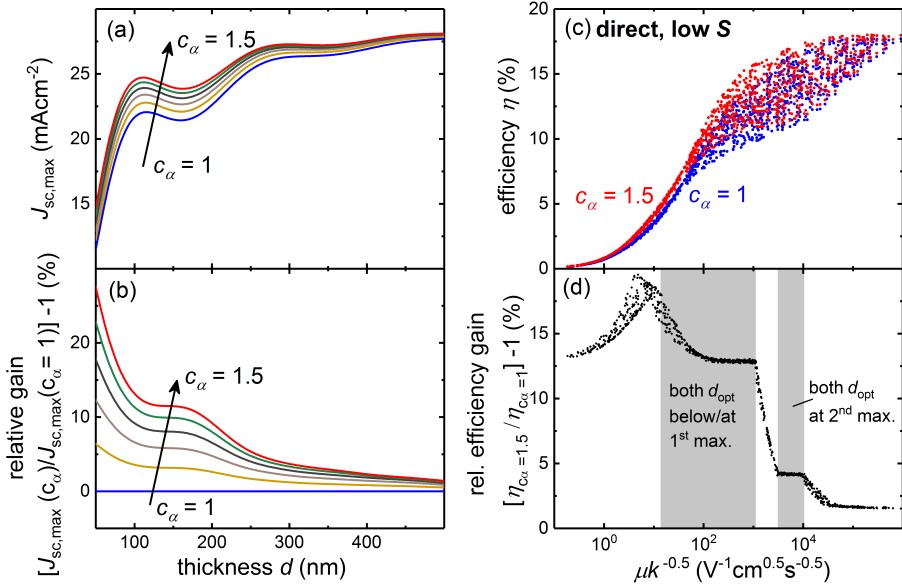


**Figure 5.16.:** Benefits of an increased absorption strength ( $\alpha = c_\alpha \alpha_{dfft}$ ) based on a representative scenario for organic solar cells where a comparable tuning of  $\alpha$  has been achieved [277]. (a) Maximum attainable short-circuit current density for ideal charge carrier collection leading to (b) relative gains around 15% for thin absorber layers. At larger thickness, the absorbance tends to the same value for different absorption strengths and the attainable gain diminishes. The data in (a,b) is only based on optical simulations. (c) Efficiency of the lowest and highest absorption strength simulated in fig. C.9 for direct recombination and low surface recombination, evaluated at the individually optimized thickness. The features in (d) coincide with jumps to higher absorption maxima as is elaborated in fig. C.10. The gain attained by stronger absorption depends heavily on  $\mu k^{-0.5}$  and reaches a value of around 15% for  $\mu k^{-0.5}$  values that are associated with a typical optimum thickness for organic solar cells of about 100 nm at the first absorption maximum.

regions, the regular absorbing blend has an optimum thickness around the second absorption maximum, whereas the strongly absorbing blend still performs best at a thickness around the first absorption maximum. The non-monotonous behavior for the lowest  $\mu k^{-0.5}$  can be attributed to the fact that no devices with thickness below 50 nm were simulated in accordance with experimentally realized absorber thicknesses, although the optimum thickness for such low  $\mu k^{-0.5}$  values is actually lower. More importantly, for a range of relevant  $\mu k^{-0.5}$  values that do not allow a jump to the second absorption maximum, a considerable gain in efficiency between 10% and almost 20% is reached.

In summary, given that the optimum absorber thickness of many organic solar cells is at the first absorption maximum, an efficiency increase of around 15% seems realistic for an increase in the absorption strength by 50% ( $c_\alpha = 1.5$ ). It is generally plausible that higher absorption strengths – leading to even larger gains in efficiency – could be reached once the parameter  $\alpha_0$  is in the focus of synthetic chemists who design new absorber materials, as has been elaborated by Vezie et al. [277]. The improvement in absorption coefficient in many novel small molecule acceptors relative to most typical polymers is promising in that respect.

#### 5.3.4. Relation between FOMs

In this thesis, I developed different material-specific figures of merits to judge the performance prospects of thin-film solar cells in general and organic solar cells in particular. The following clarifies the relation between the efficiency FOMs based on  $\alpha$ ,  $\mu$  and  $\tau$  developed in this chapter 5.2 and the electronic quality and Scharber efficiency, which were used as FOMs in chapter 5.3.1 to decipher the progress of organic solar cell efficiency. Generally, the electronic quality factor and the FOMs presented in this chapter 5.2 are applicable to all thin-film solar cells that employ a fully depleted absorber layer, whereas the Scharber efficiency is specific to organic solar cells.

As a major difference, the analysis in this chapter considers a fixed (optical and electrical) band gap and assesses how  $\alpha_0$ ,  $\mu$  and  $k$  (or  $\tau$ ) affect the solar cell efficiency until, for good values of the three parameters, the Shockley-Queisser limit [24] is

## 5. Charge Collection in Thin-Film Solar Cells

reached. The Scharber efficiency on the other hand reflects efficiency improvements that result from a decrease of the optical band gap towards the SQ optimum and a reduction of the difference between the optical and electrical bandgap (also see appendix A.4). Therefore, the OSC-specific Scharber efficiency is a complementary concept to the  $(\alpha\mu\tau)$ -based FOMs discussed in this chapter 5.2.

The analysis in chapter 5.3.1 of OSC efficiencies in terms of electronic quality and Scharber efficiency did not take any variation of the absorption strength into account, mostly because it has not been perceived as a handle on solar cell efficiency so far and does not vary for most of the studied materials [277]. The electronic quality factor as a figure of merit for the  $FF$  appears in a similar way in the FOMs for the efficiency presented in this chapter 5.2. The different weights for mobility and lifetime in the expressions (e.g.  $Q_{\text{SRH}} = \mu^2\tau^{1.6}$  versus  $FOM_{\text{SRH}}^{\text{low-}\mu} = \alpha \times (\mu\tau)$ ) results from the  $FF$  definition, which includes the ratio  $V_{\text{MPP}}/V_{\text{oc}}$ , whereas the efficiency only employs  $V_{\text{MPP}}$  (also see section 5.1.3). Note that this thesis provides a method to extract the electronic quality factor from basic solar cell characterization, whereas assessing the values of the  $(\alpha\mu\tau)$ -based FOMs requires elaborate material and device characterization. Regarding the literature data analyzed in chapter 5.3.1,  $FF_n$  values well below 1 in fig. 5.12(a) indicate that charge carrier collection has not saturated, which can already be seen from the low optimized thicknesses in fig. 2.9 in chapter 2.4. In the terminology of this chapter, all historically best performing OSCs are thus located in the low- $\mu$  regime, where the  $(\alpha\mu\tau)$ -product governs the efficiency – again highlighting that the efficiency of today’s organic solar cells would benefit from materials with comparable electronic quality but increased absorption strength.

## 5.4. Chapter Conclusion

Based on drift-diffusion simulations, I presented a comprehensive analysis of the fill factor in thin-film solar cells with a focus on the absorber material’s electronic grade. Both investigated recombination mechanisms of direct bimolecular and Shockley-Read-Hall monomolecular recombination lead to similar results. The optimized expression of the collection coefficient results in significantly reduced scatter in the

collection coefficient - fill factor relation than previously suggested analytical approximations, that are derived at short-circuit and not at the maximum power point, where the fill factor is defined. For deviations of the standard case of a fully depleted active layer, there are characteristic signatures that indicate the presence of a space-charge region or a limiting effect from the contacts. These signatures can be produced experimentally by producing a series of devices with varying active layer thickness. The close study of surface recombination showed a unreported effect of the surface recombination velocity on the fill factor that goes beyond the indirect influence via the open-circuit voltage. Finally, even for large variations in the absorber's dielectric constant, the collection coefficient remains unchanged and only the fit parameters for the fill factor normalization and its relation to the collection coefficient require slight adaptation. The results are therefore applicable to a wide range of thin-film absorber technologies, including  $\text{Sb}_2\text{S}_3$  as the experimental focuses material in this thesis. I then explored the interplay between absorption, charge transport and charge recombination and their effect on the solar cell efficiency. For a given bandgap, I found different figures of merits that correlate well with the efficiency and depend on the corresponding material parameters, as well as different regimes of the mobility and surface recombination velocity.

A practical application of the theoretical studies is the experimental extraction of a herein defined material-specific figure of merit for the fill factor. This electronic quality factor is assessable from basic solar cell characterization and allows retrospective analysis of literature data. Applied to organic solar cells, the importance of the electronic quality factor for the solar cell performance was illustrated. Improving the electronic quality factor of organic solar cell blends is a route for progress that goes beyond the well-recognized target of reducing open-circuit voltage losses associated to a better matching of energy levels. Blends with high electronic quality allow for high fill factors even at large thicknesses, which in turn increases the absorptance, external quantum efficiency and eventually the short-circuit current. In this context, the electronic quality is decisive for the optimum blend constituents with regard to their spectral absorption range. For a blend with high electronic quality that permits thick active layers, complementary absorption bands of the donor and acceptor material are favorable. However, at lower electronic qualities, congruent absorption bands yield higher efficiencies. The result is most relevant for

## *5. Charge Collection in Thin-Film Solar Cells*

solar cells based on non-fullerene acceptors, whose absorption range varies widely with the applied material and whose optimum thickness is typically around only 100 nm. I finally demonstrated, that the enhancement of the absorption coefficient presents a way to improve the efficiency whenever the electronic quality is limited, which is particularly relevant for organic solar cells.

## 6. Sb<sub>2</sub>S<sub>3</sub> Solar Cells

This chapter presents my (mostly experimental) work on Sb<sub>2</sub>S<sub>3</sub>-based solar cells in a planar configuration with the Sb<sub>2</sub>S<sub>3</sub> absorber deposited via spin-coating. Most of the studies are carried out for both process routes, that are based on different Sb<sub>2</sub>S<sub>3</sub> precursors (Sb-TU and Sb-BDC) and were introduced in chapter 3.2. The differences and similarities of the resulting layers and solar cells between the two routes are highlighted. Chapter 6.1 presents the process and layer stack optimization with regard to the absorber deposition and the choice of a suitable hole transport material from a range of different organic semiconductors. As a result of the optimization, solar cell efficiencies of 4.2% and 5.0% are achieved for the Sb-TU and Sb-BDC process, respectively, which is then put into context of other reports from literature. Chapter 6.2 identifies the main limitations of the fabricated devices, which, to a large degree, also explain the performance differences found for the two process routes. As part of this, the conceptual work on inhomogeneity and charge carrier collection presented in chapters 4 and 5, respectively, is applied to the specific case of Sb<sub>2</sub>S<sub>3</sub>. At the same time, the study offers suitable characterization methods to investigate the properties that are critical to Sb<sub>2</sub>S<sub>3</sub> solar cell performance. Some of the characterization methods have not been applied to Sb<sub>2</sub>S<sub>3</sub> solar cells previously, so that I obtain an unprecedented comprehensive picture of the challenges in the field. Since the solar cells produced in this work have a similar signature as other planar Sb<sub>2</sub>S<sub>3</sub> solar cells in terms of solar cell performance, my findings are likely to be highly relevant for other reports and future work in the field. Chapter 6.3 summarizes these findings and gives an outlook for future work and routes to improvement of Sb<sub>2</sub>S<sub>3</sub> solar cells.

## 6.1. Layer and Device Optimization

Following the rationale of section 2.4.2, I opted to prepare  $\text{Sb}_2\text{S}_3$  solar cells in a planar configuration because of a simpler film morphology, the availability of well-developed characterization methods for planar thin-film technologies [85], as well as first promising performance reports for planar ALD [60]- and CBD [164]-processed  $\text{Sb}_2\text{S}_3$  solar cells. The drawbacks of aqueous and hard-to-control [33,60] CBD leading to unfavorable phase impurities [20,174–176], motivated my choice to explore spin-coating routes of the absorber layer, which already showed promising results in an ETA architecture [33]. In a chronological perspective of this thesis, Choi's [33] report from 2015 applied the Sb-TU precursor, which I transferred to a planar cell architecture. Later during the course of this thesis in 2017, the Sb-BDC precursor route was reported [34], which I then investigated subsequently.

This chapter covers the optimization of the spin-coated  $\text{Sb}_2\text{S}_3$  absorber and the organic hole transport layer of the solar cell, which is guided by different material, film and solar cell characterization methods. Section 6.1.1 discusses the absorber deposition with a focus on the annealing conditions of the spin-coated precursor film, which is evaluated in terms of morphology, presence of sub-band gap states, as well as the resulting solar cell performance. Section 6.1.2 adds the compositional analysis via XPS to check for correlation between the absorber stoichiometry and the solar cell performance. The determination of the energy levels of  $\text{Sb}_2\text{S}_3$  via UPS prepares for section 6.1.3, where the role of the  $\text{Sb}_2\text{S}_3$ /HTM heterojunction is discussed by applying a series of different organic polymers and small molecules as HTM. Finally, section 6.1.4 shows the optimized solar cell performance and section 6.1.5 summarizes the results and compares them to other literature reports.<sup>1</sup>

### 6.1.1. Annealing Procedure

For the Sb-TU process, the direct thermal decomposition of the spin-coated solution at 180 °C leaves large parts of the substrate uncovered as can be seen in the

---

<sup>1</sup>Large parts of this chapter (6.1) closely follow or are identical to my first-author publication “Spin-coated planar  $\text{Sb}_2\text{S}_3$  hybrid solar cells reaching 5% efficiency” [283] – © 2018 Kaienburg et al., used under CC BY 4.0

Scanning Electron Microscope (SEM) image in fig. 6.1(a). Between smooth-looking domains of  $\text{Sb}_2\text{S}_3$  the FTO grains covered with spray-coated  $\text{TiO}_2$  are clearly visible (see the SEM images of the substrate in fig. 3.2 for comparison). The morphology is improved by annealing the films at 100 °C directly after spin coating for approximately 60 minutes prior to thermal decomposition. Figure 6.1(b) shows that this slow annealing step drastically reduces the area of pinholes in the film. Both images in fig. 6.1(a) and (b) are taken after crystallization at 265 °C but the holes are already present in the amorphous films as can be seen in the corresponding images in fig. 6.1(d) and (e). The existence of pinholes is thus not caused by crystallizing the film, which emphasizes that the thermal decomposition procedure is crucial for the film morphology in the Sb-TU process. While even the optimized annealing procedure cannot fully avoid the presence of pinholes for the Sb-TU process, the Sb-BDC process leads to compact layers largely free of pinholes as shown in fig. 6.1(c). Interestingly, the uncrystallized film in fig. 6.1(f) has a porous structure and the good film morphology forms only during crystallization, as was observed in the original report [34], which underlines the apparently different mechanisms governing film formation in the two processes. Grain sizes for the Sb-BDC exceed 1  $\mu\text{m}$ , which is slightly smaller than the reported average of 6  $\mu\text{m}$  [34], whereas the Sb-TU process yields smaller grain sizes on the order of 500 nm.

The Raman measurements in fig. 6.2 indicate a similar microstructure for the Sb-TU and Sb-BDC process, both in the amorphous and crystalline state. The broad peak around 280  $\text{cm}^{-1}$  of the amorphous samples splits into two peaks for the crystalline samples, with a potential third peak in the left shoulder of the 320  $\text{cm}^{-1}$  peak. These most prominent features coincide with the reported Raman signature of crystalline  $\text{Sb}_2\text{S}_3$  [284, 285].

Most deposition methods such as CBD [80, 171], ALD [60, 159], thermal evaporation [167, 286, 287] and the here discussed spin-coating [33, 34], produce amorphous films that are subsequently crystallized at temperatures above antimony sulfide's minimum crystallization temperature of 250 °C [79, 173, 198]. The typical crystallization temperature is 300 °C [20, 33, 34, 80, 91] while values of 330 °C [60, 161, 185, 288] and up to 400 °C [289] are reported. To gain insights into the crystallization behavior in terms of morphology, creation of defects and solar cell performance, I

## 6. $Sb_2S_3$ Solar Cells

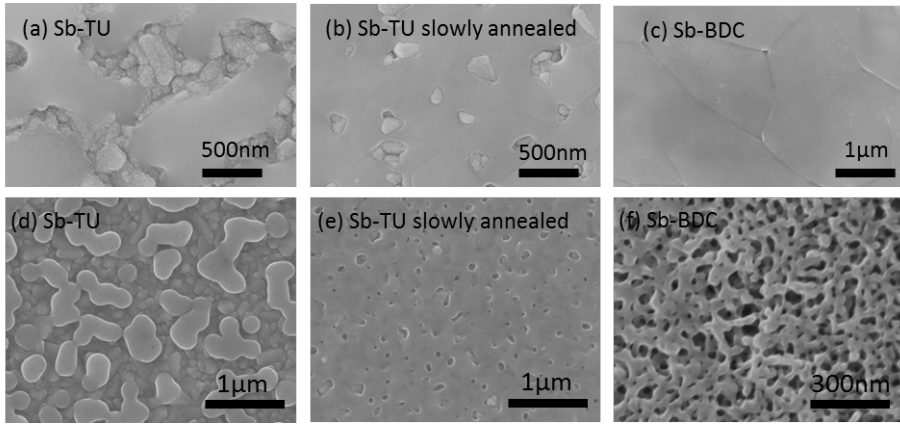


**Figure 6.1.:** SEM images of (thermally decomposed)  $Sb_2S_3$  thin films (a-c) after and (d-f) before crystallization at 265 °C. (a,d) Direct thermal decomposition of the spin-coated Sb-TU precursor solution leaves the substrate largely uncovered. (b,e) An intermediate slow annealing step at 100 °C for 60 minutes reduces the pinhole area. (c) The Sb-BDC based process leads to a pinhole-free compact layer with large grains, despite the (f) porous structure of the amorphous state.

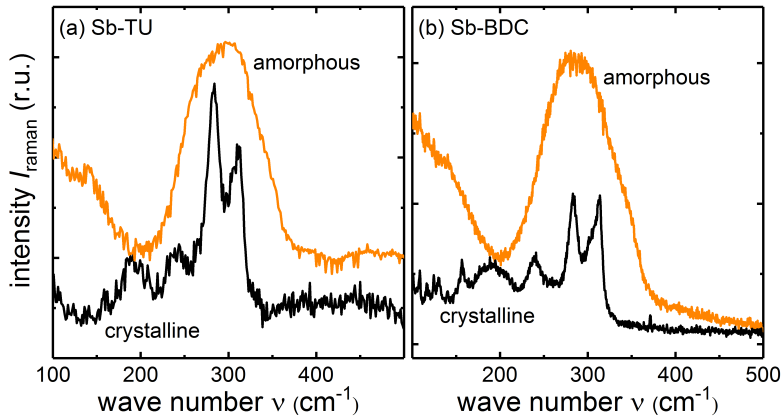


**Figure 6.2.:** Raman spectra of  $Sb_2S_3$  formed in the (a) Sb-TU and (b) Sb-BDC process show the transformation from the amorphous to the crystalline state by annealing at 265 °C.

produced samples crystallized on a hot plate at various temperatures in a nitrogen atmosphere. The lowest temperature was chosen to be 265 °C slightly above the minimum crystallization temperature of  $\text{Sb}_2\text{S}_3$ . When increasing the crystallization temperature from 265 °C in fig. 6.3(a) to 300 °C in fig. 6.3(b), the Sb-TU process shows a slight increase in uncovered substrate area. The small, bright, tapered features, that are observed in the domains not covered by  $\text{Sb}_2\text{S}_3$ , can be attributed to the peaks of large FTO grains as can be seen from the comparison of the SEM images in fig. D.1(a-h) in appendix D. The  $\text{Sb}_2\text{S}_3$  domains tend towards a droplet-like morphology with increasing temperature which can be interpreted as an on-going dewetting of the substrate and was reported before for the transition from the amorphous to the crystalline phase of  $\text{Sb}_2\text{S}_3$  for a thin layer on a mesoporous  $\text{TiO}_2$  scaffold [159,290]. This trend continues for higher crystallization temperatures as can be seen from AFM and SEM measurements in fig. D.1(a-h) in appendix D. At 400 °C the film seems to disintegrate and macroscopic holes form.

For PDS measurements of the Sb-TU process, a  $\text{TiO}_2$  layer was spray-coated onto the glass before depositing the  $\text{Sb}_2\text{S}_3$  layer, because weak adhesion prevents direct coating of glass with Sb-TU solution. The deposition conditions thus closely resemble those of the fabricated solar cells. The results for different crystallization temperatures in the Sb-TU process are shown in fig. 6.3(c). For the sample crystallized at 265 °C and 300 °C, the measurement signal quickly saturates at energies above the band gap. At low energies the absorption strength of the substrate becomes comparable to that of the  $\text{Sb}_2\text{S}_3$  film, which is evident from the characteristic  $\text{H}_2\text{O}$  absorption peak of Corning glass below 1 eV. While the layer crystallized at 265 °C and 300 °C behave almost identical, the defect absorption of the layer crystallized at 350 °C is increased drastically. The same holds true for the 400 °C sample where, due to the macroscopic holes in the film described before, the incoming light is still transmitted and not fully absorbed even at high energies which inhibits a proper analysis of the absorption coefficient. Therefore the 400 °C sample does not coincide with the other samples that match very well for energies above the band gap. The increased defect absorption for the crystallization at 350 °C or higher hints towards a lower cell performance because a higher defect density would cause increased recombination and eventually a lower open-circuit voltage. This hypothesis is confirmed by solar cells shown in fig. 6.3(d) produced in the standard configura-

## 6. $Sb_2S_3$ Solar Cells

tion described in chapter 3.2 with P3HT as the HTM. The cell from an  $Sb_2S_3$  layer crystallized at 300 °C shows a lower  $V_{oc}$  and  $J_{sc}$  than the cell crystallized at 265 °C. At 350 °C, the  $V_{oc}$  drops drastically which is consistent with the increased defect absorption observed with PDS in fig. 6.3(c). The cell performance decays further at 400 °C, where the film morphology degenerates.

Next, a similar study was conducted for the Sb-BDC process with a focus on crystallization at 265 °C and 300 °C. The SEM image in fig. 6.3(e) of the layer crystallized at 300 °C shows a similar morphology as the one crystallized at 265 °C shown in fig. 6.1(c) except that small pyramidal structures appear on top of the grains. A sample crystallized at 265 °C for 30 minutes shown in fig. 6.3(f) instead of the standard 2 minutes shows similar structures (also see the zoomed-out SEM images in fig. D.1, appendix D). The nature of these features remains unclear but similar structures were reported for chemical-bath-deposited and evaporated  $Sb_2S_3$  [164, 173, 284, 286] and seem to be present in the original Sb-BDC report [34] as well, where a temperature of 300 °C was chosen. The absorption coefficient of the Sb-BDC sample crystallized at 265 °C shown in fig. 6.3(g) is almost identical to that of the Sb-TU sample crystallized at the same temperature, shown in fig. 6.3(c) and drawn again in (g) for direct comparison. However, the defect absorption of  $Sb_2S_3$  from the Sb-BDC route crystallized at 300 °C is strongly enhanced. A sample prepared at 265 °C but with a crystallization time of 30 minutes reveals a similar increase in defect absorption. For both samples with increased defect absorption the absorption behaves non-monotonous with energy. The maxima and minima can be most-likely attributed to interference in the smooth films – which did not fully cancel out during data analysis – instead of actual variations in the materials' density of states in the sub-bandgap region. The negative impact of the increased defect density on device performance is confirmed by comparing solar cells prepared with the same annealing conditions in fig. 6.3(h) and tab. 6.1 in appendix. D.

In summary, for both investigated process routes an optimized crystallization temperature of 265 °C was found, which is lower than the commonly applied treatment at 300 °C, that was also chosen in the original publications of both process routes [33, 34]. For the Sb-TU process, higher crystallization temperatures cause a dewetting of the substrate. In the Sb-BDC process, significantly increased defect

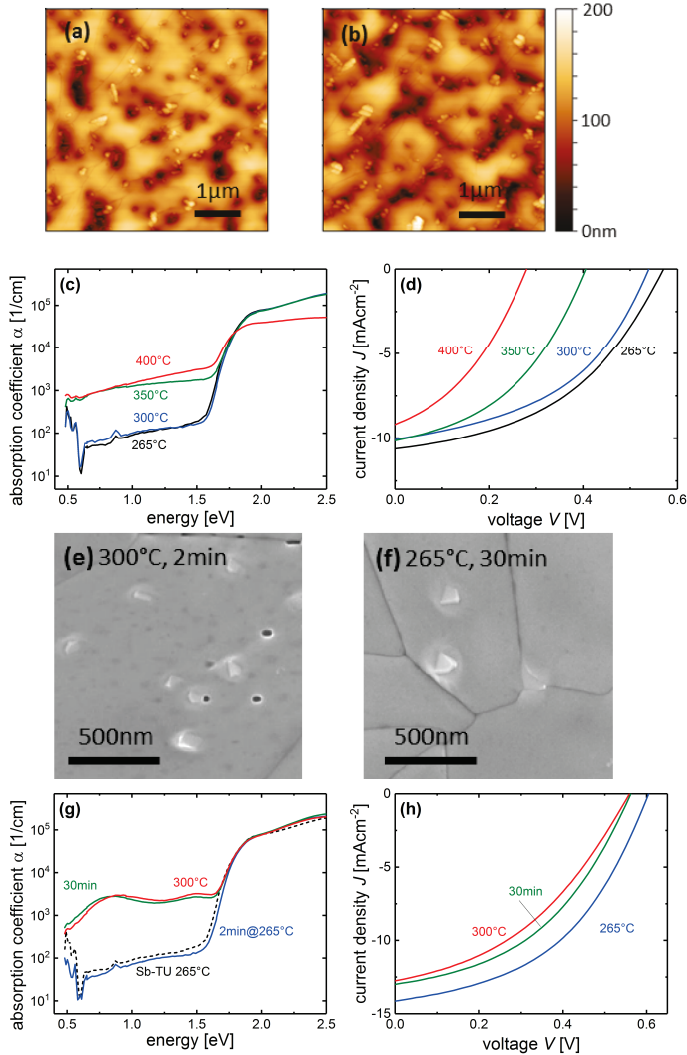


**Figure 6.3.:** Crystallization in the Sb-TU (a-d) and Sb-BDC (e-h) process. AFM measurements of the Sb-TU route show a coarsening of the morphology when the annealing temperature increases from (a) 265 °C to (b) 300 °C. (c) Electronic defects detected with PDS are created in the band gap for temperatures of 350 °C or above. (d) Corresponding solar cell performance. SEM images of the Sb-BDC process show new features in the morphology for a (e) higher crystallization temperature and (f) longer crystallization time compared to the standard procedure (265 °C, 2 min). At the same time (g) defect absorption increases and (h) device performance deteriorates for conditions that are uncritical in the Sb-TU process. Table 6.1 in appendix 6.1 lists the solar cell key parameters from (d,h).

## 6. $Sb_2S_3$ Solar Cells

formation appears along with new features on the surface of the  $Sb_2S_3$  film for longer crystallization times and higher crystallization temperatures of 300 °C. The same annealing conditions were uncritical in terms of defect absorption for the Sb-TU process where similar degradation started only at a crystallization temperature of 350 °C.

### 6.1.2. Stoichiometry and Energy Levels

Deviations from the stoichiometric  $Sb_2S_3$  composition that has an S:Sb ratio of  $3 : 2 = 1.5$  were shown to decrease solar cells performance [33]. Composition changes in the  $Sb_2S_3$  during annealing could explain the performance variations and the different degrees of defect absorption observed with PDS in fig. D.1. The stoichiometry of samples fabricated from the two processes at different crystallization temperatures was probed with X-ray photoelectron spectroscopy (XPS) as explained in chapter 3.3. Table 6.1 displays the results of the measurements. Most importantly, there is no trend in the S:Sb ratio for different annealing temperatures and the Sb-TU process yields similar values as the Sb-BDC process. The S:Sb ratios are always below the stoichiometric composition but also differ if either the Sb 4p or the Sb 3d peak is taken into the analysis, which should not be the case and puts the absolute values in doubt. Since  $Sb_2S_3$  is a relatively little investigated material system, there is no precise knowledge of all the model parameters, which are required to properly interpret the XPS data in absolute terms. The presence of carbon at the surface, which is typical for samples not processed under high vacuum conditions, further complicates the data analysis in absolute terms. Angle-resolved measurements (ARXPS) in fig. 6.1(a) show a significant increase in sulfur concentration with the X-ray incident angle relative to the surface normal. The penetration depth for larger angles is smaller, meaning that the sulfur concentration increases towards the surface. Again, the relative trend that is always based on the same analysis method contains important information, but the absolute values should be taken with care. Figure 6.1(b) shows the XPS spectrum of the Sb 4d peak of a sample fabricated by the Sb-BDC process and annealed at 265 °C. The observable peaks and fit quality is representative for all other samples except the Sb-BDC sample annealed at 300 °C shown in fig. 6.1(c). Here, a small second Sb 4d peak is visible at

**Table 6.1.:** XPS and UPS results. The S:Sb ratio is calculated from the S 2p and two different Sb peaks as indicated. No clear trends in the stoichiometry are evident and the deviations from the different Sb peaks indicate that the absolute values should be taken with care. The valence band energy ( $E_v$ ) is constant for the Sb-TU, but the Fermi level ( $E_F$ ) shifts upwards with higher crystallization temperature ( $T_{\text{cryst}}$ ). The Sb-BDC sample annealed at 300 °C yields similar results. The deviations in  $E_v$  for the Sb-BDC sample annealed at 265 °C comes along with strong fluctuations for different spots on the sample (up to 0.1 eV measured at three positions compared to typically 0.02 eV for the other samples).

Prec.	$T_{\text{cryst}}$ °C	S:Sb (Sb 3d)	S:Sb (Sb 4d)	$E_F$ eV	$E_F - E_v$ eV	$E_v$ eV
TU	265	1.40	1.21	4.96	0.85	5.81
TU	300	1.42	1.24	4.87	0.91	5.78
TU	350	1.42	1.22	4.82	0.96	5.78
BDC	265	1.41	1.22	4.49	1.06	5.55
BDC	300	1.44	1.23	4.79	0.98	5.77

lower binding energies. The higher energy peaks are attributed to Sb bonded to S in a fully coordinated bond, while the lower energy peaks indicate under-coordinated  $\text{Sb}_2\text{S}_3$  or rather elemental Sb [291]. This could explain the significant increase in defect absorption in fig. 6.3 for the Sb-BDC sample crystallized at 300 °C compared to the sample crystallized at the optimum temperature of 265 °C.

None of the investigated samples showed other undesired species such as oxidized antimony  $\text{Sb}_2\text{O}_3$  (540 eV), oxidized sulfur  $\text{Sb}_2(\text{SO}_4)_3$  (168 eV) or elemental sulfur (164 eV) as can be seen from figure D.2(b) and (c) in appendix D. Previously, oxide phases were observed for samples deposited in a chemical bath [20] and elemental sulfur was observed for high amounts of the sulfur precursor in the Sb-TU process [33]. The absence of undesired species in the  $\text{Sb}_2\text{S}_3$  material underlines the feasibility of both spin-coating routes. Additionally, the signal coming from the substrate as well as the residual carbon content were analyzed. All samples were deposited on indium tin oxide (ITO) and the holes in the  $\text{Sb}_2\text{S}_3$  layer deposited from the Sb-TU precursor give way to an indium peak that is strongest for the 350 °C sample that dewets the strongest. No In is observed for the compact layers formed by the Sb-BDC process. A significant amount of carbon, which also depends on the storage time before measurement, was observed for all samples. ARXPS in fig. D.3(c) in appendix D showed that the carbon is mostly located on the surface,

## 6. $Sb_2S_3$ Solar Cells

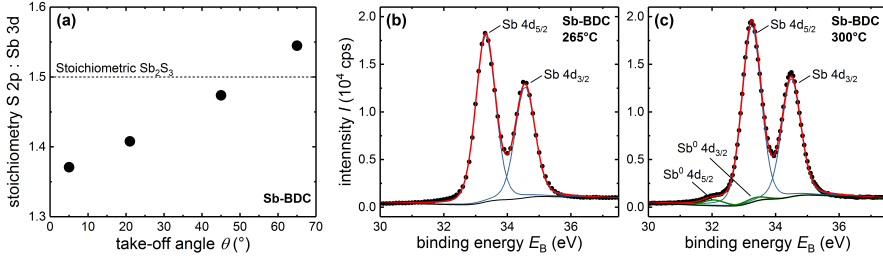


**Figure 6.4.:** Exemplary XPS measurements for the Sb-BDC process. (a) Angle dependent ARXPS measurements show an increased sulfur concentration towards the film surface. The position of the Sb 4d peak in (b) indicates the Sb-S bond for an Sb-BDC sample annealed at 265 °C. The spectrum is representative for all other measurements except the (c) Sb-BDC sample annealed at 300 °C that shows an additional peak indicating under-coordinated Sb, which might explain the increased defect absorption observed in fig. 6.3(g).

indicating that it is unlikely to originate from residues of the precursors but rather from deposition during storage. The Sb-TU samples however show an additional carbon peak in fig. D.3(b) in appendix D that might be attributed to the sulfur precursor thiourea (TU).

The same samples that were characterized by XPS were also investigated with ultraviolet photoelectron spectroscopy (UPS) to determine the work function and valence band edge. The values for the obtained energy levels are given in table. 6.1 The samples from the Sb-TU process show consistent valence band (VB) edges of about 5.8 eV and a significant trend in the work function towards more *n*-type behavior with increasing annealing temperature. Although the work function varies by 0.1 eV, all samples are quite intrinsic with a band gap of 1.78 eV (determined via the *EQE* inflection point) and a Fermi level distance to the VB of 0.85-0.95 eV, which is thus located in the middle of the band gap. Dark conductivity measurements on  $Sb_2S_3$  from the Sb-TU process showed no detectable current, implying a conductivity below  $10^{-8} \text{Scm}^{-1}$ , which is consistent with an intrinsic semiconductor. The samples prepared from the Sb-BDC process are generally of intrinsic nature as well, but the distance from the Fermi level to the VB is larger compared to the Sb-TU process. The 300 °C samples from both processes behave relatively similar. The samples from the Sb-BDC precursor annealed at 265 °C show a much larger scatter than all other samples, when comparing different positions on the same sample.

Therefore, a second sample was prepared that, however, showed similar fluctuations. Workfunctions between 4.45 eV and 4.68 eV and distances between Fermi and valence band between 0.96 eV and 1.12 eV were observed for different samples and positions. Despite the fluctuations, all measurements point to a HOMO level between 5.5 eV and 5.7 eV, which is increased compared to differently processed samples. The origin of the large fluctuations and the decreased HOMO level remains unclear. Reported HOMO levels of  $\text{Sb}_2\text{S}_3$  obtained from UPS measurements lie between 5.3 and 5.5 eV [166, 289, 292] and go up to 5.9 eV [60]. Although these values may vary with the procedure to extract energy levels from the UPS data, actual changes in the HOMO level of  $\text{Sb}_2\text{S}_3$  that depend on the deposition method cannot be excluded at this point. The Fermi level positions in all reports indicate similarly intrinsic material as found here.

In summary, samples from different process routes and annealing temperatures show very similar S:Sb compositions. Under-coordinated Sb is observed for the Sb-BDC precursor annealed at 300 °C. UPS measurements reveal the intrinsic nature of the material. Changes in the distance between Fermi level and valence band for Sb-TU with annealing temperature indicate a change in the density of states (DOS) in the band gap that might be related to small changes in the stoichiometry that are not detectable with XPS. For such intrinsic materials, even slight changes in the DOS may affect the Fermi level position. An increase in recombination centers might be related to the change of the DOS which might explain the drop in  $V_{oc}$  with annealing temperature. For Sb-BDC fewer clear statements can be made due to the observed fluctuations. The measurements indicated an increased HOMO level. Altogether, the performance variation cannot be explained by stoichiometric changes probed with XPS, but partially by changes in the energy levels probed by UPS. Apart from the  $\text{Sb}_2\text{S}_3$  itself, the energy level alignment at the heterojunction with the organic hole transport material (HTM) might be a source of loss in  $V_{oc}$  since it governs the energy that needs to be dissipated from the excited electron system.

### 6.1.3. $Sb_2S_3$ /HTM Heterojunction

An energetic offset at the  $Sb_2S_3$ /HTM heterojunction could possibly cause a serious  $V_{oc}$  limitation and reduce the built-in voltage. Consequently, I screened a variety of organic polymers and small molecules<sup>2</sup> with different HOMO levels covering a range of roughly 700 meV to test for significant trends in the solar cell performance. Example  $J$ - $V$  curves for the different HTMs, applied in the Sb-TU process and measured with the white LED inside the glovebox as light source, are shown in fig. 6.5(a,b). Both the  $V_{oc}$  and the  $J_{sc}$  of the displayed solar cells vary within a relatively limited range. P3HT is the most notable exception in terms of  $V_{oc}$ , which can be attributed to the pinholes in the absorber layer formed during the Sb-TU process as will be discussed later. The variation of the  $J_{sc}$  is partially due to the spectral mismatch of the light source. Figure 6.5(c) shows a schematic energy level diagram of the applied stack. The values for  $Sb_2S_3$  are taken from the UPS measurements of the Sb-TU process annealed at 265 °C, the  $TiO_2$  value is taken from ref. [162] and P3HT is taken as example HTM from ref. [293]. Note that the reported values for the energy of the highest occupied molecular orbital (HOMO) of the organic HTMs are typically obtained from cyclic voltammetry measurements which yield lower lying HOMO levels than UPS [294]. Additionally, the energy level alignment at a buried interface may differ substantially from the situation of an isolated material. The energy diagram has thus to be taken with care, but a large offset from the  $Sb_2S_3$  valence band to the P3HT HOMO is likely. The same data as in fig. 6.5(a,b) is included in (d) and (e), which examines the correlation between the  $V_{oc}$  and  $FF$ , respectively, to the HOMO energy of the HTM. The figures additionally include solar cells applying the small molecules IDTBR, ICBA and FBR, which have low lying HOMOs and reach low values of  $V_{oc}$  and  $FF$ , as well as  $J_{sc}$  values below 1 mAcm<sup>-2</sup> suggesting that hole extraction is inefficient for such low lying HOMOs. In the case of the low bandgap IDTBR, electrons might transfer from the  $Sb_2S_3$  to the IDTBR. Regarding the other materials, no trend in the  $V_{oc}$  or  $FF$  is observed. Note that not all deposition processes of the different HTMs were optimized, which may explain the variations of the  $FF$ . For example, decent  $FF$ s were reached with spiro [34], which is not the case in fig. 6.5. Also note that the HOMO values

---

<sup>2</sup>See appendix F for the full names of organic materials.

may vary between 0.1 eV and 0.2 eV between different reports, as is the case for P3HT [145, 293] and KP115 [147, 231]. Nevertheless, the fact that despite significant changes in the HOMO level of the HTM, no significant change in  $V_{oc}$  is observed, suggests that the  $Sb_2S_3$ /HTM interface is not limiting the device performance. The dominant recombination, at least at  $V_{oc}$ , does not take place at the interface but rather in the bulk of  $Sb_2S_3$ . An alternative explanation would be that the energetics of the HTMs at the buried heterojunction differs from the isolated materials on which the reported HOMO values are based. In the following, I focus on the two HTMs P3HT and KP115 that differ in HOMO and also show differences in the device performance in fig. 6.5(a). Additionally, the two semiconducting polymers allow high efficiencies at comparably thick layers when applied as absorbers in organic solar cells due to good transport properties [134, 231, 295]. The following study is expanded to samples from the Sb-BDC process in addition to the Sb-TU process and contains the performance-optimized solar cells fabricated in this work.

#### 6.1.4. Optimized Devices

The  $J$ - $V$  curves and solar cell performance of the best devices for the two process routes are compared in fig. 6.6(a) and tab. 6.2. The Sb-BDC process reaches higher device efficiencies compared to the Sb-TU process, mostly due to the approximately 30% higher  $J_{sc}$ , which is confirmed by  $EQE$  measurements shown in fig. 6.6(b) and (c). The higher  $J_{sc}$  in the Sb-BDC process can be explained by the thicker  $Sb_2S_3$  layer of 190 nm compared to 100 nm for the Sb-TU process. Both processes effectively did not allow a precise control over the absorber thickness. Although  $FF$  and  $V_{oc}$  do not vary as much between the processes as the  $J_{sc}$ , it is noteworthy that – despite a lower efficiency – the highest  $V_{oc}$  of 650 mV is obtained for the Sb-TU process with KP115 as HTM. As depicted in fig. 6.5, the HOMO of KP115 is better aligned with the valence band of  $Sb_2S_3$  which could be beneficial for the  $V_{oc}$  and  $FF$ . Indeed, for the Sb-TU process both values are significantly larger for the better-matching KP115. However, this is not the case for the Sb-BDC process where the  $Sb_2S_3$ /KP115 cell even shows a slightly lower  $V_{oc}$  and  $FF$  – also when compared to an  $Sb_2S_3$ /P3HT cell prepared on the same day as listed in table 6.2 and shown in fig. D.4 in appendix D. The shunt behavior caused by the pinholes in the Sb-TU

## 6. $Sb_2S_3$ Solar Cells

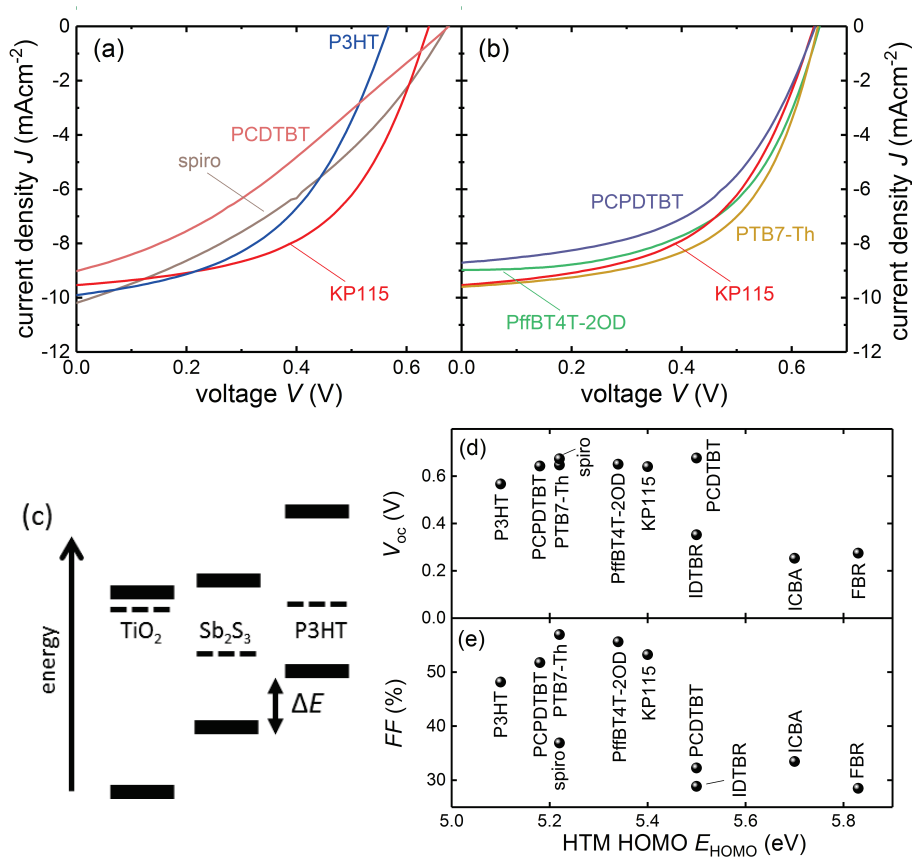


**Figure 6.5.:** (a,b) The use of different organic HTMs does not lead to a major change in  $V_{oc}$  for the Sb-TU process, maybe with the exception of P3HT. (a) displays HTMs with qualitatively different behaviour, whereas the HTMs in (b) behave similar as KP115, which is included in both panels. (c) Schematic energy diagram with energy offset  $\Delta E$  at the  $Sb_2S_3$ /HTM heterojunction. The (d)  $V_{oc}$  and (e)  $FF$  extracted from the data in (a,b) does not show any clear trends with the organic material's HOMO level (values are taken from thin-film cyclic voltammetry measurements in literature [145,194,231,266,296–301]), indicating a minor importance of the inorganic/organic interface in terms of cell performance. The  $FF$  variations might result from partially unoptimized processing conditions. The additionally included small molecules IDTBR, ICBA and FBR yield  $J_{sc} < 1\text{mAcm}^{-2}$  and do not seem to form type-II heterojunctions.

## 6.1. Layer and Device Optimization

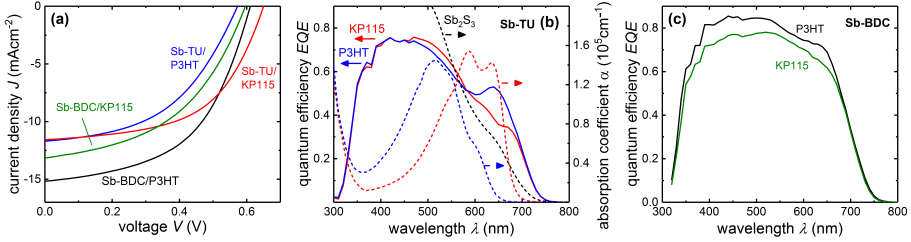


**Figure 6.6.:** Device performance of FTO/TiO<sub>2</sub>/Sb<sub>2</sub>S<sub>3</sub> /HTM/MoO<sub>x</sub>/Ag solar cells and optimized Sb<sub>2</sub>S<sub>3</sub> deposition for both process routes. The two polymers P3HT and KP115 applied for each route differ in band gap and HOMO level. (a) Sun Simulator and (b,c) *EQE* measurements of (b) Sb-TU and (c) Sb-BDC samples. The absorption coefficients of Sb<sub>2</sub>S<sub>3</sub> and the two HTMs are shown in (b) to illustrate the parasitic absorption of the HTMs.

**Table 6.2.:** Device performance of samples shown in fig. 6.6. The efficiency  $\eta_{\text{corr}}$  for the  $J_{\text{sc}}$  calculated from *EQE* is given in the last column.

Process	HTM	$V_{\text{oc}}$ (mV)	$FF$ (%)	$J_{\text{sc}}$ (mAcm <sup>-2</sup> )	$\eta$ (%)	$J_{\text{sc,EQE}}$ (mAcm <sup>-2</sup> )	$\eta_{\text{corr}}$ (%)
Sb-TU	P3HT	573	47.8	11.7	3.20	12.1	3.31
Sb-TU	KP115	650	54.8	11.6	4.13	11.7	4.16
Sb-BDC	P3HT	611	52.1	15.2	4.83	15.6	4.97
Sb-BDC	KP115	596	46.6	13.2	3.65	14.4	3.98
Sb-BDC	P3HT <sup>a</sup>	597	49.0	13.9	4.06	14.4	4.22

a: fabricated on same day as Sb-BDC/KP115 device for direct comparison, graph shown in supplement

process depends on the choice of HTM and limits  $V_{\text{oc}}$  in the case of P3HT, but not for KP115 as will be discussed in section 6.2.2. The higher  $V_{\text{oc}}$  in the Sb-TU process could then be explained by a lower recombination rate due to fewer deep defects in the material. This explanation is consistent with the negligible  $V_{\text{oc}}$  difference between different HTMs in the case of the pinhole-free layers obtained from the Sb-BDC process. The results from the Sb-BDC process support the hypothesis in the previous section, that the Sb<sub>2</sub>S<sub>3</sub>/HTM heterojunction is either not limiting to device performance or that the effective interface energetics cannot be deduced from the isolated materials.

The next paragraph is dedicated to the results of the *EQE* measurements in fig. 6.6(b) and (c). Since Sb<sub>2</sub>S<sub>3</sub> absorbs up to longer wavelengths than both polymers

## 6. $Sb_2S_3$ Solar Cells

as can be seen from fig. 6.6(b), the falling edge of the  $EQE$  can be attributed to  $Sb_2S_3$  absorption. The inflection point of the  $EQE$  yields a band gap of 1.78 eV. One drawback of using semiconducting polymers with band gaps in the visible range is parasitic absorption since most – if not all – photogenerated excitons cannot be split at a heterojunction interface. While a photocurrent contribution from the polymer was demonstrated for certain  $Sb_2S_3$  ETA cells [33] where the interface area is large and close by, polymer absorption in planar  $Sb_2S_3$  cells is to a large extent parasitic [164]. For the thinner  $Sb_2S_3$  layers from the Sb-TU process, the shape of the  $EQE$  spectra in fig. 6.6(b) differs significantly between the  $Sb_2S_3$ /P3HT and  $Sb_2S_3$ /KP115 cells for wavelengths above 500 nm. This can be explained by the polymers' different absorption spectra which are plotted together with the  $EQE$  data. P3HT has a larger band gap and absorbs only up to approximately 650 nm, while KP115 absorbs up to almost 700 nm. Organic polymers have narrow absorption bands and the absorption coefficient  $\alpha$  is not monotonous with energy as is the case for inorganic semiconductors. Therefore the larger band gap P3HT absorbs further towards short wavelengths than KP115. More specifically,  $\alpha$  is larger below 550 nm for P3HT than for KP115. Wherever the HTM absorbs weakly, the incident photons, that are not absorbed in the  $Sb_2S_3$  during their first pass, are transmitted to the metal back contact and reflected back through the HTM into the  $Sb_2S_3$  absorber where free charge carriers are generated upon absorption that contribute to the photocurrent. Altogether, the shape of the polymers' absorption spectra rationalizes the difference in the  $EQE$  spectra: The decreased parasitic absorption of P3HT at 650 nm enhances the  $EQE$  of the  $Sb_2S_3$ /P3HT solar cell at this long wavelength compared to the  $Sb_2S_3$ /KP115 cell. On the other hand, the increased parasitic absorption of P3HT at 550 nm leads to a higher  $EQE$  of the  $Sb_2S_3$ /KP115 solar cell at that wavelength. The latter difference is however less pronounced because more light with  $\lambda = 550$  nm is already absorbed during its first pass through the  $Sb_2S_3$  than the light with  $\lambda = 650$  nm. Consequently, the  $J_{sc}$  of the  $Sb_2S_3$ /P3HT cell is 4% higher than that of  $Sb_2S_3$ /KP115. For the Sb-BDC process, the  $EQE$  features are similar but less pronounced, as can be seen best from the samples prepared on the same day and shown in fig. D.4. One reason is that a thinner HTM layer (30 nm compared to 50 nm in the Sb-TU process) could be coated since the Sb-BDC route results in smoother and pinhole-free layers, whereby the amount of

parasitic absorption is decreased. Another reason is that the Sb-BDC process yields thicker  $\text{Sb}_2\text{S}_3$  layers (190 nm vs. 100 nm from the Sb-TU process) so that more light is already absorbed in the  $\text{Sb}_2\text{S}_3$  before it reaches the HTM in the first pass.

### 6.1.5. Summary and Literature Comparison

The following summarizes my findings on the optimization of planar spin-coated  $\text{Sb}_2\text{S}_3$  layers from two different precursors labeled Sb-TU and Sb-BDC. For both fabrication routes, an optimum crystallization temperature of 265°C - slightly above the minimum crystallization temperature and lower than the typically reported 300°C - was found. Depending on the process, the exact heating procedure with regard to intermediate temperature annealing or crystallization time is critical for morphology, defect density and device performance. For the Sb-TU process a drop in performance and an increase in defect density detected by PDS and supported by UPS at higher annealing temperature, cannot be traced back to changes in the Sb:S ratio or the existence of impurity phases that would be visible in XPS. For the Sb-BDC process, an under-coordinated Sb impurity phase appeared at a high annealing temperature. Some of the very recent results by the Tang group [302–305] (published simultaneously with the results presented here) and others [91, 178] support my findings on spin-coated  $\text{Sb}_2\text{S}_3$  solar cells. Well-performing cells apply an optimum crystallization temperature of 270 °C [302–304], similar to the 265 °C in this work and below the often reported 300 °C. The reports on the Sb-TU process face similar problems of dewetting [91, 178, 302, 303], which is improved by an initial vacuum annealing step at 125 °C to evaporate solvents [302, 304], similar to the slow annealing I performed. Additionally, the importance of the substrate roughness was shown [91]. The precursor ratios and resulting film composition are often off-stoichiometric [178, 302, 304], in parts because of a beneficial effect for the morphology. Nevertheless, all reports on the Sb-TU process contain pinholes in the final film, even if efficiencies >6% are reached [302, 304].

For any new process, potentially based on novel precursors, pinhole-free layers with freely tunable thickness and control over stoichiometry are desirable. Post-processing, such as sulfurization from gas [60] or liquid [20] sulfur sources might reduce the density of electronic defects in  $\text{Sb}_2\text{S}_3$  for certain deposition methods that

## 6. $Sb_2S_3$ Solar Cells

leave sulfur vacancies [33,306].

### 6.2. Limiting Factors

After the previous chapter focused on the processing conditions and optimized device configuration, this chapter concentrates on the limitations of the two precursor process routes and  $Sb_2S_3$  solar cells in general. Section 6.2.1 compares the achieved solar cell performance to other literature reports and identifies common challenges for  $Sb_2S_3$  photovoltaic technology. Section 6.2.2 applies the methodology presented in chapter 4 to assess and quantify the impact of pinholes, formed in the Sb-TU process, on the device performance. The analysis rationalizes why the Sb-TU route and the pinhole-free Sb-BDC route apply different polymers for optimum performance. Section 6.2.3 presents electroluminescence measurements (EL) on solar cells prepared via the Sb-BDC route, which allows to group the loss in open-circuit voltage into radiative and non-radiative contributions. Section 6.2.4 focuses on possible origins of the different voltage losses by mainly studying the defect density of states with different characterization methods. Finally, section 6.2.5 presents a direct measurement of the mobility-lifetime product and elaborates on the potential cause of the relatively low fill factor. To my knowledge, this is the first report of EL measurements and many other of the presented advanced characterization for  $Sb_2S_3$ .

#### 6.2.1. Performance Evaluation

My results, indicated by the stars in fig. 6.7(a) and reported in ref. [283], improved the efficiency of previously reported results [34,91,178] for both process routes of planar spin-coated  $Sb_2S_3$  solar cells (also see tab. B.3 in appendix B). Furthermore, the best efficiency of  $\approx 5\%$  reached in this thesis with the Sb-BDC process and P3HT as hole transport material, is one of the highest reported for planar  $Sb_2S_3$  devices and was, at the time when the manuscript was accepted, only outdone by fabrication via cumbersome Atomic Layer Deposition [60]. However, at almost the same time, the Tao Chen group [307] published several results [302–305] on spin-coated  $Sb_2S_3$  solar cells, some of which exceed 5% efficiency and come close to the best ETA cells, which

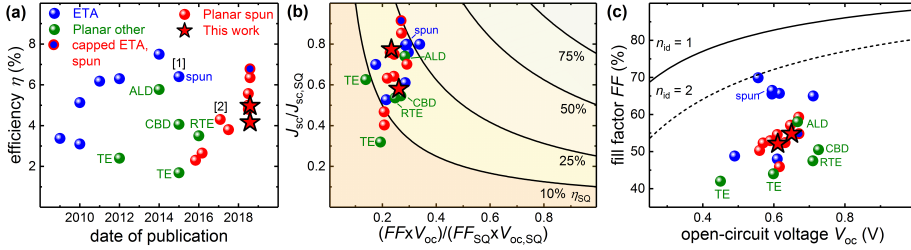


**Figure 6.7.:** (a) Development of  $\text{Sb}_2\text{S}_3$  technology. Solar cells with extremely thin absorber (ETA) architecture [20,33,80,160–162,288] reach the highest efficiencies. Planar devices have been produced via various methods such as Atomic Layer Deposition [60] (ALD), Chemical Bath Deposition [164] (CBD) and (Rapid Thermal Evaporation [167,170,286] (RTE). As the latest development, spin-coated planar solar cells reached efficiencies up to above 4% [34,90,91,178]. [1] marks the original report of the Sb-TU [33] process (ETA configuration) and [2] of the Sb-BDC [34] process. This work achieved an efficiency of 5.0% – first published in ref. [283] – which meets the simultaneously published works of the Tang group [302–304] that even reaches efficiencies above 6% (also see table B.3 in appendix B). (b) Limitations of the different approaches (same data and color code as in a) indicated by the ratio of experimental solar cell performance compared to the Shockley-Queisser (SQ) limit. High currents are realized but the  $FF \cdot V_{oc}$  product is restricted to values below 40% of the SQ limit. (c)  $FF$  data compared to the maximum obtainable  $FF$  for given experimental  $V_{oc}$  indicate that charge collection in all planar devices is imperfect, but  $V_{oc}$  losses are even more severe ( $V_{oc,SQ} = 1.49\text{V}$ ). For all data points a band gap of  $E_g = 1.78\text{eV}$ , as determined in this work, is assumed. See appendix B for the displayed values.

still constitute the best-performing  $\text{Sb}_2\text{S}_3$  solar cells.<sup>3</sup> Interestingly, the highest efficiency among these recent reports [302] employs a nanostructured ETL consisting of an array of  $\text{TiO}_2$  nanowires instead of a compact  $\text{TiO}_2$  layer. The structure nevertheless differs from the ETA configuration since the  $\text{Sb}_2\text{S}_3$  absorber completely fills up the nanowire array and even forms a capping layer – which is similar to the configuration found in the best performing perovskite solar cells [8,308,309].<sup>4</sup>

To get a first insight into the major challenges of  $\text{Sb}_2\text{S}_3$  technology, fig. 6.7(b) displays the losses relative to the Shockley-Queisser limit and fig. 6.7(c) further deconvolutes  $FF$  and  $V_{oc}$  as is done for various absorber technologies in fig. 2.3 in

<sup>3</sup>The reported efficiency of refs. [302–305] are based on  $J_{sc}$  values obtained from solar simulator measurements, which are 4 - 10% higher than the corresponding *EQE* results, which leads to 0.3% – 0.5% lower absolute efficiencies.

<sup>4</sup>It was demonstrated [33,161] that ETA cells actually employ a thin  $\text{Sb}_2\text{S}_3$  coating of the mp- $\text{TiO}_2$  nanoparticles, that does not completely fill the pores.

## 6. $Sb_2S_3$ Solar Cells

chapter 2.2. The displayed data, including the cells prepared in this thesis, paint a consistent picture. Figure 6.7(b) shows significant improvements in  $J_{sc}$ , while the  $FF \cdot V_{oc}$  product is restricted to a narrow region. Generally, high  $J_{sc}$  values can be obtained that reach up to 90% of the SQ limit, which outdoes most other emerging materials in fig. 2.3. The  $FF \times V_{oc}$  on the other hand does not exceed 40% of the SQ limit, which highlights that electronic losses are clearly more critical. Comparing different device architectures and deposition methods in fig. 6.7(c) in terms of  $FF$  and  $V_{oc}$  yields further insights. The Shockley-Queisser limit for the  $V_{oc}$  is almost 1.5 V for  $Sb_2S_3$  so that  $V_{oc}$  losses generally exceed those in the  $FF$  which are nevertheless noticeable, especially for all planar  $Sb_2S_3$  solar cells. Devices with a planar device architecture tend to have a slightly higher  $V_{oc}$  than ETA devices – except the highest reported efficiency achieved by controlling the sulfur content [20] – and spin-coating has not quite reached the  $V_{oc}$  of other deposition methods. More strikingly, ETA solar cells generally attain a significantly higher  $FF$  than planar ones, which raises the concern of charge carrier collection in  $Sb_2S_3$  solar cells. The core idea behind the ETA concept is that a thin inorganic absorber layer relaxes the requirements for electronic material quality [310, 311] since charges are quickly extracted from the absorber layer to the adjacent charge transport layers where recombination is suppressed.

While the high  $J_{sc}$  of different  $Sb_2S_3$  solar cells underlines its general suitability as a photovoltaic absorber, further improvements must tackle the deficient fill factor and low open-circuit voltage obtained for all  $Sb_2S_3$  solar cells up to date. The following chapters are dedicated to identify major loss mechanisms regarding recombination and charge carrier collection and thereby highlight critical parameters that in turn may open pathways to go beyond today's efficiency limits.

### 6.2.2. Impact of Pinholes

The influence of the observed pinholes on the performance of Sb-TU processed solar cells is estimated by applying the method presented in chapter 4 with a parameter set adapted to  $Sb_2S_3$  and the ETL/HTL combinations c-TiO<sub>2</sub>/P3HT, c-TiO<sub>2</sub>/KP115 and c-TiO<sub>2</sub>/spiro. The calculations in chapter 4 aim at a perovskite absorber that has demonstrated high performance and especially high  $V_{oc}$ . The method is however

applicable to other materials by simply adapting the parameter set of the pinhole-free device. In fact any  $J$ - $V$  characteristic can replace the ideal diode used in chapter 4, be it computed by a certain model (such as the Shockley diode equation used in chapter 4) or a dataset of current-voltage pairs. To compute a situation that is closer to  $\text{Sb}_2\text{S}_3$  solar cells fabricated from the Sb-TU process, I adapted the parameters of the ideal diode from  $J_{\text{sc,id}} = 20 \text{ mAcm}^{-2}$ ,  $n_{\text{id}} = 1$  and  $V_{\text{oc,id}} = 1.2 \text{ V}$  to  $J_{\text{sc,id}} = 13 \text{ mAcm}^{-2}$ ,  $n_{\text{id}} = 2$  and  $V_{\text{oc,id}} = 0.65 \text{ V}$ . The  $J_{\text{sc,id}}$  reflects the experimentally obtained value in tab. 6.6 (if, due to pinholes in the experimental systems, an active area loss of 10% is assumed). Even if the ideality factor of  $\text{Sb}_2\text{S}_3$  solar cells should not be 2,  $n_{\text{id}} = 2$  better reflects the observed voltage dependence of the current than  $n_{\text{id}} = 1$ , e.g. because the shape of the  $J$ - $V$  is affected by the voltage-dependence of the photocurrent (which is not covered by Shockley's diode equation used for modeling here). The  $V_{\text{oc,id}}$  value is obtained from the c-TiO<sub>2</sub>/KP115 cell in tab. 6.6. Figure 6.8(a) suggests that for the experimentally obtained  $V_{\text{oc}} = 0.65 \text{ V}$  and a pinhole area fraction of 10%, the  $V_{\text{oc}}$  of c-TiO<sub>2</sub>/KP115 is not affected by the pinholes. The calculations imply that a  $V_{\text{oc}}$  of 0.65 V would also be obtained in a pinhole-free device, which justifies the choice of  $V_{\text{oc,id}}$  for the performance calculation in fig. 6.8(b) and (c). The pinhole area fraction  $\phi$  of the optimized Sb-TU process is analyzed from the SEM image in fig. 6.1(b) to be 9.5%. At this value, no decrease in  $V_{\text{oc}}$  and  $FF$  is predicted when KP115 is used. In contrast to this, a clear loss in both parameters is expected for P3HT, although the predicted losses differ quantitatively (the predicted  $V_{\text{oc}}$  and  $FF$  losses are roughly 1/3 and 2/3, respectively, of the experimentally observed difference)

For the pinhole-free absorber layer formed in the Sb-BDC process, there is barely a difference in  $V_{\text{oc}}$  and  $FF$  between P3HT and KP115 for samples processed on the same day (see tab.6.2). Additionally, Tang et al. [304] also applied the Sb-TU process with (spin- instead of spray-coated) c-TiO<sub>2</sub>/spiro and obtained solar cell parameters that are very similar to the c-TiO<sub>2</sub>/KP115 device in tab. 6.2.<sup>5</sup> According to fig. 6.8, essentially no pinhole-related difference in performance is expected between c-TiO<sub>2</sub>/KP115 and c-TiO<sub>2</sub>/spiro. These findings support the explanation that for

---

<sup>5</sup>Tang et al. [304] obtained (for pristine  $\text{Sb}_2\text{S}_3$ , see tab. B.3 in appendix B)  $V_{\text{oc}} = 653 \text{ mV}$  and  $FF = 55.7\%$  compared to  $V_{\text{oc}} = 650 \text{ mV}$  and  $FF = 54.8\%$  for my results. The better efficiency of Tang et al. is attributed to a higher  $J_{\text{sc}}$ , probably due to the thicker absorber layer.

## 6. $Sb_2S_3$ Solar Cells

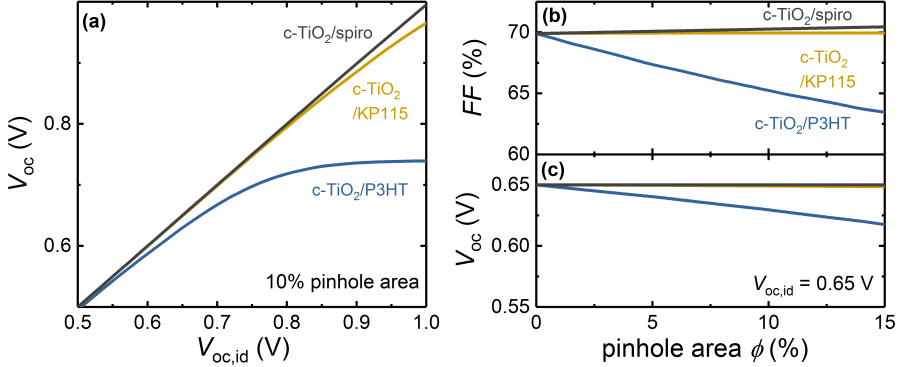


**Figure 6.8.:** Losses attributed to pinholes in the Sb-TU process applying the method presented in chapter 4. The pinhole-free device is parameterized according to the experimentally observed values by  $J_{sc,id} = 13 \text{ mAcm}^{-2}$  and  $n_{id} = 2$ . (a) The  $V_{oc}$  of c-TiO<sub>2</sub>/KP115 is unaffected by the pinholes justifying the choice of  $V_{oc,id} = 0.65$  V in (b) and (c). Here, performance deterioration is observed only for c-TiO<sub>2</sub>/P3HT

the c-TiO<sub>2</sub>/P3HT contact configuration, the lower  $V_{oc}$  and  $FF$  can be attributed at least partially to the pinholes in the Sb-TU process, while the c-TiO<sub>2</sub>/KP115 performance is – apart from the loss in active cell area – unaffected by the pinholes.

### 6.2.3. Open-Circuit Voltage Losses

Low open-circuit voltages pose a major limitation to reported  $Sb_2S_3$  solar cell performance. Before studying the distribution of defect states in detail and thereby considering possible recombination pathways, it is insightful to split the open-circuit voltage losses  $\Delta V_{oc}$  relative to the Shockley Queisser open-circuit voltage  $V_{oc,SQ}$ , into radiative ( $\Delta V_{oc,rad}$ ) and non-radiative ( $\Delta V_{oc,nr}$ ) losses. In order to determine these losses, the solar cell is operated as an LED, meaning that a current is injected in forward direction, and the light emission from the solar cell (electroluminescence, EL) is recorded. The EL signal is converted into an  $EQE$  signal via the reciprocity theorem in eq. 3.13 [207], which allows the calculation of the radiative open-circuit voltage  $V_{oc,rad}$  (see appendix A.3 for the calculations). Figure 6.9(a) shows the results for a solar cell fabricated from the Sb-BDC route with P3HT as HTM. Another cell with KP115 as HTM yields very similar results as can be seen from fig. D.5 in

appendix D. In both cases, light emission was detectable only for relatively high injection currents above  $1 \text{ A cm}^{-2}$  and the signal for both samples is quite noisy. The quantum efficiency spectrum  $Q_{e,EL}$  in fig. 6.9(a) obtained from the EL signal via the reciprocity theorem [207] matches the *EQE* data well. Because of the weak emission signal, the background noise dominates the contributions to  $V_{oc,rad}$  as is shown in fig. D.5(c) in appendix D. I therefore chose to cut-off the data at 1.4 eV to avoid underestimating  $V_{oc,rad}$ .<sup>6</sup> The analysis yields a radiative voltage loss of about 100 mV and a non-radiative voltage loss of almost 800 mV, which leads to a very low LED quantum efficiency  $Q_{LED}$ . While both losses are significant, the non-radiative one is clearly more critical to device performance. Possible origins of the non-radiative loss are discussed based on the sub-bandgap defect density of states in the following section. The  $\Delta V_{oc,rad}$  is measured relative to the Shockley-Queisser  $V_{oc,SQ}$  which is based on a single value for the absorber band gap as described in appendix A.4. A difference between  $V_{oc,rad}$  and  $V_{oc,SQ}$  arises when photon emission happens from lower energy states than photon absorption, or put into different terms: from the fact that the absorption edge of a real solar cell is not a step function as is assumed in the Shockley-Queisser limit. Here, the band tails at the band edge are of particular importance. The reduced density of states of the tails compared to the DOS above the band edge only leads to weak absorption, but at the same time charge carriers preferably occupy these lower energy states and recombine from there, leading to a mismatch between absorption and emission spectrum, which is expressed by the radiative voltage loss [312]. The band tails of  $\text{Sb}_2\text{S}_3$  are also analyzed in the next section. Figure 6.9(b) compares the solar cell EL and  $\text{Sb}_2\text{S}_3$  photoluminescence (PL) emission along with the absorbance of the pure material film. The small shift of the EL compared to the PL signal hints towards additional recombination happening at the  $\text{Sb}_2\text{S}_3/\text{P3HT}$  interface. However, the EL spectra of solar cells based on  $\text{Sb}_2\text{S}_3/\text{P3HT}$  and  $\text{Sb}_2\text{S}_3/\text{KP115}$  are very similar as asserted in fig. D.5 in appendix D, meaning that the disputed surface recombination cannot be easily tuned by changing the HTM.

Note that there is also a voltage loss arising from a  $J_{sc}$  that is lower than the Shockley-Queisser value, which is however negligible in many cases, since both

---

<sup>6</sup>If the complete spectrum is taken into account, an approximately 35 mV lower  $V_{oc,rad}$  results.

## 6. $Sb_2S_3$ Solar Cells

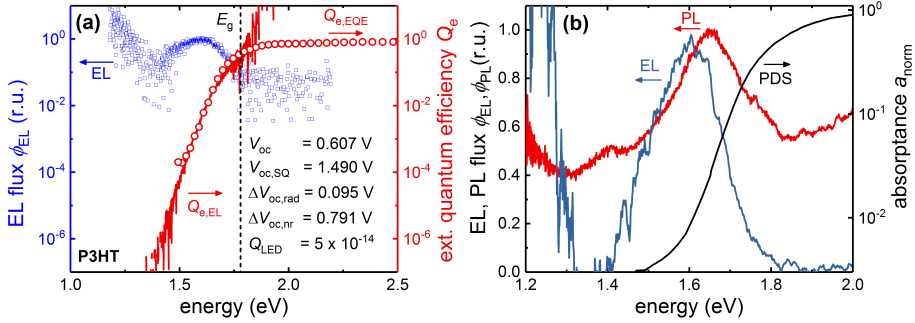


**Figure 6.9.:** Voltage loss analysis according to Rau [207] for a  $Sb_2S_3$ /P3HT solar cell produced from the Sb-BDC process. (a) The voltage losses are given in the figure and show a large non-radiative loss, as well as a considerable radiative loss. The band gap of  $E_g = 1.78$  eV, used to calculate the Shockley-Queisser limit, is indicated. (b) The EL spectrum is slightly shifted compared to the PL spectrum (measured at room temperature), suggesting losses from surface recombination. The losses cannot be tuned by applying another polymer (see fig. D.5(b) in appendix D). Note the linear scale for the emission signal in (b) as opposed to the logarithmic scale in (a).

values are on the same order of magnitude. For  $J_{sc} = 0.8 \times J_{sc,SQ}$ , which is the rough value obtained for the Sb-BDC process, the voltage loss equals less than 6 mV and even for relatively low currents of  $J_{sc} = 0.6 \times J_{sc,SQ}$  the loss is only 13 mV, which is dwarfed by the radiative and non-radiative loss. Compared to other PV technologies, the measured radiative loss of about 100 mV is smaller than that of most polymer:fullerene systems but similar to certain polymer:NFA systems [110, 313]. Considering other inorganic thin-film absorber materials, the loss is somewhat lower than for a-Si [61] ( $\approx 125$  mV) but larger than perovskites, CdTe and CIGS that all show losses below 40 mV [61].

### 6.2.4. Defect Density of States

The density of states (DOS) is probed with different methods in fig. 6.10 for both studied process routes. Photothermal deflection spectroscopy (PDS) exclusively probes the absorption of  $Sb_2S_3$  deposited on a glass substrate, whose absorption becomes dominant below 1.5 eV in fig. 6.10(a) and (b), which explains the signal saturation regime that does not contain information on the  $Sb_2S_3$  absorber material.

The constant photocurrent measurement (CPM) also probes the  $\text{Sb}_2\text{S}_3$  deposited on a glass substrate, but since the photocurrent is measured (or rather the illumination level that is required to sustain a certain photocurrent), optical and electrical properties are convoluted. Specifically, the photocurrent of both carrier types contribute to the signal. Since the substrate is non-conductive, parasitic substrate absorption does not affect the measurement and the signal range of the CPM in fig. 6.10(b) is larger than for PDS. Finally, Fourier transform photocurrent spectroscopy (FTPS) measures the photocurrent of the full solar cell made up only by the minority charge carrier species, which explains the absolute difference to the CPM. The  $\text{Sb}_2\text{S}_3$  obtained from both process routes both show two regions with elevated DOS below the bands. The band tails at the band edge are a common feature of non-crystalline materials and are observable with all three characterization techniques. For the Sb-TU sample, CPM and FTPS measurements show a second exponential DOS below roughly 1.55 eV, which is not observed with PDS because of the lower dynamic range. The  $\text{Sb}_2\text{S}_3$  formed by the Sb-BDC route shows an even more elevated DOS in the regime below 1.55 eV that could result from a superposition of an exponential DOS as found for Sb-TU and a distribution of defects around roughly 1.2 eV. To further quantify the DOS, the characteristic energies are extracted in fig. 6.10(c) and (d) from the slopes in fig. 6.10(a) and (b). The characteristic energy of the tail at the band edge obtained from FTPS yields almost the same value of  $E_{\text{ch}} = 23 \text{ meV}$  for both processes. The corresponding values from PDS and CPM measurements are slightly higher and about 30 meV for Sb-TU and 35 meV for Sb-BDC. The difference between the measurements is likely caused by the different transition regimes and that the slope has not reached a constant value, since no clear plateaus are observed in fig. 6.10(c) and (d). For the Sb-TU process in fig. 6.10(c), the second exponential DOS regime is characterized by a much higher  $E_{\text{ch}} \approx 100 \text{ meV}$  for FTPS measurements. Since Sb-BDC does not show an exponential DOS in this regime as can be seen from fig. 6.10(b), the DOS is not characterized by a second characteristic energy.

To further investigate the defect structure of  $\text{Sb}_2\text{S}_3$ , room and low temperature photoluminescence (PL) measurements were carried out and are presented in fig 6.11. Just as for EL measurements, the light emission was relatively weak. Depending on the energy, substrate emission dominates the spectra, especially for the

## 6. $Sb_2S_3$ Solar Cells

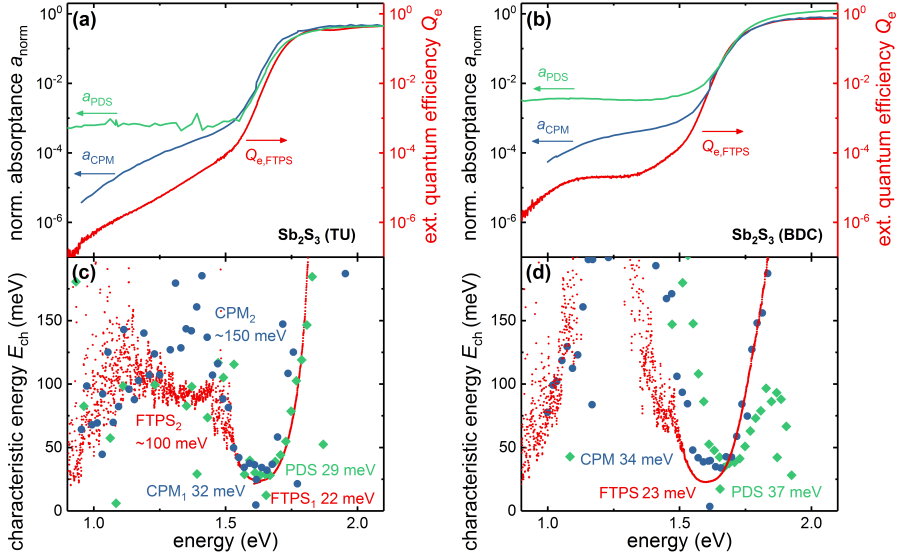


**Figure 6.10.:** Density of states (DOS) probed with photothermal deflection spectroscopy (green), constant photocurrent measurement (blue) and Fourier transform photocurrent spectroscopy. PDS and CPM is measured on layers of  $Sb_2S_3$  and FTPS is measured on full solar cells – applying KP115 as HTM – produced from (a,c) the Sb-TU and (b,d) the Sb-BDC process. Substrate absorption limits the dynamic range of PDS, while the difference between CPM and FTPS results from the fact that both charge carrier species contribute to the photocurrent for CPM, while only one carrier species governs the FTPS signal. (a,b) show the original data with the PDS and CPM data normalized to the FTPS data, which are in turn scaled to  $EQE$  measurements. The exponential tails are characterized by the characteristic energy in (c,d), that is obtained from the pointwise derivative of the data in (a,b). In addition to the tail at the band edge, another exponentially distributed DOS is observed for Sb-TU in (a), resulting in a second plateau with high characteristic energy in (c). For Sb-BDC in (b), a similar DOS seems apparent but is superimposed by a non-exponential DOS. The elevated density of defect state is likely to impede high  $V_{oc}$  values and the difference between the two processes may explain the higher  $V_{oc}$  obtained for the Sb-TU process.

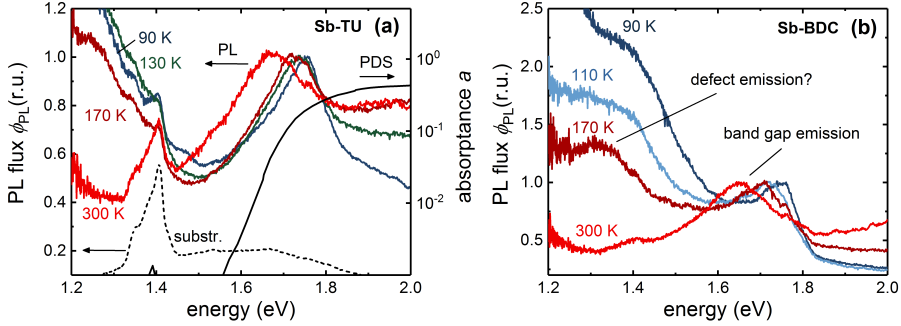


**Figure 6.11.:** Temperature dependent photoluminescence measurements for  $\text{Sb}_2\text{S}_3$  layers deposited via (a) the Sb-TU and (b) the Sb-BDC process. The PL signals are generally weak and a different, rough glass substrate with strong emission at 1.4 eV had to be used for Sb-TU in (a). The band gap emissions are as expected blue-shifted for the low-temperature spectra (red) due to an increased band gap with low temperatures. While the band gap emission is similar for both process (also see fig. D.6 in appendix D), defect emission seems discernible for the Sb-BDC process.

Sb-TU process which could only be deposited on a rough glass substrate that has a distinct emission peak at 1.4 eV in fig 6.11(a). The increase in PL peak energy with decreasing temperature is expected since the band gap of semiconductors increases at lower temperatures. The low temperature measurements of the Sb-BDC in fig 6.11(b) seems to show luminescence at roughly 1.3 eV which coincides with the feature observed in FTPLS measurements and could be attributed to photon emission from defects. However, the low signal strengths in all measurements make it hard to clearly identify emission bands and reliably detect differences between the two process routes. A direct comparison of the band edge emission for the two processes is shown in fig. D.6 in appendix D.

In the following, I put my findings in context of other literature results. Similar features of two exponentially distributed DOS were observed for the structurally similar material  $\text{Sb}_2\text{Se}_3$  [314]. Tumelero et al. [306] calculated the position of intrinsic defects such as vacancies and antisites with density functional theory (DFT) and found that several of the investigated defects are located around the middle of the bandgap. The highly intrinsic nature of  $\text{Sb}_2\text{S}_3$  discussed in section 6.1.2 could be a result of defect compensation, meaning that the existence of (possibly different)  $n$ - and/or  $p$ -type defects pin the Fermi level close to the middle of the band gap. For

## 6. $Sb_2S_3$ Solar Cells

efficient solar cells, the band gap should contain as few electronic states as possible since these may act as deep traps and facilitate non-radiative recombination. Therefore, the observed defect DOS that reaches down to the middle of the band gap, as well as the band tails at the band edge are likely to facilitate non-radiative recombination and limit the open-circuit voltage of the investigated  $Sb_2S_3$  devices. The band tails at the band edge rationalize the radiative losses found in section 6.2.3, while the non-radiative losses are likely to stem from the midgap defects, although the band tail could also facilitate non-radiative recombination. Finally, the enhanced defect DOS around midgap of the Sb-BDC process compared to the Sb-TU process, may explain the lower  $V_{oc}$  obtained from the Sb-BDC process. As other reports obtain similar  $V_{oc}$  values, the results of this thesis seem to be significant for all solar cells based on  $Sb_2S_3$ .

### 6.2.5. Charge Carrier Collection

The  $(\mu\tau)$ -product is the crucial material property that governs charge carrier collection in a solar cell and is directly accessible from constant photocurrent measurements (CPM). The absorptance obtained from a PDS measurement on the same sample allows to deconvolute the electronic and optical information contained in the CPM data in fig. 6.10. The  $(\mu\tau)$ -product is obtained according to equation 3.12 in section 3.3. The CPM study was performed for both process routes and yields similar  $(\mu\tau)$ -products on the order of several  $10^{-8} \text{ cm}^2/\text{V}$ , which corresponds to diffusion lengths of several 100 nm, with the precise values given in table. 6.3. Assuming that diffusion processes govern the charge transport and taking the resulting  $Sb_2S_3$  thickness from the respective processes into account, charge collection may not reach 100% as can be seen from table 6.3. However, the inefficient carrier collection would decrease the  $J_{sc}$ , but diffusive transport cannot explain the experimentally obtained low  $FF$ s of 50%-60%, which indicate a significant dependence of the photocurrent on the applied voltage. However, the applied layer stack intends to generate an electric field across the  $Sb_2S_3$  layer so that charge transport is governed by drift rather than diffusion, because of the significant longer transport length for drift evident from table 6.3. For a built-in voltage of 1 V, which is clearly below the limit for the  $V_{bi}$  set by the band gap of  $Sb_2S_3$ , the drift length exceeds 10  $\mu\text{m}$  and charge carrier

**Table 6.3.:** The constant photocurrent measurements (CPM) yield mobility-lifetime ( $\mu\tau$ )-products on the same order of magnitude for both precursor process routes. The corresponding length scales  $L_{\text{dif/dr}}$  and collection efficiencies ( $f_{\text{c,dif/dr}}$ ) are calculated according to the expressions in section 2.3.4 and contradict to the values of the  $FF$  obtained in devices, which is further analyzed in terms of the electronic quality factor ( $Q_{\text{SRH}}$ ) of chapter 5.1.

Prec.	$d$ nm	$(\mu\tau)_{\text{CPM}}$ $\text{cm}^2\text{V}^{-1}$	$L_{\text{dif}}$ nm	$f_{\text{c,dif}}$ %	$L_{\text{dr}}(0.1\text{V})$ nm	$f_{\text{c,dr}}$ %	$FF_{\text{n}}$	$Q_{\text{SRH}}$ $\text{cm}^4\text{V}^{-2}\text{s}^{-0.4}$
TU	100	$6 \times 10^{-8}$	390	88	6000	99	0.05	$1.0 \times 10^{-17}$
BDC	190	$2 \times 10^{-8}$	230	68	1050	91	-0.03	$1.0 \times 10^{-16}$

collection would be uncritical. While a  $V_{\text{bi}} = 1\text{V}$  roughly reflects conditions at short-circuit, the electric field at the *MPP* is certainly lower. However, for  $V_{\text{bi}} = 0.1\text{V}$ , the drift length still exceeds  $1\ \mu\text{m}$ , which would guarantee efficient charge collection even at the *MPP* and therefore a high  $FF$ . There seems to be a contradiction between the experimental results of a relatively high ( $\mu\tau$ )-product and the low  $FF$ s obtained for the fabricated solar cells.

To get further insight into the contradictory results regarding charge carrier collection, I performed drift-diffusion simulations and studied the influence of the band tails and defect distributions that were observed in CPM and FTPS measurements in fig. 6.10. The modeled system consists of a  $\text{Sb}_2\text{S}_3/\text{P3HT}$  heterojunction and a thin interfacial recombination layer. Appendix D shows the resulting band diagram in fig. D.7 and gives the model parameters in table D.2. The band diagram includes a large energetic offset at the heterojunction, which is justified by the literature reports and the UPS measurements in section 6.1.2. As discussed before, the actual energy alignment at the heterojunction is not fully understood at the moment and may not be predicted properly from the characterization of the isolated layers. The calculated band diagram also shows an enhanced electric field (steeper slope of the bands) in the P3HT compared to the  $\text{Sb}_2\text{S}_3$ , which result from the lower dielectric constant of organic materials compared to inorganic ones. The simulation parameters are extracted from literature or are based on material and device characterization performed in this thesis. Most importantly, for the given energy level diagram, the SRH lifetime  $\tau = 5 \times 10^{-8}\text{s}$  is chosen so that the simulations yield a  $V_{\text{oc}}$  close to the experimentally obtained values. Then the mobility is calculated

## 6. $Sb_2S_3$ Solar Cells

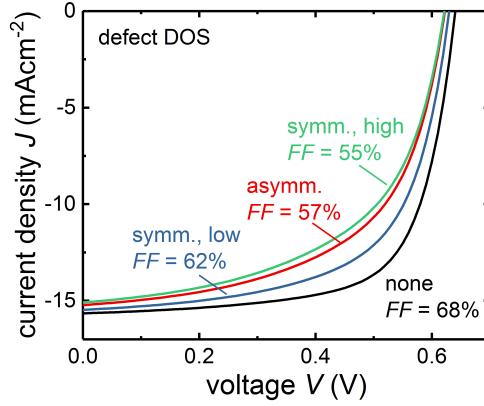


**Figure 6.12.:** Drift-diffusion simulation on the qualitative influence of the low-energy defect state distribution observed in fig. 6.10 on charge carrier collection, where the difference between CPM and FTSP measurements indicate a different trap distribution – referred to as asymmetric here – close to the valence and conduction band. There is a clear difference in  $FF$  between simulations without traps (black), equal trap density of states (DOS) for valence and conduction band (blue) and asymmetric trap DOS (red). The latter reflects the experimentally observed trap DOS. Equal, but high trap density barely decrease the  $FF$  further, indicating that the trapping from the higher defect DOS limits charge transport.

from the experimentally obtained  $(\mu\tau)$ -product to  $\mu = 0.4\text{cm}^2(\text{Vs})^{-1}$ . Both values are not untypical for inorganic semiconductors. In the absence of any additional defect distribution the simulated  $J$ - $V$  curve in fig. 6.12 is relatively rectifying. The  $FF = 68\%$  is close to the theoretical maximum (see e.g. fig. 6.7(c)) for the given  $V_{oc}$  and an ideality factor of  $n_{id} = 2$ , which results from SRH recombination.

Next, the defect distribution at lower energies observed for both process routes in fig. 6.10 is included in the simulations. For simplicity, the exponential tail-like defect distribution observed for the Sb-TU process in fig. 6.10(a) is considered to parameterize the defect distribution in the simulations. Here, the difference between the DOS observed with CPM and FTSP is crucial. For CPM, electron and hole transport contribute to the photocurrent so that both the valence and conduction band states are reflected in the CPM data. For FTSP, one charge carrier type limits the photocurrent, so that only the VB or CB states are reflected in the FTSP data. It

cannot be concluded whether VB or CB states are observed, which is not important for the discussion here. For the simulations in fig. 6.12, the parametrization of the 'high' defects DOS is taken from the CPM data and the 'low' defect DOS is taken from the FTPS data. When including a symmetric, low defect DOS (referring to  $E_{\text{ch}} = 100 \text{ meV}$ ), the  $FF$  drops to 62% because multiple trapping processes slow down the effective mobility. When an asymmetric defect DOS (referring to  $E_{\text{ch}} = 100 \text{ meV}$  for one band and  $E_{\text{ch}} = 150 \text{ meV}$  for the other band) the  $FF$  experiences another significant drop to 57%, which is close to the experimentally observed value. When both defect DOS are high, the  $FF$  only changes slightly.

In summary, the exponential defect DOS at low energies reduces the efficiency of charge carrier collection. A dominant influence of the higher defect DOS on the  $FF$  was demonstrated, which may explain the discrepancy between the value of the relatively high  $(\mu\tau)$ -product extracted from CPM and the inefficient charge carrier collection in the solar cell. The low  $FF$  is likely to result from a combination of a low  $V_{\text{oc}}$ , possibly an ideality factor given by SRH recombination, and a reduced effective mobility resulting from multiple trapping processes caused by the enhanced defect DOS that is also likely to limit the  $V_{\text{oc}}$  as discussed in the previous section. For the best performing solar cells of each process route given in table 6.2, I calculated the electronic quality factor assuming Shockley-Read-Hall recombination and a dielectric constant of  $\epsilon_r = 10$  which roughly matches that of  $\text{Sb}_2\text{S}_3$  [315] (although different values are reported due to the material's anisotropy [316]). The results in table 6.3 are a normalized fill factor ( $FF_n$ ) close to zero, meaning the devices are located in the very middle of the S-shaped curves presented in chapter 5.1 (the  $FF_n$  covers values from -1 to 1). The electronic quality factor is in the range of those organic solar cells that have rather low electronic qualities (see table B.2 in appendix B for reference). The intrinsic nature of  $\text{Sb}_2\text{S}_3$  implies a fully depleted absorber layer, which makes the analysis method generally feasible. However, the lateral inhomogeneity obtained from the Sb-TU process might limit the applicability of the analysis. More insights on the compliance with the model could be gained from preparing a series of devices with varying active layer thickness, which was however not possible in a controlled manner for both process routes.

### 6.3. Chapter Summary and outlook

The findings presented in this thesis contribute to the technological advance of planar, spin-coated  $Sb_2S_3$  solar cells by optimizing the fabrication of two process routes based on different  $Sb_2S_3$  precursors, namely Sb-TU and Sb-BDC. Eventually, solar cell efficiencies up to 5.0% are achieved which meets the latest reports from literature. Furthermore, a good understanding of the limiting factors for  $Sb_2S_3$  solar cells is obtained along with characterization methods that are suitable to investigate these factors, both of which paves the way for continuous and structured progress in the field.

Specifically, I found improved annealing conditions for the  $Sb_2S_3$  absorber layer and could correlate the device performance to the morphology and existence of defect states in the band gap. No clear variation in the film stoichiometry was found in XPS measurements, except for the appearance of under-coordinated Sb in the Sb-BDC process for an elevated annealing temperature. The two precursor routes reached the highest performance for a different choice of polymeric HTM. The significant difference in open-circuit voltage ( $V_{oc}$ ) and fill factor ( $FF$ ) could be traced back to the detrimental influence of pinholes in the Sb-TU for a certain choice of HTM. Apart from this, and contrary to the case of ETA solar cells discussed in chapter 2.4.2, different HTMs did not improve the performance or lead to major changes in the  $V_{oc}$ , although the energy level alignment at the heterojunction should vary by several 100 meV judged by reported energy level measurements on the isolated organic materials.

This finding suggests that the planar devices are limited by the  $Sb_2S_3$  absorber itself rather than an unfavorable layer stack.  $EQE$  measurements show that parasitic absorption varies for different HTMs and is more pronounced for polymers with a band gap closer to that of  $Sb_2S_3$ , for thinner layers of  $Sb_2S_3$  and for thicker polymer layers. Altogether, the Sb-BDC process reaches higher efficiencies than the Sb-TU process, which results from a higher short-circuit current that overcompensates the slightly lower  $V_{oc}$ . The gain in  $J_{sc}$  mainly stems from a thicker absorber layer obtained from the Sb-BDC process. The lower  $V_{oc}$  obtained from the Sb-BDC process goes along with a higher density of midgap defect states.

Major performance deficits of the cells produced in this thesis are the low  $V_{oc}$ , which is in line with all other literature reports on  $Sb_2S_3$  solar cells, as well as a reduced  $FF$ , which also applies to all reported planar  $Sb_2S_3$  solar cells. The considerable  $J_{sc}$  obtained in this and other works underlines the general feasibility of  $Sb_2S_3$  as an absorber material, also when embedded in a planar device architecture, in the sense that a significant amount of incoming photons are absorbed and most of the generated free charge carriers are collected at short-circuit conditions. Taking a closer look at the observed  $V_{oc}$  loss with EL measurements, I found major non-radiative recombination losses, but also considerable radiative losses. I attribute the latter one to the tails at the band edge, whose characteristic energies lies between that of a-Si and CdTe or CIGS. The large non-radiative losses coincide with a high defect density of states that reaches down to the middle of the band gap and is even enhanced for the Sb-BDC process route. Regarding charge carrier collection, the intrinsic nature of  $Sb_2S_3$  leads to a fully depleted absorber layer with homogeneous electric field, which implies that charge transport is governed by drift, which is favorable for charge carrier collection. However, the electric field in the  $Sb_2S_3$  is probably reduced because of the heterojunction with the polymer, which has a low dielectric constant and considerable energetic offset to the valence band of  $Sb_2S_3$ . Although the  $(\mu\tau)$ -product determined by CPM measurements should make charge carrier collection efficient, the observed  $FF$  stays short of its potential. Drift-diffusion simulations reflecting the defect DOS of  $Sb_2S_3$  suggest that the high midgap DOS, which is in addition asymmetric for the conduction and valence band, is not only responsible for the low  $V_{oc}$  but also for the reduced  $FF$ , since the trapping of charge carriers leads to a reduction of the effective mobility.

The electroluminescence, constant photocurrent and Fourier transform photoelectron spectroscopy measurements are, to my knowledge, the first ones reported for  $Sb_2S_3$ . The findings of this thesis are likely to apply to other  $Sb_2S_3$  solar cells, because similar features of the overall device performance are obtained for both precursor routes, as well as other reported deposition routes such as CBD or ALD. Additionally, certain properties of  $Sb_2S_3$  found in this work were reported elsewhere for different deposition routes. This includes the intrinsic nature of  $Sb_2S_3$  [60, 170, 179–183], the value of the band tail slope [176] and the  $(\mu\tau)$ -product probed by steady-state photocarrier grating method [317]. Moreover, a comprehen-

## 6. $Sb_2S_3$ Solar Cells

sive report [314] on  $Sb_2Se_3$  shares some of the observed features, indicating that this class of structurally similar  $X_2Y_3$  metal-chalcogenides behave similarly.

Currently, the non-radiative recombination loss poses the largest limitation to  $Sb_2S_3$  solar cells. An important step forward is the detailed experimental study of the defect physics of  $Sb_2S_3$  and the identification of sources for critical electronic defects, such as the low-energy tail-like defect distribution reported herein. This thesis showed that FTPS is sensitive enough to detect relevant changes in the DOS around midgap. A more detailed characterization of the defects may be obtained from electron spin resonance [318] or deep level transient spectroscopy [20, 319] where the latter yields the capture cross-section of a defect. While no major stoichiometric variations could be associated with the increase of defect density in this work, impurity phases and precursor residues may be critical even in very low (or diluted) concentrations. From an experimental point of view, characterization methods with higher sensitivity than XPS may be needed such as secondary ion mass spectroscopy [320] (SIMS), which proved useful in the context of other solar cell technologies. Other sources for electronic defects are intrinsic defects that may not necessarily affect the stoichiometry, such as interstitials, antisites or an equal number of sulfur and antimony vacancies that compensate each other. Tumelero et al. [306] provided insight to this topic via DFT simulation of intrinsic defects in  $Sb_2S_3$ . If the non-radiative loss path could be heavily reduced in a more mature state of the technology by superior process control that enables the suppression of midgap defects, the radiative loss will become relevant. The reduction of the radiative loss eventually requires a system with less energetic disorder and therefore steeper band tails. On the long term, a good understanding of the origins of the energetic disorder is needed. The characterization methods PDS, CPM or FTPS are all suitable for this purpose. In a next step, the correlation of the energetic disorder to the structural disorder in the films is a promising approach. Meaningful technological progress obviously does not stop at characterizing the defect and tail distributions, but requires to effectively control and eliminate the discussed shortcomings by finding suitable deposition, annealing and possibly post-treatment conditions. Regarding solution-based deposition, this work showed that for otherwise similarly processed samples, the choice of precursor is crucial for the resulting film morphology and device efficiency. Complex chemistry offers versatile options for the design of new precursors

### 6.3. Chapter Summary and outlook

that could further enhance the efficiency of solution processed  $\text{Sb}_2\text{S}_3$ . Vacuum-based evaporation deposition, which is commonly used for  $\text{Sb}_2\text{Se}_3$  solar cells [23], may be a valuable alternative to solution-based processing, but has not reached comparable efficiencies yet [170]. However, evaporation approaches might allow to exploit the anisotropic nature of  $\text{Sb}_2\text{S}_3$  by aligning the 1D ribbons with the direction of charge transport between the contacts. A beneficial effect was demonstrated for the structural identical  $\text{Sb}_2\text{Se}_3$  [23]. A proper substrate choice or embedding a seed layer might be another key to directed growth in  $\text{Sb}_2\text{S}_3$ .



## 7. Conclusion and Outlook

This thesis demonstrated how non-linear shunts from pinholes in the absorber layer affect the solar cell performance and how different material and device properties – above all the electronic quality – affect the fill factor of thin film solar cells. The presented methodology to evaluate the impact of pinholes based on the choice of contact layers, allows to identify combinations of electron and hole transport layers that are highly robust against shunting from pinholes and essentially prevent performance deterioration. Developed in the context of a thorough study of the fill factor, the methodology to extract the herein defined electronic quality factor from basic solar cell characterization allows to identify absorber materials or organic absorber blends with superior charge carrier collection properties. The two conceptual studies on the inhomogeneity and electronic quality of thin-film solar cell absorbers are valuable in light of recent experimental research efforts. Since many different absorber materials and contact configurations are explored currently, there is a demand for evaluation methods that allow to compare different materials, approaches and technologies. Additionally, the fabrication of solution-processed, spin-coated, planar  $\text{Sb}_2\text{S}_3$  solar cells yielded optimized processing conditions and comparably high solar cell efficiencies. More importantly, the major limitations of the technology could be identified and characterization methods to study the critical parameters were found, which provides a solid base for continuous improvements in the field.

Lateral inhomogeneity is, as an intrinsic feature of thin-film solar cells, relevant for novel absorber materials, as well as established technologies with upscaled industrial production. The presented study found that the choice of a specific combination of electron and hole transport layers determines whether pinholes in the absorber layer have a detrimental impact on the open-circuit voltage and fill factor – and thus the efficiency – of the solar cell. Experimental data showed that the shunt currents at a pinhole are non-linear (diode-like) for all tested contact layer combina-

## 7. Conclusion and Outlook

tions. However, the detailed current-voltage characteristic heavily depends on the specific interface formed by the electron and hole transport material at a pinhole. As a consequence, contact layer combinations with large and others with virtually no impact on the solar cell performance were found, meaning that the robustness against shunts from pinholes is a critical parameter in the choice of a proper contact configuration. In a more general sense, the study demonstrated that the contact layers in thin-film solar cells should not only be optimized with respect to the ideal situation where a homogeneous absorber layers covers the entire substrate. Instead, the optimization of contacts must also account for a realistic film morphology which includes structural and electrical inhomogeneity such as pinholes. Future research and production efforts must therefore produce refined contact configurations that offer a high tolerance against electrical shunting from pinholes.

The comprehensive study of charge carrier collection in thin-film solar cells via drift-diffusion simulations demonstrated a close correlation between the (normalized) fill factor and the herein defined and optimized collection coefficient. The high precision of the model allows to extract information on the electronic material quality, composed by mobility and recombination coefficient, or lifetime, from the fill factor and other basic solar characterization. Additionally, the preparation of a series of devices with varying active layer thickness allows to identify deviations from the model assumptions, which then allows to judge whether the model is applicable or not. The study illustrates the corresponding signatures of a space-charge region originating from doping or asymmetric mobilities, as well as limitations by the contacts related to contact resistance or surface recombination. The study proved especially useful in the field of organic solar cells, where charge carrier collection is one of the main obstacles for higher efficiencies. The low mobilities found in molecular materials results in mediocre fill factors and low optimum absorber thicknesses so that the incoming photon flux is only partially absorbed. However, the versatility in the design of organic compounds brought up exceptional materials where charge collection is relatively efficient. This thesis quantified the difference between a range of materials reported in literature by the electronic quality factor, which in combination with the energy level matching, gives a coherent interpretation of the historical progress of organic solar cell efficiency. Furthermore, the electronic quality of non-fullerene based blends has a major impact on whether congruent or

complimentary absorption bands of the constituting donor and acceptor materials are advantageous for the solar cell performance. Finally, by taking the absorption strength as a third parameter in addition to mobility and lifetime (or recombination coefficient) into account and applying a methodology similar to the fill factor study, a route to improve the efficiency in the presence of limited electronic qualities was found to lie in the enhancement of the absorption coefficient. Future progress in the field of organic solar cells is likely to result from the synthesis of novel materials, which need to combine low voltage losses with superior electronic quality and/or enhanced absorption, which has not been realized so far. In particular, organic blends with high electronic quality will allow to fabricate solar cells with thick active layers and high fill factors, which absorb the majority of incoming photons and efficiently collect the photogenerated charge carriers.

The fabrication of spin-coated planar  $\text{Sb}_2\text{S}_3$  solar cells lead to good solar cell performance for two processing routes based on different precursors. A detailed annealing study provided technological progress in the form of optimized processing parameters. The choice of hole transport material – which brought major improvements for  $\text{Sb}_2\text{S}_3$  in an extremely thin absorber architecture – was found to be rather uncritical for the fabricated planar devices. The highest achieved efficiency of 5.0% is comparable to the best results reported in literature. Like all other planar  $\text{Sb}_2\text{S}_3$  solar cell, the fabricated devices suffer from low open-circuit voltages and reduced fill factors, which prompted the study of the underlying loss mechanisms. By applying the methodology developed in this work, the detrimental impact of pinholes was found to be discarded if a proper polymer is chosen as hole transport material. For optimized devices, considerable radiative losses were observed, but larger non-radiative voltage losses were found to be the major limitation for solar cell performance. The observed high density of defects in the middle of the band gap is likely to provide efficient pathways for non-radiative recombination. The difference in defect density between the two processes correlates with the open-circuit voltage. As drift-diffusion simulations indicate, the elevated defect density of states is likely to also limit the fill factor of the solar cells by temporarily trapping free charges.

The analysis of losses in terms of open-circuit voltage and fill factor is largely unprecedented for  $\text{Sb}_2\text{S}_3$  and yielded a consistent interpretation where losses in

## 7. Conclusion and Outlook

both parameters are attributed to the elevated density of states in the middle of the band gap. Thereby, the major limitations of today's  $\text{Sb}_2\text{S}_3$  technology were identified and essential research questions were deduced. With respect to future work, suitable characterization techniques were highlighted to probe the critical material parameters with respect to the solar cell performance. Further advance requires detailed insight into the defect physics of  $\text{Sb}_2\text{S}_3$  in order to identify sources for the enhanced defect density of states observed in this work, as well as processing routes that avoid such losses. In a long term perspective, not only the control over midgap electronic defects will be crucial, but also the control over structural and energetic disorder reported in this work. An intriguing potential of the technology is to make use of the material's anisotropy and align the 1D ribbon-like crystal structure in direction of charge transport in the solar cell, which should facilitate charge carrier collection. The anisotropic crystal structure in combination with the polycrystalline nature of  $\text{Sb}_2\text{S}_3$  films bears interesting device physics in itself. Inhomogeneous transport properties across the device lead to regions where charge carrier collection is much more efficient than in others. The effect of this phenomenon on the solar cell performance is largely unexplored, mostly because few non-cubic absorber materials have been in the focus of photovoltaic research.

# Bibliography

- [1] I. Fraunhofer Institute for Solar Energy Systems. Photovoltaics report. [Online]. Available: <https://www.ise.fraunhofer.de/content/dam/ise/de/documents/publications/studies/Photovoltaics-Report.pdf>
- [2] Sustainable development goal no. 7. [Online]. Available: <https://sustainabledevelopment.un.org/sdg7>
- [3] V. Devabhaktuni, M. Alam, S. S. S. R. Depuru, R. C. Green, D. Nims, and C. Near, "Solar energy: Trends and enabling technologies," *Renew. Sust. Energy Rev.*, 19, 555–564, 2013.
- [4] Y. Li, G. Xu, C. Cui, and Y. Li, "Flexible and semitransparent organic solar cells," *Adv. Energy Mater.*, 8, 1701791, 2017.
- [5] B. Parida, S. Iniyani, and R. Goic, "A review of solar photovoltaic technologies," *Renew. Sust. Energy Rev.*, 15, 1625–1636, 2011.
- [6] M. Stoppa and A. Chiolerio, "Wearable electronics and smart textiles: A critical review," *Sensors*, 14, 11 957–11 992, 2014.
- [7] M. A. Green, "Third generation photovoltaics: Ultra-high conversion efficiency at low cost," *Prog. Photovoltaics Res. Appl.*, 9, 123–135, 2001.
- [8] N. J. Jeon, H. Na, E. H. Jung, T.-Y. Yang, Y. G. Lee, G. Kim, H.-W. Shin, S. I. Seok, J. Lee, and J. Seo, "A fluorene-terminated hole-transporting material for highly efficient and stable perovskite solar cells," *Nat. Energy*, 3, 682–689, 2018.
- [9] H. Li, Z. Xiao, L. Ding, and J. Wang, "Thermostable single-junction organic solar cells with a power conversion efficiency of 14.62%," *Sci. Bull.*, 63, 340–342, 2018.
- [10] K. Yoshikawa, H. Kawasaki, W. Yoshida, T. Irie, K. Konishi, K. Nakano, T. Uto, D. Adachi, M. Kanematsu, H. Uzu, and K. Yamamoto, "Silicon heterojunction solar cell with interdigitated back contacts for a photoconversion efficiency over 26%," *Nat. Energy*, 2, 17032, 2017.

## Bibliography

- [11] M. A. Green, Y. Hishikawa, E. D. Dunlop, D. H. Levi, J. Hohl-Ebinger, and A. W. Ho-Baillie, "Solar cell efficiency tables (version 52)," *Prog. Photovoltaics Res. Appl.*, 26, 427–436, 2018.
- [12] J.-P. Correa-Baena, M. Saliba, T. Buonassisi, M. Grätzel, A. Abate, W. Tress, and A. Hagfeldt, "Promises and challenges of perovskite solar cells," *Science*, 358, 739–744, 2017.
- [13] W. R. Mateker and M. D. McGehee, "Progress in understanding degradation mechanisms and improving stability in organic photovoltaics," *Adv. Mater.*, 29, 1603940, 2016.
- [14] Y. Rong, Y. Ming, W. Ji, D. Li, A. Mei, Y. Hu, and H. Han, "Toward industrial-scale production of perovskite solar cells: Screen printing, slot-die coating, and emerging techniques," *J. Phys. Chem. Lett.*, 9, 2707–2713, 2018.
- [15] R. Po, G. Bianchi, C. Carbonera, and A. Pellegrino, "'all that glitters is not gold': An analysis of the synthetic complexity of efficient polymer donors for polymer solar cells," *Macromolecules*, 48, 453–461, 2015.
- [16] Z. Shi, J. Guo, Y. Chen, Q. Li, Y. Pan, H. Zhang, Y. Xia, and W. Huang, "Lead-free organic-inorganic hybrid perovskites for photovoltaic applications: Recent advances and perspectives," *Adv. Mater.*, 29, 1605005, 2017.
- [17] F. Giustino and H. J. Snaith, "Toward lead-free perovskite solar cells," *ACS Energy Lett.*, 1, 1233–1240, 2016.
- [18] J. Zhang, L. Zhu, and Z. Wei, "Toward over 15% power conversion efficiency for organic solar cells: Current status and perspectives," *Small Methods*, 1, 1700258, 2017.
- [19] T. Minami, Y. Nishi, and T. Miyata, "Efficiency enhancement using a  $\text{Zn}_{1-x}\text{Ge}_x\text{-O}$  thin film as an n-type window layer in  $\text{Cu}_2\text{O}$ -based heterojunction solar cells," *Appl. Phys. Express*, 9, 052301, 2016.
- [20] Y. C. Choi, D. U. Lee, J. H. Noh, E. K. Kim, and S. I. Seok, "Highly improved  $\text{Sb}_2\text{S}_3$  sensitized-inorganic-organic heterojunction solar cells and quantification of traps by deep-level transient spectroscopy," *Adv. Funct. Mater.*, 24, 3587–3592, 2014.
- [21] K. W. Jung, M. R. Sohn, H. M. Lee, I. S. Yang, S. D. Sung, J. Kim, E. W.-

- G. Diau, and W. I. Lee, “Silver bismuth iodides in various compositions as potential pb-free light absorbers for hybrid solar cells,” *Sust. Energy & Fuels*, 2, 294–302, 2018.
- [22] P. Sinsermsuksakul, L. Sun, S. W. Lee, H. H. Park, S. B. Kim, C. Yang, and R. G. Gordon, “Overcoming efficiency limitations of SnS-based solar cells,” *Adv. Energy Mater.*, 4, 1400496, 2014.
- [23] Y. Zhou, L. Wang, S. Chen, S. Qin, X. Liu, J. Chen, D.-J. Xue, M. Luo, Y. Cao, Y. Cheng, E. H. Sargent, and J. Tang, “Thin-film Sb<sub>2</sub>Se<sub>3</sub> photovoltaics with oriented one-dimensional ribbons and benign grain boundaries,” *Nat. Phot.*, 9, 409–415, 2015.
- [24] W. Shockley and H. J. Queisser, “Detailed balance limit of efficiency of p-n junction solar cells,” *J. Appl. Phys.*, 32, 510, 1961.
- [25] M. A. Green, *Third Generation Photovoltaics*. Springer-Verlag GmbH, 2006.
- [26] Z. Yu, M. Leilaoui, and Z. Holman, “Selecting tandem partners for silicon solar cells,” *Nat. Energy*, 1, 2016.
- [27] J. Werner, B. Niesen, and C. Ballif, “Perovskite/silicon tandem solar cells: Marriage of convenience or true love story? - an overview,” *Adv. Mater. Interf.*, 5, 1700731, 2017.
- [28] V. G. Karpov, A. D. Compaan, and D. Shvydka, “Random diode arrays and mesoscale physics of large-area semiconductor devices,” *Phys. Rev. B*, 69, 045325, 2004.
- [29] U. Rau and M. Schmidt, “Electronic properties of ZnO/Cds/Cu (in, ga) Se<sub>2</sub> solar cells—aspects of heterojunction formation,” *Thin Solid Films*, 387, 141–146, 2001.
- [30] U. Rau, P. O. Grabitz, and J. H. Werner, “Resistive limitations to spatially inhomogeneous electronic losses in solar cells,” *Appl. Phys. Lett.*, 85, 6010–6012, 2004.
- [31] S. D. Wolf, A. Descoedres, Z. C. Holman, and C. Ballif, “High-efficiency silicon heterojunction solar cells: A review,” *green*, 2, 2012.
- [32] A. G. Aberle, “Surface passivation of crystalline silicon solar cells: a review,”

## Bibliography

- Prog. Photovoltaics Res. Appl.*, 8, 473, 2000.
- [33] Y. C. Choi and S. I. Seok, "Efficient  $\text{Sb}_2\text{S}_3$  -sensitized solar cells via single-step deposition of  $\text{Sb}_2\text{S}_3$  using s/sb-ratio-controlled  $\text{SbCl}_3$  -thiourea complex solution," *Adv. Funct. Mater.*, 25, 2892–2898, 2015.
- [34] X. Wang, J. Li, W. Liu, S. Yang, C. Zhu, and T. Chen, "A fast chemical approach towards  $\text{Sb}_2\text{S}_3$  film with a large grain size for high-performance planar heterojunction solar cells," *Nanoscale*, 9, 3386–3390, 2017.
- [35] J. Nelson, *The Physics of Solar Cells*. World Scientific Publishing Company, 2003.
- [36] W. Tress, "Organic solar cells," in *Organic Solar Cells*. Springer, 2014, 67–214.
- [37] T. Kirchartz and U. Rau, "What makes a good solar cell?" *Adv. Energy Mater.*, 1703385, 2018.
- [38] T. Kirchartz, K. Ding, and U. Rau, "Fundamental electrical characterization of thin-film solar cells," *Advanced Characterization Techniques for Thin Film Solar Cells*, 41–69, 2011.
- [39] P. W. Bridgman, "Note on the principle of detailed balancing," *Phys. Rev.*, 31, 101–102, 1928.
- [40] G. Kirchhoff, "üeber das Verhältniss zwischen dem Emissionsvermögen und dem Absorptionsvermögen der Körper für Wärme und Licht," *Annalen der Physik und Chemie*, 185, 275–301, 1860.
- [41] W. Shockley and W. T. Read, "Statistics of the recombinations of holes and electrons," *Phys. Rev.*, 87, 835–842, 1952.
- [42] R. N. Hall, "Electron-hole recombination in germanium," *Phys. Rev.*, 87, 387–387, 1952.
- [43] B. K. Ridley, "On the multiphonon capture rate in semiconductors," *Solid-State Electron.*, 21, 1319–1323, 1978.
- [44] T. Markvart, "Semiclassical theory of non-radiative transitions," *J. Phys. C: Solid State Phys.*, 14, L895, 1981.
- [45] J. Benduhn, K. Tvingstedt, F. Piersimoni, S. Ullbrich, Y. Fan, M. Tropiano,

- K. A. McGarry, O. Zeika, M. K. Riede, C. J. Douglas, S. Barlow, S. R. Marder, D. Neher, D. Spoltore, and K. Vandewal, “Intrinsic non-radiative voltage losses in fullerene-based organic solar cells,” *Nat. Energy*, 2, 17053, 2017.
- [46] T. Kirchartz, T. Markvart, U. Rau, and D. A. Egger, “Impact of small phonon energies on the charge-carrier lifetimes in metal-halide perovskites,” *J. Phys. Chem. Lett.*, 9, 939–946, 2018.
- [47] B. M. Kayes, H. Nie, R. Twist, S. G. Spruytte, F. Reinhardt, I. C. Kizilyalli, and G. S. Higashi, “27.6% conversion efficiency, a new record for single-junction solar cells under 1 sun illumination,” in *2011 37th IEEE Photovoltaic Specialists Conference*. IEEE, 2011.
- [48] T. Matsui, A. Bidiville, K. Maejima, H. Sai, T. Koida, T. Suezaki, M. Matsumoto, K. Saito, I. Yoshida, and M. Kondo, “High-efficiency amorphous silicon solar cells: Impact of deposition rate on metastability,” *Appl. Phys. Lett.*, 106, 053901, 2015.
- [49] H. Sai, K. Maejima, T. Matsui, T. Koida, M. Kondo, S. Nakao, Y. Takeuchi, H. Katayama, and I. Yoshida, “High-efficiency microcrystalline silicon solar cells on honeycomb textured substrates grown with high-rate VHF plasma-enhanced chemical vapor deposition,” *Jap. J. of Appl. Phys.*, 54, 08KB05, 2015.
- [50] X. Wen, C. Chen, S. Lu, K. Li, R. Kondrotas, Y. Zhao, W. Chen, L. Gao, C. Wang, J. Zhang, G. Niu, and J. Tang, “Vapor transport deposition of antimony selenide thin film solar cells with 7.6% efficiency,” *Nat. Commun.*, 9, 2179, 2018.
- [51] L. Martinez, A. Stavrinadis, S. Higuchi, S. L. Diedenhofen, M. Bernechea, K. Tajima, and G. Konstantatos, “Hybrid solution-processed bulk heterojunction solar cells based on bismuth sulfide nanocrystals,” *Phys. Chem. Chem. Phys.*, 15, 5482, 2013.
- [52] Z. Zhao, F. Gu, Y. Li, W. Sun, S. Ye, H. Rao, Z. Liu, Z. Bian, and C. Huang, “Mixed-organic-cation tin iodide for lead-free perovskite solar cells with an efficiency of 8.12%,” *Adv. Sci.*, 4, 1700204, 2017.

## Bibliography

- [53] J. Xu, O. Voznyy, M. Liu, A. R. Kirmani, G. Walters, R. Munir, M. Abdelsamie, A. H. Proppe, A. Sarkar, F. P. G. de Arquer, M. Wei, B. Sun, M. Liu, O. Ouellette, R. Quintero-Bermudez, J. Li, J. Fan, L. Quan, P. Todorovic, H. Tan, S. Hoogland, S. O. Kelley, M. Stefiik, A. Amassian, and E. H. Sargent, “2d matrix engineering for homogeneous quantum dot coupling in photovoltaic solids,” *Nat. Nanotechnol.*, 13, 456–462, 2018.
- [54] J.-C. Hebig, I. Kühn, J. Flohre, and T. Kirchartz, “Optoelectronic properties of (CH<sub>3</sub>NH<sub>3</sub>)<sub>3</sub>Sb<sub>2</sub>I<sub>9</sub> thin films for photovoltaic applications,” *ACS Energy Lett.*, 1, 309–314, 2016.
- [55] B.-W. Park, B. Philippe, X. Zhang, H. Rensmo, G. Boschloo, and E. M. J. Johansson, “Bismuth based hybrid perovskites A<sub>3</sub>Bi<sub>2</sub>I<sub>9</sub>(A: Methylammonium or cesium) for solar cell application,” *Adv. Mater.*, 27, 6806–6813, 2015.
- [56] D. P. McMeekin, G. Sadoughi, W. Rehman, G. E. Eperon, M. Saliba, M. T. Horantner, A. Haghighirad, N. Sakai, L. Korte, B. Rech, M. B. Johnston, L. M. Herz, and H. J. Snaith, “A mixed-cation lead mixed-halide perovskite absorber for tandem solar cells,” *Science*, 351, 151–155, 2016.
- [57] Z. Zheng, Q. Hu, S. Zhang, D. Zhang, J. Wang, S. Xie, R. Wang, Y. Qin, W. Li, L. Hong, N. Liang, F. Liu, Y. Zhang, Z. Wei, Z. Tang, T. P. Russell, J. Hou, and H. Zhou, “A highly efficient non-fullerene organic solar cell with a fill factor over 0.80 enabled by a fine-tuned hole-transporting layer,” *Adv. Mater.*, 30, 1801801, 2018.
- [58] X. Xu, T. Yu, Z. Bi, W. Ma, Y. Li, and Q. Peng, “Realizing over 13% efficiency in green-solvent-processed nonfullerene organic solar cells enabled by 1,3,4-thiadiazole-based wide-bandgap copolymers,” *Adv. Mater.*, 30, 1703973, 2017.
- [59] J. Zhao, Y. Li, G. Yang, K. Jiang, H. Lin, H. Ade, W. Ma, and H. Yan, “Efficient organic solar cells processed from hydrocarbon solvents,” *Nat. Energy*, 1, 15027, 2016.
- [60] D.-H. Kim, S.-J. Lee, M. S. Park, J.-K. Kang, J. H. Heo, S. H. Im, and S.-J. Sung, “Highly reproducible planar Sb<sub>2</sub>S<sub>3</sub>-sensitized solar cells based on atomic layer deposition,” *Nanoscale*, 6, 14549–14554, 2014.

- [61] U. Rau, B. Blank, T. C. M. Müller, and T. Kirchartz, “Efficiency potential of photovoltaic materials and devices unveiled by detailed-balance analysis,” *Phys. Rev. Appl.*, 7, 2017.
- [62] A. Richter, M. Hermle, and S. W. Glunz, “Reassessment of the limiting efficiency for crystalline silicon solar cells,” *IEEE J. of Photovoltaics*, 3, 1184–1191, 2013.
- [63] A. Polman, M. Knight, E. C. Garnett, B. Ehrler, and W. C. Sinke, “Photovoltaic materials: Present efficiencies and future challenges,” *Science*, 352, 4424, 2016.
- [64] M. A. Green, “Solar cell fill factors: General graph and empirical expressions,” *Solid-State Electron.*, 24, 788–789, 1981.
- [65] E. Yablonovitch and G. Cody, “Intensity enhancement in textured optical sheets for solar cells,” *IEEE Transactions on Electron Devices*, 29, 300–305, 1982.
- [66] U. Rau, U. W. Paetzold, and T. Kirchartz, “Thermodynamics of light management in photovoltaic devices,” *Phys. Rev. B*, 90, 2014.
- [67] F.-J. Haug and C. Ballif, “Light management in thin film silicon solar cells,” *Energy & Envir. Sci.*, 8, 824–837, 2015.
- [68] J. Müller, B. Rech, J. Springer, and M. Vanecek, “TCO and light trapping in silicon thin film solar cells,” *Sol. Energy*, 77, 917–930, 2004.
- [69] P. Spinelli, V. E. Ferry, J. van de Groep, M. van Lare, M. A. Verschuuren, R. E. I. Schropp, H. A. Atwater, and A. Polman, “Plasmonic light trapping in thin-film si solar cells,” *J. Opt.*, 14, 024002, 2012.
- [70] Y. Kim, Z. Yang, A. Jain, O. Voznyy, G.-H. Kim, M. Liu, L. N. Quan, F. P. G. de Arquer, R. Comin, J. Z. Fan, and E. H. Sargent, “Pure cubic-phase hybrid iodobismuthates AgBi<sub>2</sub>I<sub>7</sub> for thin-film photovoltaics,” *Angew. Chem. Int. Ed.*, 55, 9586–9590, 2016.
- [71] L. Whittaker-Brooks, J. Gao, A. K. Hailey, C. R. Thomas, N. Yao, and Y.-L. Loo, “Bi<sub>2</sub>S<sub>3</sub> nanowire networks as electron acceptor layers in solution-processed hybrid solar cells,” *J. Mater. Chem. C*, 3, 2686–2692, 2015.

## Bibliography

- [72] A. K. Rath, M. Bernechea, L. Martinez, F. P. G. de Arquer, J. Osmond, and G. Konstantatos, "Solution-processed inorganic bulk nano-heterojunctions and their application to solar cells," *Nat. Phot.*, 6, 529–534, 2012.
- [73] K. A. Bush, A. F. Palmstrom, Z. J. Yu, M. Boccard, R. Cheacharoen, J. P. Mailoa, D. P. McMeekin, R. L. Z. Hoyer, C. D. Bailie, T. Leijtens, I. M. Peters, M. C. Minichetti, N. Rolston, R. Prasanna, S. Sofia, D. Harwood, W. Ma, F. Moghadam, H. J. Snaith, T. Buonassisi, Z. C. Holman, S. F. Bent, and M. D. McGehee, "23.6%-efficient monolithic perovskite/silicon tandem solar cells with improved stability," *Nat. Energy*, 2, 2017.
- [74] F. Sahli, J. Werner, B. A. Kamino, M. Bräuninger, R. Monnard, B. Paviet-Salomon, L. Barraud, L. Ding, J. J. D. Leon, D. Sacchetto, G. Cattaneo, M. Despeisse, M. Boccard, S. Nicolay, Q. Jeangros, B. Niesen, and C. Ballif, "Fully textured monolithic perovskite/silicon tandem solar cells with 25.2% power conversion efficiency," *Nat. Mater.*, 17, 820–826, 2018.
- [75] E. T. Hoke, D. J. Slotcavage, E. R. Dohner, A. R. Bowring, H. I. Karunadasa, and M. D. McGehee, "Reversible photo-induced trap formation in mixed-halide hybrid perovskites for photovoltaics," *Chem. Sci.*, 6, 613–617, 2015.
- [76] T. J. Jacobsson, J.-P. Correa-Baena, M. Pazoki, M. Saliba, K. Schenk, M. Grätzel, and A. Hagfeldt, "Exploration of the compositional space for mixed lead halogen perovskites for high efficiency solar cells," *Energy & Envir. Sci.*, 9, 1706–1724, 2016.
- [77] E. L. Unger, L. Kegelmann, K. Suchan, D. Sörell, L. Korte, and S. Albrecht, "Roadmap and roadblocks for the band gap tunability of metal halide perovskites," *J. Mater. Chem. A*, 5, 11 401–11 409, 2017.
- [78] S. Rühle, "The detailed balance limit of perovskite/silicon and perovskite/CdTe tandem solar cells," *phys. stat. sol. (a)*, 214, 1600955, 2017.
- [79] M. Y. Versavel and J. A. Haber, "Structural and optical properties of amorphous and crystalline antimony sulfide thin-films," *Thin Solid Films*, 515, 7171–7176, 2007.

- [80] Y. Itzhaik, O. Niiitsoo, M. Page, and G. Hodes, "Sb<sub>2</sub>S<sub>3</sub>-sensitized nanoporous TiO<sub>2</sub> solar cells," *J. Phys. Chem. C*, 113, 4254–4256, 2009.
- [81] R. A. Street, *Technology and applications of amorphous silicon*. Springer Science & Business Media, 2013, 37.
- [82] T. Kirchartz, J. Bisquert, I. Mora-Sero, and G. Garcia-Belmonte, "Classification of solar cells according to mechanisms of charge separation and charge collection," *Phys. Chem. Chem. Phys.*, 17, 4007–4014, 2015.
- [83] T. Kirchartz, W. Gong, S. A. Hawks, T. Agostinelli, R. C. I. MacKenzie, Y. Yang, and J. Nelson, "Sensitivity of the Mott–Schottky analysis in organic solar cells," *J. Phys. Chem. C*, 116, 7672–7680, 2012.
- [84] F. Deledalle, T. Kirchartz, M. S. Vezie, M. Campoy-Quiles, P. Shakya Tuladhar, J. Nelson, and J. R. Durrant, "Understanding the effect of unintentional doping on transport optimization and analysis in efficient organic bulk-heterojunction solar cells," *Phys. Rev. X*, 5, 011032, 2015.
- [85] T. Kirchartz, D. Abou-Ras, and U. Rau, "Introduction to thin-film photovoltaics," in *Advanced Characterization Techniques for Thin Film Solar Cells*. Wiley-VCH Verlag GmbH & Co. KGaA, 2016, 1–40.
- [86] A. Shah, "Photovoltaic technology: The case for thin-film solar cells," *Science*, 285, 692–698, 1999.
- [87] P. Würfel, "Thermodynamic limitations to solar energy conversion," *Physica E*, 14, 18–26, 2002.
- [88] T. Kirchartz and U. Rau, "Decreasing radiative recombination coefficients via an indirect band gap in lead halide perovskites," *J. Phys. Chem. Lett.*, 8, 1265–1271, 2017.
- [89] V. Steinmann, R. E. Brandt, and T. Buonassisi, "Photovoltaics: Non-cubic solar cell materials," *Nat. Phot.*, 9, 355–357, 2015.
- [90] M. S. You, C.-S. Lim, D. H. Kwon, J. H. Heo, S. H. Im, and K. J. Chae, "Oxide-free Sb<sub>2</sub>S<sub>3</sub> sensitized solar cells fabricated by spin and heat-treatment of sb(iii)(thioacetamide)<sub>2</sub>Cl<sub>3</sub>," *Org. Electron.*, 21, 155–159, 2015.
- [91] S.-J. Sung, E. K. Gil, S.-J. Lee, Y. C. Choi, K.-J. Yang, J.-K. Kang, K. Y.

## Bibliography

- Cho, and D.-H. Kim, "Systematic control of nanostructured interfaces of planar  $\text{Sb}_2\text{S}_3$  solar cells by simple spin-coating process and its effect on photovoltaic properties," *J. Ind. Eng. Chem.*, 56, 196–202, 2017.
- [92] V. Steinmann, R. Chakraborty, P. H. Rekemeyer, K. Hartman, R. E. Brandt, A. Polizzotti, C. Yang, T. Moriarty, S. Gradečak, R. G. Gordon, and T. Buonassisi, "A two-step absorber deposition approach to overcome shunt losses in thin-film solar cells: Using tin sulfide as a proof-of-concept material system," *ACS Appl. Mat. & Interf.*, 8, 22 664–22 670, 2016.
- [93] N. K. Noel, S. D. Stranks, A. Abate, C. Wehrenfennig, S. Guarnera, A.-A. Haghighirad, A. Sadhanala, G. E. Eperon, S. K. Pathak, M. B. Johnston, A. Petrozza, L. M. Herz, and H. J. Snaith, "Lead-free organic–inorganic tin halide perovskites for photovoltaic applications," *Energy & Envir. Sci.*, 7, 3061–3068, 2014.
- [94] J. A. Aguiar, S. Wozny, T. G. Holesinger, T. Aoki, M. K. Patel, M. Yang, J. J. Berry, M. Al-Jassim, W. Zhou, and K. Zhu, "In situ investigation of the formation and metastability of formamidinium lead tri-iodide perovskite solar cells," *Energy & Envir. Sci.*, 9, 2372–2382, 2016.
- [95] Y. Zhou, O. S. Game, S. Pang, and N. P. Padture, "Microstructures of organometal trihalide perovskites for solar cells: Their evolution from solutions and characterization," *J. Phys. Chem. Lett.*, 6, 4827–4839, 2015.
- [96] W. Tress, "Perovskite solar cells on the way to their radiative efficiency limit - insights into a success story of high open-circuit voltage and low recombination," *Adv. Energy Mater.*, 7, 1602358, 2017.
- [97] N. Ahn, D.-Y. Son, I.-H. Jang, S. M. Kang, M. Choi, and N.-G. Park, "Highly reproducible perovskite solar cells with average efficiency of 18.3% and best efficiency of 19.7% fabricated via lewis base adduct of lead(II) iodide," *J. Am. Chem. Soc.*, 137, 8696–8699, 2015.
- [98] M. Liu, M. B. Johnston, and H. J. Snaith, "Efficient planar heterojunction perovskite solar cells by vapour deposition," *Nature*, 501, 395–398, 2013.
- [99] J. H. Heo, D. H. Song, H. J. Han, S. Y. Kim, J. H. Kim, D. Kim, H. W. Shin, T. K. Ahn, C. Wolf, T.-W. Lee, and S. H. Im, "Planar  $\text{CH}_3\text{NH}_3\text{PbI}_3$

- perovskite solar cells with constant 17.2% average power conversion efficiency irrespective of the scan rate,” *Adv. Mater.*, 27, 3424–3430, 2015.
- [100] J.-P. Correa-Baena, M. Anaya, G. Lozano, W. Tress, K. Domanski, M. Saliba, T. Matsui, T. J. Jacobsson, M. E. Calvo, A. Abate, M. Grätzel, H. Míguez, and A. Hagfeldt, “Unbroken perovskite: Interplay of morphology, electro-optical properties, and ionic movement,” *Adv. Mater.*, 28, 5031–5037, 2016.
- [101] S. Razza, S. Castro-Hermosa, A. D. Carlo, and T. M. Brown, “Research update: Large-area deposition, coating, printing, and processing techniques for the upscaling of perovskite solar cell technology,” *APL Materials*, 4, 091508, 2016.
- [102] M. Yang, Z. Li, M. O. Reese, O. G. Reid, D. H. Kim, S. Siol, T. R. Klein, Y. Yan, J. J. Berry, M. F. A. M. van Hest, and K. Zhu, “Perovskite ink with wide processing window for scalable high-efficiency solar cells,” *Nat. Energy*, 2, 17038, 2017.
- [103] S. T. Williams, A. Rajagopal, C.-C. Chueh, and A. K.-Y. Jen, “Current challenges and prospective research for upscaling hybrid perovskite photovoltaics,” *J. Phys. Chem. Lett.*, 7, 811–819, 2016.
- [104] A. Bosio, N. Romeo, S. Mazzamuto, and V. Canevari, “Polycrystalline CdTe thin films for photovoltaic applications,” *Prog. Cryst. Growth Charact. Mater.*, 52, 247–279, 2006.
- [105] E. Camacho-Espinosa, A. I. Oliva-Avilés, and A. I. Oliva, “Effect of the substrate cleaning process on pinhole formation in sputtered CdTe films,” *J. Mater. Eng. Perform.*, 26, 4020–4028, 2017.
- [106] J. Major, L. Phillips, M. A. Turkestani, L. Bowen, T. Whittles, V. Dhanak, and K. Durose, “P3HT as a pinhole blocking back contact for CdTe thin film solar cells,” *Sol. Energy Mater. Sol. Cells*, 172, 1–10, 2017.
- [107] B. L. Williams, S. Smit, B. J. Kniknie, K. J. Bakker, W. Keuning, W. M. M. Kessels, R. E. I. Schropp, and M. Creatore, “Identifying parasitic current pathways in CIGS solar cells by modelling dark J-V response,” *Prog. Photovoltaics Res. Appl.*, 23, 1516–1525, 2015.

## Bibliography

- [108] B. L. Williams, V. Zardetto, B. Kniknie, M. A. Verheijen, W. M. Kessels, and M. Creatore, "The competing roles of i-ZnO in Cu(In,Ga)Se<sub>2</sub> solar cells," *Sol. Energy Mater. Sol. Cells*, 157, 798–807, 2016.
- [109] O. Kunz, J. Wong, J. Janssens, J. Bauer, O. Breitenstein, and A. Aberle, "Shunting problems due to sub-micron pinholes in evaporated solid-phase crystallised poly-si thin-film solar cells on glass," *Prog. Photovoltaics Res. Appl.*, 17, 35–46, 2009.
- [110] T. Kirchartz, P. Kaienburg, and D. Baran, "Figures of merit guiding research on organic solar cells," *J. Phys. Chem. C*, 122, 5829–5843, 2018.
- [111] B. Mistic, B. E. Pieters, J. P. Theisen, A. Gerber, and U. Rau, "Shunt mitigation in ZnO:Al/i-ZnO/CdS/Cu(In,Ga)Se<sub>2</sub> solar modules by the i-ZnO/CdS buffer combination," *phys. stat. sol. (a)*, 212, 541–546, 2014.
- [112] M. T. Hörantner, P. K. Nayak, S. Mukhopadhyay, K. Wojciechowski, C. Beck, D. McMeekin, B. Kamino, G. E. Eperon, and H. J. Snaith, "Shunt-blocking layers for semitransparent perovskite solar cells," *Adv. Mater. Interf.*, 3, 1500837, 2016.
- [113] K. Tvingstedt, L. Gil-Escrig, C. Momblona, P. Rieder, D. Kiermasch, M. Sessolo, A. Baumann, H. J. Bolink, and V. Dyakonov, "Removing leakage and surface recombination in planar perovskite solar cells," *ACS Energy Lett.*, 2, 424–430, 2017.
- [114] C. Hartmann, G. Sadoughi, R. Félix, E. Handick, H. W. Klemm, G. Peschel, E. Madej, A. B. Fuhrich, X. Liao, S. Raoux, D. Abou-Ras, D. Wargulski, T. Schmidt, R. G. Wilks, H. Snaith, and M. Bär, "Spatially resolved insight into the chemical and electronic structure of solution-processed perovskites-why to (not) worry about pinholes," *Adv. Mater. Interf.*, 5, 1701420, 2018.
- [115] S. D. Stranks, P. K. Nayak, W. Zhang, T. Stergiopoulos, and H. J. Snaith, "Formation of thin films of organic-inorganic perovskites for high-efficiency solar cells," *Angew. Chem. Int. Ed.*, 54, 3240–3248, 2015.
- [116] M. D. McGehee, "Perovskite solar cells: Continuing to soar," *Nat. Mater.*, 13, 845–846, 2014.

- [117] W. Qiu, T. Merckx, M. Jaysankar, C. M. de la Huerta, L. Rakocevic, W. Zhang, U. W. Paetzold, R. Gehlhaar, L. Froyen, J. Poortmans, D. Cheyns, H. J. Snaith, and P. Heremans, "Pinhole-free perovskite films for efficient solar modules," *Energy & Envir. Sci.*, 9, 484–489, 2016.
- [118] M. Saliba, J.-P. Correa-Baena, M. Grätzel, A. Hagfeldt, and A. Abate, "Perovskite solar cells: From the atomic level to film quality and device performance," *Angew. Chem. Int. Ed.*, 57, 2554–2569, 2018.
- [119] M. A. Green, "Accuracy of analytical expressions for solar cell fill factors," *Sol. Cells*, 7, 337–340, 1982.
- [120] D. Neher, J. Kniepert, A. Elimelech, and L. J. A. Koster, "A new figure of merit for organic solar cells with transport-limited photocurrents," *Sci. Rep.*, 6, 24861, 2016.
- [121] M. A. Green, "Accurate expressions for solar cell fill factors including series and shunt resistances," *Appl. Phys. Lett.*, 108, 081111, 2016.
- [122] T. Kirchartz, K. Ding, and U. Rau, "Fundamental electrical characterization of thin-film solar cells," in *Advanced Characterization Techniques for Thin Film Solar Cells*. Wiley-VCH Verlag GmbH & Co. KGaA, 2016, 41–69.
- [123] R. S. Crandall, "Transport in hydrogenated amorphous silicon p-i-n solar cells," *J. Appl. Phys.*, 53, 3350, 1982.
- [124] T. Kirchartz, T. Agostinelli, M. Campoy-Quiles, W. Gong, and J. Nelson, "Understanding the thickness-dependent performance of organic bulk heterojunction solar cells: The influence of mobility, lifetime, and space charge," *J. Phys. Chem. Lett.*, 3, 3470, 2012.
- [125] R. C. I. MacKenzie, C. G. Shuttle, M. L. Chabinye, and J. Nelson, "Extracting microscopic device parameters from transient photocurrent measurements of P3HT:PCBM solar cells," *Adv. Energy Mater.*, 2, 662, 2012.
- [126] S. Schäfer, A. Petersen, T. A. Wagner, R. Kniprath, D. Lingenfeller, A. Zen, T. Kirchartz, B. Zimmermann, U. Würfel, X. Feng, and T. Mayer, "Influence of the indium tin oxide/organic interface on open-circuit voltage, recombination, and cell degradation in organic small-molecule solar cells,"

## Bibliography

- Phys. Rev. B*, 83, 165311, 2011.
- [127] W. Tress, K. Leo, and M. Riede, “Influence of hole-transport layers and donor materials on open-circuit voltage and shape of I-V curves of organic solar cells,” *Adv. Funct. Mater.*, 21, 2140, 2011.
- [128] U. Würfel, D. Neher, A. Spies, and S. Albrecht, “Impact of charge transport on current-voltage characteristics and power-conversion efficiency of organic solar cells,” *Nat. Commun.*, 6, 6951, 2015.
- [129] C. Donolato, “A reciprocity theorem for charge collection,” *Appl. Phys. Lett.*, 46, 270–272, 1985.
- [130] G. F. A. Dibb, F. C. Jamieson, A. Maurano, J. Nelson, and J. R. Durrant, “Limits on the fill factor in organic photovoltaics: Distinguishing nongeminate and geminate recombination mechanisms,” *J. Phys. Chem. Lett.*, 4, 803, 2013.
- [131] J. Mattheis, P. Rostan, U. Rau, and J. Werner, “Carrier collection in Cu(In,Ga)Se<sub>2</sub> solar cells with graded band gaps and transparent ZnO:Al back contacts,” *Sol. Energy Mater. Sol. Cells*, 91, 689–695, 2007.
- [132] O. J. Sandberg, A. Sundqvist, M. Nyman, and R. Österbacka, “Relating charge transport, contact properties, and recombination to open-circuit voltage in sandwich-type thin-film solar cells,” *Phys. Rev. Appl.*, 5, 2016.
- [133] S. E. Shaheen, C. J. Brabec, N. S. Sariciftci, F. Padinger, T. Fromherz, and J. C. Hummelen, “2.5% efficient organic plastic solar cells,” *Appl. Phys. Lett.*, 78, 841, 2001.
- [134] G. Li, V. Shrotriya, J. Huang, Y. Yao, T. Moriarty, K. Emery, and Y. Yang, “High-efficiency solution processable polymer photovoltaic cells by self-organization of polymer blends,” *Nat. Mater.*, 4, 864, 2005.
- [135] S. H. Park, A. Roy, S. Beaupré, S. Cho, N. Coates, J. S. Moon, D. Moses, M. Leclerc, K. Lee, and A. J. Heeger, “Bulk heterojunction solar cells with internal quantum efficiency approaching 100%,” *Nat. Mater.*, 7, 943–947, 2008.
- [136] Z. He, C. Zhong, S. Su, M. Xu, H. Wu, and Y. Cao, “Enhanced power-conversion efficiency in polymer solar cells using an inverted device structure,” *Nat. Phot.*, 6, 593, 2012.

- [137] V. Vohra, K. Kawashima, T. Kakara, T. Koganezawa, I. Osaka, K. Takimiya, and H. Murata, "Efficient inverted polymer solar cells employing favourable molecular orientation," *Nat. Phot.*, 9, 403, 2015.
- [138] W. Zhao, S. Li, H. Yao, S. Zhang, Y. Zhang, B. Yang, and J. Hou, "Molecular optimization enables over 13% efficiency in organic solar cells," *J. Am. Chem. Soc.*, 139, 7148–7151, 2017.
- [139] D. Baran, R. S. Ashraf, D. A. Hanifi, M. Abdelsamie, N. Gasparini, J. A. Röhr, S. Holliday, A. Wadsworth, S. Lockett, M. Neophytou, C. J. M. Emmott, J. Nelson, C. J. Brabec, A. Amassian, A. Salleo, T. Kirchartz, J. R. Durrant, and I. McCulloch, "Reducing the efficiency–stability–cost gap of organic photovoltaics with highly efficient and stable small molecule acceptor ternary solar cells," *Nat. Mater.*, 16, 363–369, 2016.
- [140] J. van Duren, X. Yang, J. Loos, C. Bulle-Lieuwma, A. Sieval, J. Hummelen, and R. Janssen, "Relating the morphology of poly(p-phenylene vinylene)/methanofullerene blends to solar-cell performance," *Adv. Funct. Mater.*, 14, 425–434, 2004.
- [141] L. Ye, H. Hu, M. Ghasemi, T. Wang, B. A. Collins, J.-H. Kim, K. Jiang, J. H. Carpenter, H. Li, Z. Li, T. McAfee, J. Zhao, X. Chen, J. L. Y. Lai, T. Ma, J.-L. Bredas, H. Yan, and H. Ade, "Quantitative relations between interaction parameter, miscibility and function in organic solar cells," *Nat. Mater.*, 17, 253–260, 2018.
- [142] L. Ye, B. A. Collins, X. Jiao, J. Zhao, H. Yan, and H. Ade, "Miscibility-function relations in organic solar cells: Significance of optimal miscibility in relation to percolation," *Adv. Energy Mater.*, 8, 1703058, 2018.
- [143] K. Maturová, S. S. van Bavel, M. M. Wienk, R. A. J. Janssen, and M. Kemerink, "Morphological device model for organic bulk heterojunction solar cells," *Nano Lett.*, 9, 3032–3037, 2009.
- [144] K. Maturová, S. S. van Bavel, M. M. Wienk, R. A. J. Janssen, and M. Kemerink, "Description of the morphology dependent charge transport and performance of polymer:fullerene bulk heterojunction solar cells," *Adv. Funct. Mater.*, 21, 261–269, 2010.

## Bibliography

- [145] M. C. Scharber, D. Mühlbacher, M. Koppe, P. Denk, C. Waldauf, A. J. Heeger, and C. J. Brabec, "Design rules for donors in bulk-heterojunction solar cells - towards 10 2006.
- [146] K. Vandewal, K. Tvingstedt, A. Gadisa, O. Inganäs, and J. V. Manca, "On the origin of the open-circuit voltage of polymer-fullerene solar cells," *Nat. Mater.*, 8, 904, 2009.
- [147] M. C. Scharber, "On the efficiency limit of conjugated polymer:fullerene-based bulk heterojunction solar cells," *Adv. Mater.*, 28, 1994–2001, 2016.
- [148] H. Yao, Y. Cui, R. Yu, B. Gao, H. Zhang, and J. Hou, "Design, synthesis, and photovoltaic characterization of a small molecular acceptor with an ultra-narrow band gap," *Angew. Chem. Int. Ed.*, 56, 3045–3049, 2017.
- [149] X. Song, N. Gasparini, L. Ye, H. Yao, J. Hou, H. Ade, and D. Baran, "Controlling blend morphology for ultrahigh current density in nonfullerene acceptor-based organic solar cells," *ACS Energy Lett.*, 3, 669–676, 2018.
- [150] W. Zhao, S. Li, S. Zhang, X. Liu, and J. Hou, "Ternary polymer solar cells based on two acceptors and one donor for achieving 12.2% efficiency," *Adv. Mater.*, 29, 1604059, 2016.
- [151] F. Zhao, S. Dai, Y. Wu, Q. Zhang, J. Wang, L. Jiang, Q. Ling, Z. Wei, W. Ma, W. You, C. Wang, and X. Zhan, "Single-junction binary-blend nonfullerene polymer solar cells with 12.1% efficiency," *Adv. Mater.*, 29, 1700144, 2017.
- [152] G. Zhang, K. Zhang, Q. Yin, X.-F. Jiang, Z. Wang, J. Xin, W. Ma, H. Yan, F. Huang, and Y. Cao, "High-performance ternary organic solar cell enabled by a thick active layer containing a liquid crystalline small molecule donor," *J. Am. Chem. Soc.*, 139, 2387–2395, 2017.
- [153] L. Ye, W. Zhao, S. Li, S. Mukherjee, J. H. Carpenter, O. Awartani, X. Jiao, J. Hou, and H. Ade, "High-efficiency nonfullerene organic solar cells: Critical factors that affect complex multi-length scale morphology and device performance," *Adv. Energy Mater.*, 7, 1602000, 2016.
- [154] J. A. Bartelt, Z. M. Beiley, E. T. Hoke, W. R. Mateker, J. D. Douglas, B. A. Collins, J. R. Tumbleston, K. R. Graham, A. Amassian, H. Ade, J. M.

- Fréchet, M. F. Toney, and M. D. McGehee, "The importance of fullerene percolation in the mixed regions of polymer-fullerene bulk heterojunction solar cells," *Adv. Energy Mater.*, 3, 364, 2012.
- [155] S. Foster, F. Deledalle, A. Mitani, T. Kimura, K.-B. Kim, T. Okachi, T. Kirchartz, J. Oguma, K. Miyake, J. R. Durrant, S. Doi, and J. Nelson, "Electron collection as a limit to polymer:pcbm solar cell efficiency: Effect of blend microstructure on carrier mobility and device performance in PTB7:PCBM," *Adv. Energy Mater.*, 4, 1400311, 2014.
- [156] M. Lenes, L. J. A. Koster, V. D. Mihailetschi, and P. W. M. Blom, "Thickness dependence of the efficiency of polymer:fullerene bulk heterojunction solar cells," *Appl. Phys. Lett.*, 88, 243502, 2006.
- [157] J. Peet, J. Y. Kim, N. E. Coates, W. L. Ma, D. Moses, A. J. Heeger, and G. C. Bazan, "Efficiency enhancement in low-bandgap polymer solar cells by processing with alkane dithiols," *Nat. Mater.*, 6, 497, 2007.
- [158] J. Albero, P. Atienzar, A. Corma, and H. Garcia, "Efficiency records in mesoscopic dye-sensitized solar cells," *Chem. Rec.*, 15, 803–828, 2015.
- [159] H. Wedemeyer, J. Michels, R. Chmielowski, S. Bourdais, T. Muto, M. Sugiura, G. Dennler, and J. Bachmann, "Nanocrystalline solar cells with an antimony sulfide solid absorber by atomic layer deposition," *Energy Environ. Sci.*, 6, 67–71, 2013.
- [160] S.-J. Moon, Y. Itzhaik, J.-H. Yum, S. M. Zakeeruddin, G. Hodes, and M. Grätzel, "Sb<sub>2</sub>S<sub>3</sub>-based mesoscopic solar cell using an organic hole conductor," *J. Phys. Chem. Lett.*, 1, 1524–1527, 2010.
- [161] J. A. Chang, J. H. Rhee, S. H. Im, Y. H. Lee, H. jung Kim, S. I. Seok, M. K. Nazeeruddin, and M. Gratzel, "High-performance nanostructured inorganic-organic heterojunction solar cells," *Nano Lett.*, 10, 2609–2612, 2010.
- [162] S. H. Im, C.-S. Lim, J. A. Chang, Y. H. Lee, N. Maiti, H.-J. Kim, M. K. Nazeeruddin, M. Grätzel, and S. I. Seok, "Toward interaction of sensitizer and functional moieties in hole-transporting materials for efficient semiconductor-sensitized solar cells," *Nano Lett.*, 11, 4789–4793, 2011.

## Bibliography

- [163] P. P. Boix, Y. H. Lee, F. Fabregat-Santiago, S. H. Im, I. Mora-Sero, J. Bisquert, and S. I. Seok, "From flat to nanostructured photovoltaics: Balance between thickness of the absorber and charge screening in sensitized solar cells," *ACS Nano*, 6, 873–880, 2012.
- [164] E. Zimmermann, T. Pfadler, J. Kalb, J. A. Dorman, D. Sommer, G. Hahn, J. Weickert, and L. Schmidt-Mende, "Toward high-efficiency solution-processed planar heterojunction  $\text{Sb}_2\text{S}_3$  Solar cells," *Adv. Sci.*, 2, 1500059, 2015.
- [165] O. Savadogo, "Low cost schottky barrier solar cells fabricated on CdSe and  $\text{sb}_2\text{s}_3$  films chemically deposited with silicotungstic acid," *J. Electrochem. Soc.*, 141, 2871, 1994.
- [166] T. Muto, G. Larramona, and G. Dennler, "Unexpected performances of flat  $\text{Sb}_2\text{S}_3$ -based hybrid extremely thin absorber solar cells," *Appl. Phys Express*, 6, 072301, 2013.
- [167] Y. Osorio Mayon, T. P. White, R. Wang, Z. Yang, and K. R. Catchpole, "Evaporated and solution deposited planar  $\text{Sb}_2\text{S}_3$  solar cells: A comparison and its significance," *phys. stat. sol. (a)*, 213, 108–113, 2015.
- [168] O. Savadogo, "Characterizations of antimony tri-sulfide chemically deposited with silicotungstic acid," *J. Electrochem. Soc.*, 139, L16, 1992.
- [169] O. Savadogo and K. Mandal, "Improved schottky barrier on n- $\text{Sb}_2\text{S}_3$  films chemically deposited with silicotungstic acid," *Electron. Lett.*, 28, 1682, 1992.
- [170] S. Yuan, H. Deng, D. Dong, X. Yang, K. Qiao, C. Hu, H. Song, H. Song, Z. He, and J. Tang, "Efficient planar antimony sulfide thin film photovoltaics with large grain and preferential growth," *Sol. Energy Mater. Sol. Cells*, 157, 887–893, 2016.
- [171] M. T. S. Nair, "Chemically deposited  $\text{Sb}_2\text{S}_3$  and  $\text{Sb}_2\text{S}_3$ -CuS thin films," *J. Electrochem. Soc.*, 145, 2113, 1998.
- [172] S. Messina, M. Nair, and P. Nair, "Antimony sulfide thin films in chemically deposited thin film photovoltaic cells," *Thin Solid Films*, 515, 5777–5782, 2007.
- [173] F. Perales, G. Lifante, F. Agulló-Rueda, and C. d. l. Heras, "Optical and

- structural properties in the amorphous to polycrystalline transition in  $\text{Sb}_2\text{S}_3$  thin films,” *J. Phys. D: Appl. Phys.*, 40, 2440–2444, 2007.
- [174] S. Pawar, B. Pawar, J. Kim, O.-S. Joo, and C. Lokhande, “Recent status of chemical bath deposited metal chalcogenide and metal oxide thin films,” *Curr. Appl Phys.*, 11, 117–161, 2011.
- [175] N. Maiti, S. H. Im, C.-S. Lim, and S. I. Seok, “A chemical precursor for depositing  $\text{Sb}_2\text{S}_3$  onto mesoporous  $\text{TiO}_2$  layers in nonaqueous media and its application to solar cells,” *Dalton Trans.*, 41, 11569, 2012.
- [176] K. C. Gödel, Y. C. Choi, B. Roose, A. Sadhanala, H. J. Snaith, S. I. Seok, U. Steiner, and S. K. Pathak, “Efficient room temperature aqueous  $\text{Sb}_2\text{S}_3$  synthesis for inorganic-organic sensitized solar cells with 5.1
- [177] K. C. Gödel, B. Roose, A. Sadhanala, Y. Vaynzof, S. K. Pathak, and U. Steiner, “Partial oxidation of the absorber layer reduces charge carrier recombination in antimony sulfide solar cells,” *Phys. Chem. Chem. Phys.*, 19, 1425–1430, 2017.
- [178] E. K. Gil, S.-J. Lee, S.-J. Sung, K. Y. Cho, and D.-H. Kim, “Spin-coating process of an inorganic  $\text{Sb}_2\text{S}_3$  thin film for photovoltaic applications,” *J. Nanosci. Nanotechnol.*, 16, 10763–10766, 2016.
- [179] R. H. Bube, “Photoelectronic analysis of high resistivity crystals: (a) GaAs, (b)  $\text{Sb}_2\text{S}_3$ ,” *J. Appl. Phys.*, 31, 315–322, 1960.
- [180] B. Roy, B. Chakraborty, R. Bhattacharya, and A. Dutta, “Electrical and magnetic properties of antimony sulphide ( $\text{Sb}_2\text{S}_3$ ) crystals and the mechanism of carrier transport in it,” *Solid State Commun.*, 25, 937–940, 1978.
- [181] N. Ţigaşu, C. Gheorghies, G. Rusu, and S. Condurache-Bota, “The influence of the post-deposition treatment on some physical properties of  $\text{Sb}_2\text{S}_3$  thin films,” *J. Non-Cryst. Solids*, 351, 987–992, 2005.
- [182] J. George and M. Radhakrishnan, “Electrical conduction in coevaporated antimony trisulphide films,” *Solid State Commun.*, 33, 987–989, 1980.
- [183] C. P. Liu, H. E. Wang, T. W. Ng, Z. H. Chen, W. F. Zhang, C. Yan, Y. B. Tang, I. Bello, L. Martinu, W. J. Zhang, and S. K. Jha, “Hybrid photovoltaic cells based on  $\text{ZnO}/\text{Sb}_2\text{S}_3/\text{P3HT}$  heterojunctions,” *phys. stat. sol. (b)*, 249,

## Bibliography

- 627–633, 2011.
- [184] B. Nayak and H. Acharya, “Electrical and thermoelectric properties of  $\text{Sb}_2\text{S}_3$  thin films prepared by the dip-dry method,” *Thin Solid Films*, 122, 93–103, 1984.
- [185] D. U. Lee, S. W. Pak, S. G. Cho, E. K. Kim, and S. I. Seok, “Defect states in hybrid solar cells consisting of  $\text{Sb}_2\text{S}_3$  quantum dots and  $\text{TiO}_2$  nanoparticles,” *Appl. Phys. Lett.*, 103, 023901, 2013.
- [186] B. E. Pieters, K. Decock, M. Burgelman, R. Stangl, and T. Kirchartz, “One-dimensional electro-optical simulations of thin-film solar cells,” in *Advanced Characterization Techniques for Thin Film Solar Cells*. Wiley-VCH Verlag GmbH & Co. KGaA, 2016, 633–657.
- [187] T. Kirchartz and J. Nelson, “Device modelling of organic bulk heterojunction solar cells,” *Top. Curr. Chem.*, 352, 279, 2014.
- [188] G. F. Burkhard, E. T. Hoke, and M. D. McGehee, “Accounting for interference, scattering, and electrode absorption to make accurate internal quantum efficiency measurements in organic and other thin solar cells,” *Adv. Mater.*, 22, 3293, 2010.
- [189] D. Kiermasch, A. Baumann, M. Fischer, V. Dyakonov, and K. Tvingstedt, “Revisiting lifetimes from transient electrical characterization of thin film solar cells; a capacitive concern evaluated for silicon, organic and perovskite devices,” *Energy & Envir. Sci.*, 11, 629–640, 2018.
- [190] S. Wang, P. Kaienburg, B. Klingebiel, D. Schillings, and T. Kirchartz, “Understanding thermal admittance spectroscopy in low-mobility semiconductors,” *J. Phys. Chem. C*, 122, 9795–9803, 2018.
- [191] B. Krogmeier, F. Staub, D. Grabowski, U. Rau, and T. Kirchartz, “Quantitative analysis of the transient photoluminescence of  $\text{CH}_3\text{NH}_3\text{PbI}_3/\text{PC61BM}$  heterojunctions by numerical simulations,” *Sust. Energy & Fuels*, 2, 1027–1034, 2018.
- [192] K. Wang, C. Liu, T. Meng, C. Yi, and X. Gong, “Inverted organic photovoltaic cells,” *Chem. Soc. Rev.*, 45, 2937–2975, 2016.
- [193] B. Walker, H. Choi, and J. Y. Kim, “Interfacial engineering for highly

- efficient organic solar cells,” *Curr. Appl Phys.*, 17, 370–391, 2017.
- [194] D. Baran, T. Kirchartz, S. Wheeler, S. Dimitrov, M. Abdelsamie, J. Gorman, R. S. Ashraf, S. Holliday, A. Wadsworth, N. Gasparini, P. Kaienburg, H. Yan, A. Amassian, C. J. Brabec, J. R. Durrant, and I. McCulloch, “Reduced voltage losses yield 10% efficient fullerene free organic solar cells with >1 v open circuit voltages,” *Energy & Envir. Sci.*, 9, 3783–3793, 2016.
- [195] M. Kröger, S. Hamwi, J. Meyer, T. Riedl, W. Kowalsky, and A. Kahn, “Role of the deep-lying electronic states of MoO<sub>3</sub> in the enhancement of hole-injection in organic thin films,” *Appl. Phys. Lett.*, 95, 123301, 2009.
- [196] G. Yang, H. Tao, P. Qin, W. Ke, and G. Fang, “Recent progress in electron transport layers for efficient perovskite solar cells,” *J. Mater. Chem.A*, 4, 3970–3990, 2016.
- [197] C. Sima, C. Grigoriu, and S. Antohe, “Comparison of the dye-sensitized solar cells performances based on transparent conductive ITO and FTO,” *Thin Solid Films*, 519, 595–597, 2010.
- [198] M. Droichi, F. Vaillant, E. Bustarret, and D. Jousse, “Study of localized states in amorphous chalcogenide Sb<sub>2</sub>S<sub>3</sub> films,” *J. Non-Cryst. Solids*, 101, 151–155, 1988.
- [199] N. Sommer, “Conductivity and Structure of Sputtered ZnO:Al on Flat and Textured Substrates for Thin-Film Solar Cells,” Dr., RWTH Aachen University, Jülich, 2016, rWTH Aachen University, Diss., 2016. [Online]. Available: <http://juser.fz-juelich.de/record/818286>
- [200] M. Nuys, “Characterization & Modification of Copper and Iron Oxide Nanoparticles for Application as Absorber Material in Silicon based Thin Film Solar Cells,” Dr., RWTH Aachen University, Jülich, 2015, rWTH Aachen University, Diss., 2015. [Online]. Available: <http://juser.fz-juelich.de/record/276128>
- [201] W. B. Jackson, N. M. Amer, A. Boccara, and D. Fournier, “Photothermal deflection spectroscopy and detection,” *Appl. Opt.*, 20, 1333–1344, 1981.
- [202] T. C. M. Müller and T. Kirchartz, “Absorption and photocurrent spectroscopy with high dynamic range,” in *Advanced Characterization Techniques for Thin*

## Bibliography

- Film Solar Cells*. Wiley-VCH Verlag GmbH & Co. KGaA, 2016, 189–214.
- [203] G. D. Cody, T. Tiedje, B. Abeles, B. Brooks, and Y. Goldstein, “Disorder and the optical-absorption edge of hydrogenated amorphous silicon,” *Phys. Rev. Lett.*, 47, 1480–1483, 1981.
- [204] W. B. Jackson and N. M. Amer, “Direct measurement of gap-state absorption in hydrogenated amorphous silicon by photothermal deflection spectroscopy,” *Phys. Rev. B*, 25, 5559, 1982.
- [205] T. Tiedje, J. M. Cebulka, D. L. Morel, and B. Abeles, “Evidence for exponential band tails in amorphous silicon hydride,” *Phys. Rev. Lett.*, 46, 1425–1428, 1981.
- [206] P. Kaienburg, “Entwicklung eines messsystems zur schnellen bestimmung der quanteneffizienz von solarzellen,” Master’s thesis, RWTH Aachen University, 2010.
- [207] U. Rau, “Reciprocity relation between photovoltaic quantum efficiency and electroluminescent emission of solar cells,” *Phys. Rev. B*, 76, 2007.
- [208] T. Kirchartz, V. Huhn, A. Gerber, B. E. Pieters, and U. Rau, “Electroluminescence analysis of solar cells and solar modules,” in *Advanced Characterization Techniques for Thin Film Solar Cells*. Wiley-VCH Verlag GmbH & Co. KGaA, 2016, 71–92.
- [209] J.-P. Correa-Baena, A. Abate, M. Saliba, W. Tress, T. J. Jacobsson, M. Grätzel, and A. Hagfeldt, “The rapid evolution of highly efficient perovskite solar cells,” *Energy & Envir. Sci.*, 10, 710–727, 2017.
- [210] R. Kondrotas, C. Chen, and J. Tang, “Sb 2 s 3 solar cells,” *Joule*, 2, 857–878, 2018.
- [211] N. M. Mangan, R. E. Brandt, V. Steinmann, R. Jaramillo, C. Yang, J. R. Poindexter, R. Chakraborty, H. H. Park, X. Zhao, R. G. Gordon, and T. Buonassisi, “Framework to predict optimal buffer layer pairing for thin film solar cell absorbers: A case study for tin sulfide/zinc oxysulfide,” *J. Appl. Phys.*, 118, 115102, 2015.
- [212] Y. Li, B. Ding, Q.-Q. Chu, G.-J. Yang, M. Wang, C.-X. Li, and C.-J. Li, “Ultra-high open-circuit voltage of perovskite solar cells induced by nucleation

- thermodynamics on rough substrates,” *Sci. Rep.*, 7, 46141, 2017.
- [213] S. Dongaonkar, J. D. Servaites, G. M. Ford, S. Loser, J. Moore, R. M. Gelfand, H. Mohseni, H. W. Hillhouse, R. Agrawal, M. A. Ratner, T. J. Marks, M. S. Lundstrom, and M. A. Alam, “Universality of non-ohmic shunt leakage in thin-film solar cells,” *J. Appl. Phys.*, 108, 124509, 2010.
- [214] K. Shen, C. Ou, T. Huang, H. Zhu, J. Li, Z. Li, and Y. Mai, “Mechanisms and modification of nonlinear shunt leakage in sb2se3 thin film solar cells,” *Sol. Energy Mater. Sol. Cells*, 186, 58–65, 2018.
- [215] O. Breitenstein, K. Iwig, and I. Kononov, “Evaluation of local electrical parameters of solar cells by dynamic (lock-in) thermography,” *phys. stat. sol. (a)*, 160, 271–282, 1997.
- [216] *Identification of Factors Reducing Voc in MC Silicon Solar Cells*. IEEE, 1996.
- [217] O. Breitenstein, J. Bauer, T. Trupke, and R. A. Bardos, “On the detection of shunts in silicon solar cells by photo- and electroluminescence imaging,” *Prog. Photovoltaics Res. Appl.*, 16, 325–330, 2008.
- [218] O. Breitenstein, J. Rakotoniaina, S. Neve, M. Al Rifai, and M. Werner, “Shunt types in multicrystalline solar cells,” 1, 987–990, 2003.
- [219] S. Dongaonkar, S. Loser, E. J. Sheets, K. Zaunbrecher, R. Agrawal, T. J. Marks, and M. A. Alam, “Universal statistics of parasitic shunt formation in solar cells, and its implications for cell to module efficiency gap,” *Energy & Envir. Sci.*, 6, 782–787, 2013.
- [220] B. Pieters. <https://github.com/iek-5> (accessed august 17, 2018). [Online]. Available: <https://github.com/IEK-5>
- [221] B. E. Pieters, “A free and open source finite-difference simulation tool for solar modules,” 1370–1375, 2014.
- [222] P. Kaienburg, P. Hartnagel, B. E. Pieters, J. Yu, D. Grabowski, Z. Liu, J. Haddad, U. Rau, and T. Kirchartz, “How contact layers control shunting losses from pinholes in thin-film solar cells,” *J. Phys. Chem. C*, 122, 27 263–27 272, 2018.
- [223] C. Bi, Q. Wang, Y. Shao, Y. Yuan, Z. Xiao, and J. Huang, “Non-wetting

## Bibliography

- surface-driven high-aspect-ratio crystalline grain growth for efficient hybrid perovskite solar cells,” *Nat. Commun.*, 6, 7747, 2015.
- [224] R. Brendel and R. Peibst, “Contact selectivity and efficiency in crystalline silicon photovoltaics,” *IEEE Journal of Photovoltaics*, 6, 1413–1420, 2016.
- [225] P. O. Grabitz, U. Rau, and J. H. Werner, “Modeling of spatially inhomogeneous solar cells by a multi-diode approach,” *phys. stat. sol. (a)*, 202, 2920–2927, 2005.
- [226] Y. Roussillon, D. M. Giolando, D. Shvydka, A. D. Compaan, and V. G. Karpov, “Blocking thin-film nonuniformities: Photovoltaic self-healing,” *Appl. Phys. Lett.*, 84, 616–618, 2004.
- [227] M. M. Tessema and D. M. Giolando, “Pinhole treatment of a CdTe photovoltaic device by electrochemical polymerization technique,” *Sol. Energy Mater. Sol. Cells*, 107, 9–12, 2012.
- [228] Q. Lin, A. Armin, D. M. Lyons, P. L. Burn, and P. Meredith, “Low noise, IR-blind organohalide perovskite photodiodes for visible light detection and imaging,” *Adv. Mater.*, 27, 2060–2064, 2015.
- [229] L. Dou, Y. Yang, J. You, Z. Hong, W.-H. Chang, G. Li, and Y. Yang, “Solution-processed hybrid perovskite photodetectors with high detectivity,” *Nat. Commun.*, 5, 5404s, 2014.
- [230] A. Armin, M. Hamsch, I. K. Kim, P. L. Burn, P. Meredith, and E. B. Namdas, “Thick junction broadband organic photodiodes,” *Laser & Photonics Rev.*, 8, 924–932, 2014.
- [231] J. Peet, L. Wen, P. Byrne, S. Rodman, K. Forberich, Y. Shao, N. Drolet, R. Gaudiana, G. Dennler, and D. Waller, “Bulk heterojunction solar cells with thick active layers and high fill factors enabled by a bithiophene-co-thiazolothiazole push-pull copolymer,” *Appl. Phys. Lett.*, 98, 043301, 2011.
- [232] L. J. A. Koster, V. D. Mihailetschi, and P. W. M. Blom, “Bimolecular recombination in polymer/fullerene bulk heterojunction solar cells,” *Appl. Phys. Lett.*, 88, 052104, 2006.
- [233] M. M. Mandoc, F. B. Kooistra, J. C. Hummelen, B. de Boer, and P. W. M.

- Blom, "Effect of traps on the performance of bulk heterojunction organic solar cells," *Appl. Phys. Lett.*, 91, 263505, 2007.
- [234] R. A. Street, A. Krakaris, and S. R. Cowan, "Recombination through different types of localized states in organic solar cells," *Adv. Funct. Mater.*, 22, 4608, 2012.
- [235] D. Bartesaghi, I. d. C. Pérez, J. Kniepert, S. Roland, M. Turbiez, D. Neher, and L. J. A. Koster, "Competition between recombination and extraction of free charges determines the fill factor of organic solar cells," *Nat. Commun.*, 6, 7083, 2015.
- [236] P. Kaienburg, U. Rau, and T. Kirchartz, "Extracting information about the electronic quality of organic solar-cell absorbers from fill factor and thickness," *Phys. Rev. Appl.*, 6, 024001–1, 2016.
- [237] T. Kirchartz, B. E. Pieters, J. Kirkpatrick, U. Rau, and J. Nelson, "Recombination via tail states in polythiophene:fullerene solar cells," *Phys. Rev. B*, 83, 115209, 2011.
- [238] T. Kirchartz, B. E. Pieters, K. Taretto, and U. Rau, "Electro-optical modeling of bulk heterojunction solar cells," *J. Appl. Phys.*, 104, 094513, 2008.
- [239] L. J. A. Koster, E. C. P. Smits, V. D. Mihailetschi, and P. W. M. Blom, "Device model for the operation of polymer/fullerene bulk heterojunction solar cells," *Phys. Rev. B*, 72, 085205, 2005.
- [240] L. A. A. Pettersson, L. S. Roman, and O. Inganäs, "Modeling photocurrent action spectra of photovoltaic devices based on organic thin films," *J. Appl. Phys.*, 86, 487, 1999.
- [241] W. Li, K. H. Hendriks, A. Furlan, W. S. C. Roelofs, M. M. Wienk, and R. A. J. Janssen, "Universal correlation between fibril width and quantum efficiency in diketopyrrolopyrrole-based polymer solar cells," *J. Am. Chem. Soc.*, 135, 18942, 2013.
- [242] S. C. Price, A. C. Stuart, L. Yang, H. Zhou, and W. You, "Fluorine substituted conjugated polymer of medium band gap yields 7% efficiency in polymer-fullerene solar cells," *J. Am. Chem. Soc.*, 133, 4625, 2011.

## Bibliography

- [243] C. Deibel, A. Baumann, and V. Dyakonov, "Polaron recombination in pristine and annealed bulk heterojunction solar cells," *Appl. Phys. Lett.*, **93**, 163303, 2008.
- [244] G. Lakhwani, A. Rao, and R. H. Friend, "Bimolecular recombination in organic photovoltaics," *Annu. Rev. Phys. Chem.*, **65**, 557, 2014.
- [245] Y. Liang, Z. Xu, J. Xia, S.-T. Tsai, Y. Wu, G. Li, C. Ray, and L. Yu, "For the bright future-bulk heterojunction polymer solar cells with power conversion efficiency of 7.4%," *Adv. Mater.*, **22**, E135, 2010.
- [246] C. M. Proctor, C. Kim, D. Neher, and T.-Q. Nguyen, "Nongeminate recombination and charge transport limitations in diketopyrrolopyrrole-based solution-processed small molecule solar cells," *Adv. Funct. Mater.*, **23**, 3584, 2013.
- [247] C. G. Shuttle, B. O'Regan, A. M. Ballantyne, J. Nelson, D. D. C. Bradley, and J. R. Durrant, "Bimolecular recombination losses in polythiophene: Fullerene solar cells," *Phys. Rev. B*, **78**, 113201, 2008.
- [248] D. Credgington, F. C. Jamieson, B. Walker, T.-Q. Nguyen, and J. R. Durrant, "Quantification of geminate and non-geminate recombination losses within a solution-processed small-molecule bulk heterojunction solar cell," *Adv. Mater.*, **24**, 2135, 2012.
- [249] J. Kniepert, I. Lange, J. Heidbrink, J. Kurpiers, T. J. K. Brenner, L. J. A. Koster, and D. Neher, "Effect of solvent additive on generation, recombination, and extraction in PTB7:PCBM solar cells: A conclusive experimental and numerical simulation study," *J. Phys. Chem. C*, **119**, 8310, 2015.
- [250] A. Maurano, R. Hamilton, C. G. Shuttle, A. M. Ballantyne, J. Nelson, B. O'Regan, W. Zhang, I. McCulloch, H. Azimi, M. Morana, C. J. Brabec, and J. R. Durrant, "Recombination dynamics as a key determinant of open circuit voltage in organic bulk heterojunction solar cells: A comparison of four different donor polymers," *Adv. Mater.*, **22**, 4987, 2010.
- [251] G. Juska, K. Arlauskas, J. Stuchlik, and R. Österbacka, "Non-langevin bimolecular recombination in low-mobility materials," *J. Non-Cryst. Sol.*,

- 352, 1167, 2006.
- [252] R. S. Crandall and I. Balberg, "Mobility-lifetime products in hydrogenated amorphous silicon," *Appl. Phys. Lett.*, 58, 508, 1991.
- [253] A. Baumann, J. Lorrmann, D. Rauh, C. Deibel, and V. Dyakonov, "A new approach for probing the mobility and lifetime of photogenerated charge carriers in organic solar cells under real operating conditions," *Adv. Mater.*, 24, 4381, 2012.
- [254] A. Pivrikas, N. S. Sariciftci, G. Juska, and R. Österbacka, "A review of charge transport and recombination in polymer/fullerene organic solar cells," *Prog. Photovoltaics Res. Appl.*, 15, 677, 2007.
- [255] X. Guo, N. Zhou, S. J. Lou, J. Smith, D. B. Tice, J. W. Hennek, R. P. Ortiz, J. T. L. Navarrete, S. Li, J. Strzalka, L. X. Chen, R. P. H. Chang, A. Facchetti, and T. J. Marks, "Polymer solar cells with enhanced fill factors," *Nat. Phot.*, 7, 825, 2013.
- [256] O. J. Sandberg, M. Nyman, and R. Österbacka, "Effect of contacts in organic bulk heterojunction solar cells," *Phys. Rev. Appl.*, 1, 024003, 2014.
- [257] Z. Tang, W. Tress, Q. Bao, M. J. Jafari, J. Bergqvist, T. Ederth, M. R. Andersson, and O. Inganäs, "Improving cathodes with a polymer interlayer in reversed organic solar cells," *Adv. Energy Mater.*, 4, 1400643, 2014.
- [258] V. D. Mihailetschi, J. Wildeman, and P. W. M. Blom, "Space-charge limited photocurrent," *Phys. Rev. Lett.*, 94, 126602, 2005.
- [259] G. F. A. Dibb, M.-A. Muth, T. Kirchartz, S. Engmann, H. Hoppe, G. Gobsch, M. Thelakkat, N. Blouin, S. Tierney, M. Carrasco-Orozco, J. R. Durrant, and J. Nelson, "Influence of doping on charge carrier collection in normal and inverted geometry polymer:fullerene solar cells," *Sci. Rep.*, 3, 3335, 2013.
- [260] T. Kirchartz and J. Nelson, "Meaning of reaction orders in polymer:fullerene solar cells," *Phys. Rev. B*, 86, 165201, 2012.
- [261] V. A. Trukhanov, V. V. Bruevich, and D. Y. Paraschuk, "Effect of doping on performance of organic solar cells," *Phys. Rev. B*, 84, 205318, 2011.
- [262] C. M. Proctor, J. A. Love, and T.-Q. Nguyen, "Mobility guidelines for high

## Bibliography

- fill factor solution-processed small molecule solar cells,” *Adv. Mater.*, 26, 5957, 2014.
- [263] J. G. Tait, U. W. Paetzold, D. Cheyns, M. Turbiez, P. Heremans, and B. P. Rand, “Interfacial depletion regions: Beyond the space charge limit in thick bulk heterojunctions,” *Am. Chem. Soc. Appl. Mater. Interf.*, 8, 2211, 2016.
- [264] H. Azimi, A. Senes, M. C. Scharber, K. Hingerl, and C. J. Brabec, “Charge transport and recombination in low-bandgap bulk heterojunction solar cell using bis-adduct fullerene,” *Adv. Energy Mater.*, 1, 1162, Oct 2011.
- [265] Z. Chen, P. Cai, J. Chen, X. Liu, L. Zhang, L. Lan, J. Peng, Y. Ma, and Y. Cao, “Low band-gap conjugated polymers with strong interchain aggregation and very high hole mobility towards highly efficient thick-film polymer solar cells,” *Adv. Mater.*, 26, 2586, 2014.
- [266] Y. Liu, J. Zhao, Z. Li, C. Mu, W. Ma, H. Hu, K. Jiang, H. Lin, H. Ade, and H. Yan, “Aggregation and morphology control enables multiple cases of high-efficiency polymer solar cells,” *Nat. Commun.*, 5, 5293, 2014.
- [267] T. L. Nguyen, H. Choi, S.-J. Ko, M. A. Uddin, B. Walker, S. Yum, J.-E. Jeong, M. H. Yun, T. J. Shin, S. Hwang, J. Kim, and H. Woo, “Semi-crystalline photovoltaic polymers with efficiency exceeding 9% in a ~300 nm thick conventional single-cell device,” *Energ. Environ. Sci.*, 7, 3040, 2014.
- [268] G. Dieker, M. P. de Haas, J. M. Warman, D. M. de Leeuw, and L. D. A. Siebbeles, “The disperse charge-carrier kinetics in regioregular poly(3-hexylthiophene),” *J. Phys. Chem. B*, 108, 17818, 2004.
- [269] Z. Liang, A. Nardes, D. Wang, J. J. Berry, and B. A. Gregg, “Defect engineering in pi-conjugated polymers,” *Chem. Mater.*, 21, 4914, 2009.
- [270] H.-H. Liao, C.-M. Yang, C.-C. Liu, S.-F. Horng, H.-F. Meng, and J.-T. Shy, “Dynamics and reversibility of oxygen doping and de-doping for conjugated polymer,” *J. Appl. Phys.*, 103, 104506, 2008.
- [271] S. Schiefer, B. Zimmermann, and U. Würfel, “Determination of the intrinsic and the injection dependent charge carrier density in organic solar cells using the suns-voc method,” *J. Appl. Phys.*, 115, 044506, 2014.

- [272] J. Liang, E. A. Schiff, S. Guha, B. Yan, and J. Yang, "Hole-mobility limit of amorphous silicon solar cells," *Appl. Phys. Lett.*, 88, 063512, 2006.
- [273] G. Garcia-Belmonte, A. Munar, E. M. Barea, J. Bisquert, I. Ugarte, and R. Pacios, "Charge carrier mobility and lifetime of organic bulk heterojunctions analyzed by impedance spectroscopy," *Org. Electron.*, 9, 847, 2008.
- [274] M. Stolterfoht, A. Armin, B. Philippa, R. D. White, P. L. Burn, P. Meredith, G. Juska, and A. Pivrikas, "Photocarrier drift distance in organic solar cells and photodetectors," *Sci. Rep.*, 5, 9949, 2015.
- [275] J. Bisquert and G. Garcia-Belmonte, "On voltage, photovoltage, and photocurrent in bulk heterojunction organic solar cells," *J. Phys. Chem. Lett.*, 2, 1950, 2011.
- [276] G. Garcia-Belmonte, A. Guerrero, and J. Bisquert, "Elucidating operating modes of bulk-heterojunction solar cells from impedance spectroscopy analysis," *J. Phys. Chem. Lett.*, 4, 877, 2013.
- [277] M. S. Vezie, S. Few, I. Meager, G. Pieridou, B. Dörfling, R. S. Ashraf, A. R. Goñi, H. Bronstein, I. McCulloch, S. C. Hayes, M. Campoy-Quiles, and J. Nelson, "Exploring the origin of high optical absorption in conjugated polymers," *Nat. Mater.*, 15, 746–753, 2016.
- [278] B. Pieters, J. Krc, and M. Zeman, "Advanced numerical simulation tool for solar cells-asa5," in *Photovoltaic Energy Conversion, Conference Record of the 2006 IEEE 4th World Conference on*, 2. IEEE, 2006, 1513–1516.
- [279] D. Credgington, R. Hamilton, P. Atienzar, J. Nelson, and J. R. Durrant, "Non-geminate recombination as the primary determinant of open-circuit voltage in polythiophene: Fullerene blend solar cells: An analysis of the influence of device processing conditions," *Adv. Funct. Mater.*, 21, 2744–2753, 2011.
- [280] B. Guo, W. Li, X. Guo, X. Meng, W. Ma, M. Zhang, and Y. Li, "High efficiency nonfullerene polymer solar cells with thick active layer and large area," *Adv. Mater.*, 29, 1702291, 2017.
- [281] L. Krückemeier, P. Kaienburg, J. Flohre, K. Bittkau, I. Zonno, B. Krogmeier,

## Bibliography

- and T. Kirchartz, “Developing design criteria for organic solar cells using well-absorbing non-fullerene acceptors,” *Commun. Phys.*, 1, 2018.
- [282] R. Brüggemann, “Steady-state photocarrier grating method,” in *Advanced Characterization Techniques for Thin Film Solar Cells*. Wiley-VCH Verlag GmbH & Co. KGaA, 2016, 163–188.
- [283] P. Kaienburg, B. Klingebiel, and T. Kirchartz, “Spin-coated planar  $\text{Sb}_2\text{S}_3$  hybrid solar cells approaching 5% efficiency,” *Beilstein J. Nanotechnol.*, 9, 2114–2124, 2018.
- [284] R. Parize, T. Cossuet, O. Chaix-Pluchery, H. Roussel, E. Appert, and V. Consonni, “In situ analysis of the crystallization process of  $\text{Sb}_2\text{S}_3$  thin films by Raman scattering and x-ray diffraction,” *Materials & Design*, 121, 1–10, 2017.
- [285] P. Sereni, M. Musso, P. Knoll, P. Blaha, K. Schwarz, G. Schmidt, P. M. Champion, and L. D. Ziegler, “Polarization-dependent Raman characterization of stibnite ( $\text{sb}_2\text{s}_3$ ).” AIP, 2010.
- [286] C. P. Liu, Z. H. Chen, H. E. Wang, S. K. Jha, W. J. Zhang, I. Bello, and J. A. Zapien, “Enhanced performance by incorporation of zinc oxide nanowire array for organic-inorganic hybrid solar cells,” *Appl. Phys. Lett.*, 100, 243102, 2012.
- [287] J. Escorcia-García, D. Becerra, M. Nair, and P. Nair, “Heterojunction  $\text{CdS}/\text{Sb}_2\text{S}_3$  solar cells using antimony sulfide thin films prepared by thermal evaporation,” *Thin Solid Films*, 569, 28–34, 2014.
- [288] J. A. Chang, S. H. Im, Y. H. Lee, H. jung Kim, C.-S. Lim, J. H. Heo, and S. I. Seok, “Panchromatic photon-harvesting by hole-conducting materials in inorganic–organic heterojunction sensitized-solar cell through the formation of nanostructured electron channels,” *Nano Lett.*, 12, 1863–1867, 2012.
- [289] Z. Qiu, C. Liu, G. Pan, W. Meng, W. Yue, J. Chen, X. Zhou, F. Zhang, and M. Wang, “Solution-processed solar cells based on inorganic bulk heterojunctions with evident hole contribution to photocurrent generation,” *Phys. Chem. Chem. Phys.*, 17, 12328, 2015.
- [290] R. B. Yang, N. Zakharov, O. Moutanabbir, K. Scheerschmidt, L.-M. Wu,

- U. Gösele, J. Bachmann, and K. Nielsch, "The transition between conformal atomic layer epitaxy and nanowire growth," *J. Am. Chem. Soc.*, 132, 7592–7594, 2010.
- [291] V. Zakaznova-Herzog, S. Harmer, H. Nesbitt, G. Bancroft, R. Flemming, and A. Pratt, "High resolution XPS study of the large-band-gap semiconductor stibnite ( $\text{Sb}_2\text{S}_3$ ): Structural contributions and surface reconstruction," *Surf. Sci.*, 600, 348–356, 2006.
- [292] P. P. Boix, G. Larramona, A. Jacob, B. Delatouche, I. Mora-Será, and J. Bisquert, "Hole transport and recombination in all-solid  $\text{Sb}_2\text{S}_3$  -sensitized  $\text{TiO}_2$  solar cells using  $\text{CuSCN}$  as hole transporter," *J. Phys. Chem. C*, 116, 1579–1587, 2012.
- [293] E. Zhou, J. Cong, Q. Wei, K. Tajima, C. Yang, and K. Hashimoto, "All-polymer solar cells from perylene diimide based copolymers: Material design and phase separation control," *Angew. Chem. Int. Ed.*, 50, 2799–2803, 2011.
- [294] Z.-L. Guan, J. B. Kim, H. Wang, C. Jaye, D. A. Fischer, Y.-L. Loo, and A. Kahn, "Direct determination of the electronic structure of the poly(3-hexylthiophene):phenyl-[6,6]-C61 butyric acid methyl ester blend," *Org. Electron.*, 11, 1779–1785, 2010.
- [295] S. Sweetnam, K. R. Graham, G. O. N. Ndjawa, T. Heumüller, J. A. Bartelt, T. M. Burke, W. Li, W. You, A. Amassian, and M. D. McGehee, "Characterization of the polymer energy landscape in polymer:fullerene bulk heterojunctions with pure and mixed phases," *J. Am. Chem. Soc.*, 136, 14078–14088, 2014.
- [296] J. You, L. Dou, K. Yoshimura, T. Kato, K. Ohya, T. Moriarty, K. Emery, C.-C. Chen, J. Gao, G. Li, and Y. Yang, "A polymer tandem solar cell with 10.6% power conversion efficiency," *Nat. Commun.*, 4, 2013.
- [297] S.-H. Liao, H.-J. Jhuo, Y.-S. Cheng, and S.-A. Chen, "Fullerene derivative-doped zinc oxide nanofilm as the cathode of inverted polymer solar cells with low-bandgap polymer (PTB7-th) for high performance," *Advanced Materials*, 25, 4766–4771, 2013.

## Bibliography

- [298] N. J. Jeon, J. Lee, J. H. Noh, M. K. Nazeeruddin, M. Grätzel, and S. I. Seok, "Efficient inorganic–organic hybrid perovskite solar cells based on pyrene arylamine derivatives as hole-transporting materials," *Journal of the American Chemical Society*, 135, 19 087–19 090, 2013.
- [299] A. Krishna, D. Sabba, H. Li, J. Yin, P. P. Boix, C. Soci, S. G. Mhaisalkar, and A. C. Grimsdale, "Novel hole transporting materials based on triptycene core for high efficiency mesoscopic perovskite solar cells," *Chem. Sci.*, 5, 2702–2709, 2014.
- [300] N. Blouin, A. Michaud, and M. Leclerc, "A low-bandgap poly(2,7-carbazole) derivative for use in high-performance solar cells," *Advanced Materials*, 19, 2295–2300, 2007.
- [301] H.-L. Yip and A. K.-Y. Jen, "Recent advances in solution-processed interfacial materials for efficient and stable polymer solar cells," *Energy & Envir. Sci.*, 5, 5994, 2012.
- [302] R. Tang, X. Wang, C. Jiang, S. Li, G. Jiang, S. Yang, C. Zhu, and T. Chen, "Vacuum assisted solution processing for highly efficient  $\text{sb}_2\text{s}_3$  solar cells," *J. Mater. Chem.A*, 6, 16 322–16 327, 2018.
- [303] S. Li, Y. Zhang, R. Tang, X. Wang, T. Zhang, G. Jiang, W. Liu, C. Zhu, and T. Chen, "Aqueous-solution-based approach towards carbon-free  $\text{sb}_2\text{s}_3$  films for high efficiency solar cells," *Chem. Sus. Chem.*, 11, 3208–3214, 2018.
- [304] R. Tang, X. Wang, C. Jiang, S. Li, W. Liu, H. Ju, S. Yang, C. Zhu, and T. Chen, "n-type doping of  $\text{Sb}_2\text{S}_3$  light-harvesting films enabling high-efficiency planar heterojunction solar cells," *ACS Applied Materials & Interfaces*, 10, 30 314–30 321, 2018.
- [305] L. Zhang, C. Jiang, C. Wu, H. Ju, G. Jiang, W. Liu, C. Zhu, and T. Chen, " $\text{V}_2\text{o}_5$  as hole transporting material for efficient all inorganic  $\text{Sb}_2\text{S}_3$  solar cells," *ACS Applied Materials & Interfaces*, 10, 27 098–27 105, 2018.
- [306] M. A. Tumelero, R. Faccio, and A. A. Pasa, "Unraveling the native conduction of trichalcogenides and its ideal band alignment for new photovoltaic interfaces," *J. Phys. Chem. C*, 120, 1390–1399, 2016.
- [307] T. Chen, "Solution processed antimony sulfide-selenide  $[\text{sb}_2(\text{s},\text{se})_3]$  for high

- efficiency solar cells,” in *2018 IEEE International Conference on Electron Devices and Solid State Circuits (EDSSC)*. IEEE, 2018.
- [308] W. S. Yang, B.-W. Park, E. H. Jung, N. J. Jeon, Y. C. Kim, D. U. Lee, S. S. Shin, J. Seo, E. K. Kim, J. H. Noh, and S. I. Seok, “Iodide management in formamidinium-lead-halide-based perovskite layers for efficient solar cells,” *Science*, 356, 1376–1379, 2017.
- [309] M. Saliba, T. Matsui, J.-Y. Seo, K. Domanski, J.-P. Correa-Baena, M. K. Nazeeruddin, S. M. Zakeeruddin, W. Tress, A. Abate, A. Hagfeldt, and M. Grätzel, “Cesium-containing triple cation perovskite solar cells: Improved stability, reproducibility and high efficiency,” *Energy & Envir. Sci.*, 9, 1989–1997, 2016.
- [310] I. Kaiser, K. Ernst, C.-H. Fischer, R. Könenkamp, C. Rost, I. Sieber, and M. Lux-Steiner, “The eta-solar cell with CuInS<sub>2</sub>: A photovoltaic cell concept using an extremely thin absorber (eta),” *Sol. Energy Mater. Sol. Cells*, 67, 89–96, 2001.
- [311] K. Taretto and U. Rau, “Modeling extremely thin absorber solar cells for optimized design,” *Prog. Photovoltaics Res. Appl.*, 12, 573–591, 2004.
- [312] U. Rau and J. H. Werner, “Radiative efficiency limits of solar cells with lateral band-gap fluctuations,” *Appl. Phys. Lett.*, 84, 3735–3737, 2004.
- [313] J. Yao, T. Kirchartz, M. S. Vezie, M. A. Faist, W. Gong, Z. He, H. Wu, J. Troughton, T. Watson, D. Bryant, and J. Nelson, “Quantifying losses in open-circuit voltage in solution-processable solar cells,” *Phys. Rev. Appl.*, 4, 2015.
- [314] C. Chen, D. C. Bobela, Y. Yang, S. Lu, K. Zeng, C. Ge, B. Yang, L. Gao, Y. Zhao, M. C. Beard, and J. Tang, “Characterization of basic physical properties of sb<sub>2</sub>se<sub>3</sub> and its relevance for photovoltaics,” *Frontiers of Optoelectronics*, 10, 18–30, 2017.
- [315] A. Farid and A. Bekheet, “AC conductivity and dielectric properties of Sb<sub>2</sub>S<sub>3</sub> films,” *Vacuum*, 59, 932–939, 2000.
- [316] “Antimony sulfide (Sb<sub>2</sub>S<sub>3</sub>) dielectric constants,” in *Non-Tetrahedrally Bonded Elements and Binary Compounds I*. Springer-Verlag, 1–7.

## Bibliography

- [317] A. Darga, D. Mencaraglia, C. Longeaud, T. J. Savenije, B. O'Regan, S. Bourdais, T. Muto, B. Delatouche, and G. Dennler, "On charge carrier recombination in  $\text{Sb}_2\text{S}_3$  and its implication for the performance of solar cells," *J. Phys. Chem. C*, 117, 20 525–20 530, 2013.
- [318] K. Lips, M. Fehr, and J. Behrends, "Electron-spin resonance (ESR) in hydrogenated amorphous silicon (a-si:h)," in *Advanced Characterization Techniques for Thin Film Solar Cells*. Wiley-VCH Verlag GmbH & Co. KGaA, 2016, 299–342.
- [319] J. Heath and P. Zabierowski, "Capacitance spectroscopy of thin-film solar cells," in *Advanced Characterization Techniques for Thin Film Solar Cells*. Wiley-VCH Verlag GmbH & Co. KGaA, 2016, 93–119.
- [320] V. Hoffmann, D. Klemm, V. Brackmann, C. Venzago, A. A. Rockett, T. Wirth, T. Nunney, C. A. Kaufmann, R. Caballero, and O. Cojocaru-Mirédin, "Accessing elemental distributions in thin films for solar cells," in *Advanced Characterization Techniques for Thin Film Solar Cells*. Wiley-VCH Verlag GmbH & Co. KGaA, 2016, 523–567.
- [321] Y. Wang, D. Qian, Y. Cui, H. Zhang, J. Hou, K. Vandewal, T. Kirchartz, and F. Gao, "Optical gaps of organic solar cells as a reference for comparing voltage losses," *Adv. Energy Mater.*, 8, 1801352, 2018.
- [322] S. Siebentritt, G. Rey, A. Finger, D. Regesch, J. Sessler, T. P. Weiss, and T. Bertram, "What is the bandgap of kesterite?" *Solar Energy Materials and Solar Cells*, 158, 126–129, 2016.
- [323] D. Yang, H. Sasabe, T. Sano, and J. Kido, "Low-band-gap small molecule for efficient organic solar cells with a low energy loss below 0.6 eV and a high open-circuit voltage of over 0.9 V," *ACS Energy Lett.*, 2, 2021–2025, 2017.
- [324] K. Kawashima, Y. Tamai, H. Ohkita, I. Osaka, and K. Takimiya, "High-efficiency polymer solar cells with small photon energy loss," *Nat. Commun.*, 6, 2015.
- [325] Y. Li, X. Liu, F.-P. Wu, Y. Zhou, Z.-Q. Jiang, B. Song, Y. Xia, Z.-G. Zhang, F. Gao, O. Inganäs, Y. Li, and L.-S. Liao, "Non-fullerene acceptor with low energy loss and high external quantum efficiency: towards high performance

- polymer solar cells,” *J. Mater. Chem.A*, 4, 5890–5897, 2016.
- [326] T. Liu, X. Pan, X. Meng, Y. Liu, D. Wei, W. Ma, L. Huo, X. Sun, T. H. Lee, M. Huang, H. Choi, J. Y. Kim, W. C. H. Choy, and Y. Sun, “Alkyl side-chain engineering in wide-bandgap copolymers leading to power conversion efficiencies over 10%,” *Adv. Mater.*, 29, 1604251, 2016.
- [327] J. Liu, S. Chen, D. Qian, B. Gautam, G. Yang, J. Zhao, J. Bergqvist, F. Zhang, W. Ma, H. Ade, O. Inganäs, K. Gundogdu, F. Gao, and H. Yan, “Fast charge separation in a non-fullerene organic solar cell with a small driving force,” *Nat. Energy*, 1, 2016.
- [328] L. Yang, S. Zhang, C. He, J. Zhang, H. Yao, Y. Yang, Y. Zhang, W. Zhao, and J. Hou, “New wide band gap donor for efficient fullerene-free all-small-molecule organic solar cells,” *J. Am. Chem. Soc.*, 139, 1958–1966, 2017.
- [329] H. Yao, L. Ye, J. Hou, B. Jang, G. Han, Y. Cui, G. M. Su, C. Wang, B. Gao, R. Yu, H. Zhang, Y. Yi, H. Y. Woo, H. Ade, and J. Hou, “Achieving highly efficient nonfullerene organic solar cells with improved intermolecular interaction and open-circuit voltage,” *Adv. Mater.*, 29, 1700254, 2017.
- [330] J. Yuan, L. Qiu, Z.-G. Zhang, Y. Li, Y. Chen, and Y. Zou, “Tetrafluoroquinoxaline based polymers for non-fullerene polymer solar cells with efficiency over 9%,” *Nano Energy*, 30, 312–320, 2016.
- [331] G. Zhang, G. Yang, H. Yan, J.-H. Kim, H. Ade, W. Wu, X. Xu, Y. Duan, and Q. Peng, “Efficient nonfullerene polymer solar cells enabled by a novel wide bandgap small molecular acceptor,” *Adv. Mater.*, 29, 1606054, 2017.
- [332] W. Zhao, D. Qian, S. Zhang, S. Li, O. Inganäs, F. Gao, and J. Hou, “Fullerene-free polymer solar cells with over 11% efficiency and excellent thermal stability,” *Adv. Mater.*, 28, 4734–4739, 2016.
- [333] H. Bin, L. Gao, Z.-G. Zhang, Y. Yang, Y. Zhang, C. Zhang, S. Chen, L. Xue, C. Yang, M. Xiao, and Y. Li, “11.4% efficiency non-fullerene polymer solar cells with trialkylsilyl substituted 2d-conjugated polymer as donor,” *Nat. Commun.*, 7, 13651, 2016.
- [334] H. Bin, Y. Yang, Z.-G. Zhang, L. Ye, M. Ghasemi, S. Chen, Y. Zhang,

## Bibliography

- C. Zhang, C. Sun, L. Xue, C. Yang, H. Ade, and Y. Li, "9.73% efficiency nonfullerene all organic small molecule solar cells with absorption-complementary donor and acceptor," *J. Am. Chem. Soc.*, 139, 5085–5094, 2017.
- [335] P. Cheng, M. Zhang, T.-K. Lau, Y. Wu, B. Jia, J. Wang, C. Yan, M. Qin, X. Lu, and X. Zhan, "Realizing small energy loss of 0.55 eV, high open-circuit voltage >1 V and high efficiency >10% in fullerene-free polymer solar cells via energy driver," *Adv. Mater.*, 29, 1605216, 2017.
- [336] Z. Li, K. Jiang, G. Yang, J. Y. L. Lai, T. Ma, J. Zhao, W. Ma, and H. Yan, "Donor polymer design enables efficient non-fullerene organic solar cells," *Nat. Commun.*, 7, 13094, 2016.
- [337] D. Liu, B. Yang, B. Jang, B. Xu, S. Zhang, C. He, H. Y. Woo, and J. Hou, "Molecular design of a wide-band-gap conjugated polymer for efficient fullerene-free polymer solar cells," *Energy & Envir. Sci.*, 10, 546–551, 2017.
- [338] Z. Fei, F. D. Eisner, X. Jiao, M. Azzouzi, J. A. Röhr, Y. Han, M. Shahid, A. S. R. Chesman, C. D. Easton, C. R. McNeill, T. D. Anthopoulos, J. Nelson, and M. Heeney, "An alkylated indacenodithieno[3,2-b]thiophene-based nonfullerene acceptor with high crystallinity exhibiting single junction solar cell efficiencies greater than 13% with low voltage losses," *Adv. Mater.*, 30, 1705209, 2018.
- [339] K. Vandewal, K. Tvingstedt, A. Gadisa, O. Inganäs, and J. V. Manca, "Relating the open-circuit voltage to interface molecular properties of donor:acceptor bulk heterojunction solar cells," *Phys. Rev. B*, 81, 2010.
- [340] M. A. Faist, T. Kirchartz, W. Gong, R. S. Ashraf, I. McCulloch, J. C. de Mello, N. J. Ekins-Daukes, D. D. C. Bradley, and J. Nelson, "Competition between the charge transfer state and the singlet states of donor or acceptor limiting the efficiency in polymer:fullerene solar cells," *J. Am. Chem. Soc.*, 134, 685, 2012.
- [341] M. A. Faist, S. Shoaee, S. Tuladhar, G. F. A. Dibb, S. Foster, W. Gong, T. Kirchartz, D. D. C. Bradley, J. R. Durrant, and J. Nelson, "Understanding the reduced efficiencies of organic solar cells employing fullerene multiadducts

- as acceptors," *Adv. Energy Mater.*, **3**, 744, 2013.
- [342] K. Vandewal, Z. Ma, J. Bergqvist, Z. Tang, E. Wang, P. Henriksson, K. Tvingstedt, M. R. Andersson, F. Zhang, and O. Inganäs, "Quantification of quantum efficiency and energy losses in low bandgap polymer:fullerene solar cells with high open-circuit voltage," *Adv. Funct. Mater.*, **22**, 3480, 2012.
- [343] E. T. Hoke, K. Vandewal, J. A. Bartelt, W. R. Mateker, J. D. Douglas, R. Noriega, K. R. Graham, J. M. J. Fréchet, A. Salleo, and M. D. McGehee, "Recombination in polymer:fullerene solar cells with open-circuit voltages approaching and exceeding 1.0 V," *Adv. Energy Mater.*, **3**, 220–230, 2012.
- [344] W. Li, K. H. Hendriks, A. Furlan, M. M. Wienk, and R. A. J. Janssen, "High quantum efficiencies in polymer solar cells at energy losses below 0.6 eV," *J. Am. Chem. Soc.*, **137**, 2231, 2015.
- [345] M. Zhang, X. Guo, W. Ma, H. Ade, and J. Hou, "A polythiophene derivative with superior properties for practical application in polymer solar cells," *Adv. Mater.*, **26**, 5880, 2014.

# A. Evaluation of Absorber Materials

## A.1. Determine the Band Gap Energy

The analysis of literature data in this thesis, such as the Shockley-Queisser plots in fig. 2.2 and the Scharber plot in fig. 2.9, depend on the band gap  $E_g$  as a parameter. For this purpose,  $E_g$  can be defined and evaluated in different ways. In the context of OSCs, absorption or quantum efficiency spectra are often fitted to obtain the band gap, which is however subject to uncertainty in the fitting, e.g. stemming from the energy at which a tangent is applied to the curves. For a valuable and consistent comparison of different solar cells and technologies a common method to determine the band gap is needed and different systematic approaches were discussed in literature [61, 321]. Because the Shockley-Queisser limit requires a single value for  $E_g$ , the broadened absorption edge that can be regarded as a distribution of band gaps [61], needs to be condensed into a single value of  $E_g$ . In this thesis I define the band gap via the inflection point of the long wavelength edge of the *EQE* spectrum, which has been discussed by Siebentritt et al. [322] and reflects the approach of Rau et al. [61]. The latter was shown to allow a comparison in terms of the Shockley-Queisser limit of different real-world solar cell technologies that do not absorb according to a step-function. One practical advantage of an *EQE* based approach is that *EQE* spectra are commonly reported along with solar cell performance data, which allows a comprehensive meta-analysis of literature data. It does not require any optical material data about the absorption onset that is not always reported, and is directly based on solar cell data. In the case of OSCs, no assumption is made whether the donor or acceptor molecule determines the absorption onset, which is especially relevant for non-fullerene acceptors that may absorb up to longer wavelengths than PCBM. The uncertainty of determining the band gap via the *EQE* inflection point lies in the wavelength resolution of the reported *EQE* spectra that are mostly linearly interpolated. In this work I either digitalized the reported *EQE* spectra or estimated the inflection by eye which resulted in difference that were always smaller than 15 nm which is about the accuracy obtained from

digitalizing the  $EQE$  data and translates to a maximum energy uncertainty below 40 mV.

## A.2. Calculate the Shockley-Queisser Limit

The assumptions of Shockley and Queisser [24] are described in section 2.2.2 and directly yield the performance limit of single junction solar cell absorbers with the band gap  $E_g$  as the only free parameter. The short-circuit current density limit is given by

$$J_{sc,SQ} = q \int_{E_g}^{\infty} \phi_{AM1.5}(E) dE, \quad (A.1)$$

with the elementary charge  $q$ , the incident spectral photon flux  $\phi_{AM1.5}$  according to the global AM1.5 spectrum, whose distinct spectral shape is responsible for the wobbling features observed in  $J_{sc,SQ}$  in fig. 2.2(c), which also translate to the efficiency  $\eta_{SQ}$  in fig. 2.2(a). The solar cell's thermal emission, at a defined operating temperature of  $T = 300$  K sets the saturation current density

$$J_{0,SQ} = q \int_{E_g}^{\infty} \phi_{bb}(E, T = 300 \text{ K}) dE, \quad (A.2)$$

with the black body radiation according to Planck's law

$$\phi_{bb}(E, T) = \frac{2\pi E^2}{h^3 c^2} \frac{1}{\exp(E/(k_b T)) - 1}, \quad (A.3)$$

with the energy  $E$ , Planck constant  $h$ , speed of light  $c$  and Boltzmann constant  $k_b$ . The open-circuit voltage is then given by

$$V_{oc,SQ} = \frac{n_{id} k_b T}{q} \ln \left( \frac{J_{sc,SQ}}{J_{0,SQ}} + 1 \right) \quad (A.4)$$

with the ideality factor  $n_{id} = 1$  in the SQ limit, since charge carriers only recombine radiatively. The Shockley-Queisser theory also yields the Shockley ideal diode equation whereby the  $FF$  can be calculated as described in section 2.3.4 and approximated via Green's formula [64]

### A. Evaluation of Absorber Materials

$$FF_{\text{SQ}} = \frac{v_{\text{oc}} - \ln(v_{\text{oc}} + 0.72)}{v_{\text{oc}} + 1}, \quad v_{\text{oc}} = \frac{qV_{\text{oc,SQ}}}{n_{\text{id}}k_{\text{b}}T}. \quad (\text{A.5})$$

Finally, the efficiency limit

$$\eta_{\text{SQ}} = \frac{J_{\text{sc}}V_{\text{oc}}FF}{\int_0^\infty E\phi_{\text{AM1.5}}(E)dE} \quad (\text{A.6})$$

is obtained, where the denominator is equal to  $P_{\text{sun}}$  in eq. 2.1. The Shockley-Queisser limit applies to the first and second generation of solar cells, while the third generation of solar cells by Green's definition [7] comprise solar cells that violate the assumptions of SQ and are thereby able to exceed the SQ limit. The most promising concept of this class of devices are tandem solar cells. Here, as in other third generation solar cell concepts, the two major loss mechanisms considered by SQ, thermalization and below band gap transmission, are reduced.

## A.3. Calculate (Non-)Radiative Voltage Losses

The difference between the SQ  $V_{\text{oc,SQ}}$  and the experimentally attained  $V_{\text{oc}}$  can be further divided into radiative and non-radiative contributions as is done for  $\text{Sb}_2\text{S}_3$  solar cells in section 6.2.3. Based on the reciprocity theorem in eq. 3.13, the quantum efficiency  $Q_e$  is calculated from electroluminescence measurements over a wide dynamic range. From the quantum efficiency, the radiative saturation current density is calculated via

$$J_{0,\text{rad}} = q \int_0^\infty Q_e(E)\phi_{\text{bb}}(E)dE. \quad (\text{A.7})$$

The equation is similar to the corresponding expression in the SQ limit in eq. A.2, but in the SQ limit, a step function quantum efficiency is assumed instead of the experimentally obtained  $Q_e$ , whose low-energy edge is smeared out.  $J_{0,\text{rad}}$  then yields the radiative open-circuit voltage

$$V_{\text{oc,rad}} = \frac{k_{\text{b}}T}{q} \ln \left( \frac{J_{\text{sc}}}{J_{0,\text{rad}}} + 1 \right). \quad (\text{A.8})$$

#### A.4. Calculate the Scharber Efficiency

The radiative loss is defined as the difference to the Shockley-Queisser limit ( $V_{oc,SQ}$ ) as

$$\Delta V_{oc,rad} = V_{oc,SQ} - V_{oc,rad} \quad (\text{A.9a})$$

and the non-radiative loss is the remaining difference to the experimentally obtained open-circuit voltage

$$\Delta V_{oc,nr} = V_{oc,rad} - V_{oc}. \quad (\text{A.9b})$$

Commonly, the external LED quantum efficiency ( $Q_e^{LED}$ ) is also calculated, which is related to the non-radiative loss via

$$\Delta V_{oc,nr} = -\frac{k_b T}{q} \ln(Q_e^{LED}). \quad (\text{A.9c})$$

## A.4. Calculate the Scharber Efficiency

To calculate the Scharber efficiency  $\eta_{Sch}$ , which as a figure of merit (FOM) represents the energy level matching of an organic solar cell blend, I use the band gap  $E_g$  as defined in appendix A.1 and the voltage loss  $\Delta V := 1/qE_g - V_{oc}$  as free parameters.<sup>1</sup> The open-circuit voltage  $V_{oc}$  is then trivially given by

$$V_{oc} = 1/qE_g - \Delta V. \quad (\text{A.10})$$

The short-circuit current  $J_{sc}$  is calculated from the band gap

$$J_{sc} = q \int_{E_g}^{\infty} EQE \times \phi_{AM1.5}(E) dE, \quad (\text{A.11})$$

with the external quantum efficiency  $EQE$  and the incident spectral photon flux  $\phi_{AM1.5}$  according to the global AM1.5 spectrum. The  $EQE$  is assumed to be a step-function and energy-independent above  $E_g$  and is set to the same value for all  $E_g$  and  $\Delta V$ . The Scharber efficiency  $\eta_{Sch} = J_{sc}V_{oc}FF/P_{sun}$  is then computed from eqs. A.10 and A.11 together with the fill factor  $FF$ . Just as the  $EQE$ , a constant

---

<sup>1</sup>The following considerations partially reflect my contributions to the second-author publication "Figures of Merit Guiding Research on Organic Solar Cells". Reprinted in part with permission from ref. [110]. © 2018 American Chemical Society

## A. Evaluation of Absorber Materials

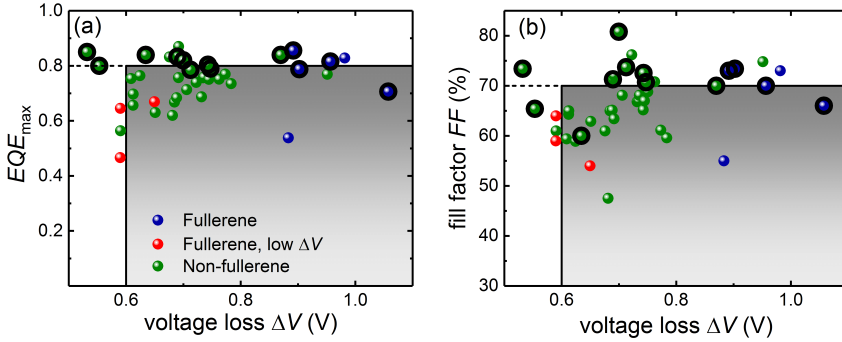


**Figure A.1.:** Correlation between voltage loss and (a) the peak of the reported  $EQE$  spectrum and (b) the  $FF$  for selected data points, divided in classes of acceptor materials. The circled data points are the same as those in fig. 2.9 and fig. 5.12 (see appendix B for values). Additional data from reports applying fullerenes [157, 267] and fullerenes yielding exceptionally low voltage loss [323, 324], as well as non-fullerene [148, 194, 280, 325–338] acceptors are included for a more comprehensive picture. The rectangle marks the  $EQE$  and  $FF$  value taken for the Scharber analysis. The boundary at  $\Delta V = 0.6$  V indicates the minimal voltage loss that was observed for many OSCs but seems not to be a true upper limit for two recent NFA-based blends that reached  $\eta > 12\%$ .

value of the  $FF$  is taken over the entire parameter space. For the Scharber plot in fig. 2.9(a), values of  $EQE = 0.8$  and  $FF = 70\%$  are chosen based on fig. A.1 that shows several OSCs based on fullerene and non-fullerene acceptors. Data points with a black edge correspond to the selection in fig. 2.9 and the indicated  $EQE$  values in fig. A.1(a) refers to the maximum of the  $EQE$  spectrum. The left edge of the rectangles in fig. A.1 indicates that most efficient solar cells show a voltage loss of at least 0.6 V. However, recent publications [9, 58], including today’s record cell, achieved high efficiencies at a lower voltage loss. It seems that  $\Delta V = 0.6$  V should not be regarded as a rigid limit. In this context, also see the discussion of the relation between  $EQE$  and  $\Delta V$  in appendix A.5. Note that the choice of  $EQE$  and  $FF$  is to some degree arbitrary and whenever the efficiency potential of OSCs is discussed based on  $\eta_{SCh}$ , the estimated absolute value will depend on this choice. In a more recent version of his analysis [147], Scharber used larger values than in his original publication [145], due to the improved performance of reported OSCs. However, the choice of  $EQE$  and  $FF$  will scale the resulting  $\eta_{SCh}$  equally over the entire parameter range, so that  $\eta_{SCh}$  serves well as a FOM.

#### A.4. Calculate the Scharber Efficiency

As mentioned in section 2.4.1 the common definition of voltage loss for organic solar cells relative to the band gap does not reflect the difference to the theoretical SQ  $V_{oc,SQ}$  which is lower than the band gap. Furthermore  $E_g - qV_{oc,SQ}$  increases linearly with increasing  $E_g$ . Most well-performing OSCs in fig. 2.9 have band gaps between  $E_g = 1.55$  eV and  $E_g = 1.7$  eV where  $E_g - qV_{oc,SQ}$  takes similar values (the deviation is merely 10 meV). However, the best-performing solar cell as of today has a remarkably low  $E_g = 1.26$  eV [9]. For this low  $E_g$ ,  $E_g - qV_{oc,SQ} \approx 255$  meV, while a large  $E_g = 1.7$  eV results in  $E_g - qV_{oc,SQ} \approx 280$  meV. This difference of 25 meV should be kept in mind when evaluating voltage losses of OSCs with largely differing band gaps, but is still small compared to the range of voltage losses covered by well-performing solar cells shown in fig. A.1. More accurate and extensive analysis of voltage losses in solar cells are presented in refs. [61, 66] and include the distinction between radiative and non-radiative voltage losses.

The previously depicted analysis is based on the work of Scharber et al. [145] in 2006, who described the potential efficiency increase that lied in the tuning of the polymer's energy levels with respect to PCBM, which was the only well-performing acceptor molecule at that time. In that case, the band gap  $E_g$  refers to the polymer band gap which is always smaller than that of PCBM. Scharber et al. found an empirical relation between the energetic offset at the polymer-PCBM (donor-acceptor) interface and the resulting open-circuit voltage

$$V_{oc} = 1/q \left( | E_{\text{HOMO}}^{\text{polymer}} | - | E_{\text{LUMO}}^{\text{PCBM}} | \right) - 0.3 \text{ V}, \quad (\text{A.12})$$

where  $q$  is the elementary charge,  $E_{\text{HOMO}}^{\text{polymer}}$  is the the energy of the (donor) polymer HOMO and  $E_{\text{LUMO}}^{\text{PCBM}}$  is the the energy of the PCBM (acceptor) HOMO. The empirically obtained loss of 0.3 V was later attributed to non-radiative losses via the CT state [146, 147]. By rewriting the polymer band gap  $E_g = | E_{\text{HOMO}}^{\text{polymer}} | - | E_{\text{LUMO}}^{\text{PCBM}} | + \Delta E_{\text{LUMO}}$  in terms of the LUMO offset  $\Delta E_{\text{LUMO}}$  at the interface as defined in fig. 2.8(a) , eq. A.12 translates to a voltage loss

$$\Delta V_{oc} = 1/q E_g - V_{oc} = \Delta E_{\text{LUMO}} - 0.3 \text{ V}. \quad (\text{A.13})$$

An offset of  $\Delta E_{\text{LUMO}} \geq 0.3 \text{ V}$  was thought to be required to efficiently split excitons

### A. Evaluation of Absorber Materials

implying a  $\Delta V_{oc}$  of at least 0.6 V, which seems to not hold true for certain OSCs as discussed above. Scharber set targets for the tailoring of the polymer's energy levels based on the necessity of PCBM as a partner in the BHJ. Through the discovery of NFAs, this necessity is obsolete and the energy levels of both, donor and acceptor, may be tuned independently. The generalized analysis based on a loss in open-circuit voltage does not explicitly contain the energy levels of the BHJ. Instead the calculated efficiency  $\eta_{Sch}$  serves as a FOM to track the progress in OSC development for reasons discussed in chapter 1.

Finally, the analysis of organic solar cells in terms of the Scharber efficiency can be understood as the efficiency potential that results from the variation of the optical and electrical band gap. In this terminology, the optical band gap is represented by the absorption onset of the lower band gap material in the blend, which is characterized by the *EQE* inflection point in this work. The smaller electrical band gap on the other hand denotes the energetic distance that governs the dynamics of (band-to-band) recombination in the material blend, which is also implicit to the effective medium approach in drift-diffusion simulations of organic solar cells (see section 3.1.3). In the original analysis by Scharber et al., this electrical band gap is given by the diagonal band gap that is part of eq. A.13. More recent results indicate that the CT state in organic solar cells takes the role of the electrical band gap [45, 339], which is compatible with the generalized calculation of the Scharber efficiency in this work.

## A.5. Relations between Photocurrent and Open-Circuit Voltage Loss

In appendix A.4 above, it was argued that most OSCs with a voltage loss  $\Delta V < 0.6$  V do not produce high efficiencies. As stated by Scharber et al. and eq. A.13 the LUMO offset at the donor-acceptor heterojunction contributes to the voltage loss. At the same time it is needed for many blends to split up excitons efficiently [340–343], which implies a tradeoff between losses in photocurrent and photovolt-

### A.5. Relations between Photocurrent and Open-Circuit Voltage Loss

age.<sup>2</sup> Instead of a simple minimal LUMO offset or voltage loss that is required to split excitons, Li et al. [344] empirically found a linear relation for the best-performing cells, that is reproduced in fig. A.2(a), between  $\Delta V_{oc}$  and  $EQE_{max}$  above a cut-off at  $\Delta V_{oc} = 0.6$  V. The displayed data points are taken from ref. [194], where the band gap  $E_{g,opt}$  is obtained from optical absorption data, which bears the uncertainties described in appendix A.1 and systematically shifts data to smaller band gaps and therefore lower voltage losses compared to band gaps defined via the inflection point, which was tested for exemplary cases. Based on this data, Baran et al. [194] suggested a linear relationship with a flatter slope. To qualitatively illustrate the consequences of a voltage-loss dependent photocurrent, I stick to the relation proposed by Scharber et al. Figure A.2(b) is a variation of the generalized Scharber plot that assumes a quantum efficiency that depends on the voltage loss as proposed by Li et al.  $EQE(\Delta V_{oc}) = 0.876\Delta V_{oc} + 0.025$  instead of setting it constant, which results in a different efficiency prediction that I term Scharber-Li efficiency  $\eta_{Sch-Li}$ . Compared to the Scharber plot for  $EQE = const.$  in fig. 2.9(a), the highest efficiencies would be obtained for higher band gaps of  $E_g = 1.6$  eV compared to  $E_g < 1.5$  eV and larger voltage losses of about 0.8 V whereas for a constant  $EQE$ , the voltage loss should be as small as possible. The scenario in fig. A.2(b) coincides with typical values for the best polymer-fullerene devices. It remains to be seen if and how large of a voltage loss is required for efficient photocurrent generation. As of now, fig. A.1(a) suggests that for well-performing NFAs there is no continuous decrease of photocurrent with decreasing voltage loss and that voltage losses well below 0.6 V are feasible. If a linear decrease of photocurrent with voltage loss was observed for the best performing material blends, the optimization target for organic material design would change towards higher band gaps and larger voltage losses.

---

<sup>2</sup>The following considerations partially reflect my contributions to the second-author publication “Figures of Merit Guiding Research on Organic Solar Cells”. Reprinted in part with permission from ref. [110]. © 2018 American Chemical Society

### A. Evaluation of Absorber Materials

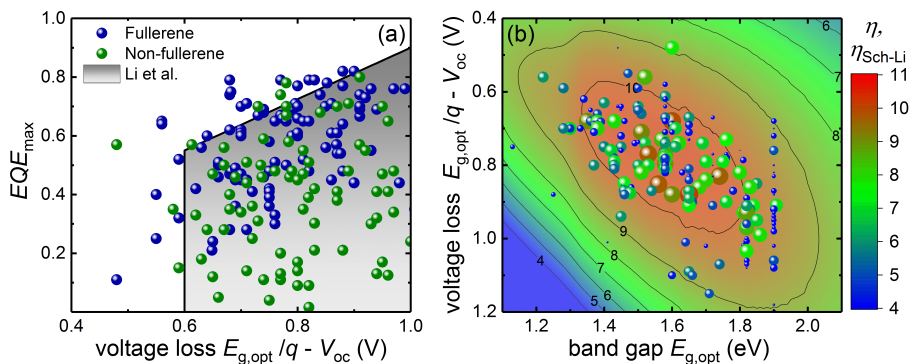


**Figure A.2.:** (a) Tradeoff between photocurrent and voltage loss as upper limit for many reported OSCs. The rectangle reproduces the linear relationship proposed by Li et al. [344]. (b) Scharber analysis for a non-constant  $EQE$  as suggested by Li et al. Given a linear dependence of  $EQE$  on voltage loss, the optimization target of OSC change towards higher band gaps and voltage loss. Band gaps are based on optical data and data points in (a) and (b) are compiled by Derya Baran and taken from ref. [194] - Published by The Royal Society of Chemistry.

### A.6. Organic Solar Cell Development Captured by Two FOMs

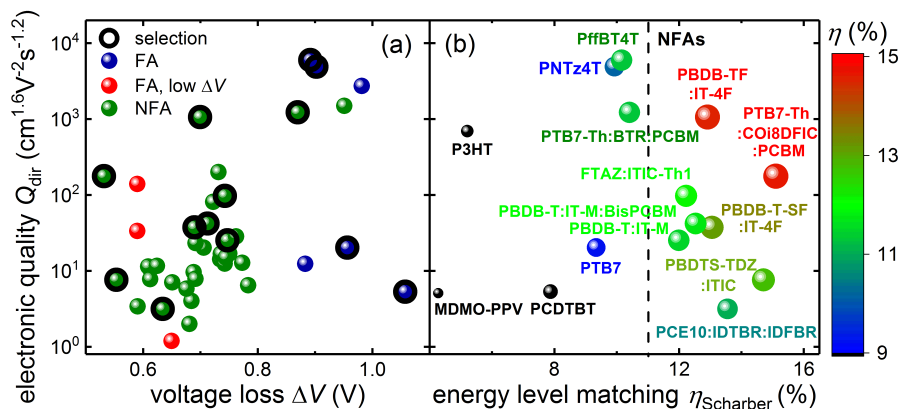


**Figure A.3.:** (a) Same as fig. 5.12(b) but with the data and legend of fig. A.1 in appendix A.5. The circled points are shown in fig. 5.12(b). (b) 2D version of fig. 5.12(c) indicating that the highest energy level matching is only obtained with NFAs.

## B. Literature Data

**Table B.1.:** Literature reports showing highest performance for various absorber technologies shown in figs. 2.2 and 2.3 in chapter 1.  $\text{Sb}_2\text{S}_3$  data is also included in fig. 6.7 in chapter 6.2 and the corresponding tab. B.3. The selected reports of polymer-based organic solar cells, including recent record performances, are also included in tab. B.2 and the corresponding figures.

category	absorber	ref.	$E_g$ eV	$J_{sc}$ $\text{mAcm}^{-2}$	$V_{oc}$ V	$FF$ %	$\eta$ %
established	c-Si	[10]	1.12	42.7	0.738	85	26.7
established	GaAs	[47]	1.42	29.7	1.122	87	28.8
established	CIGS	[11]	1.14	38.8	0.744	80	22.9
established	CdTe	[11]	1.41	31.7	0.887	79	22.1
established	a-Si	[48]	1.72	16.4	0.896	70	10.2
established	$\mu\text{c-Si}$	[49]	1.12	29.7	0.550	75	11.9
emerging	$\text{Sb}_2\text{Se}_3$	[50]	1.25	29.9	0.420	60	7.6
emerging	AgBiI	[21]	1.90	6.3	0.614	59	2.3
emerging	$\text{Bi}_2\text{S}_3$	[51]	1.45	3.8	0.300	49	0.5
emerging	SnS	[22]	1.30	20.2	0.372	58	4.4
emerging	Sn-Perovskite	[52]	1.35	21.2	0.610	63	8.1
emerging	$\text{Cu}_2\text{O}$	[19]	2.10	10.8	1.200	63	8.1
emerging	PbS-QD	[53]	1.15	29.0	0.647	64	12.0
emerging	Perovskite	[8]	1.57	24.9	1.127	81	22.6
emerging	Sb-Perovskite	[54]	2.14	1.0	0.896	55	0.5
emerging	Bi-Perovskite	[55]	2.00	2.2	0.850	60	1.1
emerging	Br-Perovskite	[56]	1.74	19.4	1.200	75	17.1
emerging	$\text{Sb}_2\text{S}_3$ , ETA	[20]	1.78	16.1	0.711	65	7.5
emerging	$\text{Sb}_2\text{S}_3$ , planar	[60]	1.78	14.9	0.667	58	5.8
organic	PBDTS-TDZ:ITIC	[58]	1.65	17.6	1.100	65	12.8
organic	PfBT4T:PC <sub>70</sub> BM	[59]	1.68	19.8	0.784	73	11.3
organic	PTB7-Th: COi8DFIC:PC <sub>70</sub> BM	[9]	1.26	27.4	0.727	73	14.6
organic	PBDB-TF:IT-4F	[57]	1.57	20.7	0.870	81	14.6

B. Literature Data

**Table B.2.:** Selected polymer-based solar cells evaluated in terms of the discussed figures of merit. The efficiency chart in fig. 2.7 in section 2.4.1 displays the first block. Both blocks are contained in the detailed performance analysis in fig. 2.9 in the same section, as well as in fig. 5.12 in chapter 5.3.1 and figs. A.1 and A.3 in appendix A. The literature data itself is displayed on this page and the calculated quantities are found on the next page.

year	blend	ref.	$d$ nm	$EQE_{\max}$	$E_g$ eV	$J_{sc}$ mAcm <sup>-2</sup>	$V_{oc}$ V	$FF$ %	$\eta$ %
2001.1	MDMO-PPV:PC <sub>60</sub> BM	[133]	100	0.51	2.28	5.3	0.820	61	2.5
2005.8	P3HT:PC <sub>60</sub> BM	[134]	220	0.63	1.97	10.6	0.610	67	4.4
2009.3	PCDTBT:PC <sub>70</sub> BM	[135]	80	0.71	1.94	10.6	0.880	66	6.1
2012.6	PTB7:PC <sub>70</sub> BM	[136]	80	0.82	1.71	17.5	0.754	70	9.2
2015.3	PNTz4T:PC <sub>70</sub> BM	[137]	290	0.79	1.61	19.4	0.708	73	10.1
2016.0	PHBT4T:PC <sub>70</sub> BM	[59]	350	0.86	1.68	19.8	0.784	73	11.3
2017.2	PBDB-T-SF:IT-4F	[138]	100	0.83	1.57	20.9	0.880	71	13.1
2018.1	PTB7-Th:COi8DFIC:PC <sub>70</sub> BM	[9]	110	0.85	1.26	27.4	0.727	73	14.6
2018.5	PBDB-TF:IT-4F	[57]	110	0.82	1.57	20.7	0.870	81	14.6
2016.8	PTB7-Th:IDTBR:IDFBR	[194]	90	0.84	1.66	17.2	1.030	60	11.0
2017.9	PBDTS-TDZ:ITIC	[58]	100	0.80	1.65	17.6	1.100	65	12.8
2016.9	PBDB-T:IT-M	[153]	100	0.79	1.69	17.3	0.940	71	11.5
2016.2	PBDB-T:IT-M:BsPC <sub>70</sub> BM	[150]	100	0.79	1.66	17.4	0.952	74	11.8
2017.2	FTAZ:ITIC-Th1	[151]	120	0.80	1.59	19.2	0.847	73	12.1
2017.0	PTB7-Th:BTTR:PC <sub>71</sub> BM	[152]	250	0.84	1.62	21.4	0.751	70	11.3

year	blend	ref.	$\Delta V$ V	$FF_n$	$\eta_{sch}$ %	$Q_{dir}^{dir}$ $cm^{1.6}V^{-2}_S^{-1.2}$	$Q_{SRH}^{SRH}$ $cm^4V^{-2}_S^{-0.4}$
2001.1	MDMO-PPV:PC <sub>60</sub> BM	[133]	1.455	0.24	4.3	$5.1 \times 10^0$	$2.3 \times 10^{-17}$
2005.8	P3HT:PC <sub>60</sub> BM	[134]	1.358	0.54	5.2	$6.9 \times 10^2$	$7.7 \times 10^{-15}$
2009.3	PCDTBT:PC <sub>70</sub> BM	[135]	1.058	0.40	7.9	$5.3 \times 10^0$	$1.9 \times 10^{-17}$
2012.6	PTB7:PC <sub>70</sub> BM	[136]	0.956	0.57	9.3	$2.0 \times 10^1$	$8.6 \times 10^{-17}$
2015.3	PN'Tz4T:PC <sub>70</sub> BM	[137]	0.902	0.71	9.9	$4.9 \times 10^3$	$8.5 \times 10^{-14}$
2016.0	PfBT4T:PC <sub>70</sub> BM	[59]	0.892	0.67	10.2	$6.0 \times 10^3$	$1.0 \times 10^{-13}$
2017.2	PBDB-T-SF:IT-4F	[138]	0.690	0.58	13.1	$3.7 \times 10^1$	$1.8 \times 10^{-16}$
2018.1	PTB7-Th:COi8DFIC:PC <sub>70</sub> BM	[9]	0.532	0.70	15.1	$1.8 \times 10^2$	$1.2 \times 10^{-15}$
2018.5	PBDB-TF:IT-4F	[57]	0.700	0.91	12.9	$1.1 \times 10^3$	$2.7 \times 10^{-14}$
2016.8	PTB7-Th:IDTBR:IDFBR	[194]	0.634	0.17	13.6	$3.1 \times 10^0$	$6.2 \times 10^{-18}$
2017.9	PBDTS-TDZ:ITIC	[58]	0.553	0.35	14.7	$7.6 \times 10^0$	$2.3 \times 10^{-17}$
2016.9	PBDB-T:IT-M	[153]	0.747	0.55	12.0	$2.5 \times 10^1$	$1.2 \times 10^{-16}$
2016.2	PBDB-T:IT-M:BisPC <sub>70</sub> BM	[150]	0.712	0.65	12.5	$4.2 \times 10^1$	$2.7 \times 10^{-16}$
2017.2	FTAZ:ITIC-Th1	[151]	0.743	0.64	12.2	$9.7 \times 10^1$	$6.5 \times 10^{-16}$
2017.0	PTB7-Th:BTR:PC <sub>71</sub> BM	[152]	0.870	0.57	10.4	$1.2 \times 10^3$	$1.2 \times 10^{-14}$

## B. Literature Data

**Table B.3.:** Literature reports and best results from this thesis for comparison (bottom, process route indicated) for  $\text{Sb}_2\text{S}_3$  solar cells shown in chapter 6. For all reports the same  $E_g = 1.78 \text{ eV}$  as determined in this thesis is assumed. An evaluation of the literature reports leads to similar values ( $\pm 20 \text{ meV}$  maximum deviation), except ref. [33] where the lower band gap HTM PCPDTBT contributes to the photocurrent.

year	ref.	architecture	deposition	$J_{sc}$ $\text{mAcm}^{-2}$	$V_{oc}$ V	$FF$ %	$\eta$ %
2009.1	[80]	ETA	CBD	14.1	0.490	49	3.4
2010.3	[160]	ETA	CBD	10.6	0.610	48	3.1
2010.3	[161]	ETA	CBD	12.3	0.556	70	5.1
2011.7	[162]	ETA	CBD	15.3	0.616	66	6.2
2012.2	[288]	ETA	CBD	16.0	0.595	66	6.3
2014.0	[20]	ETA	CBD	16.1	0.711	65	7.5
2015.3	[33]	ETA	Spin	16.1	0.596	67	6.4
2014.6	[60]	planar	ALD	14.9	0.667	58	5.8
2015.2	[164]	planar	CBD	11.0	0.726	51	4.1
2015.7	[167]	planar	TE	6.4	0.599	44	1.7
2012.4	[286]	planar	TE	12.6	0.450	42	2.4
2016.6	[170]	planar	RTE	10.8	0.710	48	3.5
2015.8	[90]	planar	Spin	8.1	0.616	46	2.3
2017.1	[34]	planar	Spin	12.9	0.632	52	4.3
2016.2	[178]	planar	Spin	9.4	0.560	50	2.7
2017.5	[91]	planar	Spin	12.7	0.570	52	3.8
2018.5	[303]	planar	Spin	14.1	0.670	59	5.6
2018.6	[304]	planar	Spin	17.2	0.647	57	6.4
2018.6	[302]	planar	Spin	18.4	0.671	55	6.8
2018.5	[305]	planar	Spin	15.3	0.590	53	4.8
2018.5	[305]	planar	Spin	15.1	0.610	55	5.0
2018.6	Sb-TU /KP115	planar	Spin	11.7	0.650	55	4.2
2018.6	Sb-BDC /P3HT	planar	Spin	15.6	0.611	52	5.0

# C. Charge Collection

## Collection Coefficients

The analytically derived collection coefficients rely on device properties such as built-in voltage  $V_{\text{bi}}$  and generation rate  $G$  that are also input to simulations and not on the resulting solar cell parameters  $V_{\text{oc}}$  or  $J_{\text{sc}}$  applied in eqs. 5.2 and are given by

$$\theta'_{\text{SRH}} = (\mu\tau)^2 \frac{V_{\text{bi}}^2}{d^4}, \quad (\text{C.1a})$$

for Shockley-Read-Hall recombination and

$$\theta'_{\text{dir}} = \frac{\mu_e\mu_h}{k} \frac{V_{\text{int}}^2}{d^4 G}. \quad (\text{C.1b})$$

for direct recombination [235]. Here, the built-in voltage  $qV_{\text{bi}} = E_{\text{g}} - \varphi_{\text{f}} - \varphi_{\text{b}}$  results from the effective band gap and the Schottky barriers and the internal voltage according to Bartesaghi et al. [235] is defined as  $qV_{\text{int}} = E_{\text{g}} - 0.4\text{eV}$ . The correction of the effective band gap by -0.4 V was attributed to band bending but can also be understood as a rough estimate of the difference between  $V_{\text{bi}}$  and  $V_{\text{MPP}}$ . The generation rate  $G$  in eq. C.1b equates  $J_{\text{sc}}d$ , assuming that  $J_{\text{sc}}$  is approximately equal to the current obtained from complete collection of all photogenerated charges  $J_{\text{sc}} \approx J_{\text{sc,max}} = q \int_0^d G dx = qGd$ . The original expressions in eqs. C.1 lead to very similar results as the adapted expressions in eqs. 5.2 as can be seen from fig. C.1(a) and (b).

### C. Charge Collection

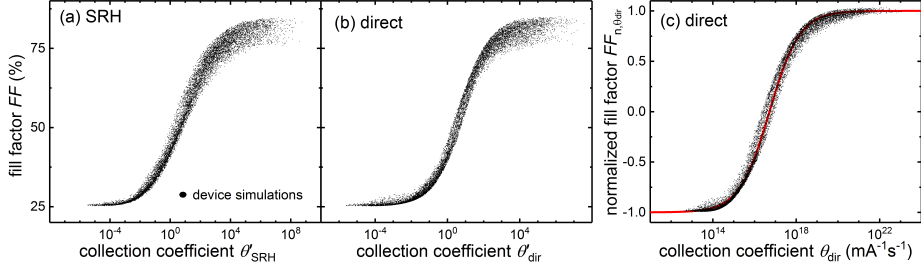


**Figure C.1.:** Originally derived collection coefficients according to eqs. C.1 for (a) SRH and (b) direct recombination, which apply  $V_{bi}$  or  $V_{int}$  instead of  $V_{oc}$  and  $G$  instead of  $J_{sc}$ . Difference to the adapted expressions in eqs. 5.2 displayed in fig. C.1(a) and (b) are negligible. (c) Adapted analytical collection coefficient for direct recombination (eq. 5.2b) after the introduction of a normalized fill factor used to compare the models' precision (fig. 5.3(c), eq. 5.10). Fit parameters result to  $a = 0.92$ ,  $b = 0.09$ ,  $\alpha = 0.3$  and  $\gamma_0 = 5.2 \times 10^{16} \text{mA}^{-1}\text{s}^{-1}$ .

### Model Assumptions and Limits

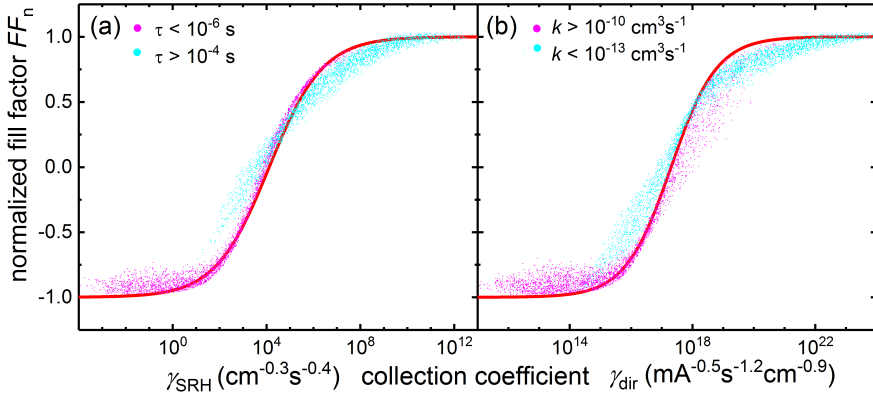


**Figure C.2.:** For exceptionally strong (pink) or weak (cyan) recombination,  $FF_n$  values differ from the model for (a) Shockley-Read-Hall and (b) direct recombination. However, long lifetimes exceeding 0.1 ms are typically reached only at low light intensities [232, 233].

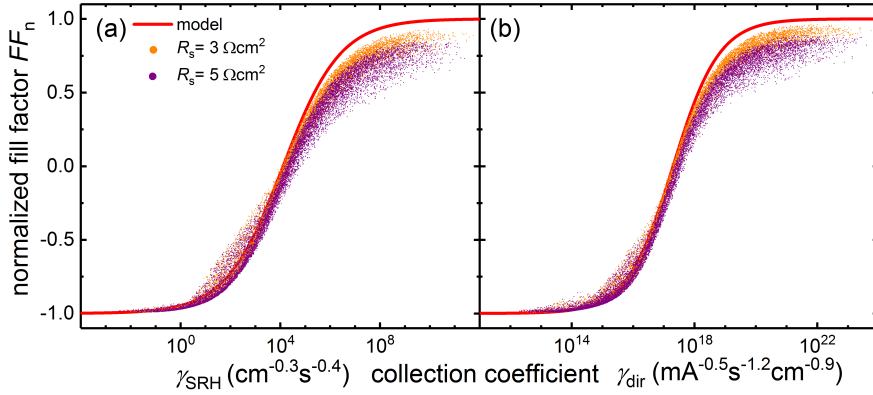


**Figure C.3.:** Effect of an external series resistance for a large ensemble of devices for (a) SRH and (b) direct recombination within the standard parameter range also used in fig. 5.3. The series shown in fig. 5.4 reflect the behaviour observed from the point cloud.

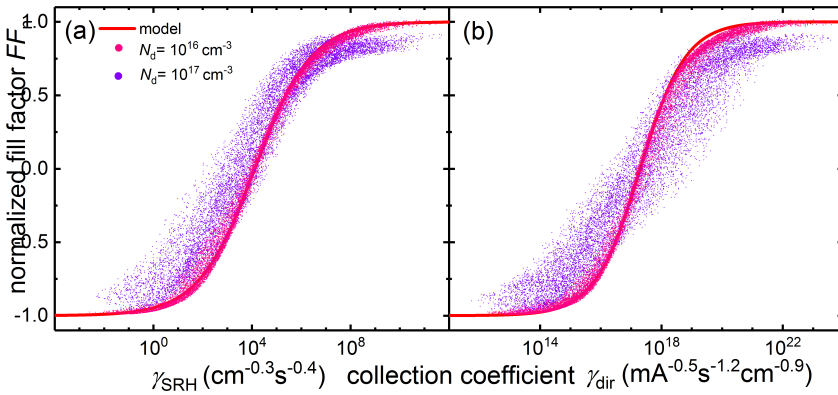


**Figure C.4.:** Effect of doping for a large ensemble of devices for (a) SRH and (b) direct recombination within the standard parameter range also used in fig. 5.3. The series shown in fig. 5.6 reflect the behaviour observed from the point cloud.

C. Charge Collection

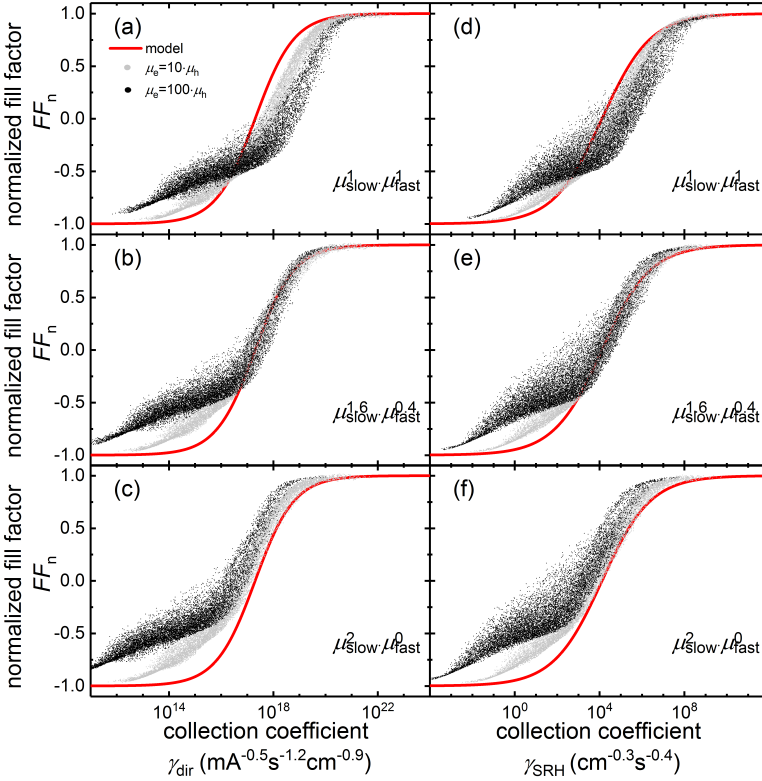


**Figure C.5.:** Effect of imbalanced mobilities for a large ensemble of devices for (a)-(c) direct recombination and (d)-(f) SRH within the standard parameter range also used in fig. 5.3. The weight of the slow and fast carrier species is varied in (a)-(c) and (d)-(f). The best overlap in (b) and (e) results from a strong emphasis of the slow carriers although the fast carriers cannot be fully neglected. Imbalanced charge transport generally increases scatter in the data. Putting equal weight on slow and fast charge carrier species – as done by Bartesaghi et al. – enhances the scatter even more. The data in (a) is similar to the publication of Bartesaghi et al. where the ratio between mobilities is varied randomly instead of superpositioning the different datasets with fixed asymmetry ratios shown here. The series shown in fig. 5.6 reflect the behaviour observed from the point cloud for a weight distribution of  $\mu_{\text{slow}}^{1.6} \mu_{\text{fast}}^{0.4}$ .

## Experimental Data

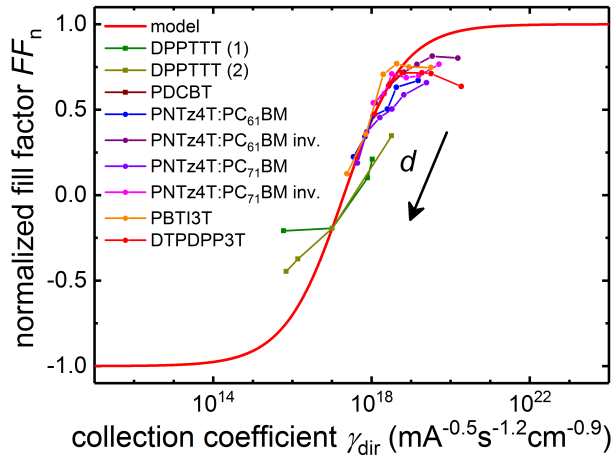


**Figure C.6.:** Additional thickness series from literature that are analyzed as described in section 5.1.5. Device series that are affected by a space-charge region are marked with squares and blends with a  $FF$  limited by the contacts are marked with circles. Colors indicate the specific experimental series. Data for DPP-TT-T:PC<sub>71</sub>BM (1) and DPP-TT-T:PC<sub>71</sub>BM (2) are extracted from ref. [84] where series (2) is shown to have a higher doping concentration than series (1). Data for PDCBT:PC<sub>71</sub>BM in a 1:1 concentration is extracted from ref. [345], different PNTz4T blends as indicated in the legend from ref. [137], PBTI3T:PC<sub>71</sub>BM from ref. [255] and data on DTPDPP3T:PC<sub>71</sub>BM is taken from ref. [241]. The drop in  $FF$  of several series for the thinnest devices that have the highest collection coefficients could be due to a decreased shunt resistance.

$(\alpha\mu\tau)$  – Additional Data

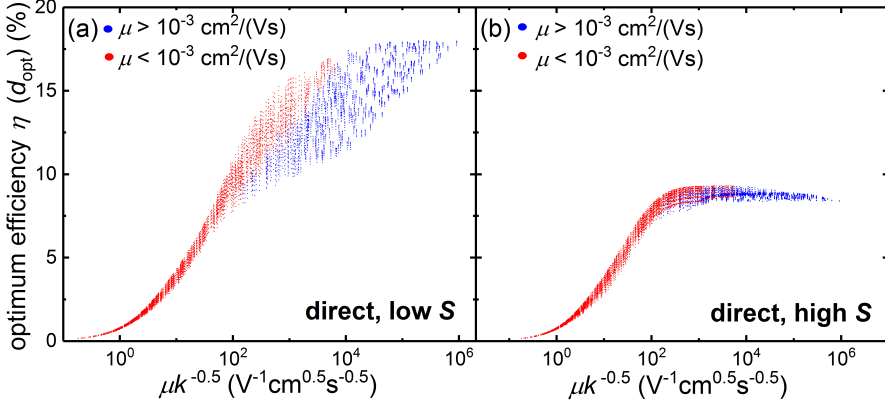


**Figure C.7.:** Although  $\alpha_0$  is only varied over a comparably small range - the largest factor is  $c_\alpha = 1.5$  - the scatter in the linear regime increases significantly if  $\alpha_0$  is excluded from the respective FOMs on the x-axis. Exemplary data for direct recombination (compare with fig. C.9) in the low mobility regime is shown for (a) low and (b) high surface recombination velocity.

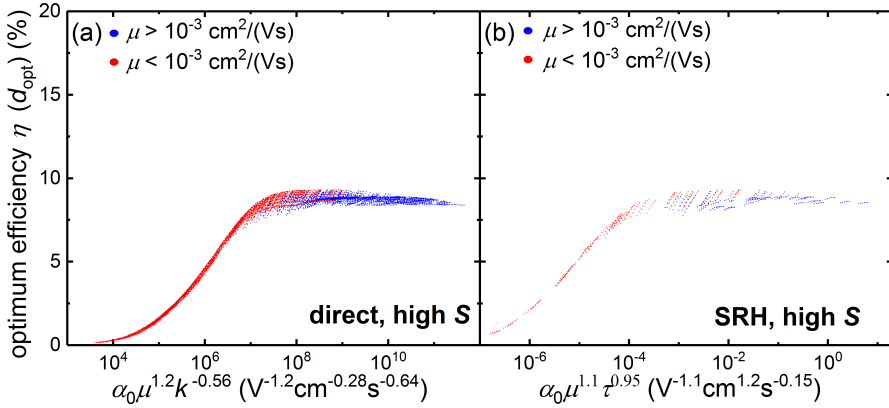


**Figure C.8.:** For the case of high surface recombination velocities and low mobilities, the correlation of the efficiency to a FOM depending on  $\alpha_0$ ,  $\mu$  and  $\tau$  (or  $k$ ) is slightly improved in the linear regime by altering the weights and emphasizing the mobility. Compare (a) with fig. C.9(c) and (b) with fig. 5.11(a).

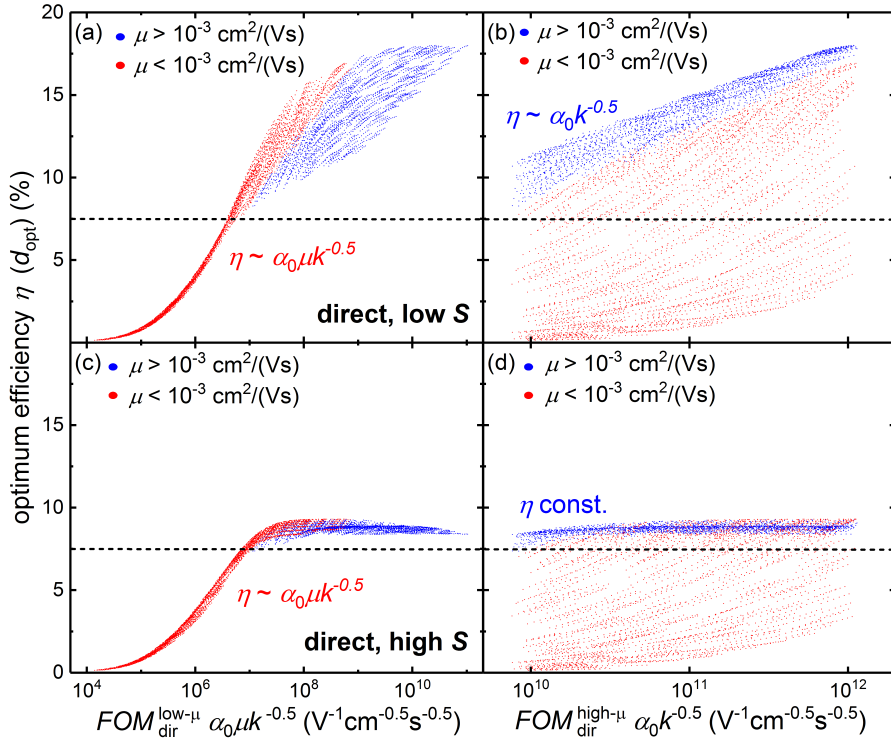


**Figure C.9.:** Simulations corresponding to fig. 5.10 and fig. 5.11 for the case of direct recombination yielding qualitatively and quantitatively similar results. The dashed lines indicate the transition to efficiency saturation for high surface recombination velocities.

### C. Charge Collection

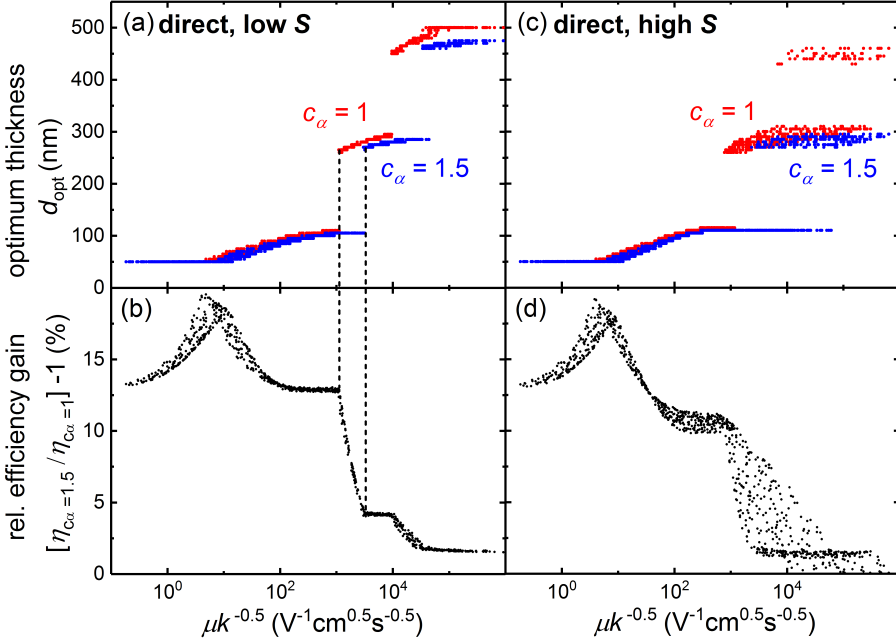


**Figure C.10.:** Connection between (a,c) optimum absorber thickness and (b,d) efficiency gain for simulated organic solar cells. (b) is identical to fig. 5.16(d). The case of strong surface recombination in (c,d) is similar to that of low surface recombination in (a,b) discussed in the following. The discretization of the optimum thickness stems from the presence of absorption maxima visible in fig. 5.16(a). The optimum thickness should in principle tend towards 0 nm for the lowest values of  $\mu k^{-0.5}$  but saturates at 50 nm simply because thinner devices were not simulated. For increasing  $\mu k^{-0.5}$ ,  $d_{\text{opt}}$  increases continuously until the first absorption maximum at 100 nm is reached. No further increase of  $d_{\text{opt}}$  with  $\mu k^{-0.5}$  is observed until an abrupt jump to the second absorption maximum occurs. The features in (b) coincide with the jumps to higher absorption maxima in (a) as can be seen from the guiding dashed lines. The  $\mu k^{-0.5}$  value at which a jump to higher maxima occurs, results from the tradeoff between a higher absorptance and lower charge collection efficiency when the absorber thickness increases. The gain in absorptance with thickness is higher at a lower absolute value of the absorptance, but charge collection is mostly independent of the absorption strength. Consequently, for the weaker absorbing blend, the tradeoff becomes favorable at lower  $\mu k^{-0.5}$  values as also observed in fig. 5.14.

# D. $\text{Sb}_2\text{S}_3$

## Absorber Film Characterization

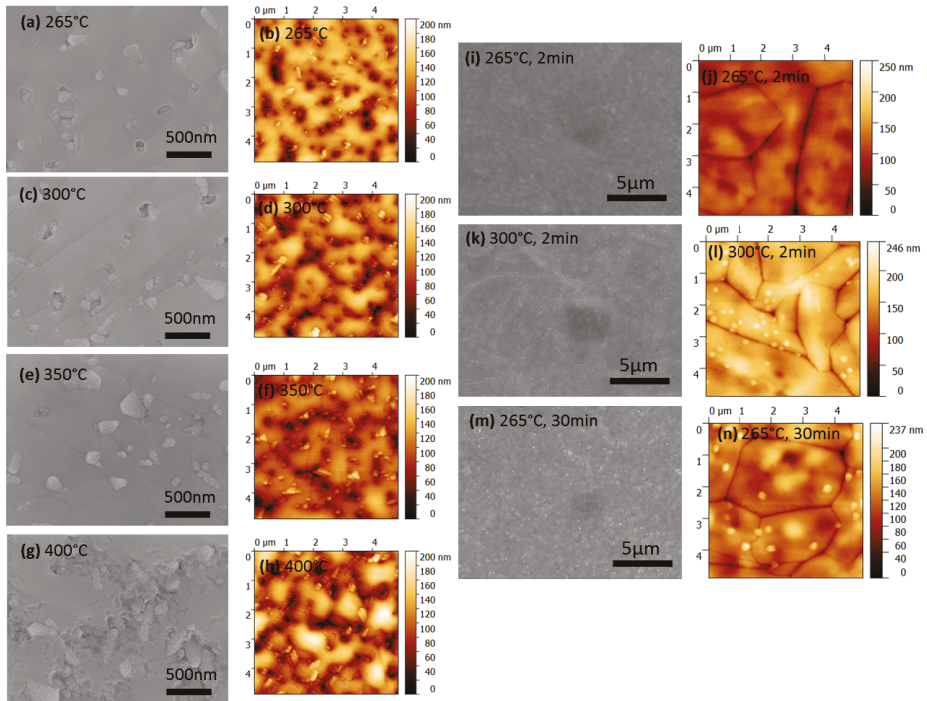


**Figure D.1.:** SEM (a,c,e,g) and AFM (b,d,f,h) images of Sb-TU samples crystallized at different temperatures. (a,b,d) are also shown in chapter 6.1. Zoomed-out SEM images (i,k,m) and AFM scans (j,l,n) of the Sb-BDC process after crystallization. Grain sizes are similar through (i,k,m). The underlying FTO morphology is visible. Unlike in (m) and especially (k) no pyramidal features are observed in (i).

## D. $Sb_2S_3$

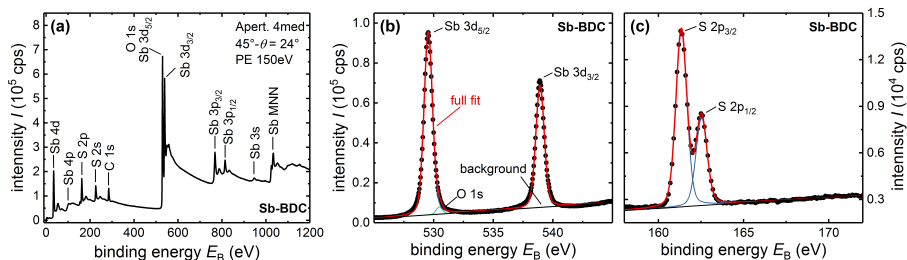


**Figure D.2.:** (a) Representative XPS survey spectrum. For Sb-TU samples an additional Indium peak would be visible. The atomic ratios in table 6.1, that express the sample stoichiometry are obtained from the ratios of the fitted peak areas. For Sb, either the 4d peaks in fig. 6.4 or the (b) Sb 3d peaks are used. For S, the (b) S 2p peaks are used. The displayed example of Sb-BDC annealed at 265 °C is representative for all measured samples. The oxygen O 1s in (b) is overlapping with the stronger Sb 3d peak, so that the extracted stoichiometry value for oxygen should be taken with care. In the case of Sb-TU, the peak could additionally origin from the substrate so that no definite information about any oxygen impurity phase can be gained from this peak. No undesired atomic or molecular species [20,33,291] of  $Sb_2O_3$  (540 eV),  $Sb_2(SO_4)_3$  (168 eV) or elemental sulfur (164 eV) are observed. In particular, the Sb  $3d_{3/2}$  is fitted with a single peak and fitting does not require an additional contribution [20] from  $Sb_2O_3$ .

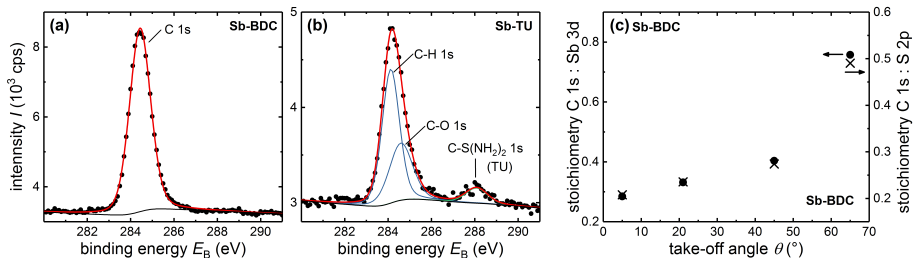


**Figure D.3.:** The carbon peak shown for (a) Sb-BDC and (b) Sb-TU can be fitted either by one or two peaks due to the strong overlap of the constituting peaks. For Sb-TU another carbon species is present that might be attributed to the precursor thiourea (TU). (c) Angle-resolved XPS shows that the carbon content decreases drastically with distance from the surface pointing towards residual carbon deposited from the atmosphere rather than residues from the deposition process. The take-off angle is measured relative to the surface normal and larger angles mean that the probed material volume is closer to the surface.

## Solar Cell Performance

**Table D.1.:** Device performance of samples shown in the annealing study in fig. 6.3 in chapter 6.1.

$T_{\text{anneal}}(^{\circ}\text{C})$	$t_{\text{anneal}}(\text{min})$	$V_{\text{oc}}(\text{mV})$	$FF(\%)$	$J_{\text{sc}}(\text{mAcm}^{-2})$	$\eta(\%)$
<b>Sb-TU</b>					
265	30	570	44.8	10.6	2.71
300	30	539	45.6	10.1	2.48
345	30	406	42.4	10.1	1.74
400	30	280	37.3	9.2	0.96
<b>Sb-BDC</b>					
265	2	605	46.1	14.1	3.94
300	2	567	41.0	13.0	3.02
265	30	563	43.7	13.0	3.19

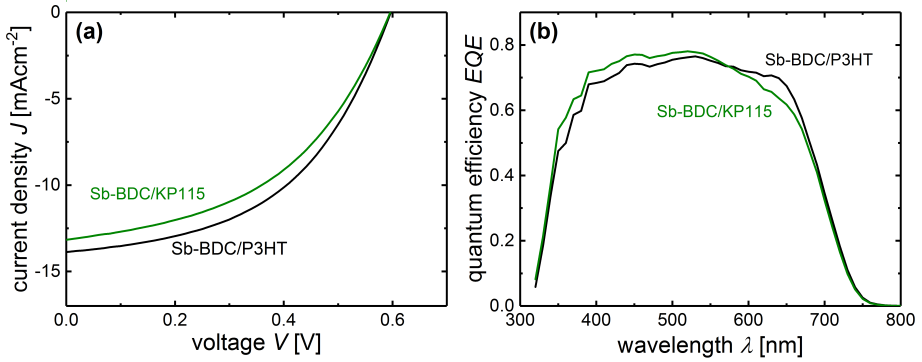


**Figure D.4.:** Comparison of the Sb-BDC process with KP115 as HTM shown in chapter 6.6 with a P3HT device fabricated on the same day which did not reach the efficiency of the  $\text{Sb}_2\text{S}_3/\text{P3HT}$  cell presented in chapter 6.6.

## Luminescence

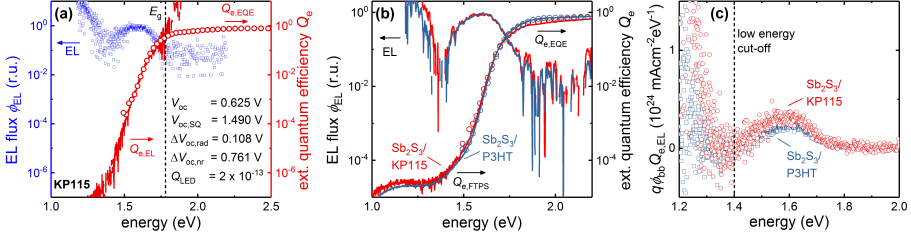


**Figure D.5.:** Voltage loss analysis for  $Sb_2S_3$  solar cells from the Sb-BDC precursor. (a) Voltage losses with KP115 as HTM instead of P3HT, which is shown shown in fig. 6.9 in section 6.2.3. (b) Comparison of electroluminescence (smoothed by 10 points moving average) and quantum efficiency (FTPS and EQE measurements) for solar cells from the Sb-BDC process, that apply the different polymers P3HT (blue curves) and KP115 (red curve). The vanishing difference between the two polymers suggest that the  $Sb_2S_3$  bulk limits the device performance or that, despite different HOMO levels in the isolated state, the polymer energy levels shift to a similar value when applied in a heterojunction with  $Sb_2S_3$ . (c) The calculations in (a) and fig. 6.9 in section 6.2.3 only consider EL data at energies above 1.4 eV due to the strong noise and background signal at lower energies. The figure shows the spectral contributions to  $V_{oc,rad}$ , which results from the area beneath the scattered curves and justifies the cut-off energy.

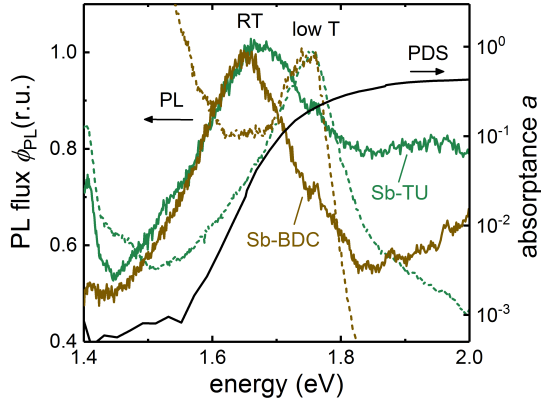


**Figure D.6.:** The Sb-TU (green) and Sb-BDC (brown) process show similar photoluminescence at room temperature (RT, solid) and 90 K (low T, dashed), when uncertainty from low emission strength in conjunction with background noise and substrate emission is considered.

## Simulations of Charge Carrier Collection

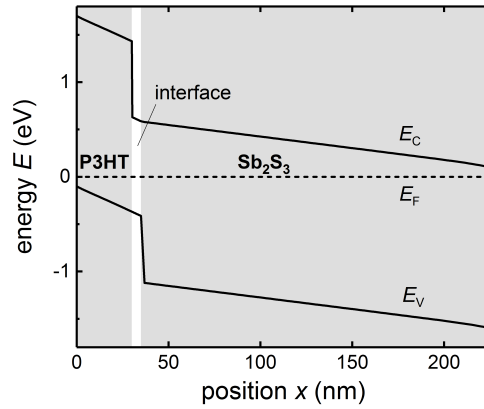
**Table D.2.:** Input parameters of the drift-diffusion simulations on the influence of the midgap defect density of states (DOS) on the  $FF$ . The stack is reduced to the  $\text{Sb}_2\text{S}_3/\text{P3HT}$  heterojunction with a recombination layer in between, which is of minor importance in this context. The resulting band diagram is shown in fig. D.7. The HTM is assumed fully transparent and only the  $\text{Sb}_2\text{S}_3$  absorbs according to Lambert-Beer and such that a short-circuit current similar to the Sb-BDC cells in section 6.1.4 is obtained. The layer thicknesses reflect Sb-BDC samples and all other parameters are rationalized in section 6.12. Schottky barriers are set to 0.1 eV and surface recombination velocities are set to  $S_{\text{min}} = 10^5 \text{ cm/s}$  and  $S_{\text{maj}} = 10^9 \text{ cm/s}$ . For simplicity of modeling, the parametrization of the defect distribution reflects the experimental results for Sb-TU, which show an exponential tail-like defect distribution with high characteristic energies ( $E_{\text{ch}}$ ) in fig. 6.10. The DOS is parametrized in the bottom table by  $E_{\text{ch}}$  and the DOS at the beginning of the tail for each of the two bands. Symmetric configurations share the same tail parametrization, which differs for the asymmetric case. The denomination of the cases is identical to fig. 6.12. The capture rates of neutral ( $C_{\text{n}}$ ) and charged ( $C_{+/-}$ ) states characterize the trapping dynamics.

parameter		P3HT	interface	$\text{Sb}_2\text{S}_3$	Unit
layer thickness	$d$	30	5	190	nm
electron affinity	$\chi$	3.3	4.1	4.1	eV
electrical band gap	$E_{\text{g}}$	1.8	1	1.7	eV
dielectric constant	$\epsilon_{\text{r}}$	3.5	3.5	13	-
absorption coeff.	$\alpha$	0	0	$1.4 \times 10^{-4}$	$\text{cm}^{-1}$
SRH lifetime	$\tau$	$5 \times 10^{-7}$	$2.5 \times 10^{-8}$	$5 \times 10^{-8}$	s
mobility	$\mu_{\text{e,h}}$	$10^{-3}$	$10^{-3}$	$4 \times 10^{-1}$	$\text{cm}^2 (\text{Vs})^{-1}$
acceptor doping	$N_{\text{d}}$	$5 \times 10^{15}$	0	$10^{13}$	$\text{cm}^{-3}$
effective DOS	$N_{\text{c,v}}$	$10^{19}$	$10^{19}$	$10^{19}$	$\text{cm}^{-3}$

		none	symm., low	asymm.	symm., high	unit
CB tail	$E_{\text{ch,CB}}$	0	0.1	0.1	0.15	eV
	$DOS_{\text{CB}}$	0	$3.5 \times 10^{16}$	$3.5 \times 10^{16}$	$9 \times 10^{16}$	$\text{cm}^{-3}$
VB tail	$E_{\text{ch,VB}}$	0	0.1	0.15	0.15	eV
	$DOS_{\text{VB}}$	0	$3.5 \times 10^{16}$	$9 \times 10^{16}$	$9 \times 10^{16}$	$\text{cm}^{-3}$
capture rates	$C_{\text{n}}$	-	$10^{-7}$	$10^{-7}$	$10^{-7}$	$\text{cm}^3 \text{s}^{-1}$
	$C_{+/-}$	-	$5 \times 10^{-8}$	$5 \times 10^{-8}$	$5 \times 10^{-8}$	$\text{cm}^3 \text{s}^{-1}$
tail length	-	-	0.55	0.55	0.55	eV

D.  $\text{Sb}_2\text{S}_3$



**Figure D.7.:** Equilibrium band diagram for the drift-diffusion simulations of  $\text{Sb}_2\text{S}_3$  resulting from the parametrization given in table D.2. There is a considerable valence band offset at the  $\text{Sb}_2\text{S}_3$ /HTM heterojunction, which reduces the electric field in the  $\text{Sb}_2\text{S}_3$ . The gradient of the energy levels is higher in the P3HT than in the  $\text{Sb}_2\text{S}_3$ , because of the lower dielectric constant of organic materials. Consequently the field in the  $\text{Sb}_2\text{S}_3$  decreases further.

## E. Recipes

### TiO<sub>2</sub>

- solution: mix 9.6 ml titaniumdisopropoxidbis(acetylacetonate) 75wt% with 90.4 ml dry ethanol to obtain 0.2M solution.
- treat substrates in ozone cleaner or in O<sub>2</sub> plasma.
- place substrates on a pre-heated (~200 °C) hot plate. Cover edges with metal mask (16 mm slit width for 20 mm substrates) to later enable low resistance front contact (TiO<sub>2</sub> cannot be scratched away easily). Protect unused surface of hot plate with aluminum foil to avoid TiO<sub>2</sub> deposition on the hot plate.
- heat up to ~470 °C (measure with suitable probe thermometer) within ~10 min.
- move sprayer (column chromatographer from Sigma Aldrich) vertically across substrates in a distance of ~15 cm. Start spraying next to substrates, move over within ~1 s across substrates and stop spraying after passing the last substrate. Repeat 3 cycles (back and forth).
- let hot plate cool down to ~200 °C before moving the hot substrates to the glovebox.

### Sb<sub>2</sub>S<sub>3</sub> from Sb-TU

coated with SCC-200 coater by KLM.

- solution: dissolve 1 mmol/ml SbCl<sub>3</sub> (228.11 g/mol) in DMF by stirring for at least 30 min. Add solution to 1.8 mmol/ml thiourea (76.12 g/mol) and stir again for at least 30 min. Solution is stable for several days.
- filter clear yellow solution with 200 nm PTFE filter
- spin-coating: dispense 150 μl for on 2 cm x 2 cm substrates and spin-coat at 70 rps for 40 s with 3 s acceleration
- annealing: ~60 min at 100°C (when processing multiple substrates, annealing time might vary over 15 min, which did not lead to notable changes in de-

## *E. Recipes*

vice performance). Then heat up to 180 °C and leave for 10 min to obtain amorphous Sb<sub>2</sub>S<sub>3</sub> film. Crystallize on a second hot plate at 265 °C for 30 min.

### **Sb<sub>2</sub>S<sub>3</sub> from Sb-BDC**

coated with SCC-200 coater by KLM.

- solution: mix 1.5 ml CS<sub>2</sub> (25 mmol) with 2 ml ethanol. Add solution to 1 mmol Sb<sub>2</sub>O<sub>3</sub> powder (291.5 mg) and mix for ~30 min. Add 2 ml n-butylamine (20 mmol) dropwise, let solution cool down each time after adding 0.5 ml to avoid evaporation of C<sub>2</sub>S and n-butylamine (boiling point 40°C) in the exothermal reaction. Red phases form temporarily, solution is first hazy and turns clear yellow after ~2 h stirring. Solution is stable for few days.
- filter clear yellow solution with 200 nm PTFE filter
- spin-coating: dispose 200 µl for on 2 cm x 2 cm substrates and spin-coat at 133 rps for 30 s with 3 s acceleration.
- annealing: 1 min at 200°C. Crystallize on a second hot plate at 265 °C for 2 min. Results are sensitive to precise annealing times and temperature.

### **HTM**

coated with SPIN150i coater by SPS-Europe.

- P3HT for Sb-TU (Sb-BDC) process: 15 mg/ml (10 mg/ml) in CB, stir overnight at 65 °C, dispose 130 µl and coat at 6000 rpm for 120 s with 3 s acceleration, dry at 130 °C for 15 min on hot plate.
- KP115 for Sb-TU (Sb-BDC) process: 10 mg/ml in DCB, stir overnight at 110 °C, dispose 150 µl of hot solution and coat at 1500 rpm (4000 rpm) for 120 s with 3 s acceleration, dry in petri dish for ~3h.
- PCPDTBT: 10 mg/ml in CB, stir overnight at 70 °C, dispose 150 µl of hot solution and coat at 2000 rpm for 110 s with 10 s acceleration, dry in petri dish.
- PTB7-Th: 10 mg/ml in CB, stir 4 h at 85 °C, dispose 150 µl of hot solution and coat at 1000 rpm for 60 s with 2 s acceleration, dry in petri dish for ~3h.

- spiro: 72.6 mg/ml in CB, add 17.5  $\mu\text{l}$  of Li-TFSI solution (520 mg/ml in acetonitrile) and 28.8  $\mu\text{l}$  of 4-tert-butylpyridine (TBP), stir at 100  $^{\circ}\text{C}$  for 3 min and cool for at least 30 min, dispose 150  $\mu\text{l}$  and coat at 3000 rpm for 60 s with 3 s acceleration, dry in dehydrated climate chamber of artificial air overnight.
- PffBT4T-2OD: 10 mg/ml in DCB, stir 4 h at 110  $^{\circ}\text{C}$ , dispose 150  $\mu\text{l}$  of hot solution on pre-heated substrate and coat at 1000 rpm for 60 s with 2 s acceleration, dry at 85  $^{\circ}\text{C}$  for 5 min on hot plate.
- PCDTBT: 7 mg/ml in CB, stir overnight at 110  $^{\circ}\text{C}$ , dispose 150  $\mu\text{l}$  of hot solution and coat at 2000 rpm for 110 s with 10 s acceleration, dry in petri dish.
- IDTBR: 20 mg/ml in CB, stir overnight at 70  $^{\circ}\text{C}$ , dispose 150  $\mu\text{l}$  of hot solution and coat at 1000 rpm for 110 s with 10 s acceleration, dry in petri dish.
- ICBA: 22 mg/ml in CB, stir overnight, dispose 110  $\mu\text{l}$  and coat at 3000 rpm for 60 s with 3 s acceleration, dry in petri dish.
- FBR: 20 mg/ml in CB, stir overnight at 70  $^{\circ}\text{C}$ , dispose 150  $\mu\text{l}$  of hot solution and coat at 1000 rpm for 110 s with 10 s acceleration, dry in petri dish.

# F. Glossary

## Abbreviations

PV – photovoltaic

TF – thin-film

c-Si – (mono/multi) crystalline silicon

CIQS – Cu(In,Ga)Se<sub>2</sub>

a-Si – amorphous silicon

μc-Si – microcrystalline silicon

QD – quantum dots

OPV – organic photovoltaics

OSC – organic solar cell

BHJ – bulk heterojunction

SQ – Shockley-Queisser

TCO – transparent conductive oxide

ETL, ETM – electron transport layer/material

HTL, HTM – hole transport layer/material

SCR – space-charge region

SRH – Shockley-Read-Hall

ETA – extremely thin absorber

ALD – atomic layer deposition

(R)TE – (rapid) thermal evaporation

rps/rpm – sounds per second/minute (spin-coating)

## Physical Constants and Quantities

$q$  – elementary charge

$c$  – speed of light  
 $h, \hbar$ , – Planck constant, reduced Planck constant  
 $k_b$  – Boltzmann constant  
 $\epsilon_0$  – vacuum permittivity  
 $EQE$  – external quantum efficiency  
 $V_{bi}$  – built-in voltage  
 $E_c$  – conduction band energy  
 $E_v$  – valence band energy  
 $E_g$  – band gap energy  
 $E_F$  – Fermi level, Fermi energy  
 $E_{F,n}$  – electron quasi-Fermi level/energy  
 $E_{F,p}$  – hole quasi-Fermi level/energy  
 $\lambda$  – wavelength  
 $T$  – temperature  
 $\eta$  or PCE – (power conversion) efficiency  
 $V_{oc}$  – open-circuit voltage  
 $J_{sc}$  – short-circuit current  
 $FF$  – fill factor  
 $MPP$  – maximum power point  
 $n_{id}$  – diode ideality factor  
 $J_0$  – saturation current density  
 $J_{ph}$  – photocurrent  
 $J$  – current density  
 $V$  – voltage  
 $G$  – (free) charge carrier generation rate  
 $d$  – absorber layer thickness  
 $\epsilon_r$  – relative permittivity, also: dielectric constant

## F. Glossary

$\alpha$  – absorption coefficient

$\mu$  – mobility

$\tau$  – (Shockley-Read-Hall) lifetime

$f_c$  – charge carrier collection efficiency

$S$  – surface recombination velocity

## Organic Polymer Donors and Acceptor Molecules

P3HT – poly(3-hexylthiophene)

KP115 – poly[(4,4'-bis(2-ethylhexyl)dithieno[3,2-b:2',3'-d]silole)-2,6-diyl-alt-(2,5-bis(3-tetradecylthiophen-2-yl)thiazolo[5,4-d]thiazole)-2,5-diyl]

PCPDTBT – poly[2,6-(4,4-bis-(2-ethylhexyl)-4H-cyclopenta[2,1-b:3,4-b']-dithiophene)-alt-4,7-(2,1,3-benzothiadiazole)]

spiro or spiro-OMeTAD – 2,2',7,7'-tetrakis-(N,N-di-p-methoxyphenylamine)9,9'-spirobifluorene

PfBT4T – poly[(5,6-difluoro-2,1,3-benzothiadiazol-4,7-diyl)-alt-(3,3''-di(2-nonyltridecyl)-2,2';5',2'';5'',2''')-quaterthiophen-5,5''-diyl)]

MDMO-PPV – (poly)[2-methyl,5-(3\*,7\*\* dimethyloctyloxy)]- p-phenylene vinylene

PCDTBT – (poly)N-9''-hepta-decanyl-2,7-carbazole-alt-5,5-(4',7'-di-2-thienyl-2',1',3''-benzothiadiazole)

PTB7 – (poly)[4,8-bis[(2-ethylhexyl)oxy]benzo[1,2-b:4,5-b']dithiophene-2,6-diyl][3-fluoro-2-[(2-ethylhexyl)carbonyl]thieno[3,4-b]thiophenediyl]

PTB7-Th – (poly)4,8-bis(5-(2-ethylhexyl)thiophen-2-yl)-benzo[1,2-b:4,5-b']dithiophene-co-3-fluorothieno[3,4-b]-thiophene-2-carboxylate

PNTz4T – (poly)quaterthiophene-naphtho[1,2-c:5,6-c']bis[1,2,5]thiadiazole

PBDB-T – (poly)(2,6-(4,8-bis(5-(2-ethylhexyl)thiophen-2-yl)benzo[1,2-b:4,5-b']dithiophene)-co-(1,3-di(5-thiophene-2-yl)-5,7-bis(2-ethylhexyl)benzo[1,2-c:4,5-c']dithiophene-4,8-dione)

BTR – benzodithiophene terthiophene rhodanine

PBnDT – benzodithiophene

HTAZ – 2-alkyl-benzo[d][1,2,3]triazole

FTAZ – fluorinated analogue of HTAZ

PBDTS-TDZ – (poly)[benzo[1,2-b:4,5-b']dithiophene] 1,3,4-thiadiazole

PBDB-T-SF – (poly)(2,6-(4,8-bis(5-(2-ethylhexylthio)-4-fluorothiophen-2-yl)-benzo[1,2-b:4,5-b']dithiophene))-alt-(5,5-(1',3'-di-2-thienyl-5',7'-bis(2-ethylhexyl)benzo[1',2'-c:4',5'-c']dithiophene-4,8-dione)

DPPTTT – thieno[3,2-b]thiophene-diketopyrrolopyrrole

PC<sub>60</sub>BM – [6,6]- phenyl C<sub>61</sub>-butyric acid methyl ester

PC<sub>70</sub>BM – [6,6]- phenyl C<sub>71</sub>-butyric acid methyl ester

BisPC<sub>70</sub>BM – bis-adduct of PC<sub>70</sub>BM

ITIC – 3,9-bis(2-methylene- (3-(1,1-dicyanomethylene)-indanone)-5,5,11,11-tetrakis(4-hexylphenyl)-dithieno[2,3-d:2',3'-d']-s-indaceno[1,2-b:5,6-b']-dithiophene

IT-M – 3,9-bis(2-methylene- (5&6-methyl- (3-(1,1-dicyanomethylene)-indanone)-5,5,11,11-tetrakis(4-hexylphenyl)-dithieno[2,3-d:2',3'-d']-s-indaceno[1,2-b:5,6-b']-dithiophene

IT-4F – 3,9-bis(2-methylene- (5,6-difluoro- (3-(1,1-dicyanomethylene)-indanone)-5,5,11,11-tetrakis(4-hexylphenyl)-dithieno[2,3-d:2',3'-d']-s-indaceno[1,2-b:5,6-b']-dithiophene

FBR – (5Z,50Z)-5,50-[(9,9-dioctyl-9H-fluorene-2,7-diyl)bis[2,1,3-benzothiadiazole-7,4-diyl(Z)methylidene]]bis(3-ethyl-2-thioxo-1,3-thiazolidin-4-one)]

IDTBR – [(Z)-5- {[5-(15-{5-[(Z)-(3-Ethyl-4-oxo-2-thioxo-1,3-thiazolidin-5-ylidene)methyl]-8-thia-7.9-diazabicyclo[4.3.0]nona-1(9),2,4,6-tetraen-2-yl]-9,9,18,18-tetrakis(2-ethylhexyl)-5.14-dithiapentacyclo[10.6.0.0.3,10.0.4,8,0.13,17] octadeca-1(12),2,4(8),6,10,13(17),15-heptaen-6-yl)-8-thia-7.9-diazabicyclo[4.3.0]nona-1(9),2,4,6-tetraen-2-yl]methylidene}-3-ethyl-2-thioxo-1,3-thiazolidin-4-one]

## Solvents & Other Chemicals

CB – chlorobenzene

DBC – 1,2-dichlorobenzene

DMF – N,N-dimethylformamide

TU – thiourea (NH<sub>2</sub>CSNH<sub>2</sub>)

TA – thioacetamide (CH<sub>3</sub>CSNH<sub>2</sub>)



# Acknowledgements

Despite the fact that a PhD thesis is a single author work, this does not quite reflect the reality scientific work. During my years of doctoral research, I received support from many people - both on a professional and personal level. First of all, I have to cherish the supporting, considerate and helpful atmosphere at the IEK-5: Photovoltaics. Whenever I took on activities outside of my routine work, I could find people who were happy and capable in helping to find solutions. In the following, I would like to take the chance and express my gratitude to several individuals who have enabled the success of this thesis.

**Prof. Dr. Kirchartz** for everything: for accepting me as a doctoral researcher, teaching me and directing me towards most of what I know about solar cells, for coming up with creative, clever and knowledgeable ideas, for guiding me in scientific communication regarding publishing, presenting and being audience-centered, for being approachable, open and helpful in discussions, and finally for his support in obtaining a postdoc position. **Prof. Dr. Jan Anton Koster** for agreeing on being the second examiner, and for an interesting and non-defence-like discussion during my defence. **Prof. Dr. Czulwik**, **Prof. Dr. Stöhr**, and **Prof. Dr. Grabmaier**, for being members of the examination committee and getting me to broaden my horizon in preparation for my defence.

**Prof. Dr. Reinhard Carius** for sharing his extensive knowledge and small secrets about many refined characterization setups at Jülich, and for his insights and provocative doubt about all kinds of scientific and non-scientific topics. **Prof. Dr. Uwe Rau** for many insightful conversations on the conceptual level of solar cells, especially in the later stage of my thesis, and also for his lecture on photovoltaics that I took during my master's, which provided a basic understanding of photovoltaics and - most importantly - amplified my fascination for solar cell research. **Dr. Benjamin Klingebiel** for narrowing my knowledge gap on practical and textbook chemistry, for taking care of equipment and people in the chemistry lab, for performing UPS/XPS measurements and finally for his feedback on this thesis. **Ulrike Gerhards** for her aid in establishing reproducible fabrication pro-

## *Acknowledgements*

cesses for  $\text{Sb}_2\text{S}_3$ , and for suffering through my sometimes volatile sample planning. **Irina Kühn** and **Dorothea Lennartz** for keeping the chemistry lab going on a daily base and Dorothea also for sharing an office for most of my time in Jülich. **Oliver Thimm** for numerous PDS and CPM measurements and his “sure, let’s try it” attitude. **Markus Hülsbeck** for several PL and Raman measurements, getting the EL ready and for his support in all questions about optical and electronic setups. **Wilfried Reetz** and **Christoph Zahren** for taking care of proper and trustworthy EQE and Solar Simulator setups and for accompanying my first steps in the IEK-5 during my Bachelor thesis along with **Dirk Erdweg** and **Willi Hilgers**. Many other IEK-5 professionals for generally enabling controlled environments for fabrication and characterization allowing good data quality. **Dr. Jan Flohre** for support on spectroscopic measurements and their interpretation. **Dr. Jan Mock** for sticking through many frustrating thermopower measurements of apparently non-conductive samples and for introducing me to the events around a closeby forest and pit. **Lisa Krückemeier** for help with EL measurements, for providing optical data, and for detailed feedback on the defence trial talk. **Dr. Senol Öz** for transferring the  $\text{TiO}_2$  process. **Dr. Bart Pieters** for contributing a real understanding of the malice of simulations and how to work around them. **Johanna Siekmann** for joining me on team  $\text{Sb}_2\text{S}_3$  and sticking through non-negligible nuisances. **Paula Hartnagel** for agreeing to sit in a rather musty office and mastering PVMOS.

**Dr. Yong Chan Choi** for being my external Hitec mentor and hosting me in Daegu. **Prof. Dr. Josef Granwehr** for being my internal Hitec mentor and roughly lying out the international research landscape for postdocs. **Prof. Dr. Moritz Riede** for speeding up my thesis submission by hiring me and then for enabling me to wrap up the remaining work. **Dr. Christian Dickel** and **Dr. Jens Kellner** for feedback and improvements on this manuscript. **David Grabowski** for (successful if anyone reads this) logistics in the submission. **Dr. Paolo Cadiz-Bedini** and **Aryak Singh** (and certainly others) for organizing a lovely farewell from the institute, for inspiring as well as absurd conversations. **Jinane Haddad** for relaxing breaks. All members of the **Kirchartz group** and many other PhDs and postdocs at the institute, who became allies and friends. Friends from the monthly **beverage-centered meet-up of IEK-5 alumni** or soon-to-be alumni for fun and shifting the mindset to a time after the PhD. My housemates, mates from music sessions and all

other mates for enjoyable times away from research. **Dr. Alberto Privitera** and **Ross Warren** for successful distraction from defence preparations on our Berlin conference boat. Everyone from Jülich, studies, school and hometown - especially the several surprise visitors - for celebrating my defence with me and leaving me with amazing and slightly vague memories of the day. **Franzi**, for being the encouraging, challenging and completing element of my personal life for the largest part of this thesis. And finally and probably most outstandingly, my **parents** and **family** for too many things to be listed here. Finally, I have come to recognize that even in enjoyable, exciting and demanding professional times, it is vital to create enough space for social life, for fun and for one's various passions.

# List of Journal Publications

- P. Kaienburg, U. Rau, and T. Kirchartz, “Extracting information about the electronic quality of organic solar-cell absorbers from fill factor and thickness”, *Phys. Rev. Appl.*, 6, 024001–1, 2016.
- P. Kaienburg, B. Klingebiel, and T. Kirchartz, “Spin-coated planar Sb<sub>2</sub>S<sub>3</sub> hybrid solar cells approaching 5% efficiency”, *Beilstein J. Nanotech.*, 9, 2114–2124, 2018.
- P. Kaienburg, P. Hartnagel, B. E. Pieters, J. Yu, D. Grabowski, Z. Liu, J. Haddad, U. Rau, and T. Kirchartz, “How contact layers control shunting losses from pinholes in thin-film solar cells”, *J. Phys. Chem. C*, 122, 27263–27272, 2018.
- P. Kaienburg, L. Krückemeier, D. Lübke, J. Nelson, U. Rau, and T. Kirchartz, “The  $\alpha\mu\tau$ -Product as a Figure of Merit for Solar Cell Absorber Materials”, *Phys. Rev. Research*, submitted.
- T. Kirchartz, P. Kaienburg, and D. Baran, “Figures of merit guiding research on organic solar cells”, *J. Phys. Chem. C*, 122, 5829–5843, 2018.
- L. Krückemeier, P. Kaienburg, J. Flohre, K. Bittkau, I. Zonno, B. Krogmeier, and T. Kirchartz, “Developing design criteria for organic solar cells using well-absorbing non-fullerene acceptors”, *Commun. Phys.*, 1, 2018.
- S. Wang, P. Kaienburg, B. Klingebiel, D. Schillings, and T. Kirchartz, “Understanding thermal admittance spectroscopy in low-mobility semiconductors”, *J. Phys. Chem. C*, 122, 9795–9803, 2018.
- D. Baran, T. Kirchartz, S. Wheeler, S. Dimitrov, M. Abdelsamie, J. Gorman, R. S. Ashraf, S. Holliday, A. Wadsworth, N. Gasparini, P. Kaienburg, H. Yan, A. Amassian, C. J. Brabec, J. R. Durrant, and I. McCulloch, “Reduced voltage losses yield 10% efficient fullerene free organic solar cells with >1 V open circuit voltages”, *Energy & Envir. Science*, 9, 3783–3793, 2016.

Band / Volume 468

**Study on a miniaturized satellite payload  
for atmospheric temperature measurements**

J. Liu (2019), 153 pp

ISBN: 978-3-95806-415-7

Band / Volume 469

**Partitioning Water Vapor Fluxes by the Use of Their Water Stable  
Isotopologues: From the Lab to the Field**

M. E. Quade (2019), XVI, 113 pp

ISBN: 978-3-95806-417-1

Band / Volume 470

**Entwicklung von Reparaturmethoden für Nickel-Superlegierungen  
mittels thermischer Spritzverfahren**

T. Kalfhaus (2019), VI, 126, XXX pp

ISBN: 978-3-95806-418-8

Band / Volume 471

**Entwicklung von korrosionsstabilen Schutzschichten für oxidische  
Faserverbundwerkstoffe**

C. S. Gatzert (2019), II, 143 pp

ISBN: 978-3-95806-422-5

Band / Volume 472

**Coatings for Metallic Bipolar Plates in High-Temperature  
Polymer Electrolyte Fuel Cells**

R. Li (2019), II, 119 pp

ISBN: 978-3-95806-425-6

Band / Volume 473

**Thermochemische Eigenschaften von kombinierten Katalysator- und  
Sauerstoffträgersystemen für die partielle Oxidation von Teeren aus der  
Biomassevergasung**

M. Ma (2019), VII, 157 pp

ISBN: 978-3-95806-426-3

Band / Volume 474

**Einfluss der klimatischen Fertigungsumgebung auf die Mechanik und  
Rissstrukturierung der elektrodenbeschichteten Membran einer PEM-  
Brennstoffzelle**

B. Wienk-Borgert (2019), IV, 141 pp

ISBN: 978-3-95806-428-7

Band / Volume 475

**Reversible wasserstoffbetriebene Festoxidzellensysteme**

M. H. Frank (2019), 187 pp

ISBN: 978-3-95806-430-0

Band / Volume 476

**Partitioning of carbon dioxide exchange  
in rapidly and slowly changing ecosystems**

P. Ney (2019), xvi, 95 pp

ISBN: 978-3-95806-431-7

Band / Volume 477

**Massentransportphänomene in Schichtsystemen eines Elektrolyseurs**

U. Panchenko (2019), 107 pp

ISBN: 978-3-95806-433-1

Band / Volume 478

**Mechanische Eigenschaften von Polymer-Elektrolyt-Membran-  
Brennstoffzellen**

P. Irmischer (2019), vii, 177 pp

ISBN: 978-3-95806-435-5

Band / Volume 479

**Morphology and Degradation of High Temperature  
Polymer Electrolyte Fuel Cell Electrodes**

S. Liu (2019), III, 162 pp

ISBN: 978-3-95806-436-2

Band / Volume 480

**Structural uptake and retention of safety relevant radionuclides by  
cementitious materials**

S. Lange (2019), 133 pp

ISBN: 978-3-95806-437-9

Band / Volume 481

**Quantifying the Impact of Inhomogeneity, Transport and  
Recombination in Emerging Thin-Film Solar Cells**

P. Kaienburg (2019), vii, 258 pp

ISBN: 978-3-95806-440-9

Weitere *Schriften des Verlags im Forschungszentrum Jülich* unter  
<http://www.zbw1.fz-juelich.de/verlagextern1/index.asp>



Energie & Umwelt / Energy & Environment  
Band / Volume 481  
ISBN 978-3-95806-440-9